THE UNIVERSITY *of* EDINBURGH

Functional Imaging of the Human Brain using Electrical Impedance Tomography

Taweechai Ouypornkochagorn

Doctor of Philosophy The University of Edinburgh 2016

Table of Contents

Acknowledgements

I would like to thank both of my supervisors, Dr Nick Polydorides (principal supervisor) and Prof Hugh McCann (assistant supervisor and former principal supervisor). No need to explain how fortunate I am to have Dr Polydorides as my supervisor, as he is one of the world's EIT foremost experts. He became my supervisor after I had been on the doctoral program for 1 year and 11 months. His arrival gave me confidence to enter the world of "reconstruction", even though, at that time, I knew very little about it and had only a year left to complete my research. Similarly, I would like to give my sincere thanks to Prof McCann who accepted me as his PhD student in September 2012. I appreciate his patience with my English language during the PhD journey. Thank you for the great opportunity from him in July 2013 to continue my research at the University of Edinburgh. I also appreciate the financial support for house-hunting and moving my personal stuffs to Edinburgh. I am even more grateful for Prof McCann's readiness to purchase necessary new instruments and research equipment. Our research group started here in Edinburgh from scratch, but due to Prof McCann's help and encouragement, my research continued to move forward. Thanks also for introducing me to Dr Polydorides.

I am grateful to all the members in the Agile Tomography group: Andrea Chighine, Dimitris Kamilis, Yang Yunjie, Dr Alex Tsekenis, and Dr Edward Fisher. They supported me in various ways, even though, in fact, they may not have realised it! Also, I would like to acknowledge the Sensing, Imaging and Signal Processing (SISP) Group in the University of Manchester (UoM) where I spent my first year as a PhD student for 9.5 months.

I also want to thank the people in the fEITER project who constructed the functional Electrical Impedance Tomography for Evoked Response (fEITER) system and carried out the human experiments for a long period. I would like to give my special thanks to Dr John Davidson (UoM) and Dr Natasa Terzija (Elektronische Fahrwerksysteme GmbH, Germany) who taught me how to use the fEITER machine, signal program, and essential matlab codes for encoding fEITER data. I am more than grateful to Dr Paul Wright (UoM) who helped me to investigate and upgrade the fEITER system and for becoming the volunteer on my first human experiment.

Furthermore, I would like to thank the Brain Research Imaging Centre (BRIC) of the University of Edinburgh who provided excellent MR images to my research group.

My PhD could not have been accomplished without the financial support from the Royal Thai Government Scholarship Fund. I would like to thank the staff of the Office of Educational Affairs at the Royal Thai Embassy for advice and co-ordinating with the funding body in Thailand.

Rory and Roslyn Mackenzie, my best friends here, were a blessing from God. They were supportive during the hard times of the PhD journey and proofread the important sections of my thesis. Thanks to them and their friends at *Englishcorner* for the English conversation classes.

Thanks to my family in Thailand. They were always there to encourage me to keep going. I greatly appreciated having my wife and two children with me and for opportunities to explore together the world outside the research lab! Edinburgh became a more beautiful and warmer place due to their company.

Last, and most of all, thanks to my wife Mutita Dechokietawan for her excellent support. It was here in Edinburgh that she gave birth to our lovely daughter, and taught our son to be a good boy.

Taweechai Ouypornkochagorn

Edinburgh

2016

Abstract

Electrical Impedance Tomography (EIT) is a technique for imaging the spatial distribution of conductivity inside a body using the boundary voltages, in response to applied current patterns, to reconstruct an image. Even though EIT has been proved useful in several medical applications such as mechanical respiration and ventilation monitoring of the lungs, its reported success in localising cerebral conductivity changes due to brain stimulation is very scant.

In the case of the human head, the amplitude of the brain response to stimulation is usually very small and gets contaminated with physiological noise initiated from inside the cranium or the scalp. Three types of evoked responses were experimentally investigated: auditory startle response (ASR), CO_2 reactivity response, and transient hyperaemic response (THR). ASR is expected to be a result of the brain's functioning processes. However, the responses to CO_2 and THR are expected to be due to cerebral blood volume or flow, due to physiological intervention in blood supply. According to the results, even when the amplitude of EIT measurements shows profound variation as in the case of CO_2 reactivation, those could not be physiologically linked to the targeted responses and have been shown to be initiated from the scalp. The consistency of the measurements in the case of CO_2 reactivation response was poor (37.50-50%). Meanwhile in the case of THR, although the magnitude of conductivity changes was overall 50% smaller than the previous cases, the subject movement was not necessary. This could be a reason that the consistency of THR case was very good (87%), and this can emphasize the necessity to maintain the changes in the scalp at minimum levels. In the case of ASR the response magnitude was very small (six times smaller than the CO_2 reactivity case), and the evoked response can be detected with only 50% consistency.

To measure very small EIT signals (such as those expected due to brain function) effectively, one must improve the sensitivity of the measurements to conductivity changes by increasing the excitation current. The functional EIT for Evoked Response (fEITER) system used in our investigations was modified from its initial configuration to increase its excitation current from 1 mA_{pk-pk} to 2 mA_{pk-pk} or 1

mA_{rms}. The bit-truncation in the process of Phase-Sensitive Detection (PSD) has also been improved, to modify the original 16-bit data readout to be 24-bit data readout. These improvements have doubled the instrument's sensitivity, and have substantially reduced the truncation error to about 183 times. The quality of the physiological waveform was also significantly improved. Therefore, one could study more effectively very fast brain response using the modified system. For example, the latency of responses can be more precisely extracted, or the monitoring of the conductivity change in a period of only a few tens of milliseconds is then possible.

The reconstruction of brain images corresponding to these physiologically evoked responses has been the ultimate goal of this thesis. To ensure obtaining the correct images, some crucial issues regarding EIT reconstruction were firstly investigated. One of these issues concerns the modelling error of the numerical head models. The reconstruction requires an accurate model capturing the geometry of the subject's head with electrodes attached and accurate in-vivo tissue conductivities. However, since it is usually impractical to have a personalised model for each subject, many different head models (including a subject model) were constructed and investigated, to evaluate the possibility of using a generic model for all subjects. The electrode geometry was also carefully included into the models to minimise error. Another issue concerns the appropriate reconstruction algorithm. A novel non-linear reconstruction method, based on the difference imaging approach and Generalized Minimal Residual method (GMRes) algorithm, with optimal parameters and prior information, was proposed to deal with significant modelling errors. With this algorithm, the experimental results showed that it is possible to use a generic model for reconstructing an impedance change, but the magnitude of the change should be rather small. The last issue tackled was regarding the a priori choice of model parameters, and in particular the tissue conductivities. The tissue conductivities of the scalp and the skull were also estimated by a proposed methodology based on the Gauss-Newton method. The estimation showed that, compared to previous reported values, the conductivity of the scalp was higher, at 0.58 S/m, and that of the skull lower, at 0.008 S/m. Eventually, by exploiting the hardware and firmware advances in the measuring instrument in conjunction with the

proposed modelling and reconstruction algorithm, processing our experimental EIT data captured on human heads and a head-like tank confirm that the localisation and imaging of conductivity changes occurring within the head is indeed possible.

From the low quality measurements in the case of the CO_2 reactivity response, the reconstructed images of this response do not reflect the true conductivity change. The consistency of the images to localise the sources of the changes was very poor (0-50%), i.e. the conductivity changing locations in the images were likely to be random. Our analysis suggests that the changes inside the cranium are likely to be due to the large change in the scalp. In the case of THR, the reconstructed images were able to localise the response in a similar manner to what had been found on the measurements, and the consistency was quite high (76%). Meanwhile, in the case of ASR, surprisingly the consistency of the images was 82%, much higher than the consistency of the measurements, which was only 50%. This was because the changing amplitude of the measurements was too small to be noticed by visualisation, and it was practically cumbersome to investigate all measurements. This statistic confirms that image reconstruction can reveal information that is not directly apparent by observing the measurements.

In summary, EIT can be used in brain (function) imaging applications to some extent. The targeted response, which typically originates from inside the cranium is always infused with neurophysiological noise or physical noise at the scalp, and the amplitude of noise determines the possibility to localise the changes. It is also necessary for the desired response to have sufficiently large amplitude. These results show that EIT has been successful in THR and ASR, but for CO2 reactivity response, EIT lacks the necessary sensitivity.

Lay Summary

Electrical Impedance Tomography (EIT) is an imaging technique which has advantages due to portability, low cost, and the ability to use it continuously for a long period. Essentially, it requires only an array of electrodes, an excitation current source, a high speed voltage recording system, and a model of a measured subject. The measured voltage data is used to compute the image of the electrical conductivity distribution within the subject. Although the spatial resolution of the image is typically poor, i.e. the fine internal structure detail cannot be exposed, the temporal resolution of the time-series images is excellent. It has been reported that EIT can reveal the changing behaviour with the timescale of 0.5 ms on industrial applications, and of 10 ms on medical applications. Therefore, EIT is an optional tomography technique which has many areas of application, including medical applications. It has been reported that EIT has been successful with mechanical respiration and the ventilation monitoring of human lungs. EIT is also expected to be applicable for monitoring the functional response of the brain. However, implementing EIT on brain applications is very difficult. The lack of an accurate subject head model introduces a large modelling error. The very small excitation current, to be compliant with medical standards, and the signal attenuation due to the presence of the skull, cause huge difficulty to sense the conductivity change within the brain region. In addition, the physiological noise, i.e. respiratory regulation, is troublesome. All of this means that EIT on head applications is exceptionally difficult due to it being very sensitive to noise and error.

In this thesis, EIT was investigated as to whether it was possible to use it on brain applications. Certain brain stimulations were performed with the employment of a novel image reconstruction method which can handle the large modelling error to some extent. Head models were constructed for this investigation, and the tissue conductivities (that are important to model parameters) were estimated. The performance of an EIT instrument was also evaluated and some modifications were carried out. The EIT measurements were carefully investigated to identify the desirable signal and the noise. The investigation results indicate that, to some extent, EIT can be used for brain applications. EIT use in this context largely depends on

two factors: the amplitude of brain responses and the amplitude of noise. The pre-investigation on EIT measurement voltages is then a mandatory procedure to determine the possibility to obtain the expected images. In addition, the proposed novel reconstruction method was able to correctly reconstruct the situation, even when there is large modelling error.

Abbreviations

ºC	Degrees Celsius
Ω, Ω.m, Ω·m^2	Ohm, Ohm metre, Ohm square-metre
2D, 3D	2 dimensional, 3 dimensional
A, mA, μA, nA	Ampere, milli-Ampere, micro-Ampere, nano-Ampere
ABP	Artery Blood Pressure
AC	Alternating current
ADC	Analogue-to-Digital Converter
AER	Auditory Evoked Response
ASR	Auditory Startle Response
BOLD	Blood Oxygenation Level Dependent level
CBF	Cerebral Blood Flow
CG	Conjugate Gradient
CMRR	Common-Mode Rejection Ratio
CO_2	Carbon dioxide
CPLD	Complex Programmable Logic Device
CSF	Cerebrospinal Fluid
DAC	Digital-to-Analog Converter
DAQ	Data Acquisition Unit
dB	Decibel
DC	Direct Current
DP	Discrepancy Principle
ECG or EKG	Electrocardiographic signal
EEG	Electroencephalogram or Electroencephalographic signal
EIT	Electrical Impedance Tomography
EMG	Electromyography
ERG	Electroretinographic signal
ERT	Electrical Resistance Tomography
$EtCO_2$	End-tidal Carbon dioxide
fEITER	functional Electrical Impedance Tomography of Evoked Responses

FEM	Finite Element Method
FPGA	Field-Programmable Gate Array
fps	frames per second
FV	Flow Velocity
GCV	Generalized Cross-Validation
GMRes	Generalized Minimal Residual method
Hz, kHz, MHz	Hertz, kilo-Hertz, Mega-Hertz
ICP	Intracranial Pressure
IEC	International Electrotechnical Commission
IP	Ingress Protection
m, mm	Metre, Millimetre
MAP	Maximum A Posteriori
MCA	Middle Carotid Artery
MEG	Magnetoencephalogram or Magnetoencephalographic signal
MFEIT	Multi-Frequency Electrical Impedance Tomography
MHRA	Medicines and Healthcare products Regulatory Agency
MiMSEE	Minimum Mean Squared Error Estimator
mmHg	A millimetre of Mercury
MRI, fMRI, MR	Magnetic Resonance Imaging, functional Magnetic Resonance Imaging, Magnetic Resonance
ms, µs	Second, milli-Second, micro-Second
NA	Not Available
NEMA	National Electrical Manufacturers Association
NHS RECs	National Health Service Research Ethics Committees
PEEP	Positive End-Expiratory Pressure
pk-pk	Peak-to-peak
ppm	part per million
PSD	Phase-Sensitive Detection
QMR	Quasi-Minimal Residual
rCBV	regional Cerebral Blood Volume
REG	Rheoencephalographic signal
RHS	Right-Hand-Side

rms	root mean square
ROI	Region of Interest
S/m	Siemens per metre
S/s	Samples per second
SD	Standard Deviation
SEF/SEP	Somatosensory Evoked Field and Somatosensory Evoked Potential
SER	Sensory Evoked Response
SNR	Signal-to-Noise Ratio
SVD	Singular Value Decomposition
TCD	Transcranial Doppler
THR, THRT	Transient Hyperaemic Response, Transient Hyperaemic Response Test
TSVD	Truncated Singular Value Decomposition
UPRE	Unbiased Predictive Risk Estimator
USB	Universal Serial Bus
V, mV, nV	Volt, milli-Volt, nano-Volt

Chapter 1 Introduction

1.1 Electrical Impedance Imaging

Electrical Impedance Tomography (EIT) is an imaging modality presenting the spatial distribution of impedance within the boundary of a measured subject. The term "impedance" in this context commonly refers to "conductivity" (or "resistivity"). Therefore EIT is often called "Electrical Resistance Tomography (ERT)". The conductivity distribution is derived from the boundary voltage information obtained from the measurement from an array of electrodes while a small current is injected. Accurate geometry and structure of the subject is required for EIT, as well as the accurate conductivity of the measured materials in order to construct a computation model. With this model, the boundary voltages can be predicted by forward computation. However, without prior knowledge of the conductivity distribution, it can be computed by the inverse reconstruction of the boundary voltage information. The best estimated distribution (or "image") is the distribution providing the minimum prediction error.

Since the emerging of EIT in 1984 (Barber and Brown, 1984), EIT to date has been widely used in several imaging applications. For examples, EIT was used for imaging fluid flow (industrial application) or sub-surface structures (geophysical application). To use EIT for imaging in the medical area is the most challenging area of EIT to date. EIT has been used for investigating gastric emptying and pH (Vaisman et al., 1999, Watson et al., 1996), respiration and ventilation monitoring of the lungs (Davidson et al., 2012, Frerichs et al., 2006, Khambete et al., 2000, Reinius et al., 2015), breast cancer detecting (Halter et al., 2008, Saulnier et al., 2007, Ultchin et al., 2002), cardiac monitoring (Patterson et al., 2001), prostate investigating (Murphy et al., 2016, Syed et al., 2012), edema treating (Fu et al., 2014), and brain function examining (Tidswell et al., 2001a, Tidswell et al., 2001b, Tidswell et al., 2001c).

EIT is a non-invasive imaging technique where the spatial resolution is relatively poor (approximately 24 mm in the case of the human head (Abascal et al., 2008a)), but the temporal resolution is very good (up to 100 frames per second (fps)

for medical EIT (McCann et al., 2011a, Oh et al., 2011b), and up to 2,000 fps for industrial EIT (Wilkinson et al., 2005). As a (potential) medical instrument, compared to other imaging instruments, the cost of EIT instruments (also the maintenance cost) is significantly cheaper. It can be used in real-time at the bedside of a patient for a long term period (Brown, 2001, Frerichs et al., 2006, Holder, 1992c, Holder, 1993, Holder, 2005). Compared to functional magnetic resonance imaging (fMRI), the best brain function imaging technique widely used nowadays, the spatial resolution of ordinary fMRI is much finer than from the EIT i.e. approximately 1-2 mm, but the temporal resolution is much slower i.e. of the order of 1 second (Durduran and Yodh, 2014, Murrieta-Lee et al., 2004). In the applications to the brain, however, fMRI is actually sensitive only to cerebral haemodynamic responses, rather than the cortex neuronal responses to a brain function. Therefore, the use of fMRI for studying brain functions is still limited. Whilst Electroencephalogram (EEG) and Magnetoencephalogram (MEG) are able to measure neuroelectric or neuromagnetic signals directly, the strength of these signals depend on the alignment of excited dendrites, and the occurrence of excitatory and inhibitory activity in close proximity (Liston et al., 2012, Mayhew et al., 2010b, Murrieta-Lee et al., 2004, Oh et al., 2011a). The cancellation possibility of opposing fields then causes these techniques to have insufficient sensitivity to the deep regions of the brain.

EIT does, however, have some limitations when used in medical practice (Frerichs et al., 2006). Apart from the poor spatial resolution, EIT is very sensitive to noise or computation error. Noise can be electronic noise initiated from the EIT instrument itself or from other devices nearby, or it can be physiological noise initiated from physiological sources e.g. respiratory regulation. The inaccuracy of the model's geometry and structure, tissue conductivities, contact impedance, the changing of the model's boundary (e.g. due to subject/ body movement), and/or the quality of electrode attachment, cause modelling error; and this error is very difficult to evaluate and eliminate. Another difficulty regarding the image interpretation is that the magnitude of a reconstructed image may be unable to reflect the true magnitude of conductivity change. Therefore, although EIT reconstructed images can address the regions of conductivity changing, identifying the physiological causes

may be difficult. For instance in the EIT to the lung applications, the increase of conductivity seen in an image may be the result of the decrement of air content, the increment of fluid content, or the combination of the both.

The use of EIT on the human brain is the focus of this thesis. It has been widely recognised that EIT's use for head applications is one of the most difficult areas of EIT technology. Only a few studies on the real human head have been reported, and the success to obtain the expected images of brain responses was quite low i.e. only between 11.11% and 69.23% (based on the number of images showing the significant change in the expected area to the total number of images) (Tidswell et al., 2001a, Tidswell et al., 2001b, Tidswell et al., 2001c). The possible reasons to explain the causes of these low success rates are associated with many issues residing in different research areas. These issues could be grouped into four categories (adapted from (Cheney et al., 1999)): 1) the geometry and the structure of the head model and the tissue conductivities, 2) the measuring instrument, 3) the reconstruction methodology, and 4) the behaviour of physiological responses.

1.2 Possible Causes of Failure in Application of EIT to the Human Brain

Accurate geometry and structure of the head are fundamental requirements to solve an EIT problem, as the EIT problem is model dependent. However, to acquire every single small detail of head tissue geometry and structure is practically impossible, even when using the most sophisticated imaging technique available to date. Electrode geometry with accurate placing locations is very difficult to include into a model as well. However, employing EIT with a generic head model is still practically attractive, even though it can cause a larger error than using a subject model. Another source of the estimation error is the use of inaccurate tissue conductivities. Many tissue conductivity values which have been reported are based on several evaluation techniques. However, they are the conductivities of only certain regions or the mean value based on particular measuring circumstances and subjects. Therefore, no doubt, the uses of inaccurate models and/or conductivity

values introduce unavoidable modelling error, which is usually large in the applications of EIT to the human head. This modelling error then becomes a serious challenge for reconstruction.

In addition to modelling error, noise emerging from EIT instrument and physiological processes is another possible cause of the failure of EIT, as EIT is very sensitive to noise. To comply with the required medical standard, requires that the amplitude of the excitation current must be very small (usually less than 1 mA_{rms}). The small current entails the very poor sensitivity of the boundary voltages to conductivity change, in particular in the brain region. Therefore, the boundary (voltage) response to brain function is extremely small, and consequently the interference by both the physiological noise and instrument noise easily obscures the target signal. The very small amplitude can be easily overwhelmed by the instrument's quantisation as well. Regarding the physiological noise, it is actually composed from several types of physiological signal which are unrelated. This noise is very difficult to be identified and to be eliminated by the EIT instrument. A reconstructed image is then usually overlaid with the image of physiological noise. Therefore, to understand the nature of the physiological noise is crucial for interpreting an EIT image or EIT measurement traces. The ignorance of this task could be a cause of misinterpretation. One example of this is the Rheoencephalographic signal (REG). REG is a technique to measure electrical conductivity over a head or the cortex that can indicate the pulsatility of the cerebral blood volume (CBV) (and also the cerebral blood flow (CBF)) associated with the cardiac cycle. Without the early investigation of the amplitude and the period of REG, the addressing of very small response to brain stimulation cannot be achieved.

Reconstruction is the main task of EIT for obtaining images of conductivity distribution. However, for application to brain imaging, the instrumental noise, the physiological noise, and the modelling error seem large compared to other applications of EIT e.g. lung applications. Furthermore the severity of ill-posedness of head models is very high, due to the presence of the skull. The same regularisation parameter is also highly recommended for reconstructing time series images. These create many difficulties to reconstruct the physiological change as well. Even though

many reconstruction methodologies have been considered, taking into consideration these concerns, they may be unsuitable in the circumstance of head applications.

The clinical applications where the response amplitude to brain stimulation is large and the physiological noise amplitude is small are expected. However, the desirable brain response is usually very small due to the signal attenuation by the skull. On the other hand, the noise may be large instead due to the changing of blood flow inside the scalp region. The movement of the subject also could have happened during the investigation. This would cause the slight deformation of the head geometry and the movement of scalp muscles and blood vessels.

The consecutive responses to the stimulation i.e. the changing of cerebral blood flow (CBF) or the Blood Oxygenation Level Dependent level (BOLD) are usually easier to be detected due to the larger response amplitude. However, the changes may be complex and their causes may be difficult to identify. A number of repetitions over a type of brain stimulation is then necessary to confirm the presence of the response. However, unfortunately, the amplitude of the later responses of these consecutive responses naturally tends, due to habituation, to be smaller than the previous ones (may be smaller than the noise amplitude). This creates another difficulty in obtaining a robust image of all investigated responses.

1.3 Aim and Objectives

The aim of this thesis is to investigate whether EIT can be used in detecting neurophysiology from brain stimulation. Therefore, in order to attain the aim, this research engages with head model construction, head tissue conductivities estimation, EIT instrument modification, developing a new approach for reconstruction, reconstruction parameter optimization, and experimenting and analysing EIT data obtained from a certain number of brain stimulations. Particular challenges were intensely investigated as follows.

1. As explained in the previous section, it is impossible to eliminate the modelling error due to the high complexity of the geometry and structure of the human head. However, minimising the error is still an essential

procedure. Therefore, a subject model including electrode geometry was constructed. The tissue conductivities were newly estimated based on this subject model and from measurements with an EIT instrument. Furthermore, several generic head models were constructed to investigate the possibility to substitute the subject model.

2. To deal with the very low sensitivity problem and the large quantisation problem of the currently used EIT instrument, the EIT instrument was modified for higher excitation currents. It still complied with the medical standard IEC60601-1:2006. The bit-truncation of the Phase-Sensitive Detection (PSD) process was improved. The physiological noise was also examined to determine the amplitude of the noise. This amplitude value can be used as the minimum expected amplitude of desirable responses i.e. if the amplitude of desirable response is smaller than this minimum value, it implies that the reconstructed image will be the image of the noise rather than that of the response.
3. In the case of head applications, the traditional reconstruction methodologies may be unsuitable. A novel reconstruction approach has been developed for the head situation i.e. the situation infused with the large modelling error. The optimised reconstruction parameter was explored based on the experimental data and used as the common parameter. The image magnitude was also investigated by simulation. This was to determine whether it was able to reflect the true changing magnitude, or not.
4. Finally, the most important objective, since EIT may be applicable on only particular head applications, three types of brain stimulations were investigated: auditory startle response (ASR), CO_2 reactivity response, and transient hyperaemic response (THR). Both the interpretation of the measurement and the images were performed on a certain number of trials and subjects. The amplitude and the consistency of each response was a matter of particular focus.

Collectively, the aim of this thesis is primarily to investigate the possibility of EIT for functional brain imaging. The head model and its parameters i.e. tissue conductivities, the measuring hardware, the reconstruction methodology and algorithm, including the reconstruction configuration, were prepared as accurately as practically possible. Physiological noise was intensively studied, and a number of brain stimulations were conducted to attain the aim. However, the purpose of this thesis is not to determine the readiness of EIT for head clinical applications. Many implementation concerns and optimisation concerns were not considered in this thesis. For example, the speed of computation was very slow due to the use of very fine resolution models for both the forward and the inverse calculations. The real electrode sticking positions on the subjects were not intensively verified to the electrode locations on the used models. The measurement data was not filtered or particularly selected for only good responding measurement pairs. The image post-processes were not employed e.g. image filtering. None of particular reconstruction configurations were designed for any particular data or recording frames. On the negative side, lack of knowledge of these issues contributed to some inaccuracies in the research. However, on the positive side, the investigations were conducted in straightforward manner on the practical basis. Moreover, all of this also implies that further improvement of EIT experimental outcomes is still possible.

1.4 Thesis Organisation

This thesis is divided into eight chapters. The background and literature review are discussed in Chapter 2. The methodology to estimate head tissue conductivities with EIT data, and the new proposed values, are shown in Chapter 3. Bulk conductivity, which is able to represent the global conductivity change, is also explained in this chapter. In Chapter 4, the modification of the instrument is explained. In Chapter 5, a novel nonlinear difference imaging approach for image reconstruction of head applications is proposed. The suitable reconstruction algorithm and the optimum regularisation parameter are explained. In addition, the comparison between the use of generic head models and the use of a subject head model is reported in this chapter. Accordingly, in Chapter 6, the investigation of EIT

measurement based on several types of brain stimulations, and the amplitude of physiology noise i.e. REG signal and measurement baseline fluctuation, are reported. The misinterpretation due to false response on EIT measurement is also described in this chapter. The reconstruction outcomes of the use of the proposed reconstruction configuration (Chapter 5), the modified/non-modified EIT instrument (Chapter 4), and the proposed tissues conductivities (Chapter 3) on the several types of brain stimulations (Chapter 6), are shown in Chapter 7. Finally, the main ideas of the research are concluded and ideas for future research are mentioned in the last chapter (Chapter 8).

Chapter 2 Background and Literature Review

2.1 Conductivity of Human Head Tissues

Tissue conductivities are important parameters for predicting the boundary voltages and also for EIT image reconstruction. Regarding the voltage prediction, the conductivities determine the propagation of electric fields or current densities, as calculated by forward modelling. Whilst regarding the reconstruction, the accuracy of the conductivities vitally determines the outcome of inverse image reconstruction. The methodology to obtain the head tissue conductivities could be invasive or non-invasive. The invasive method is performed by taking some pieces of tissue, storing, and then measuring them; or by piercing needle electrodes and then measuring. The accuracy of the conductivities obtained by the first method entirely depends on the freshness of tissue samples and the body region sampled. In piercing needle electrodes case, it depends on the measured location. The freshness of tissue samples can, in fact, deteriorate through exposure to air, cooling, drying, or even cleaning. The water content may be changed, and/or some tissue matters may be washed out or dissolved, and/or the tissue cell property may change over time. Also, (Hoekema et al., 2003) reported that the temperature of the sample and the blood bath were critical. This statement is supported by the measurement during post-mortem examinations. Several studies have been reported where the conductivity of cadaver tissues was lower than that of living tissues (Akhtari et al., 2002, Latikkal et al., 2001, Wendel and Malmivuo, 2006). Regarding the body region sampled, even though the general physiology of the samples is the same, the conductivity may be different depending on the area the samples have been taken from. For example, the conductivity of the two pieces of the skull taken from two regions where the sample thicknesses were approximately the same, may be two times different in conductivity value due to the different thickness of the diploe layer (Tang et al., 2008).

Meanwhile, in the case of the non-invasive method, the estimation of tissue conductivities is performed on scalp measurement voltages or magnetic flux densities (Ferree et al., 2000, Gao et al., 2005, Salman et al., 2005, Salman et al.,

2007, Turovets et al., 2006). Complex mathematical calculation is involved in the estimation in conjunction with head models. Essentially, the tissue conductivities chosen are those yielding the minimum error between the true measurement voltages and the predicted voltages (obtained from the computational model). With this method, the accuracy of the model geometry is very important, and noise is required to be kept to a minimum. The estimated values are good to represent the (global) mean values (called "nominal values"). One approach to estimate the head tissue conductivities was proposed in this research (Chapter 3). However, we need to bear in mind that true local values can be much different to the mean values. This means that the error still remains even in the best estimation values. The literature review of important head tissue conductivities are discussed in the following sections, and tabulated details are given in Appendix A.

Instead of being interested in every single small tissue volume contained in the head, as is the usual approach in image reconstruction, interest in the head as a single large volume is a possible option for studying the brain functions. Every material residing in the head boundary is determined as a single bulk material. The reconstruction of the bulk material then yields the conductivity of a single voxel image, which is called "bulk conductivity". The bulk conductivity principally should reflect global change inside the measured subject, and therefore, it could be useful information for certain types of brain study e.g. CO_2 reactivity test where the evoked response is supposed to be globally distributed inside the cranium. This method of estimation of the bulk conductivity will be explained in Chapter 3.

2.1.1 Scalp Conductivity

Scalp is a kind of skin. However, in general, the scalp and the skin are different in conductivity (Rosell et al., 1988). The skin consists of two stacks: dermis (the inner layer) and epidermis (the outer layer). The epidermis has less water content than the dermis. Therefore, the epidermis is less conductive than the dermis. The conductivity of the outermost layer of the epidermis, i.e. stratum corneum layer (sometimes called "dead skin" layer), is approximately 2,200 times lower than that of the dermis (Yamamoto and Yamamoto, 1976). The presence of these two layers

creates some difficulties to evaluate the conductivity and/ or to rely on the resulting conductivity value. For example, regarding the frequency of the excitation current used with the scalp, the dead skin does not obey the Cole-Cole law, but the dermis does (Martinsen and Grimnes, 2001, Yamamoto and Yamamoto, 1976). The dead skin can also absorb water over time, which may come from sweat (produced from the inner layer) or electrode gel. It is able to be dried or lose its moisture to the air. Consequently, the conductivity (and the permittivity) can be naturally changed over time. In fact, these phenomena are more complicated due to uncertain thicknesses of the dermis and the epidermis (as well as the stratum corneum) on different regions of scalp. Moreover, the conductivity of the moist scalp could be 10 times higher than that of the dry scalp (Faes et al., 1999, Raicu et al., 2000). The reported conductivities of the scalp and also the skin are shown in Figure 2-1, where the values of scalp conductivity range between 0.32 and 0.43 S/m. The conductivity of the stratum corneum was extremely low. In addition, some studies have been reported where the scalp has the anisotropic properties (Horesh et al., 2005). The ratio of the tangential conductivity to the radial (or normal) conductivity of the scalp was reported to be 1.5:1; and 4.3:1 when determining the conductivity of muscles (Abascal et al., 2008a, Foster and Lukaski, 1996).

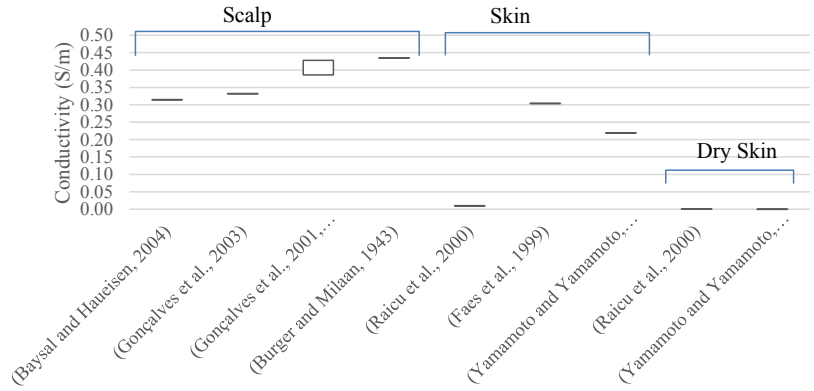

Figure 2-1 Conductivity of the human scalp/ skin obtained from literature

2.1.2 Skull Conductivity

Skull is a poorly conductive material which has the most complex bony structure (Marieb and Hoehn, 2007). It consists of many pieces of bone, connected

together where the joints can be noticed as shallow grooves (called “sutures” or “unossified bones” or “cancellous bones”) on the outer surface of the skull. It comprises three compartments: outer and inner compact bones, and spongy bone (or called “spongiosum” bone or “diploe”) residing in between the two compact bones. Spongy bone is usually filled with marrow and blood, and it is 3.5-10 times more conductive than the compact bone (Akhtari et al., 2002, Dannhauer et al., 2011, Tang et al., 2008). The average thickness of the skull is 8-10 mm: the thickness of the outer compact bone is typically 2.2-2.4 mm, the thicknesses of the spongy bone and the inner compact bone, however, have various values (Akhtari et al., 2000, Akhtari et al., 2002, Tang et al., 2008). Even though the thicker piece of the skull tends to be less conductive (Tang et al., 2008), due to the various thicknesses of the two inner-layer bones, the thickness of the skull has no strong correlation to the conductivity. Additionally, the presence of sutures causes higher conductivity (Law, 1993). The age of the skull also substantially influences the conductivity. For example, as reported in (Hoekema et al., 2003), the skull conductivity was found to be about 0.080 S/m for an 11-year-old subject falling to about 0.021 S/m for a 68-year-old subject.

Anisotropic property of the skull has been of interest in many studies (Bashar et al., 2008, Dannhauer et al., 2011, Marin et al., 1998, Suh et al., 2012). The electrical conductivity of the skull behaves differently in the tangential and the radial directions. The tangential conductivity was found to be 10 times higher than the radial conductivity (Abascal et al., 2008a, Rush and Driscoll, 1968, Wolters et al., 2006), but only 1.6 times higher as recently reported by (Dannhauer et al., 2011). These ratios can be changed when the applied current frequency of EIT instrument is changed (Saha and Williams, 1989). Beside, to implement the anisotropic property on a computational forward model is quite difficult. Conventionally, the radial conductivity is selected i.e. the skull is considered as an isotropic material, and this may cause 10-30% prediction error in the ECG forward solution or approximately 8-24 mm localisation error (Abascal et al., 2007, Abascal et al., 2008b).

The reported (isotropic) conductivities of the skull are summarised in Figure 2-2. The typical skull conductivity reported in most studies was between 0.008 and

0.016 S/m. The variation of the conductivity depended on the internal structure of the skull samples, the age of the subject, the presence of sutures. Furthermore, the ratios between the scalp conductivity, the skull conductivity, and the brain conductivity are of interest as well. With these ratios, one can ensure that the conductivity values acquired from the same bases of computation, configuration, and measuring instrument are rational. (Rush and Driscoll, 1968) reported that the ratios are 80:1:80 for scalp, skull, and brain respectively. However, recent studies found lower ratios, i.e. these ratios should be 15-40:1:15-47.8 (Baysal and Haueisen, 2004, Clerc et al., 2005, Gonçalves et al., 2001, Gonçalves et al., 2003a, Gonçalves et al., 2003b, Lai et al., 2005, Oostendorp et al., 2000, Wang et al., 2009, Zhang et al., 2006).

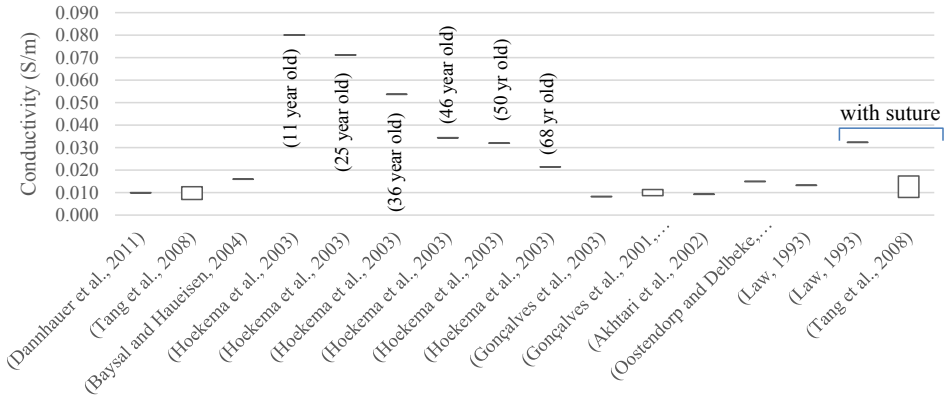

Figure 2-2 Conductivity of the human skull obtained from literature

2.1.3 Cerebrospinal Fluid (CSF) Conductivity

Cerebrospinal fluid (CSF) is liquid matter residing inside the cranium and encompassing the brain. Its volume is typically about 18% of the brain volume (Lüders et al., 2002). Its composition is similar to blood plasma, but the protein and the ion concentration are different. The reported values of conductivity of CSF are very diverse depending on temperature as shown in Figure 2-3, i.e. between 1 and 1.802 S/m, and remarkably higher than the conductivity of other head tissues. CSF is crucial for computational forward model calculation (Ferree et al., 2000, Liston et al., 2004, Ramon et al., 2004, Ramon et al., 2006).

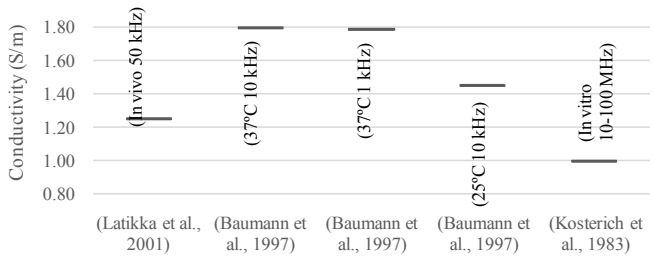

Figure 2-3 Conductivity of the human cerebrospinal fluid (CSF) obtained from literature

2.1.4 Grey Matter and White Matter Conductivity

Even though grey matter and white matter are usually implemented in computational models as the same tissue i.e. the brain, they are physically different. The grey matter or cerebral cortex comprises neuron cells, dendrites, associated glia, and blood vessels. Its thickness is only 2-4 mm, but it accounts for 54% of the brain volume (Lüders et al., 2002). Meanwhile, the white matter consists of substantial tracts i.e. the bundles of myelinated fibres and nerve bundles. Its volume is 28% of the brain volume.

The reported conductivities of the grey and the white matter are shown in Figure 2-4. The conductivity of the grey matter was between 0.33 and 0.43 S/m, and that of the white matter was between 0.26 and 0.76 S/m. However, the white matter is indeed anisotropic. The longitudinal conductivity (or parallel conductivity) was 8-10 times higher than the two transversal conductivities (or normal conductivities) (Nicholson, 1965, Suh et al., 2012). The white matter is usually implemented as a homogeneous isotropic tissue, and the transversal conductivity is typically selected.

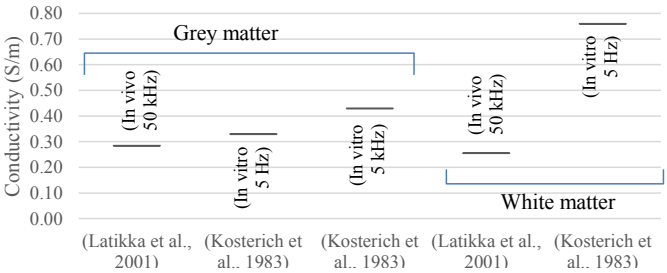

Figure 2-4 Conductivity of the human grey matter and the white matter obtained from literature

2.1.5 Blood Conductivity

Blood comprises erythrocytes (red blood cells), leukocytes (white blood cells), platelets, and plasma protein. Erythrocytes constitute approximately 45% of the total blood volume, and this percentage is known as "haematocrit". Haematocrit influences the conductivity of the blood: the higher haematocrit causes the lower conductivity (Hirsch et al., 1950, Pfützner, 1984). The conductivity of blood depends on the orientation of erythrocytes that could be changed due to blood flow changing: the increase of blood flow tends to decrease the conductivity in the radial direction and increase in the longitudinal direction due to the orientation of erythrocytes (Sakamoto and Kanai, 1979, Visser, 1989, Wtorek and Polinski, 2005). This phenomenon, therefore, develops the anisotropic property of the blood (vessel) (Visser et al., 1976, Wtorek and Polinski, 2005). The longitudinal conductivity (the evaluation is undergone along the length of vessels) is approximately 1.8 times higher than the transversal conductivity (or axial/ radial conductivity, the evaluation is undergone in the radial direction). This could be used to explain the origination of the anisotropic property of the scalp. The reported conductivities of blood are shown in Figure 2-5, i.e. between 0.45 and 0.80 S/m.

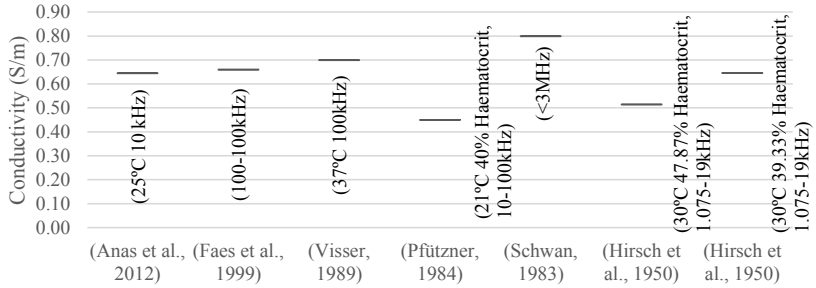

Figure 2-5 Conductivity of the human blood obtained from literature

2.2 fEITER System

fEITER (functional Electrical Impedance Tomography of Evoked Responses) is one of the most powerful electrical impedance tomography (EIT) instruments which is particularly designed for medical applications (Ahsan and McCann, 2008, Ahsan, 2010, Davidson et al., 2010, McCann et al., 2011b, Rafiei-Naeini and

McCann, 2008) (Figure 2-6 and Figure 2-7). It has compliance with the medical standard IEC60601-1:2006 (http://www.iso.org/), and it has been employed to study brain functions (McCann et al., 2011a, Pollard et al., 2011, Robinson, 2011, Ouypornkochagorn et al., 2015b). These studies have verified that the distinguishability of fEITER to identify the perturbation of conductivity distribution inside human heads is sufficient.

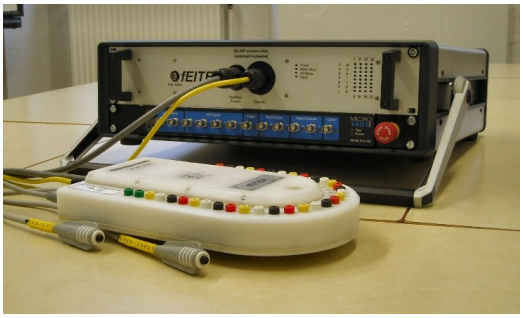

Figure 2-6 fEITER system: base unit and head box (the white box)

Figure 2-7 Installation between the head box and scalp electrodes

Conventional EIT instruments work by injecting electrical current into a subject, and then measuring induced voltages via an electrode array attached to the subject (Figure 2-8). Alternatively, EIT could operate by using voltage sources instead of using current sources (Dehghani et al., 2005, Hartov et al., 2002, Sansen et al., 1992), this kind of EIT instrument, however, is not widely used. There are many EIT systems developed by several research groups, and some of them have been implemented on real medical applications, e.g. finding parameter for Positive End-Expiratory Pressure (PEEP) trials for reducing ventilator-associated lung injury (Frerichs et al., 2011), or screening breast cancer (Halter et al., 2008). Some recent well-known EIT systems are shown in Appendix B. Noticeably, the trend of EIT is towards Multi-Frequency Electrical Impedance Tomography (MFEIT). MFEIT can produce impedance information over multiple frequencies, but certainly the complexity of its firmware is more complex than that of the single frequency EIT. Fortunately, recent technology breakthrough allows the multi-frequency system to be built more easily. Therefore, new emerging EIT systems tend to be MFEIT, even though they might be used as a single frequency EIT instrument in practice. In fact, reconstructing MFEIT images is more complicated and requires more computational resources than reconstructing single-frequency EIT images. Whatever the reasons, it

is unnecessary in this study to discuss the advantages and disadvantages of using MFEIT over the single frequency EIT in detail, since fEITER is based on a single frequency.

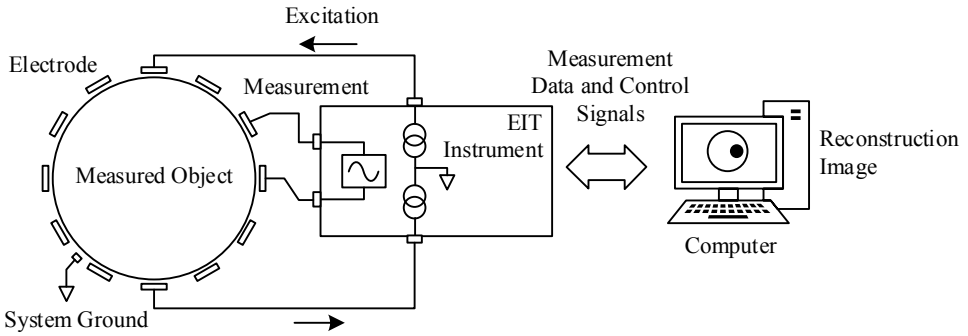

Figure 2-8 Conventional EIT system

In designing fEITER as a medical instrument, patient safety was of paramount concern. The safety limit of the IEC60601-1:2006 standard is shown in Table 2-1. Since fEITER is based on 10 kHz frequency, the maximum limit of the excitation current is then 1 mA_{rms}. However, the original fEITER version uses only 1 $mA_{pk\text{-}pk}$ or only 35.36% of the safety limit. Increasing the current is a straightforward option to increase measurement sensitivity towards conductivity distribution change, and has been done in the modified fEITER system (shown in Chapter 4). In fact, this maximum safety limit could be higher than the number specified in the standard. (Boone and Holder, 1995, Gilad et al., 2007) have been reported that the current limit can be eight times higher than instruments using the frequency lower than 1 kHz.

Table 2-1 Allowable excitation (auxiliary) AC current according to IEC 60601-1 standard

Excitation Frequency	Allowable AC Current	Remark
< 1 kHz	0.1 mA_{rms}	
1 kHz ≤ f ≤ 100 kHz	0.1 × f mA_{rms}	f is the excitation frequency in kHz
> 100 kHz	10 mA_{rms}	

2.2.1 Composition of fEITER System

fEITER consists of two main parts: base unit and head box (Figure 2-9). The base unit is a composite unit that basically accounts for transferring measurement data to a computer (via two USB ports). It is composed of the base unit CPU, the

data acquisition interface - CED Micro 1401 mkII, and the multifunction data acquisition unit – NI M Series DAQ. The base unit CPU is based on a Complex Programmable Logic Device (CPLD). In detail, it accounts for 1) passing stimulation marker signals generated from CED Micro 1401 to the head box, 2) receiving measurement data from the head box, and then 3) transferring the data to the computer through the first USB port. Additionally, external signals captured by CED Micro 1401 can be transmitted to the computer through another USB port.

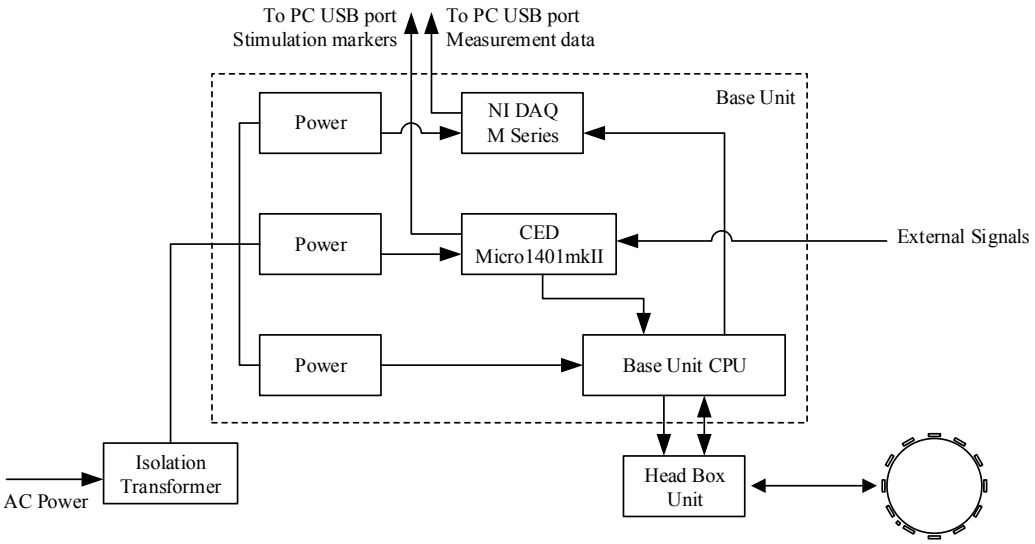

Figure 2-9 Main parts of fEITER system: isolation transformer, the base unit, and the head box

The head box is based on a Field-Programmable Gate Array (FPGA). Current generating, current driving and multiplexing, and voltage measuring are performed by the head box. Thirty-two electrode receptacles in addition to two ground receptacles are provided. The overall specification of the original version of fEITER is shown in Appendix C.

In the fEITER system, 20 current patterns were programmed to drive current in near-diametric directions (or called “opposite” driving). This driving scheme is widely recommended (Adler et al., 2011, Boone and Holder, 1996, Fabrizi et al., 2009, Koksal and Eyuboglu, 1995, Peters and Barra, 2010, Shi et al., 2006)), because the sensitivity could be 100 times higher than the adjacent excitation scheme (Bayford et al., 1996). The total measurements taken over all current patterns are

546, in nearest-neighbour voltages. The detail of the electrode configuration of current driving and voltage measuring can be found in Appendix D.

2.2.2 Excitation current generating and monitoring subsystem

The rough schematic of the excitation current subsystem is shown in Figure 2-10. The FPGA (Xilinx Virtex-4) firstly generates 16-bit encoding of a sinusoidal waveform which is input to a Digital-to-Analog Converter (DAC), and the DAC decodes this data to provide an analogue sinusoidal signal. This analogue signal is filtered and is passed through the buffer to two Howland circuits. These Howland circuits transform the incoming sinusoidal voltage signal to two sinusoidal currents: one is 180-degree out of phase with to the other one. Next, each current flows through the sensing resistor of 100 Ω to the current switch which controlled by FPGA to produce desired current driving patterns. Finally, the generated current sent out to the measured subject through the source and the sink electrode receptacles. For current monitoring, two measurement circuits (explained in the next section) are used to measure the voltage across the sensing resistor. The value of the excitation current is simply computed by (2.1) and (2.2).

$$I = V/100\Omega \tag{2.1}$$

$$I_{average} = \left(I_{source} + I_{sink}\right)/2 \tag{2.2}$$

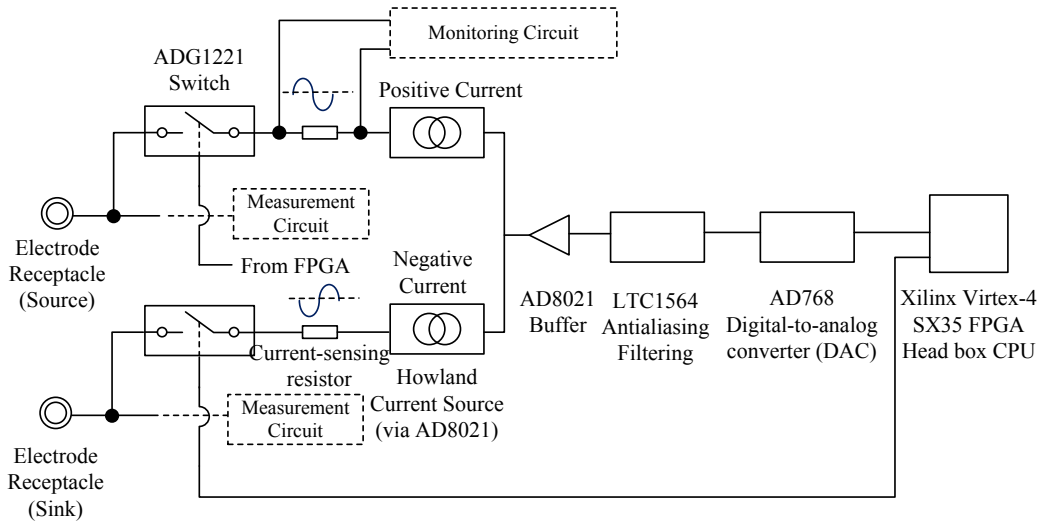

Figure 2-10 The schematic of current excitation subsystem

2.2.3 Difference voltage measuring subsystem

The rough schematic of the voltage measuring subsystem is shown in Figure 2-11. The difference between two electrode voltages is amplified by the precision amplifier (AD8221) where the CMRR is very high (over 92 dB at 10 kHz). The difference signal is lifted to the middle of the operation range (0 V_{DC} - 3 V_{DC}) by V_{ref} i.e. lifting with 1.5 V_{DC}, to avoid non-measurable negative voltage. Next, the lifted signal is filtered with an RC low pass filter (with 106.4 kHz-cut-off frequency), and passed to the 16-bit Analog-to-Digital Converter (ADC). Finally, the ADC converts the incoming analogue signal to serial digital data. The converted data is then sent to the FPGA via the serial protocol interface port of ADC. The measurable voltage range can be computed in (2.3), where *Gain* is the gain of the AD8221 amplifier. The DC offset is supposed to be zero.

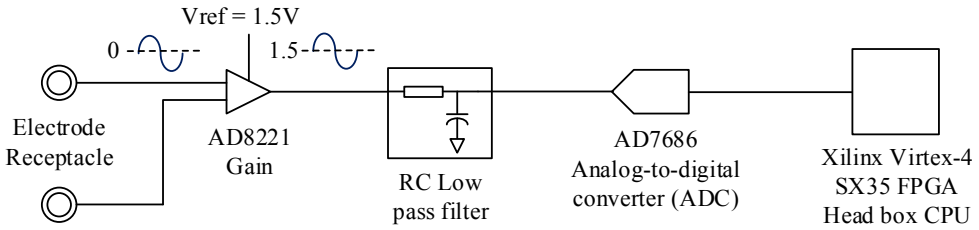

Figure 2-11 The schematic of difference voltage measurement subsystem

$$MaximumMeasurableACVoltage_{pk-pk} = \frac{1.5\,Volt}{Gain} \times 2 \tag{2.3}$$

The sampling rate of the ADC is 500 kS/s (2 µs sampling period). Regarding the EIT current injection frequency of 10 kHz, there are 50 samplings performed for each cycle of the sinusoidal waveform. Since the application period of each current pattern is 500 µs, there are 250 samples (or 5 sinusoidal cycles of the 10 kHz waveform) available for each voltage measurement.

To detect very small changes in the amplitude of the AC signal in the situation that a desirable signal is swamped with noise, a lock-in amplifier can handle this task, and is used in fEITER. The lock-in amplifier uses the technique known as phase-sensitive detection (PSD) or lock-in detection. Any signals (or signal

components) where the frequency differs from the frequency of reference signal (called the "reference frequency" or the "lock-in frequency") are attenuated to be approximately zero. Similarly, any signals even having the same frequency to the reference frequency but different in phase are also attenuated in a certain degree. Therefore, this technique is sensitive to both the frequency and the phase.

Suppose that the measurement signal (V_{sig}) is defined in (2.4). Two reference signals ($V_{ref,I}$ and $V_{ref,Q}$) where the frequencies are the same, i.e. the reference frequency, but differ by 180 degrees in phase, are expressed in (2.5) and (2.6) respectively.

$$V_{sig} = |V_{sig}| \sin(\omega_{sig} t + \theta_{sig}) \tag{2.4}$$

$$V_{ref,I} = |V_{ref}| \sin(\omega_{ref} t + \theta_{ref}) \tag{2.5}$$

$$V_{ref,Q} = |V_{ref}| \cos(\omega_{ref} t + \theta_{ref}) \tag{2.6}$$

To detect V_{sig} by using PSD, each reference signal is multiplied by V_{sig} as in (2.7) - (2.8) and (2.10) - (2.11). The multiplication outcomes, $V_{PSD,I}$ and $V_{PSD,Q}$, are the composite signal of the component of the difference frequency (ω_{ref} - ω_{sig}) and the component of the sum of frequency (ω_{ref} + ω_{sig}). Two facts are 1) if the frequency of the measurement signal is different to the reference frequency ($\omega_{ref} \neq \omega_{sig}$), the average of PSD outcomes will be zero, but 2) if they are equal ($\omega_{ref} = \omega_{sig}$), the averages will be a constant number as in (2.9) and (2.12). Note that the process of averaging can be replaced by using low-pass filtering in the case of using analogue PSD.

$$V_{PSD,I} = |V_{ref}||V_{sig}| \sin(\omega_{ref} t + \theta_{ref}) \sin(\omega_{sig} t + \theta_{sig}) \tag{2.7}$$

$$= \tfrac{1}{2}|V_{ref}||V_{sig}| \cos((\omega_{ref} - \omega_{sig})t + (\theta_{ref} - \theta_{sig})) - \tfrac{1}{2}|V_{ref}||V_{sig}| \cos((\omega_{ref} + \omega_{sig})t + (\theta_{ref} + \theta_{sig})) \tag{2.8}$$

$$V_{PSD,I,avg} = \begin{cases} \tfrac{1}{2}|V_{ref}||V_{sig}| \cos(\theta_{ref} - \theta_{sig}) & if\ \omega_{ref} = \omega_{sig} \\ 0 & if\ \omega_{ref} \neq \omega_{sig} \end{cases} \tag{2.9}$$

$$V_{PSD,Q} = |V_{ref}||V_{sig}|\cos(\omega_{ref}t+\theta_{ref})\sin(\omega_{sig}t+\theta_{sig}) \quad (2.10)$$

$$= -\tfrac{1}{2}|V_{ref}||V_{sig}|\sin((\omega_{ref}-\omega_{sig})t+(\theta_{ref}-\theta_{sig}))+ \quad (2.11)$$
$$\tfrac{1}{2}|V_{ref}||V_{sig}|\sin((\omega_{ref}+\omega_{sig})t+(\theta_{ref}+\theta_{sig}))$$

$$V_{PSD,Q,avg} = \begin{cases} \tfrac{1}{2}|V_{ref}||V_{sig}|\sin(\theta_{ref}-\theta_{sig}) & if\ \omega_{ref}=\omega_{sig} \\ 0 & if\ \omega_{ref}\neq\omega_{sig} \end{cases} \quad (2.12)$$

Therefore with PSD, irrelevant signals (noise) where the frequencies are different to the reference frequency are filtered out and only the desired signal is left. According to (Ahsan, 2010), the lock-in amplifier's bandwidth of fEITER is approximately ±2 kHz. The "in-phase" component and the "quadrature" component of the desired signal can be extracted by (2.13) and (2.14) respectively. Because the amplitude of V_{ref} ($|V_{ref}|$) is known, the amplitude of the signal and the phase difference to the reference signal can be computed from (2.15) and (2.16).

$$V_I = \frac{V_{PSD,I,avg}}{\tfrac{1}{2}|V_{ref}|} \quad (2.13)$$

$$V_Q = \frac{V_{PSD,Q,avg}}{\tfrac{1}{2}|V_{ref}|} \quad (2.14)$$

$$|V_{sig}| = \sqrt{V_I^2+V_Q^2} \quad (2.15)$$

$$\theta_{sig} = \theta_{ref} + \tan^{-1}\left(\frac{V_Q}{V_I}\right) \quad (2.16)$$

According to the design philosophy of fEITER, the reference frequency is 10 kHz, i.e. the frequency of the excitation current. The DC level added at the gain (i.e. "AD8221" in Figure 2-11) is automatically filtered out because the frequency of DC is zero which is different to the reference frequency.

fEITER uses the digital version of PSD. To acquire a measured voltage value, the computation is based on two components of (2.9) and (2.12). Suppose that 1) the readable range of ADC is between zero and R_{ADC} (V_{DC}) meaning the maximum measurable amplitude of the signal is R_{ADC} ($V_{pk\text{-}pk}$), 2) the signal voltage and the reference voltage are digitised and stored in the B_{sig} and B_{ref} bit-length resistors of

FPGA respectively, and 3) the amplitude of the reference signal is R_{ref} ($V_{pk\text{-}pk}$); the measurement value V_I as in (2.13) can be computed over periods of sinusoidal waves as shown in (2.17) where $V_{PSD,I(ADC)}$ is the digital value of $V_{PSD,I}$ (ranges between 0 and $2^{Bsig} \times 2^{Bref}$ -1).

$$V_{I(period)(ADC)pk-GND} = mean\left(\frac{V_{PSD,I(ADC)}}{½ \times R_{ref}} \times \frac{R_{ADC}}{2^{Bsig}} \times \frac{R_{ref}}{2^{Bref}}\right) \tag{2.17}$$

The peak-to-peak amplitude of $V_{I(period)(ADC)}$ is practically computed from (2.18). Since, the values of the in-phase component and the quadrature component are computed from N samples, the mean in (2.17) is then computed from the sum of $V_{PSD,I(ADC)}$, that is $\Sigma_N V_{PSD,I(ADC)}$ (called the "sum of multiplications"), divided by N. Furthermore, since the ADC is usually used with an amplifier, the ADC voltage is then required to scale back to the real measurement value with the gain of the amplifier *Gain*. Moreover, since the very least significant bits (LSBs) of the FPGA's resistors keeping the sum of multiplications are less significant in value, it is very practical to reduce the number of resistor's bits with bit truncation. The truncation ignores $B_{truncation}$ bits started from the LSB, so that the computation then needs to scale up for compensation. No doubt, the number of truncated bits worsens the quantisation error, called "truncation error". The maximum truncation error is obtained from the maximum error resulting from the ignored bits that introduce the insensitivity to the accumulation of $\Sigma_N V_{PSD,I(ADC)}$ as shown in (2.19).

$$V_{I(period)pk-pk} = \frac{1}{N}\left(\frac{\sum_N V_{PSD,I(ADC)}}{½ \times R_{ref}} \times \frac{R_{ADC}}{2^{Bsig}} \times \frac{R_{ref}}{2^{Bref}}\right) \times 2^{Btruncation} \times \frac{1}{Gain} \times 2 \tag{2.18}$$

$$MaxTruncationError_{pk-pk} = \frac{1}{N}\left(\frac{2^{Btruncation}-1}{½ \times R_{ref}} \times \frac{R_{ADC}}{2^{Bsig}} \times \frac{R_{ref}}{2^{Bref}}\right) \times \frac{1}{Gain} \times 2 \tag{2.19}$$

Apart from the truncation error, another source of quantisation error originates from the conversion resolution of the ADC and the gain of amplifier. When the number of conversion bits of ADC is B_{ADC}, the reading resolution can be computed from (2.20) or (2.21).

$$ADC\,Reading\,Resolution_{DC} = \frac{R_{ADC}}{2^{B_{ADC}}} \times \frac{1}{Gain} \tag{2.20}$$

$$ADC\,Reading\,Resolution_{pk-pk} = ADC\,Reading\,Resolution_{DC} \times 2 \tag{2.21}$$

According to the formulae above, the number of bits used in truncation influences the effective quantisation error of the system. This number was improved in the modified version of fEITER as detailed in Chapter 4. Note that all fEITER voltage measurements shown in this thesis are the root-mean-square (rms) of the in-phase amplitude V_I given in (2.13), i.e. all measurements are $V_{rms} = V_I / \sqrt{2}$. With the exception of Table 4-4, all fEITER current measurements given in this thesis are peak-to-peak values.

2.3 Electrophysiological Response due to Evoked Response

The characteristic of electrophysiological response to brain functions is a key issue to determine the possibility of using EIT in the application to the human brain. A physiological change which is sufficiently large can induce a detectable change on the boundary measurements. The change can be initiated from different sources with different magnitudes. The changes caused from diseases or from brain stimulation are initiated at the cell level i.e. depolarization or cell swelling, are extremely small in magnitude. Meanwhile, the large number/volume of tiny changes can induce significant voltage change on the boundary, e.g. the change of epilepsy or spread depression. The consequences of brain activation, e.g. the increasing of cerebral blood flow or the changing of local temperature, also can induce change on the boundary as well.

2.3.1 Causes of Electrophysiological Change

Physiological change straightforwardly influences the electrical property of tissues. At cell level, the electrical property of cells depends on how large the extracellular space and the intracellular space and the conductivity of the cell membrane (Galambos and Velluti, 1968). The change in the conductivity of the

spaces and membrane is initiated from ionic shift which is caused by several reasons. The opening of the ion channels conducts the entering of ions and water into the soma (cell body), and consequently this reduces the extracellular space. The smaller extracellular space results in lower conductivity, because the electrical current can flow more easily in the extracellular space than in the intracellular space (Tidswell et al., 2001c). The opening of ion channels also causes the increase of membrane conductivity by approximately 80 times (Gilad and Holder, 2009, Oh et al., 2011a). Furthermore, the presence of the membrane causes the cell to be able to store ions like a capacitor. Therefore, the cell is sensitive to the current excitation frequency in the manner of current dispersion (Blad and Baldetorp, 1996). (However since the fEITER system used in this research is operated on a single frequency, the detail of the dispersion will not be explained here.)

Neuropathological diseases or neuronal activities can lead to different types of cell physiological change. For diseases like epilepsy or ischaemia, neuronal cells and glial cells tend to swell. This results in the reduction of the extracellular space (Holder, 1992a, Tidswell et al., 2001c). Meanwhile, functional activities or evoked responses to stimulation are mainly relevant to cell depolarization, to produce action potential or graded potential (Marieb and Hoehn, 2007). During the depolarization, the ion channels of the cell membrane are opened to generate potentials. However, the depolarization does not cause the significant change of the extracellular space (Tidswell et al., 2001c). In the case of myelinated cells i.e. those of the white matter, to detect the depolarization change is more difficult, because myelin is a kind of fat substance acting like an insulator (Liston et al., 2012). Therefore, the electrical property changing due to depolarization is usually very small.

Apart from the change on cells, alternation in regional cerebral blood volume (rCBV) or cerebral blood flow (CBF) also causes change where the magnitude is usually larger. Blood contributes to the conductivity of the cortex by approximately 10% (Galambos and Velluti, 1968). Physiological mechanism of the brain towards a neuronal activity usually leads to the increase of rCBV, and in certain types of brain activations, e.g. CO_2 inhalation, it also leads to the slight change of global CBF. The increase of rCBV could imply the increase of conductivity, because the conductivity

of the blood is higher than that of the brain tissues about 1.5 times as mentioned in Section 2.1. Nevertheless, the increase of rCBV also leads to the decrease of regional temperature that influences the regional conductivity as well. (Holder, 1992b) reported that 1ºC decrement of temperature can lead to 1% decrement of regional conductivity. The conductivity measured, therefore, is the sum of these opposite changes (the increase of blood volume leads to the increase of conductivity, but it simultaneously leads to the decrease of conductivity due to the temperature decreasing). However, the change of conductivity due to the cortical temperature change could be 10 times smaller than the predominant change due to rCBV (Tidswell et al., 2001c). Additionally, some neuropathological diseases or brain functional examinations could lead to the massive change of CBF. Cerebral ischaemia can decrease blood flow by 5-8% (Holder, 1992d). Theoretically, the large change due to CBF allows EIT to detect the change more easily. However, the change due to CBF changing behaves in a very complicated manner in practice due to the autoregulation mechanism of the brain. The response latency of this change is also slower than the change due to depolarization. This then creates a difficulty to explore for the true desired response for the CBF change.

CBF is closely coupled to neural activity. Neural activation requires more cerebral metabolism. Oxygen and glucose are required more during the activation of neurons. The blood flow is then increased to supply them. However, the increase of the oxygen consumption is much less than the increase of CBF, i.e. the oxygen is oversupplied. With this fact, the Blood-Oxygenation Level Dependent (BOLD) measurement is commonly used to determine CBF via functional magnetic resonance imaging (fMRI). The increase of BOLD implies the increase of CBF, i.e. the increase of cerebral blood volume. It can be interpreted as the increase of cerebral blood perfusion as well (Mayhew et al., 2010b). However, some studies (Logothetis and Wandell, 2004, Mayhew et al., 2010b) reported that BOLD did not have a straightforward correlation to depolarization (more precisely, BOLD did not have a straightforward correlation to the local field potential that is the sum of emerging action potentials and grade potentials), because the response of BOLD to the depolarization was slower. For example, as depicted in (Logothetis and Wandell, 2004), the BOLD latency of the visual or motor stimulation with a two-second-

stimulus was two seconds, and the peak of BOLD was at 6-9 seconds after the stimulus onset. These can indicate that the change of CBF was slower than the depolarization. According to this example, even if the change due to the depolarization is too small to measure, it could be fortunate to localise the activated regions via CBF instead where the change is larger. However, the latency issue raises concerns.

The concentration of red blood cells in blood (called "haematocrit") also influences the conductivity of blood. When the haematocrit is decreased, the conductivity increases (Hirsch et al., 1950, Pfützner, 1984, Sapkota et al., 2015), and consequently CBF is then slightly increased to maintain the oxygen level. However, in a very short period after depolarization, only the haematocrit is considered (CBF changing is slower). This then could be another change happening during depolarization as well.

Not only blood can introduce large conductivity change inside the cranium, but the change of cerebrospinal fluid (CSF) is also another possibility. CSF, where the conductivity is 1.63 times higher than that of the blood (5.8 times higher than that of the brain), can be changed in volume due to the change of intracranial pressure (ICP), for example during Valsalva manoeuvre or cerebral venous thrombosis. This possibility of change is not negligible.

2.3.2 Magnitude of Electrophysiological Changes

The magnitude of electrophysiological change directly affects the possibility to detect the change by the fEITER instrument (see Appendix H for a tabular summary of the data presented in this section). The decrease of conductivity due to ischaemia (blood flow shortage) was reported to be between 13% and 67% (equivalent to the increase in impedance between 15% and 200%) (Holder, 1992a, Holder, 1992d, Hossman, 1971). Similarly, (Manwaring et al., 2013) found that the local shortage of blood flow (by ballooning) led to the conductivity decrement of 8.98% - smaller than the previous studies, while the bleeding produced the conductivity increment of 15.35%. In the case of spreading depression which is possibly caused from ischaemia, the conductivity was decreased between 5% and

43% (Boone, 1995, Freygang and Landau, 1955, Holder and Gardner-Medwin, 1988, Holder, 1992b, Ranck, 1964). Beside, the volume change of intracranial fluids can cause a large change. The conductivity could decrease between 21% (hypotension case, (Gamache et al., 1975)) and 84% (edema case in humans, (Fu et al., 2014)).

The changes which are mainly caused by depolarization are usually smaller than those caused by intracranial fluids. Overall, the conductivity change due to epilepsy was negative, but that due to direct stimulation, sensory evoked response (SER), motor response, auditory evoked response (AER), visual evoked response (VER), or nerve stimulation was positive. The decrease of conductivity due to epilepsy was between 3% and 11% (Dowrick et al., 2015, Elazar et al., 1966, Harreveld and Schadé, 1962, Rao, 2000). However, it was reported to be much larger, up to 450%, when the experiment was carried on human, probably due to the subject movement during measuring (Fabrizi et al., 2006). The conductivity change due to direct cortical stimulation was only between 0.01% and 3.2% (Freygang and Landau, 1955, Holder and Gardner-Medwin, 1988). The conductivity change due to SER was up to 2.8% on rabbits, but only 0.19% on humans (Holder et al., 1996, Oh et al., 2011a, Tidswell et al., 2001a, Tidswell et al., 2001c). The change due to motor response on humans was slightly larger, i.e. 0.34% (Tidswell et al., 2001c). This value was not significantly different to the human VER case, which was between 0.001% and 0.43% (but it was up to 4.7% on rabbit trials) (Gilad et al., 2009b, Gilad and Holder, 2009, Holder and Gardner-Medwin, 1988, Holder, 1989, Holder et al., 1996, Tidswell et al., 2001a, Tidswell et al., 2001c, Gilad et al., 2005a). Unfortunately, there was no report of the change on humans in the case of AER. (Klivington and Galambos, 1968, Gilad et al., 2009a, Gilad et al., 2009b) reported that the change due to AER was 0.003% on cats – very low compared to other responses. Beside, these reported values were not significantly different to the estimation value, i.e. 0.6% on average, of the depolarization simulation on a human model (Liston et al., 2012). (Holder et al., 1996) also reported that the negative change of conductivity in neighbouring areas could emerge: the magnitude of the change in the neighbouring area was possibly between -62% and +7% of that in the activated area.

According to the magnitude of the changes illustrated above, the changes in conductivity could be grouped into four categories: large, medium, small, and very small (partially adapted from (Bayford et al., 1996)). The magnitude of the "large change" is over 11%. The change could be caused by ischaemia, haemorrhage, spreading depression, hypotension, or edema (according to the values explained above of these diseases, it was between 5% and 84%). The magnitude of the "medium change" is smaller i.e. between 3% and 11%. The example of this change is due to epilepsy. The next category, the "small change", is determined from the magnitude lower than 4.7% (according to the values explained above, the magnitude obtained from the investigation on humans was much smaller, i.e. only between 0.001% and 0.43%). This change is associated with neuronal responses towards evoked activities e.g. SER, motor response, VER, or AER. Due to the small magnitude of this change, the neighbouring negative-change could be frequently noticeable. The last category, the "very small change", originates only from the depolarization process. The change due to depolarization is directly measured on the nerve. The maximum magnitude was only 1% obtained from the measurement on an electrode pair where the distance between the electrodes was less than 2 mm.

The possibility to measure these changes with an EIT instrument to date is remaining under investigation. (Sadleir et al., 2009) reported that EIT could localise the conductivity change due to saline injecting in a piglet head (where the saline conductivity was approximately 160% higher than that of the brain tissue, and the injecting volume was less than 1% of the head volume). However, (Liston et al., 2012) stated that in the case of very small change (and very small changing volume) like nerve depolarization, no single tomographic technique to date including EIT was capable of imaging the change. In fact, the capability to localise change depends on the magnitude and volume of the change, and the performance of EIT instruments. (Towers et al., 2000) suggested, based on simulations, that the signal to noise ratio (SNR) to detect the small change (1%) must be over 120 dB, and must be over 80 dB to detect the large change (15%), when the volume of the change was 0.191% of the head volume. The difference between the two requirements was very high (40 dB). This implies that the large change was much easier to detect.

2.3.3 Signal Attenuation and Interference

When the measurement is performed on the scalp, the degree of signal attenuation is exceptionally high, as well as the interference of irrelevant signals. The skull has been widely admitted to be the root cause of the attenuation (Holder, 1992a). The skull behaves like an insulator, i.e. against the entering of the current into the brain. Only approximately 15% of the current can pass through the skull (Liston et al., 2002, Tidswell et al., 2001a), and this leads to the substantial attenuation by a factor of five to ten (or higher) (Bagshaw et al., 2003, Holder, 1992a, Liston et al., 2002, Tidswell et al., 2001c).

One important phenomenon occurring in the scalp during EIT operation is the "shunt effect". Since the skull is very resistive, the excitation current does not straightforwardly pass through the skull into the brain; instead, it is mostly shunted by the scalp (Fabrizi et al., 2006, Holder, 1992b). This effect causes very low sensitivity of EIT to the brain region, and causes very high sensitivity to the scalp region which is usually not the interesting region. Furthermore, CSF, which is very highly conductive, also behaves like a trap to shunt the current to other regions on the cortex (Gibson et al., 2000). The uncertainty of the CSF thickness over time leads to an uncertain degree of the shunt effect as well (Tidswell et al., 2001a). This phenomenon results in large instrument response from undesirable regions, but small instrument response from the brain, from brain stimulation.

Although the interesting region of functional brain studying is absolutely in the brain region (more specifically, the cortex region), the signal measured on the scalp could be overwhelmed by signals initiated from anywhere else. The change in the scalp due to brain stimulation could be larger than the change in the brain (Holder, 1992a). (Holder and Gardner-Medwin, 1988) reported that during spreading depression, the scalp conductivity was increased while the cortex conductivity was decreased. This means the changes can behave in different manners in different tissues. Indeed, even if the change in the scalp is smaller than that in the brain, the influence on boundary voltages could be more profound due to the very high sensitivity of the scalp. Additionally, the activation of neurons can induce the change

of cerebral blood flow (CBF), and possibly induce the small change of intracranial temperature (Holder, 1992a). The changing of the CBF could occur outside the changing region of the brain (Tidswell et al., 2001a), and it could occur even on the scalp (Holder, 1992b, Holder and Gardner-Medwin, 1988). Furthermore, (Fabrizi et al., 2006) found that subject movement can dominate all of the changes explained above. In addition, the electrophysiology of tissues could vary over time due to regulation mechanisms of the brain, resulting in shifting of tissue conductivity baseline (Holder, 1992a, Holder, 1992b). The shift could be 1% over a few minutes, and it could be two orders larger than the desired signal (Oh et al., 2011a).

2.3.4 Rheoencephalographic signal (REG)

Rheoencephalography (REG) is the recording of electrical cerebrovascular alteration on the scalp or the cortex (Bodo et al., 2003, Bodo and Pearce, 2004, Bodo et al., 2005). REG is believed to reflect global Cerebral Blood Flow (CBF) which is closely related to the process of systemic arterial blood pressure. REG is usually in step with Electrocardiographic signal (ECG or EKG), but they are different in waveform due to the intracranial cerebral autoregulation (Bodo et al., 2005, Popovic et al., 2013). However, the REG waveform is very similar to the change of flow velocity of middle cerebral artery (MCA) (but in negative correlation), as shown in Figure 2-12. (Bodo et al., 2005) also reported that the pulsatile change of REG is caused by the 1-10% change of the total conductivity of the tissue in the measurement region.

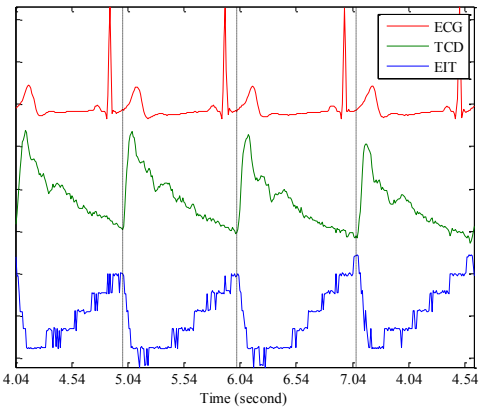

Figure 2-12 Rheoencephalographic signal (REG) measured by the original version of fEITER system (labelled with "EIT"), Electrocardiographic signal (ECG or EKG), and middle cerebral artery (MCA) flow velocity signal measured by transcranial Doppler (TCD)

2.3.5 EIT Reconstructed Images of Neurophysiological Response

Surprisingly, very few images of human brain response have been published using EIT since its inception in 1984 (Barber and Brown, 1984). The reasons could be due to the small response amplitude and the infusion of noise explained in the previous sections. The presence of unavoidable modelling error occurring when implementing EIT in real situations is another crucial obstacle.

Apart from the successful simulation results shown in many EIT studies, EIT has been successfully verified in reconstructed images in tank situations with and without a human skull (sometimes, this tank is referred to as a "Phantom") (Dowrick et al., 2015, Holder, 1992d, Liston et al., 2002, Tidswell et al., 2001a, Tidswell et al., 2001b, Tidswell et al., 2001c). EIT images also have been verified on a piglet cadaver (Sadleir et al., 2009). In this case, the researchers could satisfactorily localise the conductivity change inside the cranium. However, when EIT was implemented on living subjects, the success rate to obtain satisfactory images of the brain responding to stimulation was very low. The previous brain response studies on humans are summarised in Table 2-2. In human subjects, when reconstructing with a 2D circular model, it was reported that the consistency to localise the activated brain regions was only 28% and 44% for the cases of somatosensory response and visual evoked response respectively (Tidswell et al., 2001a). Meanwhile, when reconstructing with a 3D spherical model, (Tidswell et al., 2001c) reported that the possibility to localise the activated regions was only 11% for somatosensory response and 69% for visual evoked response. Therefore, these statistics confirm explicitly the difficulty of EIT with scalp electrodes. However, when the measurement was performed on the cortex instead, many difficulties were eliminated e.g. the physiological noise was dramatically reduced. (Holder et al., 1996) reported that the activated regions displayed in the reconstructed images of visual and somatosensory response on eight rabbit cortices were all consistent. Therefore, the trend of imaging very small change (or implicitly, the fast response) of the brain with EIT may be going towards the cortical application of EIT rather than the scalp application of EIT, like some recent studies (Aristovich et al., 2014, Dowrick et al.,

2015). Indeed, the reconstructed images of visual and auditory response on a human subject obtained from scalp measurement were also demonstrated in (McCann et al., 2011a, McCann et al., 2011b, McCann et al., 2006, Murrieta-Lee et al., 2004, Murrieta-Lee et al., 2005). However, since these studies were based on only one subject, any concrete conclusions cannot be established. Actually, (Pollard et al., 2011) has also shown a series of images during the loss of consciousness by inducing with propofol, but the image verification is also required. It is also good to note that the reconstruction algorithm used in all of above studies which explicitly denoted the used algorithm was the one-step Truncated Singular Value Decomposition Method (TSVD). However, it is different to the algorithm used in the research presented in this thesis.

Table 2-2 Reported consistency and localisation accuracy of brain evoked response

#	Studies	Human subjects	Localisation accuracy / Consistency of responses among trials
1	(Tidswell et al., 2001a)	19	Visual evoked response: 43.75% consistency Somatosensory response: 27.78% consistency
2	(Tidswell et al., 2001c)	39	Visual evoked response: 69.23% correct localisation Motor response: 40.00% correct localization (15% no response) Somatosensory response: 11.11% correct localisation (61.11% no response)
3	(Fabrizi et al., 2006)	7	Epilepsy: 0% consistency

When EIT was employed to detect the larger change in living subjects e.g. the change due to intracranial blood or water volume (large change but slow), the reconstructed images were effectively able to expose the locations of the change inside the cranium with good consistency. (Fu et al., 2014) used EIT to imaging edema disease on 23 patients. The reconstructed images of this study supported the conclusion of previous clinical studies that edema treatment by mannitol was required to be more personalised for different outcomes. The good imaging outcomes for monitoring blood volume change were also reported in (Manwaring et al., 2013) and (Xu et al., 2010). These were carried out on eight piglets and five piglets respectively. However, an intracranial electrode was used in these two studies.

A frequently asked question of EIT imaging is regarding the image resolution. It is widely perceived that EIT has a very good temporal resolution.

However, even though the temporal resolution of the recent EIT machines can be down to 1 ms per frame (Dowrick et al., 2015), recent functional magnetic resonance imaging (fMRI) technology can now provide the temporal resolution of 30 ms or better (Parkes et al., 2007) – sufficiently for capturing the fast response of the brain. On the other hand, the spatial resolution of ordinary fMRI machines is about 1 mm, but the spatial resolution of EIT is still obscure, and there may be no possibility to improve upon it in the near future. One possible way to know the spatial resolution of EIT is to determine it from the localisation error. (Bagshaw et al., 2003) reported that the localisation error of EIT was 40 mm based on a spherical model. (McCann et al., 2006) and (Abascal et al., 2008a) also reported something very similar, with localisation error was equivalently about 24 mm. However, (Aristovich et al., 2014) is a recent study which directly measured the cortex boundary voltages of a rat from a very dense epicortical planar 30 electrode array. With direct reconstruction of the cortex image, the spatial resolution could be substantially improved to 0.2 mm. Therefore, in general, the spatial resolution of EIT with scalp electrodes is still much coarser than the best technology, i.e. the spatial resolution of fMRI is 24 – 40 times better. However, EIT could be improved to the equivalent level of fMRI with invasive measurement by using a very dense cortical electrode array.

2.4 Characteristic of Evoked Responses

For neurological examination, the characteristic of evoked responses is very useful preliminary information for revealing neurophysiological disorders. It can indicate the response expected over a period of time from relevant regions of the brain. Many response characteristics to brain stimulation have been proposed and widely accepted by the use of well-known measuring technology e.g. EEG, and some of them are explained as follows.

2.4.1 Auditory Startle Response (ASR)

Auditory Startle response (ASR) is used for primarily investigating the auditory cortex on the temporal lobes. However, this response is also relevant to non-

primary regions i.e. the brainstem (responding at a very first few milliseconds), the auditory thalamocortical pathway, and the frontal cortex (Billings et al., 2009, Cosmo et al., 2004, Garrido et al., 2009, Näätänen et al., 2004, Walsh et al., 2005). The stimulus could be delivered any time without prior subject awareness with a single pulse (or 1 kHz frequency tone) or pulse(s) in addition with pre-pulse(s). The intensity of the main pulse is usually 110-116 dB with 30-120 ms burst time, whilst the intensity of the pre-pulse is lower, i.e. 75-85 dB with 30-40 ms burst time. The interstimulus interval between main pulse and pre-pulse is 30-120 ms (Muller et al., 2007, Pascalis et al., 2013, Schwarzkopf et al., 1993).

The characteristic of ASR is shown in Figure 2-13. The component N100 (or N1, with latency 100 ms) and P200 (or P2, with latency 200 ms) are usually of interest. The activated regions towards ASR of N100 are the temporal, frontocentral regions, and probably limbic lobe. Meanwhile, those of P200 are centroparietal regions. The reflex due to startling could induce eye-blink and face muscle response. According to some studies regarding electromyography (EMG), the extra-P50 (the latency is 50 ms) near the eyelids could be measured. This extra-component can be reduced by adding the pre-pulse. In the case of face muscle response, it could emerge at 30-500 ms after stimulation onset.

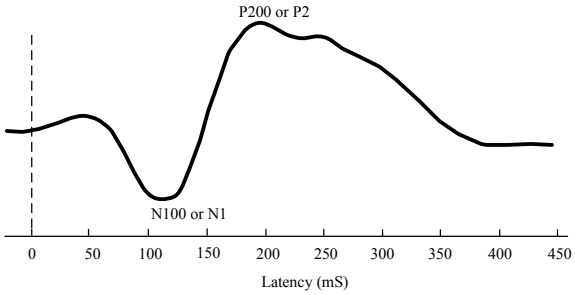

Figure 2-13 Example waveform pattern of Auditory Startle Response (ASR), measured by EEG

The amplitude of ASR is relevant to subject experience and innate emotional responses. Evidently, the response amplitude is smaller when the subject is more familiar with the stimuli (Schwarzkopf et al., 1993). The higher level of anxiety could induce the higher amplitude of ASR and as well as EMG (Pascalis et al., 2013). However, low fear could induce lesser amplitude at P200. The responses due to anxiety and fear are mostly relevant to the response from the prefrontal cortex.

2.4.2 CO_2 Reactivity Response

CO_2 reactivity is one of the clinical examinations for assessing cerebral haemodynamics, and a large change is expected. The experiment begins with normal air breathing (CO_2 concentration is approximately 2.5-3.5%) for 10 minutes. Then the subject is asked to breathe 5% concentration CO_2 for the next 10 minutes, and finally, breathe the normal air again. The increase of CO_2 induces many cerebral activities as shown in Figure 2-14. The artery blood pressure (ABP) and flow velocity (FV) (or CBF) are increased and correspond to the increase of CO_2 (usually determined by the level of carbon dioxide released at the end of expiration, i.e. End-tidal Carbon Dioxide: $EtCO_2$) (Gooskens et al., 2003, Roy, 1890). However, the contradictory response can be induced due to hypercapnia (the elevation of CO_2 level). The increase of ABP and CBF are caused from vasoconstriction, but the hypercapnia induces vasodilation instead. However, the response due to hypercapnia is smaller than the responses due to ABP and CBF regulation. Furthermore, hypercapnia introduces the change of haematocrit (the percent of red blood cells). The change of haematocrit is straightforwardly relevant to the change of blood conductivity (Levin et al., 2001, Sapkota et al., 2015) – when the haematocrit is decreased, the conductivity is increased.

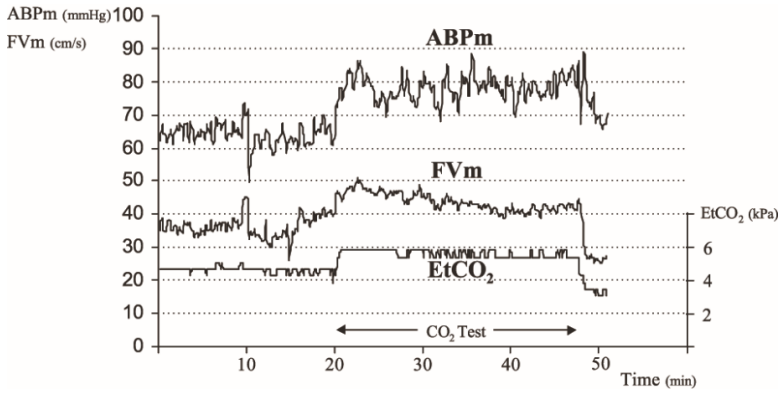

Figure 2-14 Example responses from CO_2 reactivity test. ABPm is the mean of artery blood pressure, FVm is the mean of flow velocity, $EtCO_2$ is the end tidal CO_2 (Gooskens et al., 2003)

2.4.3 Transient Hyperaemic Response (THR)

Transient Hyperaemic Response (THR) is used as a regular clinical examination for cerebral autoregulation assessment. A carotid artery compression is performed on a side of the neck for at least 5 seconds, and the blood flow velocity (FV) is then measured usually at middle cerebral arteries (MCAs). At the moment of compression i.e. a carotid artery is occluded, it causes the decrease in cerebral blood flow (CBF) and perfusion pressure throughout the entire MCA territory, and induces the vasodilation of small cerebral vessels in order to compensate for the missing blood (Giller, 1991, Smielewski et al., 1996, Webster and Mahajan, 2002). When the occlusion is released, the CBF is briefly increased as a consequence of compensatory vasodilation (lasting less than 0.5 second) i.e. a reflection of cerebral autoregulation (Figure 2-15). Transcranial Doppler ultrasound (TCD) is usually used for measuring FV changing of MCA (near the ears). The change of FV during the occlusion measured by TCD can be between 35% and 57%. It should be noted that TCD cannot directly measure CBF. However, the change of FV can be used to infer the change of CBF because the diameter of MCA does not significantly change for the brief compression.

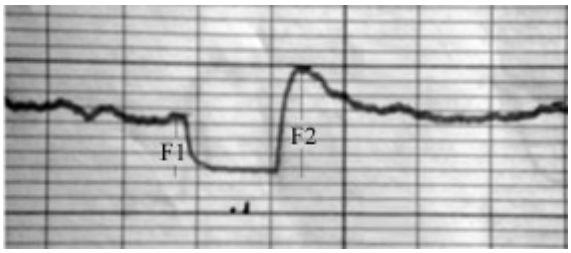

Figure 2-15 Example response from transient hyperaemic response test (THRT), measured from transcranial Doppler ultrasound (TCD), adapted from (Webster and Mahajan, 2002).

2.5 Image Reconstruction

Image reconstruction is the primary task of EIT to estimate conductivity distribution within the boundary of a measured subject from a finite number of measurements obtained from an array of electrodes. The conductivity of small regions within the boundary, i.e. “elements” in the term of Finite Element Method

(FEM), is the unknown parameter that EIT method is intended to determine. However, due to the huge difference between the numbers of unknown parameters, i.e. element conductivities, and known parameters, i.e. measurement voltages, the EIT image reconstruction problem is naturally ill-posed. The term "ill-posed" is commonly used to identify a problem that breaks at least one of the "well-posed" conditions (Hadamard, 1902), i.e. the problem is well-posed when a) a solution exists - existence, b) the solution is unique - uniqueness, and c) the solution changes continuously depending on the observed data – stability. The problem of EIT severely suffers from its instability, so that it is unable to comply with the third criterion. The solution of EIT problems naturally is susceptible to noise. Tiny additive noise can produce huge conductivity perturbation which is not real. This situation becomes very much more severe in applications of EIT to the human head due to the substantially high number of elements relative to the number of measurements, very low measurement sensitivity to conductivity perturbation, and the infusion of large noise components.

Head EIT is undoubtedly a large ill-posed inverse problem due to the large number of elements, and consequently the large computational memory and computation time are concerned (Boyle et al., 2012). Furthermore, due to the extremely small sensitivity of EIT to the brain conductivity, it leads to a severe level of ill-posedness, which mathematically can be observed via the condition number of the Jacobian matrix (or "sensitivity matrix"). The Jacobian matrix contains the sensitivity information of the boundary voltages to conductivity perturbation (Polydorides, 2002). An example situation is shown in Table 2-3. Obviously, the condition number of the sensitivity matrix of the heterogeneous case is much higher than that of the homogeneous case for approximately 21 times. Compared to the homogeneous case commonly used on other medical EIT applications, e.g. lung EIT or breast EIT, this examination confirms explicitly that the head EIT is more difficult and challenging to solve.

Table 2-3 The means of sensitivity of head tissues, and the condition number of sensitivity matrix (Jacobian matrix), based on the simulation of 1 mA_{rms} current excitation

	heterogeneous Case (Practical Case)	**Homogeneous Case (The conductivity of all elements were set to 0.58 S/m)**
Tissues	**Mean Sensitivity (V.m/S)**	**Mean Sensitivity (V.m/S)**
Scalp	-13.809×10^{-9}	-1.406×10^{-9}
Skull	-344.669×10^{-9}	-2.340×10^{-9}
CSF	-0.254×10^{-9}	-1.299×10^{-9}
Grey matter	-0.684×10^{-9}	-2.309×10^{-9}
White matter	-0.564×10^{-9}	-1.269×10^{-9}
Condition Number	116.501×10^{14}	5.523×10^{14}

Another critical error that is mainly focused on in this thesis is modelling error. The EIT problem is model dependent i.e. the accuracy of the model used is crucial (Brown and Barber, 1988). However, the human head has complex geometry and structure form which is extremely difficult to construct an accurate head model. The coarse mesh resolution, inaccurate electrode position, and unknown contact impedance can also introduce the modelling error. Unfortunately, since the modelling error of a head model is impossible to evaluate in practice, solving the problem with ignorance of this error by conventional inverse algorithms could fail. Even though the difference imaging approach has been reported to be able to handle the presence of modelling error to some extent, since it is a linear method, it is not suitable for the high degree of nonlinearity as encountered in the head EIT problem.

There are many tools to help for constructing a head model. However, a subject model (i.e. a head model determined from anatomical head images of the human subject) is still difficult to obtain in practice. A generic head model is practically of interest, with the expectation that the error of the use of the generic model is acceptable for obtaining accurate images. Since the spatial resolution of EIT for head applications is generally poor, the localisation error due to the use of generic models could be insignificant i.e. the use of generic models might be possible. However, this statement is still required to be investigated.

2.5.1 Modelling Error in EIT Forward Computation

Modelling error is usually ignored even though it is influenced to the accuracy of forward computation. The modelling error mitigation has been intensively investigated in EIT (Dehghani and Soleimani, 2007, Kaipio et al., 2000, Kaipio and Somersalo, 2007, Kolehmainen et al., 1997, NissinenVille et al., 2011, Nissinen et al., 2008, Nissinen et al., 2009, Nissinen et al., 2010) and on the closed tomographic technique i.e. optical diffusion tomography (Arridge et al., 2006, Kolehmainen et al., 2009, Mozumder et al., 2014). However, the term "modelling error" is ambiguous regarding its literal meaning and the implementation meaning. For the literal meaning, the modelling error is the difference between the exact geometry of the structure and geometry of the model used. However, for the implementation meaning which is taken by most previous studies, is based on the idea that the used model is sufficiently accurate, but the actual geometry and structure can change over time, e.g. in the situation of lung EIT. In the work presented in this thesis, since the deformation of the head is very small, the literal meaning is preferred. Sometimes, the modelling error in this meaning is called "discretization error" instead (Nissinen et al., 2008).

Regarding the measurement time series V, the forward problem of EIT for the recording frame index i can be written as

$$V_i = U(\sigma_i) + \varepsilon(\sigma_i) + e_m; \quad where \quad e_m \sim N(0, \Gamma_e) \tag{2.22}$$

where U is the discretization function of the conductivity σ, ε is the modelling error function, and e_m is the measurement error which is zero-mean Gaussian with the covariance Γ_e. The estimation $\hat{\sigma}$ is determined from the least square of the residual of the difference between the real measurement and the measurement prediction in addition to the modelling error, as shown in (2.23) where R is the regularisation function (obtained from prior information of σ), and λ is the regularisation parameter. The estimation $\hat{\sigma}$ can be referred to as the "absolute image" of a time. However, in most applications of EIT, the difference between two estimations, i.e. two difference times, i.e. the "time-difference image", is more interesting.

$$\hat{\sigma}_i = \underset{\sigma}{\operatorname{argmin}} \left\{ \left\| V_i - U(\sigma) - \varepsilon(\sigma) \right\|^2 + \lambda \left\| R(\sigma) \right\|^2 \right\} \tag{2.23}$$

Modelling error ε is practically difficult to know, in particular in the head application, and it is usually assumed to be zero (Horesh, 2006). Since ε may not be zero mean, the ignorance of ε can cause imaging error. However, if the distribution of conductivity changes only slightly over time, the imaging error on reconstructed images should be very similar. Therefore, to reduce the impact of modelling error, the subtraction between two absolute images $\delta\hat{\sigma}_{(i+1,i)}$ is usually performed as in (2.24). This methodology is named the "absolute imaging approach" and it works only when the model used is only slightly inaccurate.

$$\begin{aligned} \delta\hat{\sigma}_{(i+1,i)} = \hat{\sigma}_{i+1} - \hat{\sigma}_i = & \underset{\sigma}{\operatorname{argmin}} \left\{ \left\| V_{i+1} - U(\sigma) \right\|^2 + \lambda \left\| R(\sigma) \right\|^2 \right\} \\ & - \underset{\sigma}{\operatorname{argmin}} \left\{ \left\| V_i - U(\sigma) \right\|^2 + \lambda \left\| R(\sigma) \right\|^2 \right\} \end{aligned} \tag{2.24}$$

Alternatively, the "linear difference imaging approach" can directly reconstruct the image of difference by assuming the problem is linear and also the modelling error is zero. The measurement prediction is estimated by the use of the Jacobian matrix which is based on the "reference state" σ_0 as shown in (2.25). The difference between two measurement vectors is determined from (2.26), and the difference image can be computed from $\delta V_{(i+1,i)}$ as in (2.27). It has been shown that this approach is more robust to modelling error than the absolute imaging approach in many homogenous situations (Liu et al., 2015a, Liu et al., 2015b, Mozumder et al., 2014). However, this approach is theoretically not suitable for head EIT due to the fact that the head EIT problem is very inhomogeneous and it is a high-degree nonlinear problem. Also, note that the modelling error function is not considered in these equations.

$$V_i \approx U(\sigma_0) + J\delta\sigma_{(i,0)} + e_m; \quad where \quad J = \frac{\partial U(\sigma_0)}{\partial \sigma}, \delta\sigma_{(i,0)} = (\sigma_i - \sigma_0) \tag{2.25}$$

$$\delta V_{(i+1,i)} = V_{i+1} - V_i \approx J\delta\sigma_{(i+1,i)} + \delta e_{m(i+1,i)}; \quad where \quad \delta e_{m(i+1,i)} = e_{mi+1} - e_{mi} \tag{2.26}$$

$$\delta\hat{\sigma}_{(i+1,i)} = \underset{\delta\sigma}{\operatorname{argmin}} \left\{ \left\| \delta V_{(i+1,i)} - J\delta\sigma \right\|^2 + \lambda \left\| R(\sigma) \right\|^2 \right\} \tag{2.27}$$

2.5.2 Reconstruction Algorithms for Large-Scale Problems

Indeed, there are many algorithms developed for solving an inverse problem. However, most of them were designed for small-scale problems. In fact, the general EIT problem naturally is supposed to be a small-scale problem, considered from the complexity of a model, i.e. the structure is simple and the number of unknown parameters is low. Head EIT problem, however, usually has a high number of unknown parameters, i.e. elements, implying that it requires large computational memory to solve the problem. Regarding the process of solving an EIT problem, the Jacobian matrix (J) is computed during the reconstruction process, where the matrix size is the number of measurements multiplied by the number of mesh elements of the inverse model. The computation for the term $J^{\mathrm{T}}J$ which is required in ordinary reconstruction algorithms causes the overflow of memory. For example, with a "very rough" head model having 50,000 elements, the memory required for J corresponding with 500 measurements is 200 MBytes, but that for $J^{\mathrm{T}}J$ is 20 GBytes which is beyond the memory limit of ordinary computers.

Certain reconstruction techniques have the capability to solve large-scale problems e.g. Conjugate Gradient method (CG), Singular Value Decomposition method (SVD), and Hybrid Krylov-Tikhonov regularisation method. However, the performance of CG method largely depends on the selected number of iterations which is very difficult to determine. CG and SVD methods are also restrained to use with the standard Tikhonov regularisation, i.e. the prior information is imposed to be the identity matrix. The modification for using more complicated prior information can cause the overflow of computational memory. Therefore, only the Hybrid Krylov-Tikhonov regularisation methods are suitable and are explained here.

In principle, the hybrid method solves a projected problem obtained from a Krylov projection method (Bouhamidi et al., 2012, Gazzola et al., 2014). More specifically, Krylov-projection is applied to a problem as shown in (2.28) first, where A is the known matrix (sometimes, it is called the "system matrix" or "transfer matrix"), x is the unknown variable, and b is the known variable (sometimes, it is called the "observation").

$$Ax = b \tag{2.28}$$

This projection results in a new much smaller problem which can be solved by particular algorithms. Two Krylov projection methods are usually used: Arnoldi projection method (Algorithm 2.1) and Lanczos projection method (one variation, i.e. non-symmetric Lanczos biorthogonalization algorithm, is shown in Algorithm 2.2). Both of them have been used on EIT problems, e.g. (Horesh et al., 2007) for Arnoldi projection method, and (Hu et al., 2007) for Lanczos projection method. Actually, they are orthogonal projection methods for approximating eigenvalues of a large sparse matrix. The Lanczos projection method is a simplified version of the Arnoldi projection method, but it has much more detail and more variations than the Arnoldi projection method. The Lanczos projection method has greater risk of serious breakdown during the approximation in certain situations (Saad, 2011).

Many hybrid methods to solve these projection methods have been proposed, however only few of them are popular. The Generalized Minimal Residual method (GMRes) is the most popular among the methods based on Arnoldi projection which is workable with severely ill-conditioned problems (Novati and Russo, 2014). The Arnoldi projection (Algorithm 2.1) solves a problem by spanning Krylov subspace $K_m(A,b)$ to an upper Hessenberg matrix H, with the orthonormal vectors $\{w_1, w_2, \ldots, w_m\}$ containing in the orthonormal basis matrix W, i.e. $W^T AW=H$. The number of the Arnoldi iteration m, imposed by a user, specifies the size of Hessenberg matrix $\overline{H}$, and it indicates the computational memory required. The Hessenberg matrix is used as the new system matrix of the new projection problem as in (2.29). The scale of this new problem is a much smaller than the original problem, and the new problem can be solved for $\hat{y}$ by any conventional methods, e.g. Gauss-Newton method. Finally, the solution of this problem $\hat{x}$ can be readily acquired by simple multiplication with W as shown in (2.30).

$$\hat{y} = \underset{y}{\arg\min}\left\{ \left\| \|b\| e_{m+1} - \overline{H} y \right\|^2 \right\}; \quad where \quad y \in \Re^m, e_{m+1} = [0,0,\ldots,1]^T \in \Re^{(m+1)} \tag{2.29}$$

$$\hat{x} = W\hat{y} \tag{2.30}$$

Algorithm 2.1: Arnoldi projection algorithm (Gazzola et al., 2014, Saad, 2011)

Inputs: b, A

Initially set: $w_1 = b/\|b\|$

For $j = 1, 2, \ldots, m$

Set $w = Aw_j$

For $i = 1, 2, \ldots, j$

Set $h_{i,j} = \langle w, w_i \rangle$

Set $w = w - h_{i,j} w_i$

Set $h_{j+1,j} = \|w\|$

If $h_{j+1,j} = 0$ or $j+1 > m$ then stop, else Set $w_{j+1} = w/h_{j+1,j}$

Return $W = \{w_1, w_2, \ldots, w_m\} \in \Re^{m \times m}$, $H = [h_{i,j}]_{i,j=1,\cdots,m} \in \Re^{m \times m}$, and $\overline{H} = \begin{bmatrix} H \\ h_{m+1,m} e_m^T \end{bmatrix} \in \Re^{(m+1) \times m}$ where $e_m \in \Re^m$ is the basis vector

In the case of the Lanczos projection based method, there are many variations. LSQR is a first option that is based on the primitive version, the Lanczos bidiagonalization algorithm. It is mathematically equivalent to CGLS with better stability properties. Quasi-Minimal Residual (QMR) is another popular one that is based on the Lanczos biorthogonalization algorithm as shown in Algorithm 2.2. QMR uses the orthonormal basis matrix W and the tridiagonal matrix $\overline{T}$ to create the new problem as (2.31). The solution can be found by using the same equation to GMRes, i.e. (2.30).

$$\hat{y} = \arg\min_{y} \left\{ \left\| \|b\| e_{m+1} - \overline{T} y \right\|^2 \right\}; \quad where \quad y \in \Re^m, e_{m+1} = [0,0,\ldots,1]^T \in \Re^{(m+1)} \tag{2.31}$$

According to Algorithm 2.2, essentially, two sets of basis vectors $\{w_1, w_2, \ldots, w_m\}$, containing in W, and $\{k_1, k_2, \ldots, k_m\}$, containing in K, are used for spanning the Krylov subspaces of $K_m(A,b)$ and $K_m(A^T,b)$ respectively to the tridiagonal matrix T. It complies the relation $K^T A W = T$ and $W^T A^T K = T^T$. Similar to the Arnoldi projection, the number of the iteration m, imposed by a user, indicates the requirement of computational memory. The new projection problem as in (2.31) is also in the similar format as that of the Arnoldi projection.

Algorithm 2.2: Nonsymmetric Lanczos biorthogonalization projection algorithm (Gazzola et al., 2014)

Inputs: b, A

Initially set: $w_1 = b/\|b\|, k_1 = w_1, w_0 = k_0 = 0, \beta_1 = \delta_1 = 0$

For $j = 1, 2, \ldots, m$

Set $\alpha_j = \langle Aw_j, k_j \rangle$

Set $w = Aw_j - \alpha_j w_j - \beta_j w_{j-1}$

Set $k = A^T k_j - \alpha_j k_j - \delta_j k_{j-1}$

Set $\delta_{j+1} = \sqrt{|\langle w, k \rangle|}$

If $\delta_{j+1} = 0$ then stop

Set $\beta_{j+1} = \langle w, k \rangle / \delta_{j+1}$

Set $k_{j+1} = k/\beta_{j+1}$

If $j+1 > m$ then stop, else Set $w_{j+1} = w/\delta_{j+1}$

$$T = \begin{bmatrix} \alpha_1 & \beta_2 & & & \\ \delta_2 & \alpha_2 & \beta_3 & & \\ & \ddots & \ddots & \ddots & \\ & & \delta_{m-1} & \alpha_{m-1} & \beta_m \\ & & & \delta_m & \delta_{m+1} \end{bmatrix}$$

Return $W = \{w_1, w_2, \ldots, w_m\} \in \Re^{m \times m}$, $T \in \Re^{m \times m}$, and $\overline{T} = \begin{bmatrix} T \\ \delta_{m+1,m} e_m^T \end{bmatrix} \in \Re^{(m+1) \times m}$ where $e_m \in \Re^m$ is the basis vector

However, these methods are supported only for square transfer matrix of A, whilst in the problem of EIT, this matrix is the Jacobian matrix which is a rectangular matrix. Furthermore, they were not designed for including prior information. An adaptive version to answer these needs has been proposed by (Horesh, 2006, Horesh et al., 2007, Schweiger et al., 2005). In general, the second-order (or L_2) Tikhonov regularisation as shown in (2.32) where R is the prior information, is re-written into (2.33), and then (2.33) is solved by a Hybrid Krylov method explained above. This method was named "Newton-Krylov General Minimal Residual" when it is based on GMRes. Therefore, (2.28) is now replaced with (2.33), where A becomes $\widetilde{A}$, x becomes δx, and b becomes $\delta\widetilde{b}$. This version has been carried out on head EIT data, and it can fit into the memory when the matrix

multiplications are ordered properly in the projection process. Another option is the generalized global Arnoldi method (Bouhamidi et al., 2012) that is included the regularisation during projection. This method can optimise the regularisation parameter during the reconstruction by including an evaluation technique e.g. Generalized Cross-Validation (GCV) or L-curve into the reconstruction process. However, it was initially designed for large-scale linear discrete ill-posed problems like image deblurring, and it has not yet been implemented in the problem of EIT.

$$\hat{x}_{i+1} = \hat{x}_i + \left(A^T A + \lambda R^T R\right)^{-1} A^T \left(b - A\hat{x}_i\right) \tag{2.32}$$

$$\widetilde{A}\delta x = \delta\widetilde{b}\,; \quad where \quad \widetilde{A} = \left(A^T A + \lambda R^T R\right), \delta x = \left(\hat{x}_{i+1} - \hat{x}_i\right), \delta\widetilde{b} = A^T\left(b - A\hat{x}_i\right) \tag{2.33}$$

2.5.3 Regularisation

Regularisation is a necessary process to deal with the ill-posed condition by adding solution information into the least square equation i.e. the term $\lambda\|R(\sigma)\|^2$ in (2.23). It is transformed to the additional information term $\lambda R^T R$ in the equation of Tikhonov regularisation as shown in (2.32). The degree of regularisation is controlled by the regularisation parameter λ. Mathematically, the regularisation improves the condition number of the transfer matrix A i.e. it decreases the degree of ill-posedness of the problem. In another words, it is used to tune the fitness of solution. If the regularisation causes the solution to be underfitted, the solution is only rough information. But if the regularisation causes the solution to be overfitted, the solution is then close to both the expected answer and noise. Therefore, suitable fitting is an imperative task in regularisation. Note that $\lambda R^T R$ is sometimes called the "penalty" of problem complexity or "filter", whilst $R^T R$ or R is sometimes called "solution information" or "prior information".

The solution information matrix could be the identity matrix, as used in the standard Tikhonov regularisation (however, in this case, it is not precise to use the name of "prior information"), or it could be more complicated e.g. popular ones are the smoothness prior, the Laplace prior, or the total variation prior. The smoothness prior and Laplace prior are Gaussian smoothing filters obtained from the first derivative of solution x. They essentially contain model geometry information

where the element volumes could be used as the weights of the derivative (the smoothness prior) (Calvetti and Somersalo, 2007), or not used (the Laplace prior) (Gersch, 1984). However, these priors prevent sharp transitions of solution, which seems preferable for medical EIT. The total variation prior allows reconstructing the step transition of solution by determining the integral of the derivative of the solution, that is the integral of $|\nabla x|$, instead. The distribution of the solution is not necessary to be smooth for this prior. However, it is more complicated and requires more computational resources (Lionheart, 2004).

The regularisation parameter λ in fact is explainable by the statistical principle of the Maximum A Posteriori (MAP) estimator (Adler and Guardo, 1996, Calvetti and Somersalo, 2007). λ is actually the square root of the ratio between the variance of the observation b and the variance of the solution x, where the distributions are all Gaussian. However since EIT is actually a nonlinear problem, to obtain λ by the statistical method is difficult. The investigation of λ obtained by statistical method is also necessary (Tarits et al., 1994). Conventionally, four non-statistical methods to obtain λ are chosen instead: Discrepancy Principle (DP), Minimum Predictive Error (MPE), Generalized Cross Validation (GCV), and L-Curve. These four evaluation methods have been investigated for EIT on four neonatal infants (however, the model used was homogeneous) (Abascal et al., 2008b). No significant differences of these methods were found in this study, but the L-Curve method and the GCV method were recommended because they did not require knowledge of empirical measurement uncertainty or prediction error. However, only the L-Curve method has been recommended in this thesis. With L-Curve, the modelling error can be taken into account in the data misfit term. Meanwhile, DP, MPE, and GCV are not suitable because they rely on linear problems without the presence of modelling error.

L-Curve is a heuristic method to evaluate the trade-off between the measurement data misfit norm (or residual norm) $\| A\hat{x}-\hat{b} \|$, and the regularisation norm (or solution norm) $\| R(x-x_0) \|$ (Farquharson and Oldenburg, 2004, Hansen, 1998, Viklands and Gulliksson, 2000). The graphical relationship between these two terms is an "L" shape (an example can be seen in Section 5.3.4). Overfitting data (i.e.

small residual) by small filtering (i.e. small regularisation parameter) results in a large number of high contrast undesirable artefacts. Underfitting data (i.e. large residual) by high filtering (i.e. large regularisation parameter) results in a blurred image. The λ producing the data misfit at the corner of the "L" curve is preferable to balance between these two norms. However, to obtain this curve, many trials on different values of λ are required. Therefore, this method undoubtedly requires lots of time to evaluate. Moreover, in many situations, the curve may be too shallow to address the corner (Graham and Adler, 2006).

2.5.4 Guaranteeing Convergence

Guaranteeing convergence is a process of optimization to find a local minimum of residual, i.e. the measurement misfit of prediction in the context of EIT, by a globalisation strategy. The local minimum found will be used as the new estimate of the solution. The line search strategy is the most popular method (and the oldest method) by adding step length α into the search direction $\delta\hat{\sigma}_{(i+1,i)}$ as in (2.34) (referred to (2.24)) (Nash and Sofer, 1996). Basically, the step length can be between zero and one. The length that yields the lowest measurement misfit is chosen, as (2.35). The testing step lengths are usually generated manually. The short step size is certainly better to find the local minimum, but it could lead to overfitting to the noise infused in the measurements. The process of line searching requires extra-computation time to compute, and this is seriously troublesome in large-scale non-linear problems. Furthermore, if the problem is infused with large unknown-modelling error and noise, the line search strategy may be unable to work correctly.

$$\hat{\sigma}_{i+1} = \hat{\sigma}_i + \alpha\delta\hat{\sigma}_{(i+1,i)}\ ; \quad 0 < \alpha \le 1 \tag{2.34}$$

$$\alpha = \arg\min_{\alpha}\left\{V_{i+1} - U\left(\hat{\sigma}_{i+1,\alpha_k}\right)\right\}; \quad \alpha_k \in \alpha \tag{2.35}$$

Chapter 3 Estimating Conductivity of Human Head Tissues

3.1 In-vivo Scalp and Skull Conductivity Estimation

3.1.1 Principle of Estimation

The measurement data of EIT can be used to non-invasively estimate the nominal conductivities of the head tissues. However, an accurate subject head model is required. According to the capability of most software packages for tissue surface extraction to date, only maximum five conductivities can be estimated: the conductivity of the scalp, the skull, CSF, and the grey and the white matter.

Regarding the measurement forward problem of EIT described by (3.1), the measurement voltage V can be predicted from the discretization model function U of the conductivity distribution σ, in addition with the modelling error ε and the measurement error e_m. In the case that the model used is a good subject model, ε is supposed to be small and then ignorable. Employing Taylor series, V can be approximated nonlinearly by (3.2) where J is the Jacobian matrix and i is the iteration index. The estimated conductivity $\hat{\sigma}$ can be computed by minimising the error between V and U by (3.3) with the iterative non-regularised Gauss-Newton method as shown in (3.4).

$$V = U(\sigma) + \varepsilon(\sigma) + e_m \tag{3.1}$$

$$V_i \approx U(\sigma_{i-1}) + J_{i-1}(\sigma_i - \sigma_{i-1}); \quad where \quad J_{i-1} = \frac{\partial U(\sigma_{i-1})}{\partial \sigma} \tag{3.2}$$

$$\hat{\sigma}_i = \underset{\sigma}{\operatorname{argmin}} \left\{ \| V_i - U(\sigma) \|^2 \right\} \tag{3.3}$$

$$\hat{\sigma}_i = \sigma_{i-1} + \left(J_{i-1}^T J_{i-1} \right)^{-1} J_{i-1}^T \left(V_i - U(\sigma_{i-1}) \right) \tag{3.4}$$

The nominal tissue conductivities can be estimated in a similar way to (3.4). All small regions of the same tissue are determined as a single region with a single nominal conductivity value. The sensitivity of each single region is then averaged here. The average sensitivity of the CSF and the brain regions is very low: 20-54 times lower than that of the scalp, and 500-1,360 times lower than that of the skull

(Table 2-3). To include the estimation of the CSF and the brain conductivity could be inappropriate since they are very sensitive to noise (and also sensitive to the error arising during the estimation process). Therefore, the conductivities of the CSF, the grey and the white matter were fixed at the constant values of 1.802 S/m for CSF (Baumann et al., 1997), and 0.2849 S/m and 0.2556 S/m for the grey and white matter respectively (Latikka et al., 2001). Only two nominal conductivities then remain to be evaluated: the scalp conductivity and the skull conductivity, and that is the objective of this section. The equation (3.4) can be rewritten as (3.5) where $\hat{\sigma}_{sc-sk}$ is the vector of the scalp conductivity and the skull conductivity, and $J_{sc\text{-}sk}$ is the matrix of the average sensitivity of the scalp and the skull regions. The quality of the estimates can be evaluated by the relative error as shown in (3.6).

$$\hat{\sigma}_{sc-sk,i} = \sigma_{sc-sk,i-1} + \left(J^T_{sc-sk,i-1} J_{sc-sk,i-1}\right)^{-1} J^T_{sc-sk,i-1}\left(V_i - U(\sigma_{i-1})\right) \tag{3.5}$$

$$RelativeError = \frac{\|V - U(\sigma)\|}{\|V\|} \tag{3.6}$$

3.1.2 Estimation Methods

The estimation was carried out on EIT data from a subject. Three experiments were performed on different days with the 1 $mA_{pk\text{-}pk}$ fEITER system (explained in Chapter 4). A subject model with electrode geometry was constructed containing 337,774 elements. The code name of the model was "JD_CIR" (see Figure 3-1). Approximately 11 seconds (1,100 records) of each experimental data recording session were selected. In order to reduce noise, the 1,100 records of each day were averaged to give one voltage measurement vector for each day. The estimation was performed by equation (3.5) with 15 iterations.

In addition, the prediction accuracy based on the acquired estimates was compared to those based on conductivity values used in the previous studies (Davidson et al., 2007, McCann et al., 2006, Murrieta-Lee et al., 2004, Towers et al., 2000), i.e. 0.172 S/m for scalp, and 0.006 S/m or 0.0533 S/m for skull. Seven head models from three subjects were used in the investigation. The used models were coded: "UCL1", "UCL2", "UCL3", and "UCL4" constructed from a non-subject head geometry, containing 53k, 158k, 208k, and 274k elements respectively;

"BRIC3" constructed from an another non-subject MR image, containing 301k elements; and "JD" and "JD_CIR" constructed from a subject MR image, containing 338k and 342k elements respectively. Only the "UCL1" and "JD" models did not include the electrode geometry, the comparison between including and the non-including versions are shown in Figure 3-1. Another three data obtained from different experimental days and the same subject to the conductivities estimation were selected to evaluate the prediction performance of the new estimated scalp and skull conductivity values. The record data of 40 second-session (4,000 records) of each data were averaged before using in the evaluation.

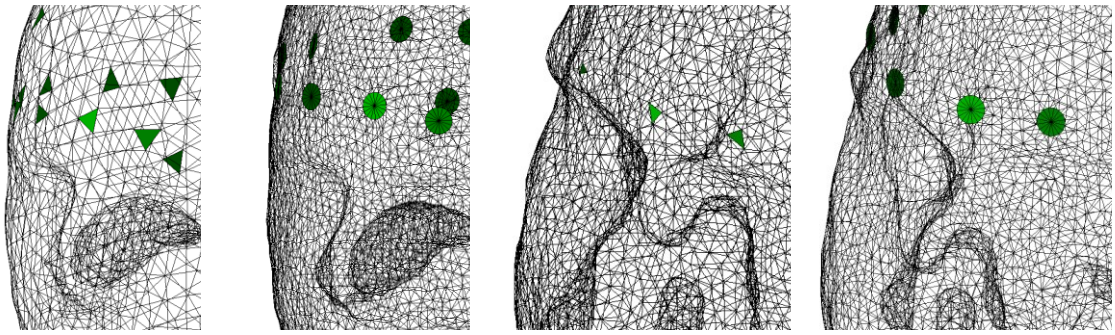

(a) UCL1 (b) UCL3 (c) JD (d) JD_CIR

Figure 3-1 Comparison between the models including electrode geometry: (b) and (d), and those non-including: (a) and (c).

3.1.3 Results

The converged solutions after 15 iterations indicated that the average conductivity of the scalp was 0.584±0.026 S/m and that of the skull was 0.0084±0.0005 S/m (Figure 3-2) (Ouypornkochagorn et al., 2014). Interestingly, the conductivity of the scalp was significantly higher than the reported conductivities shown in Section 2.1.1, and the conductivity of the skull was at the low end of the reported conductivities shown in Section 2.1.2. There is small variation between the results found from different dates (less than 6%). The conductivity ratios of scalp: skull: brain found here were approximately 70:1:34, i.e. a relatively high ratio for the scalp to skull values. The comparison between the prediction voltages and the averaged measurement voltages of one of the evaluation data sets are shown in Figure 3-3 and Figure 3-4. Generally, they are consistent. The large unmatched

differences tend to be of the non-adjacent electrode-pair measurements (see the measurement configuration in Appendix D).

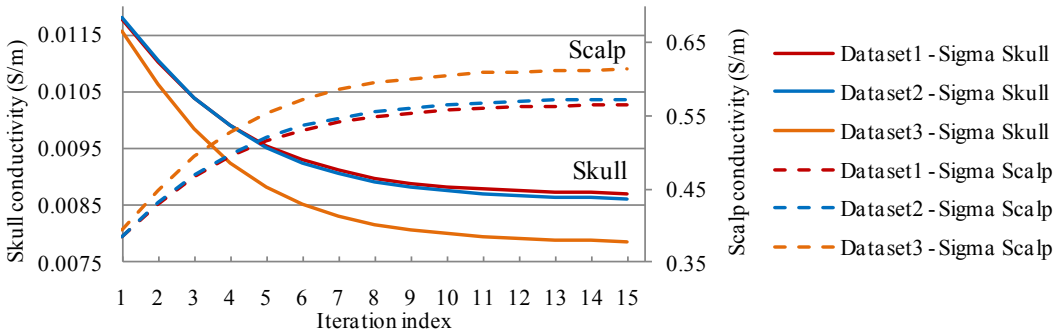

Figure 3-2 Conductivity estimation of the scalp (the dash lines) and the skull (the solid lines); the different line colour indicates the different experiment days.

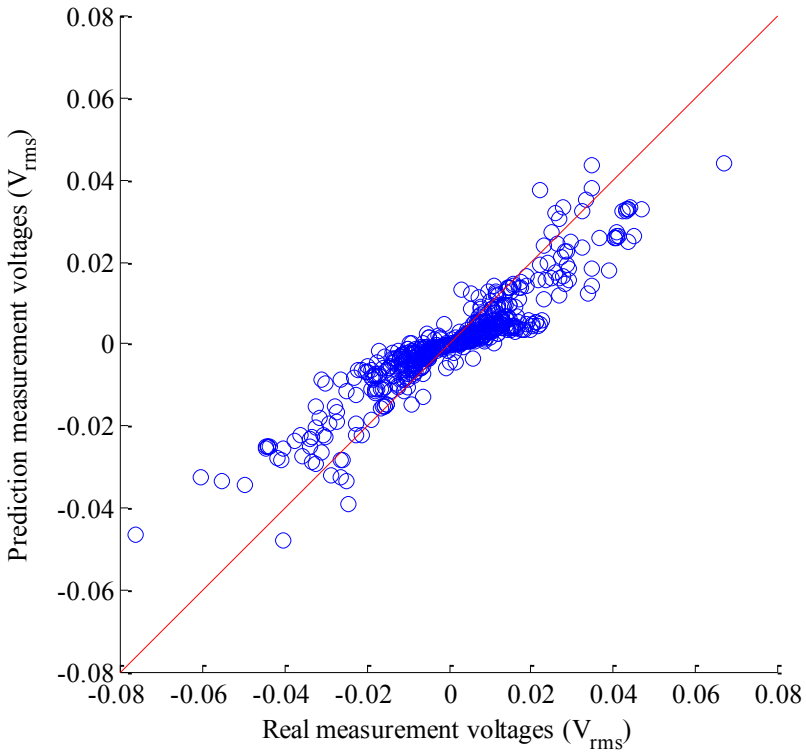

Figure 3-3 Scatter-plot comparison between the measurement voltages and the prediction voltage in Figure 3-4.

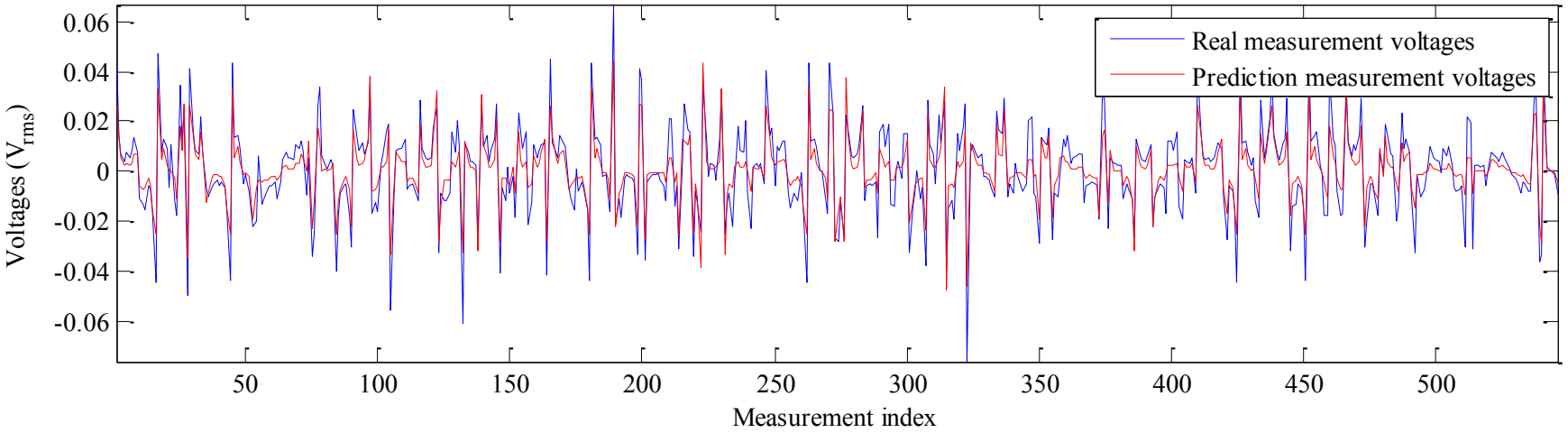

Figure 3-4 Comparison between the measurement and the prediction voltages of an example data using the estimated values of conductivity.

The averaged relative error of the predictions based on three sets of scalp and skull conductivity values are shown in Figure 3-5. Obviously, with the use of the new estimated scalp and skull conductivity values, the prediction on the subject model with electrode geometry inclusion provided the smallest error (i.e. 0.32). When these values were employed on the other models, the error was increased by a maximum of 0.18 (on "BRIC3" model). It can be also noticed that including electrode geometry can reduce the error by 0.04. The use of conductivity values from previous literature caused the error to increase by a maximum of 0.77, i.e. 4.3 times larger than that caused by using a different head model. The use of lower conductivity values of the skull (29% lower, i.e. 0.006 S/m) and the scalp (71% lower, i.e. 0.172 S/m) than the new estimated values found here had a very large effect on the mismatch. However, the use of 535% higher conductivity value (i.e. 0.0533 S/m) of the skull, but 71% lower value of the scalp only had a small effect on the mismatch. This implies that in the situation that a subject model is unavailable, a high value of skull conductivity should be selected from the reported values. Additionally, it could be noticed that the mesh resolution did not significantly influence the prediction accuracy. Less than 1% of error was removed due to the use of 32% finer mesh resolution (regarding the outcomes of the model “UCL3” and “UCL4”).

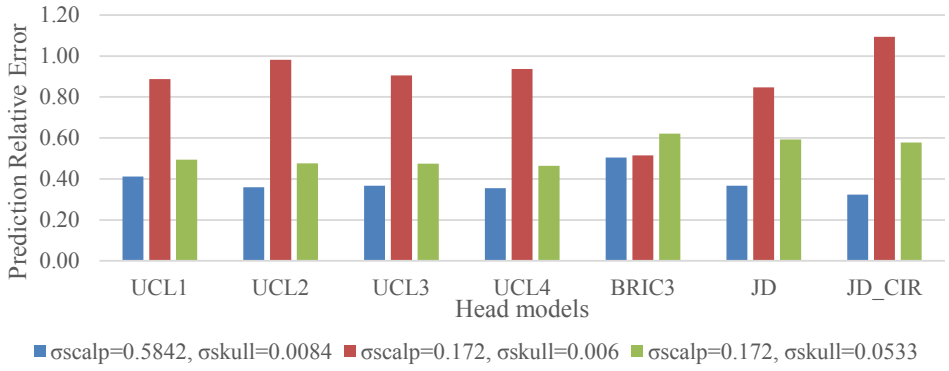

Figure 3-5 Relative error of the three schemes of conductivity values: 1) 0.5842 S/m and 0.0084 S/m (the estimated values found in this research), 2) 0.172 S/m and 0.006 S/m, and 3) 0.172 S/m and 0.0533 S/m for scalp and skull conductivity values respectively. The model coded “JD_CIR” was used in the conductivities estimation. All models included electrode geometry, except for the models coded “UCL1” and “JD”. The models coded “JD” and “JD_CIR” were subject models.

3.2 Bulk Conductivity

3.2.1 Principle of Bulk Conductivity

The bulk conductivity approach considers the entire head as a single homogeneous bulk material. The bulk conductivity can reflect the global change, and accordingly it could be suitable for certain kinds of brain response study, e.g. CO_2 reactivity response. The principal idea to obtain the bulk conductivity is similar to that in the previous section. However, only one parameter is of interest, i.e. $\hat{\sigma}_{bulk}$, as in equation (3.7) where J_{bulk} is the average sensitivity of the whole head. The changing of the bulk conductivity ($\delta\hat{\sigma}_{bulk}$) represents the global change inside the measurement boundary (Ouypornkochagorn et al., 2015b).

$$\delta\hat{\sigma}_{bulk} = \left(J_{bulk}^T J_{bulk}\right)^{-1} J_{bulk}^T \left(V_i - U\left(\sigma_{i-1}\right)\right); \delta\hat{\sigma}_{bulk} = \hat{\sigma}_{bulk,i} - \hat{\sigma}_{bulk,i-1} \tag{3.7}$$

3.2.2 Investigation Methods

The bulk conductivity method was implemented here on two response applications: CO_2 reactivity response and Transient Hyperaemic Response (THR). The response expected inside the cranium due to CO_2 inhalation is global, but the response in the scalp region is still unrevealed to date. Meanwhile, the response expected due to THR test is local (on the occlusion side), whilst the response in the scalp region is supposed to be small. (The details of these tests are discussed in Chapter 6.) In the case of CO_2 reactivity, the increase of the conductivity during breathing 5%-concentration CO_2 (named “Phase 2”) and the return of the conductivity (named “Phase 4”) after return to breathing normal air were predicted due to the known effect of CO_2 inhalation on cerebral blood flow (Section 2.4.2). Eight trials on seven subjects were carried out. In the case of THR, 21 trials on six subjects were carried out. Since the decrease of the cerebral blood flow on the occlusion side is more profound than the increase on the non-occlusion side (Durduran and Yodh, 2014, Shang et al., 2011), a net decrease is expected for the bulk conductivity traces during the occlusion. Since the transcranial Doppler (TCD) signal can be used to monitor the localised cerebral blood flow velocity in the middle carotid artery (MCA), the expected response of the conductivity change was then determined from the TCD signal.

3.2.3 Results

The examples of bulk conductivity change observed in these tests are shown in Figure 3-6 and Figure 3-7. In general, the bulk conductivity was completely in step with the Rheoencephalographic signal (REG) of all investigated data sets. Since the REG occurs due to the perfusion of head tissues in response to the cardiac cycle (Perez et al., 2004), this indicates the preliminary success of the use of the bulk conductivity. The trends of the change on the bulk conductivity trace are compared with those on the TCD trace, the latter being sensitive to the localised blood flow. In the case of CO_2 reactivity test, 50% of the experiments on Phase 2 (Figure 3-6(a)) and 37.50% of that on Phase 4 (Figure 3-6(b)) correspond to the changes in TCD (the detail will be shown in Section 6.2.3). In the case of THR, bulk conductivity changes in 71.4% of 15 tests (tested on both the left and the right side) correspond to the changes in TCD of the occlusion side (Figure 3-7(a)) rather than those of the non-occlusion side (Figure 3-7(b)). The success percentage of the CO_2 reactivity case was lower than that of the THR case, possibly because the conductivity change in the scalp region during the CO_2 inhalation was larger than the change inside the cranium. This indicates that the bulk conductivity estimation is sensitive to the change in the scalp region.

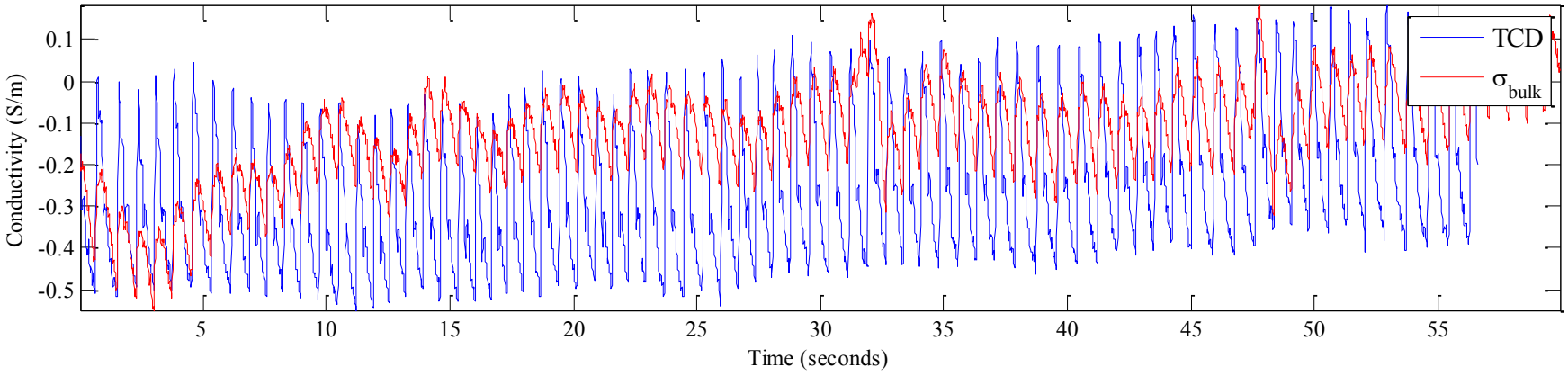

(a) Phase 2

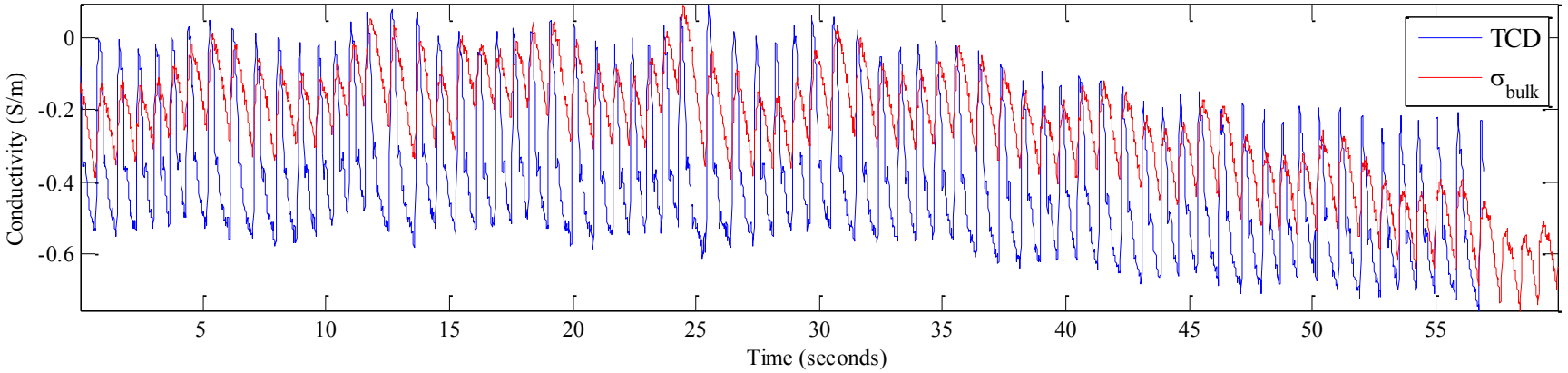

(b) Phase 4

Figure 3-6 Example of bulk conductivity data on CO_2 reactivity test compared to transcranial Doppler (TCD): (a) breathe the room air at the first 10 second, and then begin to breathe 5%-CO_2 (Phase 2), (b) (after breathing CO_2 for 110 seconds) continue breathing 5%-CO_2 for the next 10 second, and then breathe the room air (Phase 4).

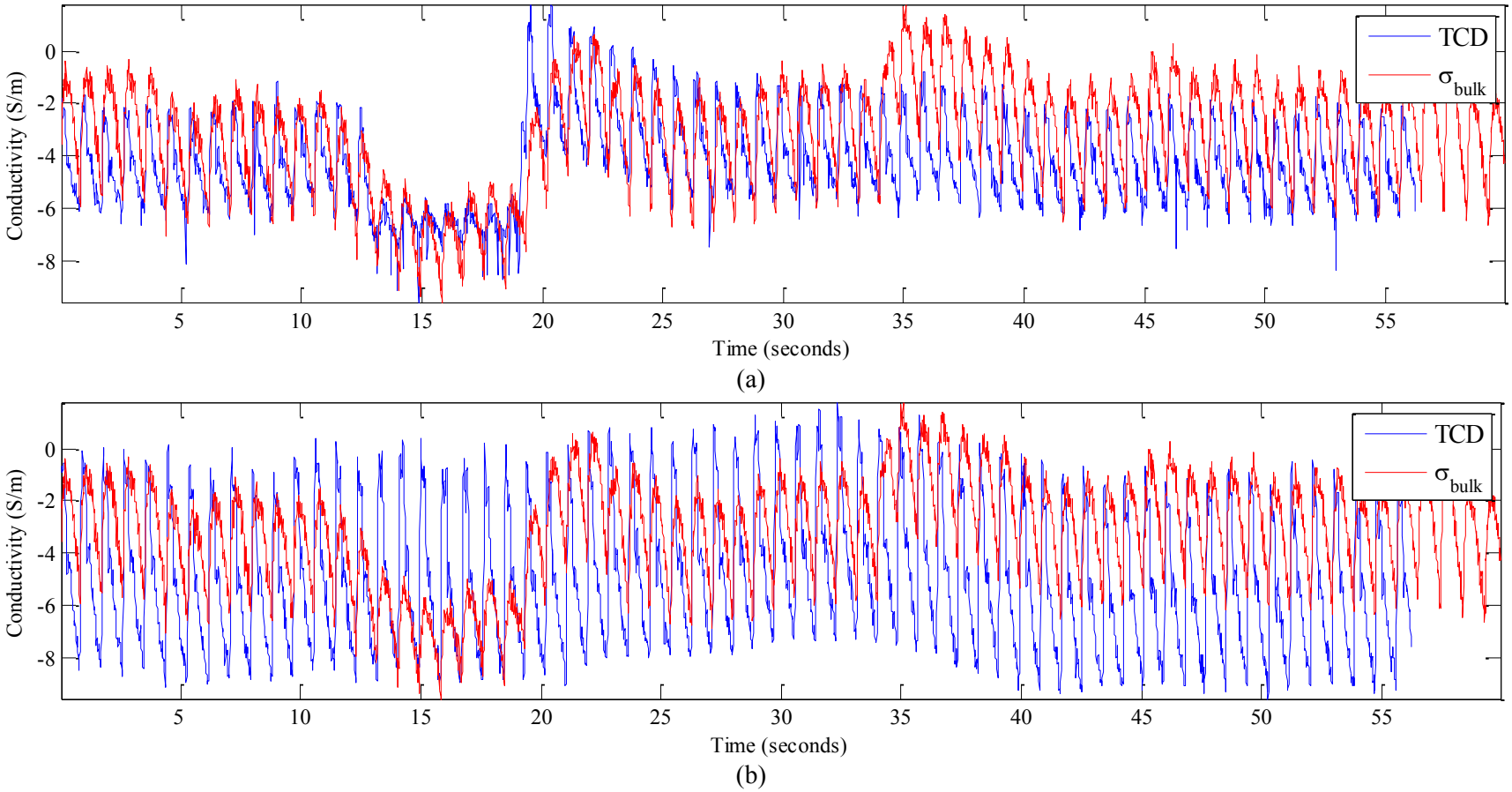

Figure 3-7 Example of bulk conductivity data on Transient Hyperaemic Response (THR) test where the occlusion was on the left side. The bulk conductivity is compared to transcranial Doppler (TCD) measured on the left side (the occlusion side) (a), and measured on the right side (the non-occlusion side) (b). The occlusion period was approximately from the 13th second to the 19th second.

3.3 Discussion and Conclusion

Tissue conductivities are very important parameters in EIT for both the boundary voltage prediction (the forward model problem) and the image reconstruction (the inverse problem). Many studies have proposed values based on invasive and non-invasive methods in various configurations. A non-invasive method was used here to estimate the nominal values of tissue conductivities, using EIT. The iterative Gauss-Newton method was employed to estimate the conductivities on three sets of experimental data obtained from a subject. However, due to the very low sensitivity of the tissues residing inside the cranium, only two conductivities, i.e. the scalp conductivity and the skull conductivity, were of interest.

The estimated conductivity of the scalp was 0.5842 S/m, which is high compared to reported values, and that of the skull was 0.0084 S/m, at the low boundary of reported values. In the forward calculation, these values reduced the voltage prediction error to approximately 32%, which is much smaller than when values estimated in the previous studies were used. Collectively, the recommended conductivity values are summarised in Table 3-1.

Table 3-1 Summary of the recommended conductivity values (and were used in this thesis)

No	Tissues	Recommended Conductivity (S/m)	Referred study
1	Scalp	0.5842	(Ouypornkochagorn et al., 2014)
2	Skull	0.0084	(Ouypornkochagorn et al., 2014)
3	CSF	1.802	(Baumann et al., 1997)
4	Grey matter	0.2849	(Latikka et al., 2001)
5	White matter	0.2556	(Latikka et al., 2001)
6	Blood	0.646	(Hirsch et al., 1950)

When a head is treated as a single bulk homogeneous material, the experimental results show that the bulk conductivity can reflect physiological change. The Rheoencephalographic signal (REG) can be clearly observed. However, when the bulk conductivity was compared with the (localised) transcranial Doppler (TCD) of CO_2 inhalation trials, where global intracranial change was expected, only a small fraction of the trials showed consistency with TCD: 50% during the period of

commencement of CO_2 breathing, and 37.50% during the period of commencement of breathing the room air again. On Transient Hyperaemic Response (THR) tests, 71.4% of the trials showed good consistency with TCD. The bulk conductivity and the TCD actually indicate different changes: the bulk conductivity indicates the global change of the head conductivity (including the change in the scalp) whereas the TCD indicates the localised cerebral haemodynamic change only inside the cranium. Since the sensitivity of the scalp region is 20-24 times higher than that inside the cranium region, the bulk conductivity therefore is more sensitive to the change in the scalp region. Thus, the bulk conductivity can reflect the brain responses to some extent. To use the bulk conductivity for studying brain functions, there must be an awareness of the functional response which may possibly emerge in scalp region.

Chapter 4 New fEITER System

4.1 The New fEITER

4.1.1 Excitation Current Improvement

Since the excitation current of the original version of fEITER is 1 mA_{pk-pk} which is only 35% of the IEC60601-1 safety limit of 1 mA_{rms} at 10 kHz, the excitation current was increased in the new fEITER system in order to improve sensitivity. The current generator of fEITER is based on a Howland circuit that converts the input voltage from the DAC to the output current. Therefore, this task was achieved simply by changing the input voltage by only replacing a resistor (Figure 4-1). However, due to the limited availability of very high precision resistors provided by manufacturers, and the placing space of the resistor chip in the circuit board, two options were possible as shown in Table 4-1: doubling current size and maximising current size. Both of them were investigated in this research, but the doubling current size option is preferable to keep the precision of the fEITER system.

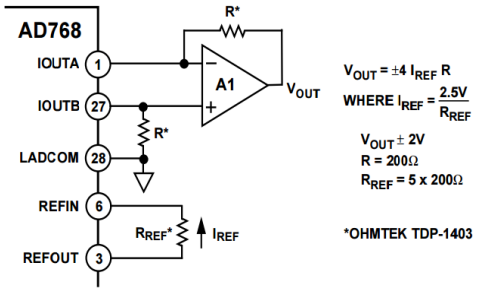

Figure 4-1 The circuit to control the amplitude of current (see the detail in the specification of D/A Converter: AD768). The resistor "R*" of "A1" sets the output current.

Table 4-1 Two options to increase the excitation current of the original fEITER version

No	Options	Target current	Remark
1	Doubling current size	2 mA_{pk-pk} (0.7071 mA_{rms})	The new 100Ω resistor has the same precision of ±0.01% resistance tolerance and the no change of ± 2 ppm/ºC temperature coefficient.
2	Maximizing current size	1 mA_{rms}	The new 140Ω resistor precision is ±1% resistance tolerance and ± 50 ppm/ºC temperature coefficient.

The increase of the excitation current leads to the increase of the measurement voltages. This increased voltage can possibly exceed the measurable range of the measurement circuit (discussed in the next section). Therefore, the change of baseline voltages after upsizing the current must be investigated. The baseline voltages were determined from averaging measurement data performed on humans over several types of studies e.g. auditory and visual stimulation data, CO_2 reactivity data, and Valsalva manoeuvre data, as summarised in Table 4-2 and Figure 4-2. The increases of the excitation current for both options led to the increases of the measurement voltages which were in the measurable range. The doubling size of current (Option1) led to approximately the doubling of measurement voltages. In other words, the measurement sensitivity was approximately double. This statement has been verified as in the experimental result shown in Figure 4-3 obtained from doubling the current (Option1). Regarding this result, the increased average of measurement voltages is 1.9918 times. This number was consistent with the doubled size of the current. However, the increased average in the case of Option2 was 2.2312 times. This number was significantly less than the increase of the current which was 2.8284 times higher. However, this number may not be accurate, since the number of analysed data files is too few, and it was obtained from only one subject. Note that the variance of the ratios shown in Figure 4-3 is pretty high possibly due to the large difference of the number of determining data files, i.e. 1,260 files for the original version and 21 files for the Option1. The very large ratios also mostly belonged to very low sensitivity measurements.

Table 4-2 The measurement baselines of the original and the modified version of fEITER

No	fEITER version/ Options	Current	Min/ Max of the baseline voltages obtained from 546 measurements (mV_{rms})	Voltage measurable range [(1)] (mV_{rms})	Number of analysed data
1	The original version of fEITER	1 mA_{pk-pk}	-21.0215 / 21.2063	± 107.995	1,260 data files, 43 subjects
2	New fEITER option1: Double current size	2 mA_{pk-pk}	-40.9478 / 49.9921	± 150.997	21 data files, 2 subjects
3	New fEITER option2: Maximum current size	1 mA_{rms}	-41.9757 / 35.7745	± 150.997	3 data files, 1 subject

[(1)] The measurable range is the range of the voltage measurement circuit computed by (2.3).

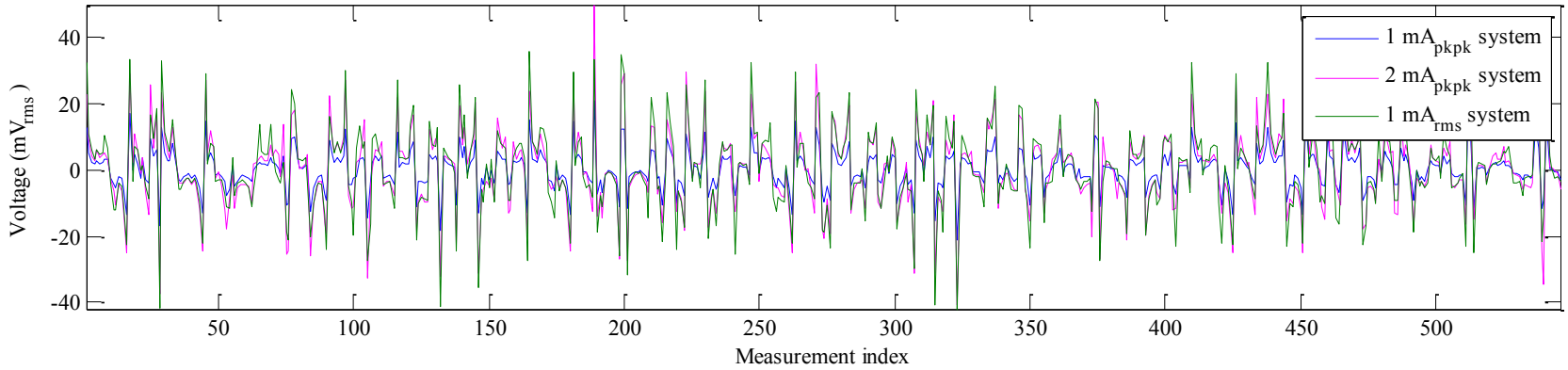

Figure 4-2 Baseline measurement voltages of the original fEITER version (with 1 $mA_{pk\text{-}pk}$ excitation current), and that of the Option1 (with 2 $mA_{pk\text{-}pk}$ current) and Option2 (with 1 mA_{rms} current) of the new fEITER

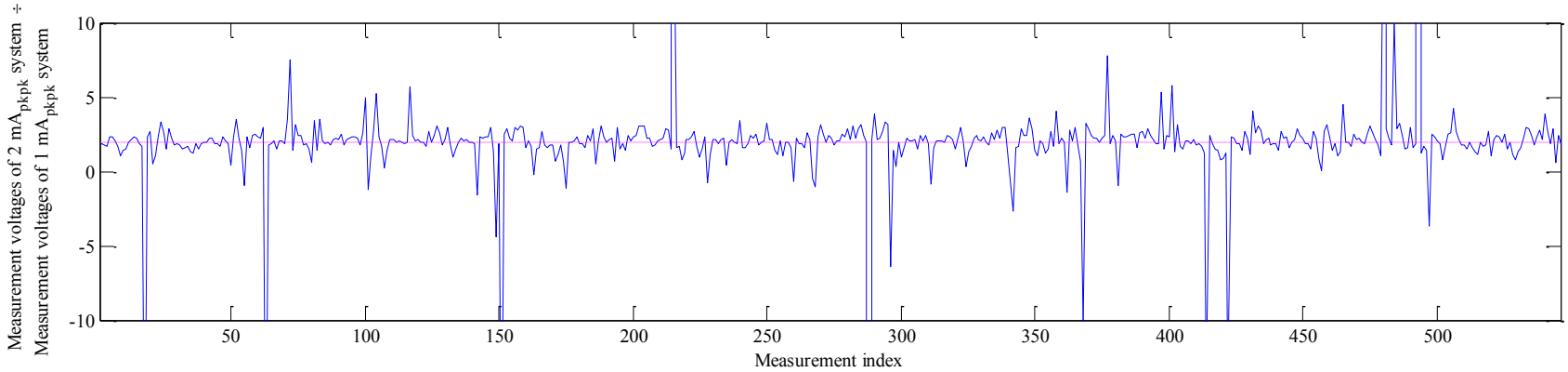

Figure 4-3 The increment of measurement voltages after doubling the current size (Option1 of the new fEITER), the dash straight line is the mean of measurements, 1.9918.

The amplitude of the excitation current of fEITER is measured by the in-built current monitor circuit which actually is the same circuit as the voltage measurement circuit as discussed in Section 2.2.2. Therefore, the measurable current range is calculated by dividing the measurable voltage range with the current sensing resistance (100 Ω), yielding ± 1.07995 mA_{rms} for the original version of fEITER. Since, this range covers the excitation current amplitude of both options of the new fEITER, hardware modification for the current monitoring circuit is unnecessary.

The increase of excitation current leads to the increase of the measurement voltages which could be close to the maximum readable range of the measurement circuit. Therefore, the expansion of measurable voltage range is advisable, even though this introduces additional quantisation error. The new fEITER has reduced voltage measurement gain from 9.8214 to 7.0244, or 28.48% decrement, to expand the measurable range from ± 107.995 mV_{rms} to ± 150.997 mV_{rms}, or 39.82% wider. This new gain leads to poorer ADC reading resolution, from 3.2957 μV_{rms} to 4.6080 μV_{rms}, or 39.82% less sensitive.

Additionally, not only AC signals are present in the system, undesirable DC level could be present also, which can reduce the range of the measurement circuit. Actually due to the use of AC excitation, the DC level should not occur. However, it could be induced by instrument leakage or unbalanced current sources. Therefore, it is necessary to investigate the DC level on human trials, in particular in the situation that the excitation current is modified. The DC level measured between the electrode receptacles and ground on a human subject with 2 mA_{pk-pk} current excitation is shown in Figure 4-4. It ranged between -33.17 and 19.93 mV_{DC}. When converting these values to DC level across two adjacent electrodes (i.e. in the measurement scheme of fEITER), the difference DC level then ranged between -35.59 and 53.10 mV_{DC}. When including this range into the baseline voltages shown in Table 4-2, the possible measurement voltages still suit the new measurable range of ± 150.997 mV_{rms}.

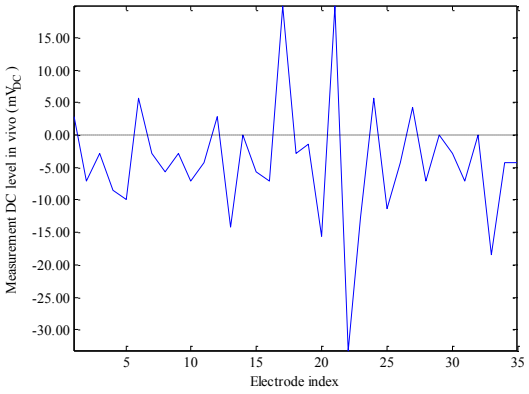

Figure 4-4 DC level measured between the electrode receptacles and ground on a human subject

4.1.2 Improvement of Measurement Precision

One influence to the precision of instrument is relevant to the signal distortion due to the quantisation process. Apart from the sensing resolution of the ADC, the truncation in the process of PSD also introduces quantisation error which affects the precision of the fEITER system. The quantisation error obtained from bit truncation was reduced in the new system. Regarding the firmware design of fEITER, 38-bit length registers are used to keep the sum of multiplications in the process of PSD. The 22-bit truncation was performed on the original fEITER version, i.e. 16-bit data readout. This led to 4.2185 μV_{rms} truncation error which was pretty high. The number of truncated bits was reduced to 14 bits on the new fEITER i.e. 24-bit data readout as shown in detail in Appendix E and Appendix F. The truncation error was then reduced to 0.0230 μV_{rms} or 183 times reduction from the original version. However, this modification impacted the volume of data sent out to the computer (from 16-bit data readout to 24-bit data readout, or 50% longer). The summary of the improvement is displayed in Table 4-3.

Some examples of the current and the voltage measurements over 50-second periods (5,000 samples) are shown in Figure 4-5 to Figure 4-16. When the investigation was performed on the resistor phantom (see Appendix G), using 16-bit data readout and 1 mA_{pk-pk} excitation current, the quantisation can be seen obviously in both the current (Figure 4-5) and the voltage measurement (Figure 4-9). Meanwhile, using 24-bit data readout and the same 1 mA_{pk-pk} excitation current, the

quantisation noise disappeared on both the current (Figure 4-6) and the voltage measurement (Figure 4-10). The quantisation can also be investigated by plotting the histogram of the data. The histograms of the 16-bit data readout case are like a multimode distribution (Figure 4-7) or like a single-bar histogram (Figure 4-11). On the other hand, in the 24-bit data readout case, the histograms are like normal distributions (Figure 4-8 and Figure 4-12). This indicated the decrease of quantisation error. Furthermore, since the truncation error is substantially reduced by reducing the number of truncated bits, the resolution of measurement signals is then better despite the measurement being performed on very low measurement sensitivity regions. Some examples obtained from human subject measurements over 10-second periods (1,000 samples) are shown in Figure 4-13 to Figure 4-16. Using 16-bit data readout and 1 mA_{pk-pk} excitation current, the quantisation noticeably distorted the quality of signals. The measurement signal became a profoundly quantised Rheoencephalographic signal when it was obtained from a high sensitivity region (Figure 4-13), or it became a pulse-train signal when it was obtained from a low sensitivity region (Figure 4-15). On the other hand, using 24-bit data readout (using 2 mA_{pk-pk} current in this example), these signals were read expectedly as shown in Figure 4-14 and Figure 4-16.

Table 4-3 The specification of voltage measurement circuit of the original fEITER version and the new fEITER version (with both options)

No	Specification of voltage measurement circuit	The original version of fEITER	New fEITER both options
	Configuration R_{ADC} = 3 Volt R_{ref} = 1 Volt B_{sig} = 16 bits B_{ref} = 15 bits B_{ADC} = 16 bits N = 200 samples	*Gain* = 9.8214 $B_{truncation}$ = 22 bits (16-bit data readout)	*Gain* = 7.0244 $B_{truncation}$ = 14 bits (24-bit data readout)
1	Maximum Measurable AC Voltage (mV_{pk-pk}), Eq. (2.3)	305.4554 mV_{pk-pk} (107.9948 mV_{rms})	427.0827 mV_{pk-pk} (150.9966 mV_{rms})
2	Maximum truncation error (mV_{pk-pk}), Eq. (2.19)	11.9319 μV_{pk-pk} (4.2185 μV_{rms})	0.0652 μV_{pk-pk} (0.0230 μV_{rms})
3	ADC Reading Resolution, Eq. (2.21)	9.3218 μV_{pk-pk} (3.2957 μV_{rms})	13.0335 μV_{pk-pk} (4.6080 μV_{rms})

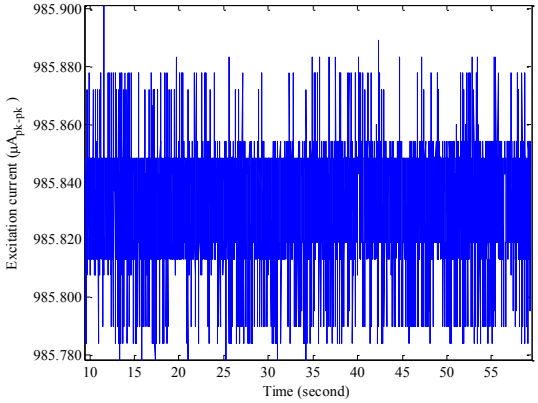

Figure 4-5 Excitation current on the resistor phantom, using 16-bit readout and 1 mA_{pk-pk} current (the original fEITER version)

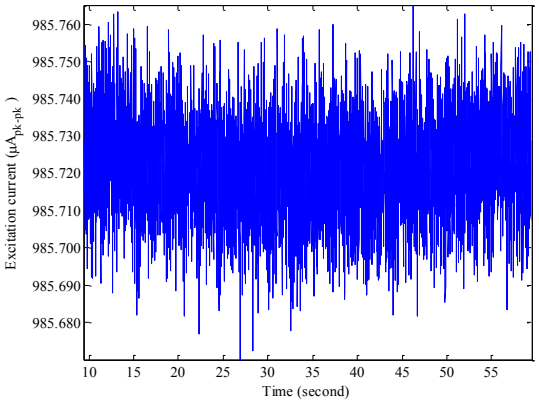

Figure 4-6 Excitation current on the resistor phantom, using 24-bit readout and 1 mA_{pk-pk} current (the new fEITER)

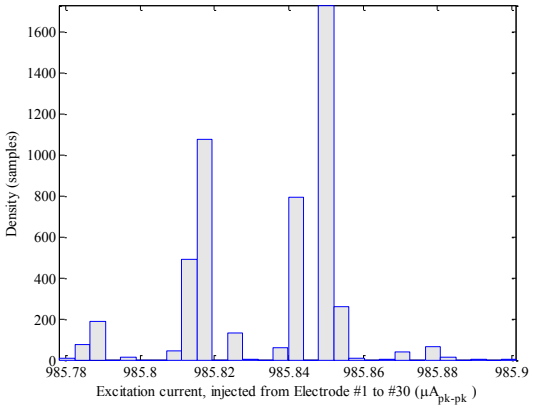

Figure 4-7 Histogram of the data in Figure 4-5 (the original fEITER version)

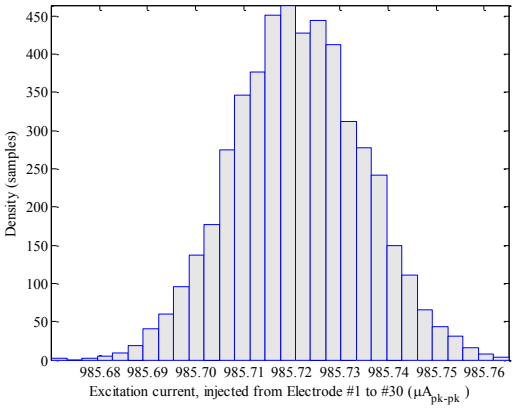

Figure 4-8 Histogram of the data in Figure 4-6 (the new fEITER)

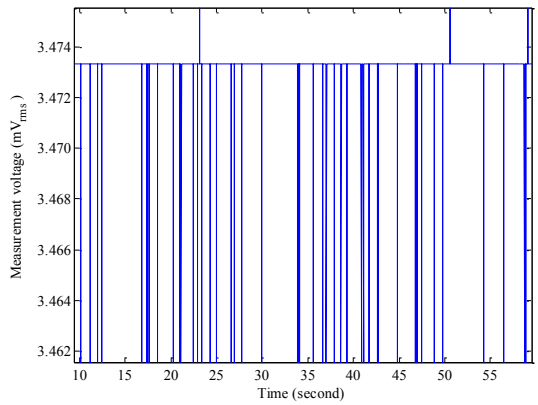

Figure 4-9 Voltage measurement between electrode#2 and #3 (the current driven from electrode#1 to #30) on the resistor phantom, using16-bit readout and 1 mA_{pk-pk} current (the original fEITER version)

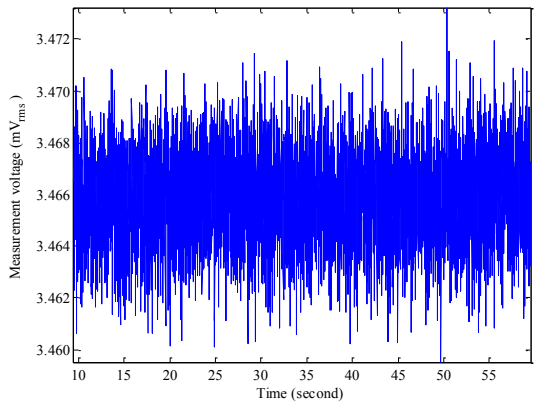

Figure 4-10 Voltage measurement between electrode#2 and #3 (the current driven from electrode#1 to #30) on the resistor phantom, using 24-bit readout and 1 mA_{pk-pk} current (the new fEITER)

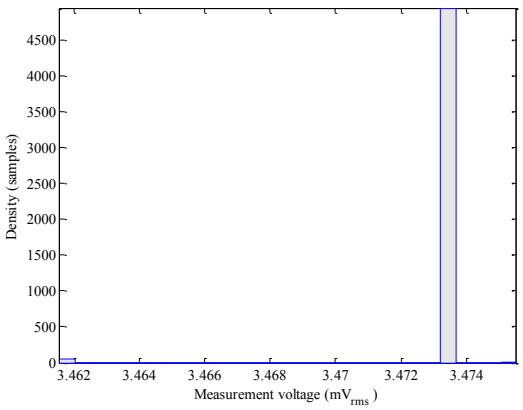

Figure 4-11 Histogram of the data in Figure 4-9 (the original fEITER version)

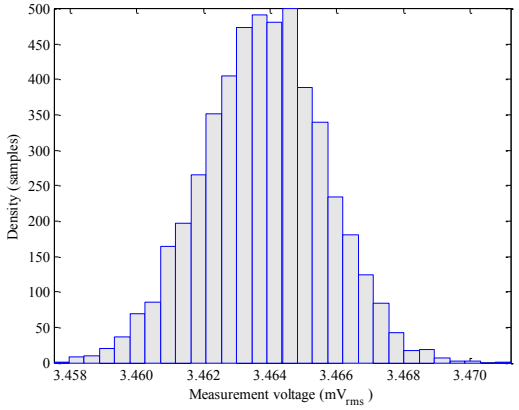

Figure 4-12 Histogram of the data in Figure 4-10 (the new fEITER)

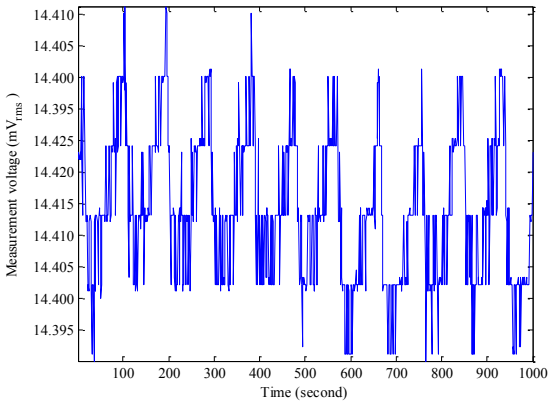

Figure 4-13 Voltage measurement on a human subject between electrode#2 and #3 (the current driven from electrode#1 to #30), using 16-bit readout and 1 mA$_{pk-pk}$ current (the original fEITER version)

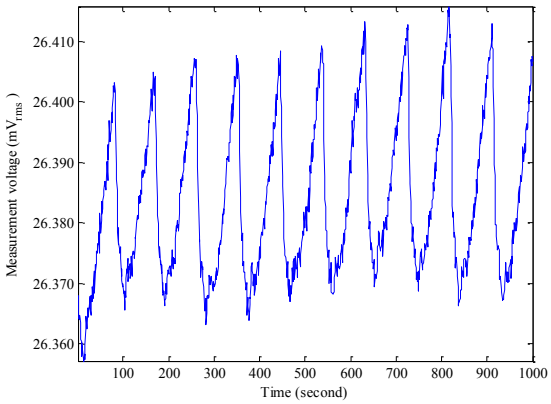

Figure 4-14 Voltage measurement on a human subject between electrode#2 and #3 (the current driven from electrode#1 to #30), using 24-bit readout and 2 mA$_{pk-pk}$ current (the new fEITER)

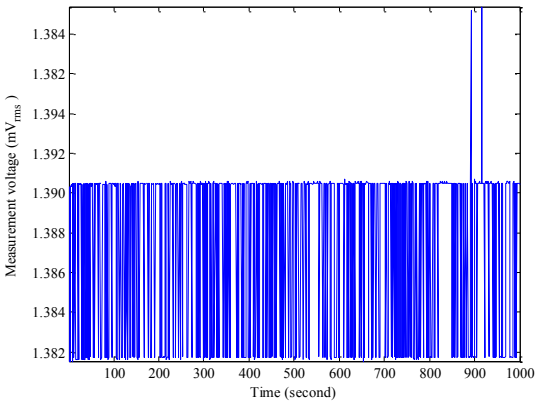

Figure 4-15 Voltage measurement on a human subject between electrode#5 and #6 (the current driven from electrode#1 to #30), using 16-bit readout and 1 mA$_{pk-pk}$ current (the original fEITER version)

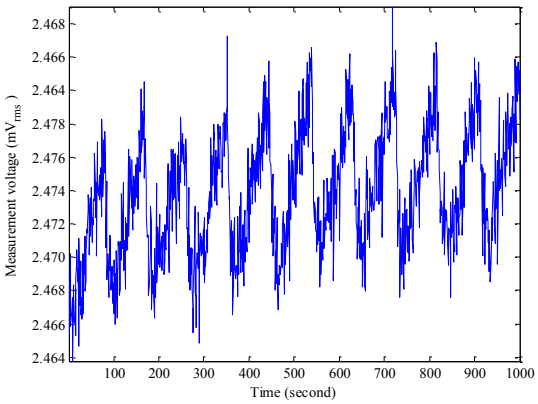

Figure 4-16 Voltage measurement on a human subject between electrode#5 and #6 (the current driven from electrode#1 to #30), using 24-bit readout and 2 mA$_{pk-pk}$ current (the new fEITER)

The summary of the experimental precision performance of the original and the new systems are shown in Table 4-4. The experiments were carried out on the resistor phantom (Appendix G) for 50-second periods. The root-mean-square error (RMSE) of the signals was used to determine the precision performance of the circuits as shown in (4.1) where x is the recorded data, μ_x is the mean of data, and N is the number of samples (i.e. N was 5,000 in this investigation). In the case of the current generating circuit, the mean precision (i.e. $\mu RMSE_{Current}$) and its standard deviation (i.e. $\sigma RMSE_{Current}$) over all patterns are computed from (4.2) and (4.3) respectively. In the case of the voltage measurement circuit, since the excitation current slightly varied over the time, the measurement voltages were firstly normalized by (4.4), where I_{ideal} is the expected current amplitude (i.e. 1 $mA_{pk\text{-}pk}$, 2 $mA_{pk\text{-}pk}$, or 1 mA_{rms}) and I_{real} is the real measured current amplitude. Then, the mean precision (i.e. $\mu RMSE_{Measurement}$) and its standard deviation (i.e. $\sigma RMSE_{Measurement}$) are computed from (4.5) and (4.6) respectively.

$$RMSE = \sqrt{\frac{1}{N}\sum_{i=1}^{N}(x_i - \mu_x)^2} \quad where \quad \mu_x = \frac{\sum_{i=1}^{N} x_i}{N} \tag{4.1}$$

$$\mu RMSE_{Current} = \frac{1}{20}\sum_{i=1}^{20}\left(RMSE_{Current\,i}\right); \text{ (The number of patterns is 20.)} \tag{4.2}$$

$$\sigma RMSE_{Current} = \sqrt{\frac{1}{20}\sum_{i=1}^{20}\left(RMSE_{Current\,i} - \mu RMSE_{Current}\right)^2} \tag{4.3}$$

$$x_{normalized\,measurement} = \frac{x \times I_{ideal}}{I_{real}} \tag{4.4}$$

$$\mu RMSE_{Measurement} = \frac{1}{546}\sum_{i=1}^{546}\left(RMSE_{Measurement\,i}\right); \text{ (The number of measurements is 546.)} \tag{4.5}$$

$$\sigma RMSE_{Measurement} = \sqrt{\frac{1}{546}\sum_{i=1}^{546}\left(RMSE_{Measurement\,i} - \mu RMSE_{Measurement}\right)^2} \tag{4.6}$$

Obviously, when the data readout was changed to 24-bit length (but the current amplitude was the same at 1 $mA_{pk\text{-}pk}$), the precision of the current circuit (i.e. $\mu RMSE_{Current}$) was improved by 25%, and that of the voltage measurement circuit (i.e. $\mu RMSE_{Measurement}$) was improved by 36%. However, when the excitation current

was increased, the precision was poorer in both circuits. This could indicate that the system noise was larger in a larger-current system. In the current circuit, doubling the current from 1 mA_{pk-pk} to 2 mA_{pk-pk} resulted in 14% poorer precision, whilst increasing the current from 1 mA_{pk-pk} to 1 mA_{rms} resulted in 11% poorer precision – no significant difference to the 2 mA_{pk-pk} case. In the voltage measurement circuit, noticeably, the voltage measurement precision was poorer when the excitation current was increased, in a similar way to the case of the current circuit.

Table 4-4 The mean precision (RMSE) on the current circuit (over 20 current patterns) and the measurement circuit (over 546 measurement pairs)(1) and the standard deviation of the mean of all fEITER versions

#	Version of fEITER	$\mu RMSE_{Current} \pm \sigma RMSE_{Current}$	$\mu RMSE_{Measurement} \pm \sigma RMSE_{Measurement}$
1	$1mA_{pk-pk}$, 16-bit data readout	6.37± 0.44 nA_{rms}	1,060.73± 642.82 nV_{rms}
2	$1mA_{pk-pk}$, 24-bit data readout	4.77± 0.03 nA_{rms}	674.57± 79.18 nV_{rms}
3	$2mA_{pk-pk}$, 24-bit data readout	5.42± 0.08 nA_{rms}	802.82± 72.38 nV_{rms}
4	$1mA_{rms}$, 24-bit data readout	5.30± 0.08 nA_{rms}	794.09± 74.80 nV_{rms}

(1) Based on normalized measurement voltages

The distribution of $\mu RMSE$ over measurements, i.e. $\sigma RMSE$, could represent the degree of quantisation error to some extent, i.e. the smaller $\sigma RMSE$ implies the smaller quantisation error. According to Table 4-4, obviously, the bit-truncation improvement substantially reduced $\sigma RMSE_{Current}$ and $\sigma RMSE_{Measurement}$ by 82-93% and 88-89% respectively. These statistics support the need in this thesis to improve the truncation which is an important process causing quantisation error in the fEITER system.

In the cases of upsizing the current excitation and reducing the hardware gain, there are some issues to consider. The more the excitation current is increased, the more system noise occurs; and the more the hardware gain is decreased, the less the measurement resolution is decreased. The new fEITER was doubled in current to 2 mA_{pk-pk} leading to about 100% more measurement sensitivity (Figure 4-3), and was reduced the gain from 9.8214 (with 16-bit data readout) to 7.0244 (with 24-bit data readout) leading to 9% coarser resolution to the voltage change. This indicates that the change of the gain had less influence to the instrument performance compared to that of the increase of current. Actually, the option of increasing the current to 1

mA_{rms} ideally should be better than the option of 2 mA_{pk-pk}, but it was not chosen in this research due to lower replacement component accuracy. Anyway, according to the reading resolution shown in Table 4-3, it is ideal practice to rely only on signals where the changing amplitude is larger than 4.2185 μV_{rms} for the original version fEITER, and 4.6080 μV_{rms} for the new fEITER.

The maximum SNR_{dB} following the methodology mentioned in (McCann et al., 2011b) can be evaluated by (4.7). The $\mu RMSE_{Measurement}$ values shown in Table 4-4 are determined as the noise of each system. Regarding the measurable ranges shown in Table 4-2, the maximum SNR of all fEITER versions are summarised in Table 4-5. SNRs of all versions are above 100 dB. These SNR values are decreased when fEITER is used to measure low-level voltages, e.g. scalp voltages. However, based on the baseline scalp voltages shown in Table 4-2, the SNRs are still admirable, i.e. 86-95 dB.

$$MaximumSNR_{dB} = 20\log_{10}\frac{VoltageMeasurableRange}{\mu RMSE_{Measurement}} \tag{4.7}$$

Table 4-5 Maximum Signal-to-noise ratio (SNR) of all fEITER versions

No	Version of fEITER	SNR (dB)
1	1mA_{pk-pk}, 16-bit data readout	100.16
2	1mA_{pk-pk}, 24-bit data readout	107.00
3	2mA_{pk-pk}, 24-bit data readout	105.49
4	1mA_{rms}, 24-bit data readout	105.58

4.1.3 Sensing Capability of fEITER to Brain Response

A possible way to determine the sensing capability to the change of EIT is to determine the measuring resolution of EIT instruments. The resolution must be sufficiently fine to sense the boundary voltage change induced from conductivity change. However, the relationship between the voltage change and the conductivity change is complicated. It depends on the volume, the location, and the magnitude of the change. It also depends on the amplitude of the excitation current and the site of measurement. (McCann et al., 2006) simulated a 64-millilitre inclusion (approximately 1.7% of the human head volume) in a realistic head model with 15% conductivity change. This inclusion led to 0.01-1% change on the boundary voltages,

or 15-1,500 times smaller than the percentage of conductivity change. Meanwhile, (Tehrani et al., 2010) simulated with 1-millilitre inclusion (approximately 0.03% of the human head volume) and approximately 160% conductivity change. This induced less than 0.05% change in the boundary voltages or 3,200 times smaller. According to these values in regard to the specification of fEITER systems (Table 4-2 and Table 4-3), the capability to sense the conductivity change could be estimated as shown in Table 4-6. The fEITER systems could sense the small change if the conductivity change is larger than 0.14% (for the new fEITER system) or 0.30% (for the original fEITER system). However, as already mentioned, it also depends on many factors e.g. volume and measurement location.

Table 4-6 Sensibility to conductivity changing of fEITER systems

#	fEITER versions	Excitation current/ Total resolution(1)	Max of the baseline voltages (mV_{rms}) (1)	Capability to sense referred to (McCann et al., 2006) based on a 64-millilitre inclusion with 15% change of conductivity	Capability to sense referred to (Tehrani et al., 2010) based on a 1-millilitre inclusion with 160% change of conductivity
1	The original version of fEITER	1 mA_{pk-pk} / 4.2185 μV_{rms}	21.2063	0.30-29.84% of conductivity change	63.66% of conductivity change
2	New fEITER (option1: Double current size)	2 mA_{pk-pk} / 4.6080 μV_{rms}	49.9921	0.14-13.83% of conductivity change	29.50% of conductivity change

(1) Refer to the investigation in Table 4-2.

4.2 Discussion and Conclusion

fEITER is an EIT instrument that was designed for studying human brain function and it complies with the medical standard IEC60601-1:2006. Collectively, it works at 1 mA_{pk-pk} 10 kHz (single frequency) of the excitation current, supports up to 32 electrodes, and can record difference voltage measurements with very high recording rate (100 frames per second with 546 measurements per frame). fEITER has been used to study brain responses to particular kinds of stimulations. These uses, therefore, confirm the distinguishability of fEITER as being sufficient to work with human heads. However, the performance of fEITER can be upgraded by only slight modifications.

Hardware modification for upsizing the excitation current is the first achievement to create the new fEITER. The current size of the previous fEITER version is only 35.36% of the safety limit. Two attempts were performed: upsizing to 2 mA_{pk-pk} and to 1 mA_{rms}, by just replacing a resistor (Table 4-1). However, due to the limited availability of very high precision resistors provided by manufacturers, the option of 2 mA_{pk-pk} upsizing is preferable in order to keep the same precision of the replaced resistor. After doubling the current, the measurement voltages are approximately doubled (Figure 4-3), i.e. the measurement sensitivity becomes approximately double.

The new fEITER reduced the measurement gain by 28% to expand the measurable range. This reduction led to less sensitivity to the small variation of measurement voltages, which could be both noise and physiological change. Regarding the summarised specification shown in Table 4-3, it is ideal practice to rely on signals (at fastest temporal resolution) where the changing amplitude is higher than 4.2185 μV_{rms} measured with the original fEITER version, and 4.6080 μV_{rms} measured with the new fEITER; i.e. the overall reliable resolution of the new system is slightly coarser (9.23%). Nevertheless, the measurement amplitude of the new system is doubled due to the doubling of measurement sensitivity. This, therefore, leads the new system to have a superior performance than that of the original version.

Another crucial improvement is the reduction of the number of truncated bits. Voltage measurement mechanism of fEITER is based on the phase-sensitive detection (PSD) technique. Firstly, the voltage measured is multiplied with lock-in frequency signals. Then, the multiplication outcomes are accumulated and stored in the internal registers of the computation unit i.e. the Field-Programmable Gate Array (FPGA). These accumulation values are then computed for the in-phase component and the quadrature component of measurement. However, since the right-hand-side (RHS) bits of these accumulation values are less significant in value, the truncation of RHS bits is usually performed. In fEITER processes, 38-bit accumulators are used, and the number of truncated bits of the original fEITER version is 22 bits; this is referred to as the "16-bit data readout". According to the investigation results

(shown in Figure 4-5 to Figure 4-16), it is obvious that this number of truncated bits was too much. It introduced significant truncation error up to 4.2185 μV_{rms} (Table 4-3). This error was clearly too high for measuring voltages on human subjects over low measurement sensitivity regions (Figure 4-15). In the new fEITER, this number of truncated bits was changed to 14 bits, referred to as the "24-bit data readout". This improvement substantially reduces quantisation error: the truncation error is reduced to 0.0230 μV_{rms} or 183 times smaller than that of the 16-bit data readout version (Table 4-3). The precision of the excitation current generating circuit and that of the voltage measurement circuit were also improved by 25% and 36% respectively from the original version (Table 4-4). Furthermore, the sensing capability of fEITER to detect brain evoked response was estimated. The smallest conductivity change which is able to be detected is 0.30% (for the $1mA_{pk-pk}$ system), or 0.14% (for the $2mA_{pk-pk}$ system). This implies that there are about 2 times higher possibility to detect small conductivity change of the brain in the new system.

To summarize the fEITER improvements, the excitation current was upsized to 2 mA_{pk-pk} in order to double measurement sensitivity. The measurement gain was reduced by 28.48% to expand the voltage measurement range. The number of truncated bits was reduced by 36.36%, i.e. the data readout was changed from 16-bit data to 24-bit data. This improvement substantially reduces truncation error by 183 times, and improves the precision of the excitation current generating circuit and that of the voltage measurement circuit by 25% and 36% respectively. However, with these improvements, the reliable change in voltage amplitude should be higher than 4.6080 μV_{rms} (slightly higher than that of the original version, i.e. 4.2185 μV_{rms}) when operating the system at highest speed (100 fps).

Chapter 5 Novel Image Reconstruction Approach for Human Head Applications

5.1 A Novel Method for Modelling Error Mitigation

A novel method is proposed here, the "nonlinear difference imaging approach", based on the well-known difference imaging approach. According to the forward problem as shown in (5.1) where V_i is the measurement voltage of the time index i, U is the discretization function of the conductivity σ, ε is the modelling error function, and e_m is the measurement error; the difference of measurement vectors can be written as in (5.2). When applying Taylor series to U, (5.2) then becomes (5.3) where e_L is the linearization error due to neglecting of the high-order Taylor series terms.

$$V_i = U(\sigma_i) + \varepsilon(\sigma_i) + e_m \tag{5.1}$$

$$\delta V_{(i+1,i)} = U(\sigma_{i+1}) - U(\sigma_i) + \delta\varepsilon_{(i+1,i)} + \delta e_{m(i+1,i)}; \quad where \quad \delta\varepsilon_{(i+1,i)} = \varepsilon_{i+1} - \varepsilon_i \tag{5.2}$$

$$and \ \delta e_{m(i+1,i)} = e_{mi+1} - e_{mi}$$

$$\delta V_{(i+1,i)} = J(\sigma_i)\delta\sigma_{(i+1,i)} + e_L + \delta\varepsilon_{(i+1,i)} + \delta e_{m(i+1,i)} \tag{5.3}$$

Since σ_i is unknown, the exact Jacobian $J(\sigma_i)$ is then unknown. However, the nominal value of conductivity σ, denoted σ_N, can be found by the methods proposed in Chapter 3. The Jacobian $J(\sigma_N)$ is similar to $J(\sigma_i)$ if σ_N is close to σ_i. In this novel approach, we propose to use $J(\sigma_N)$ instead of $J(\sigma_i)$ as shown in (5.4). The estimated conductivity obtained from this method could be slightly drifted from the exact conductivity σ_i. The great benefit is that it is based on σ_N, not σ_i anymore. Therefore, we denote the new estimation as $\tilde{\sigma}_{i+1}$ to remind the reader that the estimation is based on σ_N. More specifically, $\tilde{\sigma}_{i+1}$ cannot reflect the true absolute image of the time stance *i+1* because it is based on σ_N.

$$J(\sigma_i)\delta\sigma_{(i+1,i)} \approx J(\sigma_N)\delta\tilde{\sigma}_{(i+1,N)}; \quad where \quad \delta\tilde{\sigma}_{(i+1,N)} = \tilde{\sigma}_{i+1} - \sigma_N \tag{5.4}$$

The right-hand side of (5.4) can be transformed backward to the difference of the measurement function of $\tilde{\sigma}_{i+1}$ and that of σ_N with Jacobian error e_J as shown in (5.5). e_J is the result of using $J(\sigma_N)$ in addition to the linearization error. The new equation of measurement difference shown in (5.2) then can be estimated by (5.6).

$$J(\sigma_i)\delta\sigma_{(i+1,i)} = U(\tilde{\sigma}_{i+1}) - U(\sigma_N) + e_J \tag{5.5}$$

$$\delta V_{(i+1,i)} = U(\tilde{\sigma}_{i+1}) - U(\sigma_N) + \varepsilon_{\delta(i+1,i)} + \delta e_{m(i+1,i)}; \tag{5.6}$$

$$where \quad \varepsilon_{\delta(i+1,i)} = e_J + e_L + \delta\varepsilon_{(i+1,i)}$$

Since $U(\sigma_N)$ is a known constant vector as well as $\delta V_{(i+1,i)}$, the new known-parameter $\tilde{V}_{(i+1,i)}(\sigma_N)$ then is defined, and then (5.6) can be rewriten to a new compact equation as (5.7). Noticeably, although (5.7) was based on the difference approach, it looks similar to (5.1). Similarly, the new modelling error term $\varepsilon_{\delta(i+1,i)}$ is practically impossible to estimate, and it essentially has to be ignored. However, ε_{i+1} or ε_i is expected to be substantially larger than $\varepsilon_{\delta(i+1,i)}$. The absolute image based on σ_N can be computed by (5.8), and the desired difference image can be computed from (5.9).

$$\tilde{V}_{(i+1,i)}(\sigma_N) = U(\tilde{\sigma}_{i+1}) + \varepsilon_{\delta(i+1,i)} + \delta e_{m(i+1,i)}; \tag{5.7}$$

$$where \quad \tilde{V}_{(i+1,i)}(\sigma_N) = U(\sigma_N) + \delta V_{(i+1,i)}$$

$$\tilde{\sigma}_{(i+1,i)} = \arg\min_{\tilde{\sigma}} \left\{ \left\| \tilde{V}_{(i+1,i)}(\sigma_N) - U(\tilde{\sigma}) \right\|^2 + \lambda \left\| R(\sigma) \right\|^2 \right\} \tag{5.8}$$

$$\delta\hat{\sigma}_{(i+1,i)} = \tilde{\sigma}_{(i+1,i)} - \sigma_N \tag{5.9}$$

The prominent advantages of this novel method are that 1) it is a nonlinear method and 2) the modelling error is substantially reduced to be smaller than ε_{i+1} or ε_i. However, the qualitative performance of reconstruction by the novel method depends on the magnitude of the ignored term $\varepsilon_{\delta(i+1,i)}$, which is expected to be very small. In order to obtain the small $\varepsilon_{\delta(i+1,i)}$, $\delta\sigma_{(i+1,i)}$ should be small and σ_N should be accurate. Additionally, in the case of using a generic model rather than using a

subject model, it impacts the magnitude of $\varepsilon_{\delta(i+1,i)}$ as well. Anyway, the error from this novel approach is still smaller than that of the absolute imaging approach.

5.2 A Novel Strategy for Avoiding Divergence

A novel strategy named "past step length strategy" is proposed in Algorithm 5.3. It is particularly designed for iterative algorithms and the difference imaging approach. Rather than exploring for a step length for finding the local minimum of residual, the maximum limit of the step is explored instead. This strategy is based on the ideal assumption that when the $\hat{\sigma}$ comes closer to the exact solution, the norm of $\delta\hat{\sigma}$ should be smaller or not significantly different to the norm of previous iterations. More specifically, this strategy attempts to directly shape the trend of the solution, i.e. $\hat{\sigma}$, to be a converged trend, by imposing the maximum of $\delta\hat{\sigma}$ norm for every iteration. The maximum limit is then used as the step length if the norm of $\delta\hat{\sigma}$ is over the limit. The limit is computed by averaging the certain number of the lengths obtained from the recent past iterations. In this work, we proposed to use three lengths. At the very first iterations (the 1st to the 3rd iteration for this work), the norm of $\delta\hat{\sigma}$ is large i.e. the estimate is far from the exact solution. The need to put the maximum limit is unnecessary. Meanwhile at the late iterations, the $\delta\hat{\sigma}$ should not too much different to the $\delta\hat{\sigma}$ of previous iterations. Therefore, this strategy does not allow the solution to significantly diverge.

Algorithm 5.3: Three-past step length strategy for avoiding divergence

For $iteration \quad k = 1, 2, \ldots$
(supposed that working on the measurement time $i+1$ and i)

Set $length_k = \left\| \delta\hat{\sigma}_{(i+1,i),k} \right\|$

If $k \le 3$ then $limit_k = \infty$,

else $limit_k = average\{length_{k-1}, length_{k-2}, length_{k-3}\}$

If $length_k \le limit_k$ then $\alpha_k = 1$,

else $\alpha_k = \dfrac{limit_k}{length_k}$

Return α_k

5.3 Numerical Results

5.3.1 Imaging Approaches

Two imaging approaches have been implemented. The absolute imaging approach and the novel difference imaging approach were investigated in different degrees and different sources of modelling error. Four test cases were set up as the details in Appendix I.

First, a simulation was performed on a 175mm-diameter circular model, i.e. Case 1. The thickness of the scalp and the skull layer of the reconstruction model were a few millimetres inaccurate, i.e. 1.87-2.46 mm error. The initial guess of the tissue conductivities was inaccurate (but it was still in the range of the values reported in literature), i.e. -25% and 93% error for the scalp and the skull conductivity respectively. Three inclusions with two schemes of conductivity changes were simulated (see Appendix I.1). The reconstructed images are shown in Figure 5-1. The absolute imaging approach cannot reconstruct for the inclusions, but the novel difference imaging approach can. The modelling error was 30-110 times reduced by using the novel difference imaging approach as shown in Table 5-1. However, even using the novel approach, the magnitude of conductivity change of the reconstructed inclusions did not reflect the exact magnitude. This phenomenon was more noticeable in the inner layers. The magnitude of the inclusion in the brain region was about eight times less than the exact magnitude. This phenomenon is consistent with what was reported by (Adler, 2004) and (Fabrizi et al., 2006) that heterogeneity can lead to the inexact magnitude of conductivity change. Furthermore, large artifacts always occur in the outermost layer (corresponding to the scalp), in particular beneath the electrodes. This phenomenon was consistent with what was reported by (Dehghani and Soleimani, 2007) that the large artifacts could be frequently seen near the electrodes and the boundary. It is also noticeable that the artefact magnitude corresponded to the magnitude of conductivity change of the reconstructed inclusions.

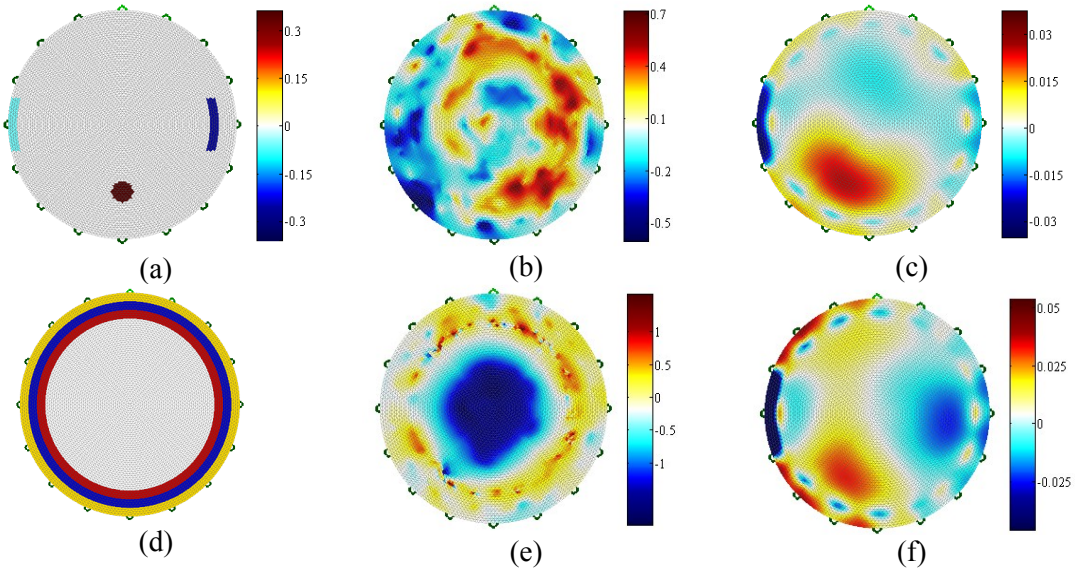

Figure 5-1 Reconstruction difference images of Case 1: the absolute imaging approach (b,e) and the novel difference imaging approach (c,f), where the images of the small change scheme are in the top row, and those of the large change scheme are in the bottom row. The inclusion locations are shown in (a). The forward model is shown in (d). The colour bar indicates the difference magnitude of the change.

Table 5-1 The (norm) size of errors of the small change scheme and the large change scheme in Case 1 (the simulated case)

Errors	**Scheme1: Small change**	**Scheme2: Large change**
$\|\varepsilon + e_m\|$ (ref.(5.1))	0.7176	0.7224
$\|\varepsilon_\delta + \delta e_m\|$ (ref. (5.7))	0.0066	0.0231

The next test case, i.e. Case 2, was an experiment on a tank filled with saline, accounting for homogeneous circumstance testing where the modelling error was supposed to be small. In this case, the electrode plane locations were intentionally misconfigured in the reconstruction model used (2-10 mm error). An aluminium rod was used as the inclusion. The reconstructed images of the two approaches are shown in Figure 5-2. The inclusion was able to be reconstructed by the absolute imaging approach in this case. However, the novel approach was more efficient to deal with the modelling error. The artefacts were smaller, and the location of the inclusion was more accurate.

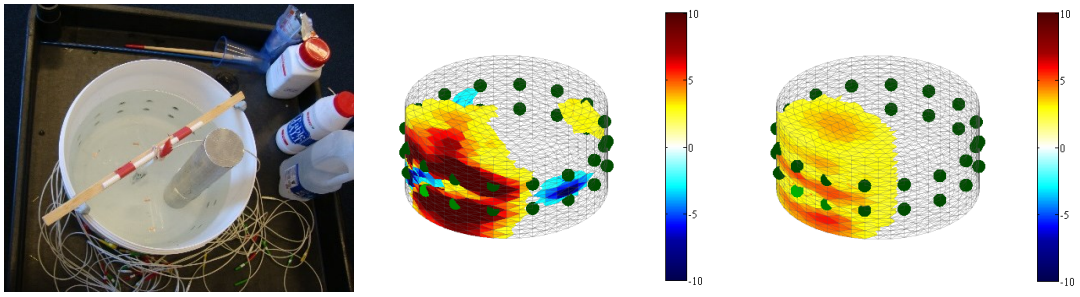

(a) (b) (c)

Figure 5-2 Reconstruction difference images of Case 2 – cylindrical tank with aluminium rod inclusion (a): the absolute imaging approach (b), and the difference imaging approach (c).

In Case 3, the modelling error was very large. A head-like tank filled only with saline was used, i.e. it was another homogeneous situation. The head-like tank model was not created from the geometry of the tank, but it was created from the geometry of a real human head. A carrot was used as the inclusion. The modelling error, in this case, is then supposed to be larger than the previous case (Case 2). The reconstructed images are shown in Figure 5-3. The movement of testing carrot cannot be detected with the absolute imaging approach (even though this situation was homogeneous), but it can with the novel approach (Ouypornkochagorn et al., 2015a).

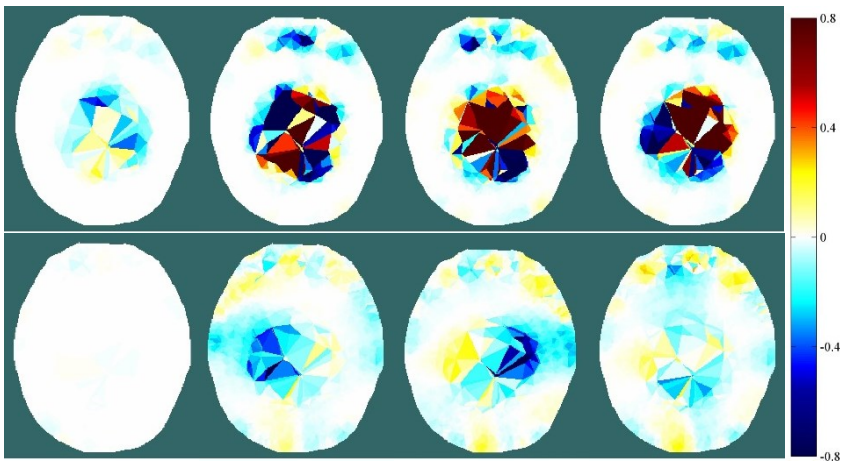

Figure 5-3 Reconstruction difference images of Case 3 – head-like tank with carrot inclusion, from no inclusion (the leftmost column) to full inclusion of the carrot on the left (the second column), then on the right (the third column), and finally the carrot was removed (the rightmost column): the absolute imaging approach (top row), and the difference imaging approach (bottom row).

The last case, i.e. Case 4, is the extreme case. The circumstance of Case 3 was repeated, but a dried honeydew melon peel was put inside the tank. This peel was to act like the human skull, where the conductivity of the peel was about five times lower than that of the skull. The reconstructed images of this case are shown in Figure 5-4. Similar to the previous case, the absolute imaging approach cannot reconstruct for the change, but the novel approach was still able to reconstruct (Ouypornkochagorn et al., 2015a).

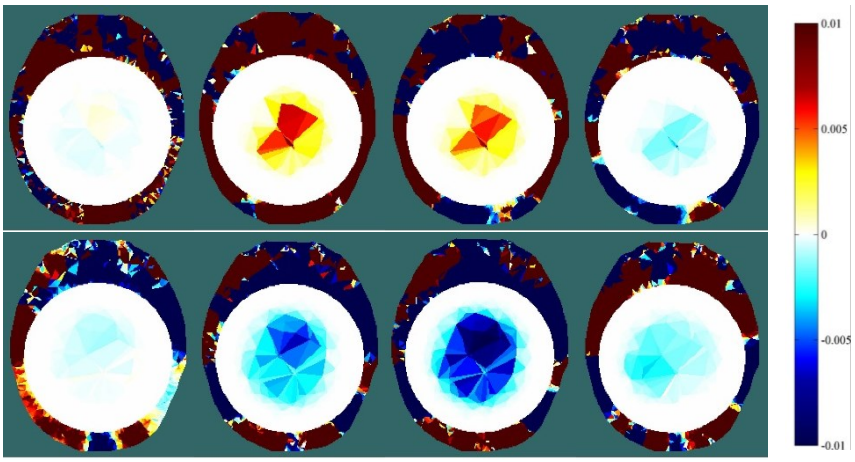

Figure 5-4 Reconstruction difference images of Case 4 – head-like tank with honeydew melon peel and carrot inclusion, from no inclusion (the leftmost column) to the beginning to the end of inclusion (the second column to the rightmost column): the absolute imaging approach (top row), and the difference imaging approach (bottom row).

Apart from the issues above, due to the substantial reduction norm of the error term of the novel difference imaging approach, the selection of the regularisation parameter became much easier in the experiments. The parameter was not required to be high and was maintained for the whole sequence of records. It can be evaluated from a data frame in the time-series. This utilization of the same regularisation parameter is impossible for the absolute imaging approach due to the large size of the modelling error term.

5.3.2 Krylov Subspace Methods

As mentioned in Section 2.5.2, due to the large dimensionality of the problem and the need to include complicated prior information of the head, Krylov Subspace methods are suitable for these needs. The original problem is projected into a new problem. The Hessenberg matrix $\overline{H}$ (2.29), in the case of Arnoldi projection method (Algorithm 2.1), or the tridiagonal matrix $\overline{T}$ (2.31), in the case of Lanczos projection based method (Algorithm 2.2) becomes the new transfer matrix of the new problem. These new transfer matrices contain important information, and can substitute the original one. They are much smaller, and therefore, they require substantially lower computational resources. However, they are required to be investigated when they are used to solve a severely ill-posed problem such as head EIT problems.

The possibility to use Krylov Subspace methods in EIT was investigated on Case 5 (see Appendix I). The non-projection matrix (i.e. $A^T A$ or $J^T J$ in the EIT context) of the first iteration was extracted for eigenvalues which can represent the main features of the problem. The eigenvalues of the $\overline{H}$ and those of the $\overline{T}$ were extracted and compared to those of the non-projection matrix as shown in Figure 5-5. Obviously in this EIT problem, the Arnoldi projection method can extract the features more accurately than the Lanczos projection method.

The inclusion reconstructions of Case 5 were performed by Newton-Krylov GMRes method (on Arnoldi projection method basis) and QMR method (on Lanczos projection method basis). The Arnoldi projection method yielded superior outcomes compared with the Lanczos projection method, determined from the measurement data misfit (Figure 5-6) and the reconstructed images (Figure 5-7). It was also found that the regularisation parameter (λ) in the Lanczos case was difficult to find. When λ was changed from a very small value ($1\text{x}10^{-14}$) to a slightly higher value ($1\text{x}10^{-12}$), this tiny change of λ may cause the reconstruction to fail, as shown in Figure 5-7(d).

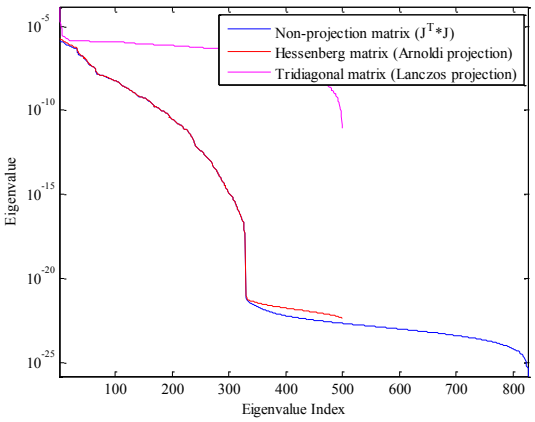

Figure 5-5 Eigenvalues of non-projection matrix $J^T J$, Hessenberg matrix $\overline{H}$ (based on Arnoldi projection method), and tridiagonal matrix $\overline{T}$ (based on Lanczos projection method)

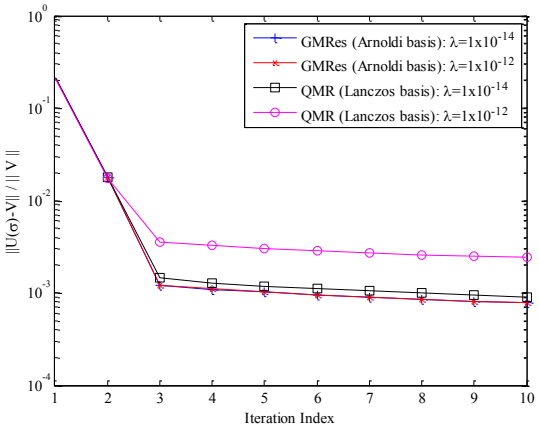

Figure 5-6 Measurement data misfit norm of GMRes (based on Arnoldi projection method) and QMR (based on Lanczos projection method) with the regularisation parameter of $1x10^{-14}$ and $1x10^{-12}$

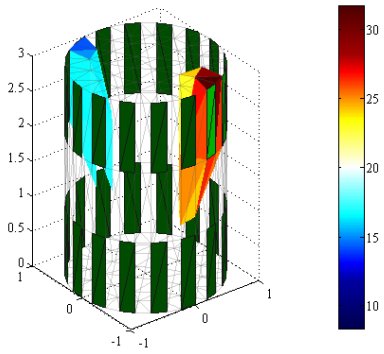

(a) GMRes (Arnoldi projection) $\lambda = 1\times10^{-14}$

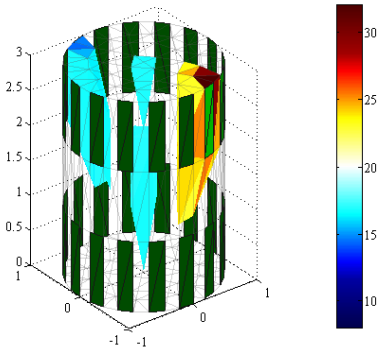

(b) QMR (Lanczos projection) $\lambda = 1\times10^{-14}$

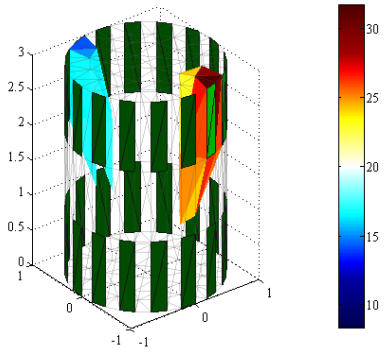

(c) GMRes (Arnoldi projection) $\lambda = 1\times10^{-12}$

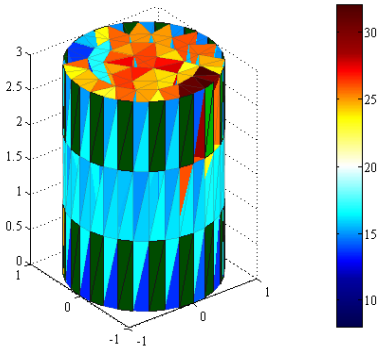

(d) QMR (Lanczos projection) $\lambda = 1\times10^{-12}$

Figure 5-7 Absolute images of Case 5, the reference image is displayed in Appendix I.5

5.3.3 Generic Head Model and Mesh Resolution

Generic model is of interest since an accurate model is not easy to be obtained from a subject. The coarse mesh resolution is also of interest to reduce the computation time. However, the use of a generic model, as well as a coarse mesh resolution model, can introduce modelling error. The novel difference imaging approach could mitigate the impact of this error to some extent, but the error must not be too large. Therefore, the investigation on a real human head was performed (Case 6, see Appendix I) to determine the possibility to use a generic model in practical situations. Transient Hyperaemic Response Test (THRT) data was selected, and the decrease of conductivity on the left side of the head was expected to be seen (left carotid artery compression). Two generic models (four mesh resolution variations) and one subject model (two mesh resolution variations) were chosen in the investigation (however, the skull geometry of the subject models was inaccurate).

As expected, using the subject models yielded the better fitting performance to the measurement data (Figure 5-8). The fitting performance by using the generic synthesized models held the second place, and that of the generic non-subject model held the last place. However, the mesh resolution did not correlate with this performance, i.e. using a coarse model could yield the better fit. The reconstructed images (using the novel difference imaging approach) of these six models were generally similar, as the examples shown in Figure 5-9. All images can show the explicit change corresponding with the artery occlusion i.e. the decrease of conductivity on the left side (the occlusion side). The mesh resolution was less impactful to the quality of reconstructed images, but it notably impacted the need of the computational resources as shown in Table 5-2. These indicate that the use of a coarse generic model is possible.

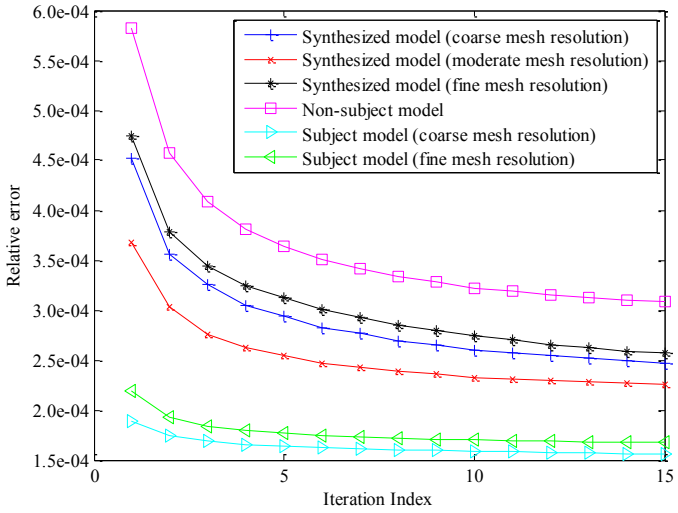

Figure 5-8 Relative measurement misfit of using the models in Case 6

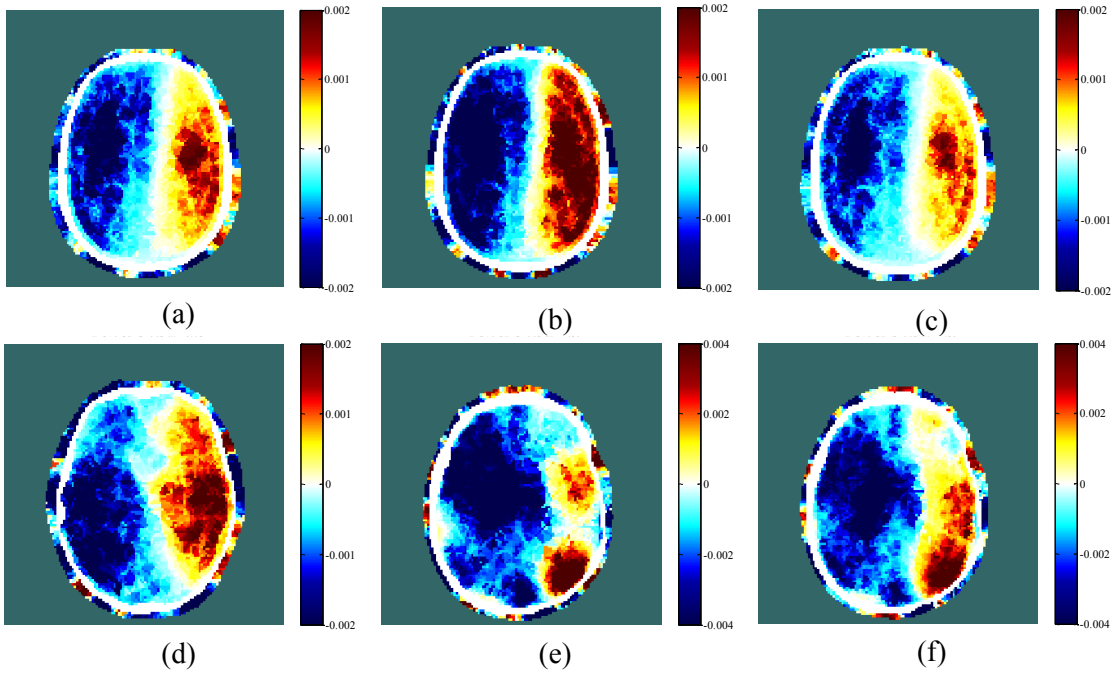

Figure 5-9 Reconstruction difference images of Case 6 on nasion-transversal section plane: (a-c) obtained from the synthesized models (top left to top right: coarse/ moderate/ fine mesh resolution, respectively), (d) obtained from the non-subject model, and (e-f) obtained from the subject models (bottom middle to bottom right: coarse/ fine mesh resolution, respectively)

Table 5-2 The required computational resources of each head model in Case 6

No	Models	Number of Elements	Computa-tional Time (s) (15 Iterations)	Memory Requirement for Jacobian Matrix (MByte)	Relative Measurement Misfit of the Last Iteration
1.1	Synthesized model 1 (Coarse mesh resolution)	158,168	637.35	690.88	2.472×10^{-4}
1.2	Synthesized model 2 (Moderate mesh resolution)	208,311	1,560.63	909.90	2.255×10^{-4}
1.3	Synthesized model 3 (Fine mesh resolution)	274,128	2,409.44	1,197.39	2.568×10^{-4}
2	Non-subject model	212,658	1,618.18	928.89	3.082×10^{-4}
3.1	Subject model (Coarse mesh resolution)	178,480	1,578.94	779.60	1.562×10^{-4}
3.2	Subject model (Fine mesh resolution)	298,312	3,272.12	1,303.03	1.672×10^{-4}

5.3.4 Regularisation Parameter Evaluation by L-Curve

The L-Curve is analogously a selection sheet to choose the optimal setting of an individual problem. Therefore, to find a suitable regularisation parameter of a problem by the L-Curve method, at least a measurement data and a model of the problem must be available first. Real measurement data on THRT (during occlusion) (Case 6 of Appendix I) and a generic head model (the synthesized model) with the moderate mesh resolution were used in this evaluation.

The L-Curve of this real situation is shown in Figure 5-10. The corner of the "L" is of the parameter of 1×10^{-7}. Some reconstructed images based on certain parameters in the curve are shown in Figure 5-11. The best image is supposed to be the image that can show the occlusion on the left side, and that was the image of using the parameter at corner, i.e.1×10^{-7}. It is also noticeable that a smaller parameter value led to, less filtered – noisy images.

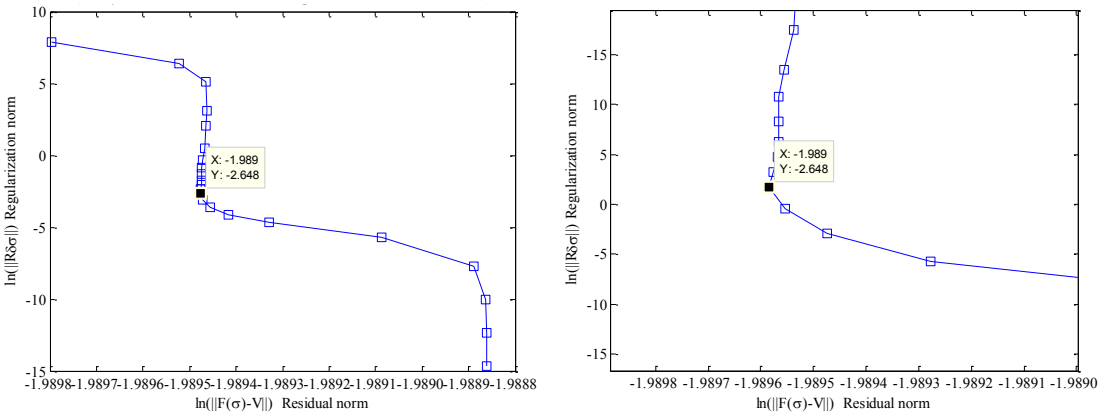

(a) (b)

Figure 5-10 L-Curve between the residual norm and the solution norm of the real head situation (Case 6): (a) from the regularisation parameter of $1x10^{-19}$ (the most top left) to that of $1x10^{1}$ (the bottom right) (with the increasing order of 10), (b) the zoom-in at the corner of (a); the marked value, the corner point, is the value of $1x10^{-7}$ – the chosen parameter.

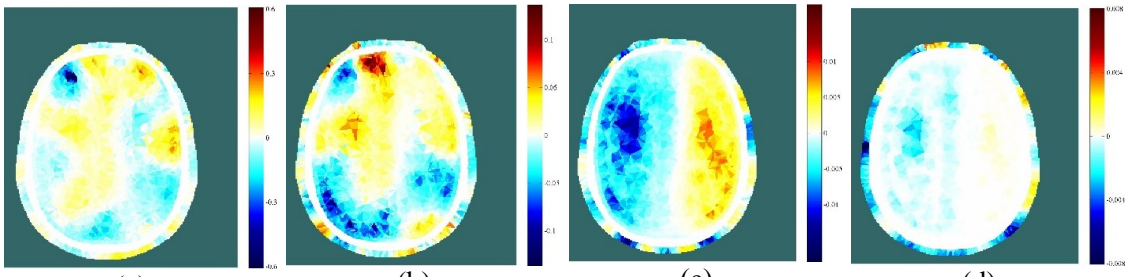

(a) (b) (c) (d)

Figure 5-11 Reconstructed images of various regularisation parameters: (a) $1x10^{-19}$, (b) $1x10^{-13}$, (c) $1x10^{-7}$ (the chosen parameter in this research), and (d) $1x10^{-4}$

5.4 Discussion and Conclusion

In the applications to the human head, the presence of modelling error and the large scale of the problem are the important issues to be addressed. In the aspect of modelling error, the absolute imaging approach that is the conventional approach cannot deal with this error effectively. On the other hand, the linear difference imaging approach has reported that it can deal with the modelling error. However, since it is based on a linear approximation, it might not be suitable for nonlinear problems like the problem of EIT. The improved version of the difference imaging approach (Section 5.1), named "nonlinear difference imaging approach", enables reconstruction in a nonlinear manner by iterative minimizing for the solution like the absolute imaging approach usually does. Therefore, this approach is well suited here. With this novel approach, the norm of the error term is substantially reduced, and

this mitigates the presence of the modelling error (Section 5.3.1). The qualitative performance of the difference imaging approach depends on the accuracy of the initial guess of the conductivity that actually is the exact conductivity of the reference frame (or reference time stance/ record). Since the tissue conductivities of the reference frame are unknown in head EIT applications, with the difference imaging approach, to acquire the initial guess is then impossible. Therefore, in order to obtain the initial guess, the values reported in literature and the experimental estimation as performed in Chapter 3 are the best option for using as the initial guess. However, in a heterogeneous head EIT model, even when using the novel approach, the change in the conductivity magnitude does not reflect the true magnitude (much smaller in brain region). Also, the artefacts are still noticeable, in particular in the scalp region (Section 5.3.1).

For iterative non-linear reconstruction, when the noise is large, the solution deviated more from the exact solution in the late iterations. The "past step length" strategy is proposed to avoid the divergence of the solution (Section 5.2). This strategy limits the changing magnitude of the solutions by the average magnitude of the changes occurring in the previous recent iterations. Comparing to the conventional strategy i.e. line search strategy, the proposed strategy is much faster and theoretically more robust. In fact, using line search strategy is also not suitable for head EIT, because it disregards the presence of the modelling error.

Using a generic head model, i.e. a non-subject-specific head model, seems to influence the reconstruction outcome because EIT is model dependent. Using the generic model in forward calculation certainly yields less accurate prediction than using a subject model. However, these customised models are often difficult to obtain. The use of some generic models was investigated here, and the experimental results indicated that it was possible to be used (Section 5.3.3). However, 1) the generic model must be similar to the subject model as much as possible, and 2) conductivity perturbation must be small.

The dimensionality of the problem in 3D head EIT, which is large, is another concern. Certain reconstruction algorithms are able to solve large-scale problems e.g. Conjugate gradient (CG), Singular Value Decomposition Method (SVD), and Hybrid

Krylov Subspace method. However, CG and SVD have some limitations when implemented for the head EIT problem. For example, the number of suitable iterations is difficult to know a priori in the case of CG, and both methods cannot facilitate complicated prior information with the moderate amount of computational memory.

The hybrid Krylov-Tikhonov method is able to nonlinearly solve the problem with the memory of ordinary computers and with including complicated prior information. This method performs the Krylov projection to approximate a problem to be a much smaller problem. The two popular projection methods: Arnoldi projection method and Lanczos projection method are possible. However, only the Arnoldi projection method can approximate EIT problems accurately and robustly (Section 5.3.2). Furthermore, since the original version of hybrid methods does not support to include prior information, "Newton-Krylov General Minimal Residual", a variation of General Minimal Residual (GMRes) method based on Arnoldi projection is advisable here. This method allows to include complicated prior information.

Prior information suitable for head EIT used during the reconstruction process is the smoothness prior. This is because it is in accordance with the changing behaviour of neurophysiology, i.e. the change in an activated region of the brain is relevant to the process of the neurotransmission of surround neurons (Marieb and Hoehn, 2007). In fact, the total variation prior was strongly suggested to be used according to the ability to reconstruct the sharp edge of the change. However, it seems unnecessary in head EIT applications. Subsequently, the regularisation parameter used to control the influence of prior information must be appropriate. Selecting the regularisation parameter by the Discrepancy Principle (DP) or the Minimum Predictive Error (or unbiased predictive risk estimator (UPRE)) is restrained by the knowledge of measurement uncertainty or prediction error. Generalized Cross Validation (GCV) is a popular option that is easy to implement. However, all of these methods are based on modelling error-free and linear approximation. Therefore, they are not suitable for head EIT which is infused with large modelling error. The naïve method, i.e. L-Curve, then is the most suitable, even though it requires lots of time to evaluate the curve. L-Curve is the plot of residual

norm and solution norm which can be determined without the need to know the size of modelling error. In this context, an additional benefit in using the difference imaging approach, where the norm of the error term is small, is that the chosen regularisation parameter can be utilised for the whole sequence of frames. Therefore, it suffices to determine the L-Curve on only a particular frame.

Chapter 6 Electrophysiology towards Evoked Responses

6.1 Behaviour of EIT Measurements towards Changes

Determining the origin of an evoked response from the electrode data and location is not straightforward in EIT. When there is only a small perturbation of conductivity in the brain, the change in boundary voltages could be observed everywhere, not only in the data of electrodes near the perturbation location. The possibility to utilise the voltage change data to localise the response is then necessary to be investigated, and simulations were carried out in this direction.

The simulation was performed on a 2D concentric layers model i.e. the forward model in Case 1 explained in Appendix I. When a circular inclusion (eight mm in radius) with the conductivity 127% higher than that of the homogeneous background brain was placed in the model as shown in Figure 6-1, most measurement voltages were decreased as expected. The voltage change of the measurement performed near the inclusion was the highest (the measurement pair 2-3 of Figure 6-1(a) and (b)). The largest change in percentage is supposed to be on the measurement near the inclusion, but the largest voltage change in percentage was found on the least sensitive site instead, regardless of the location of the inclusion (the measurement pair 13-14 of Figure 6-1(a) and the pair 7-8 of Figure 6-1(b)). Furthermore, the change can also be observed even in the site far from the inclusion (the measurement pair 7-8 of Figure 6-1(a)). Additionally, when the current pattern was different, even though the measurement was performed on the same site (the measurement pair 2-3 of Figure 6-1(a) and (b)), the percentages of voltage change were not close in percentage (in this example, 7.5 times in difference).

According to the observation above, the conductive inclusion mostly led to the decrease of boundary measurement voltages. In order to localise the inclusion by boundary measurements, the measurements where the sensitivity is poor must not be considered (indicated by red crosses in the figures). However, the utmost concern is that the small voltage change occurred at the non-inclusion region (the measurement

pair 7-8 of Figure 6-1(a)). This change can be called “false response”, which was 14% of the percentage change occurring near the inclusion region.

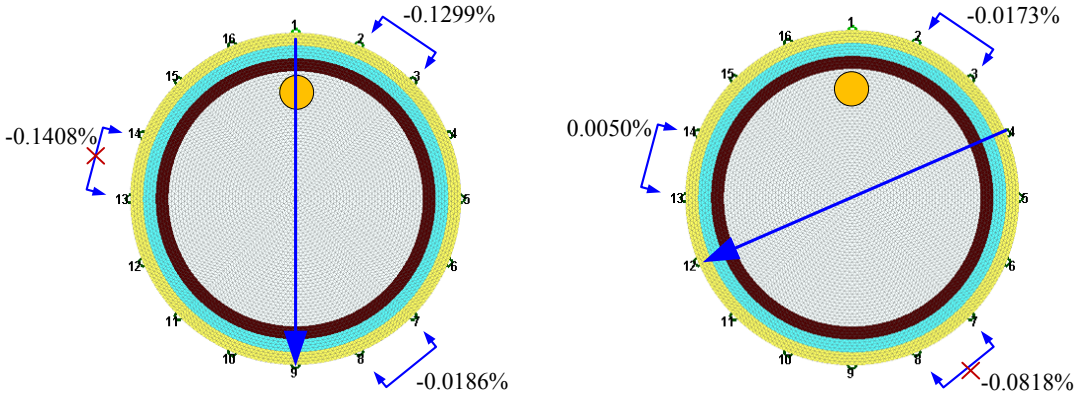

(a) Current driven from #1 to #9 (b) Current driven from #4 to #12

Figure 6-1 Boundary voltage changing after putting an inclusion near electrode#1 (small orange circular object in the brain region). The simulation was carried on two current patterns: a) from electrode #1 to #9 (in the path of the inclusion), and b) from #4 to #12 (not in the path of the inclusion). The measurements which are marked with the red cross are very low in sensitivity.

When a second inclusion was added to the model (Figure 6-2), the observation were similar to those above. However, the false response of this case (the measurement 7-8 of Figure 6-2(a)) was 3.24 times larger than that of the single inclusion case. It also was 35% of the percentage change occurring near the inclusion region (the measurement 2-3 of Figure 6-2(a)) in this case, i.e. 2.5 times larger than the single inclusion case. The larger false response leads to a difficulty in identifying.

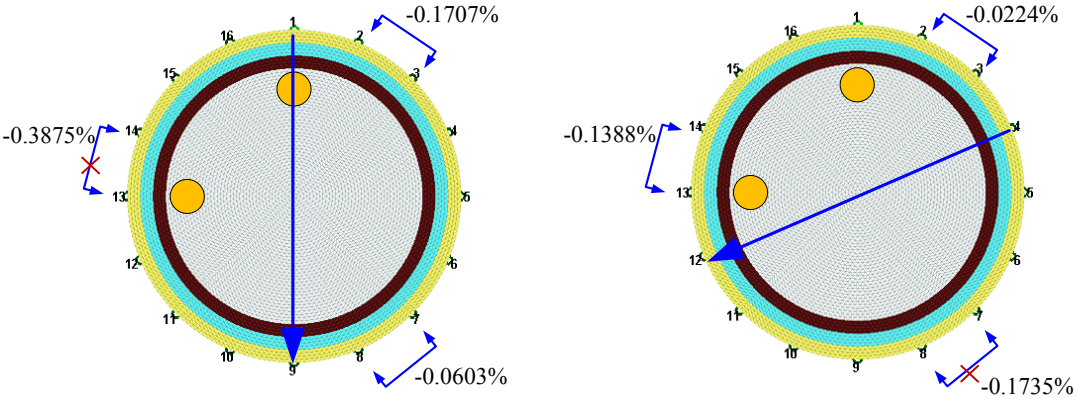

(a) Current driven from #1 to #9 (b) Current driven from #4 to #12

Figure 6-2 Boundary voltage changing after putting two inclusions near electrode#1 and #13 (small orange circular objects in the brain region). The simulation was carried on two current patterns: a) from electrode #1 to #9, and b) from #4 to #12. The measurements which are marked with the red cross are very low in sensitivity.

6.2 EIT Measurement Characteristic to Evoked Responses

6.2.1 Baseline Fluctuation and REG Amplitude

Before beginning to process the responses, understanding the physiological behaviour of a stimulus-free state, called "reference state" of the brain, is imperative. As there is no stimulation, the change of boundary voltages should be mainly due to changes in physiological regulations e.g. respiratory regulation, and REG cardiac pulses. The effect of both changes should be addressed independently. To investigate the change caused from regulations, we first average the data over a REG cardiac cycle to mitigate the effect of REG. The period of a REG cycle is determined from the two consecutive peaks of REG signal (containing approximately 100 frames with the recording speed of fEITER system). This averaging yields the "baseline" of the reference state, and the variation of the baseline called "baseline fluctuation". This fluctuation indicates the regular change due to physiological regulations. Intuitively, any responses on the measurement traces at amplitudes lower than the amplitude of the baseline fluctuation should be regarded as physiological noise (or called "resting noise").

The amplitude of the baseline fluctuation correlates to evoked response investigated. Since the characteristic of response could be "fast" or "slow", the fluctuation should be determined as fast or slow respectively. In this research, the fast fluctuation was investigated by determining the voltage change from the previous consecutive REG pulse. The slow fluctuation was computed from the maximum change over eight REG pulses. The choice of "eight" is based on a study regarding BOLD response (Logothetis and Wandell, 2004). With two-second duration visual and motor stimuli, the peak of the BOLD response occurred between six and nine seconds after the stimulation onset, roughly equivalent to between the 8^{th} and the 11^{th} REG cycle in the EIT data measured here. Therefore, this fluctuation accounts for the change mainly due to the BOLD response (haemodynamic response). The investigation was performed on the data obtained from the 1 mA_{pk-pk} original version and 2 mA_{pk-pk} modified version of fEITER: seven trials (on six subjects) for the original version and four trials (on one subject) for the modified

version. The period of about 59 seconds were chosen. The measurements were performed at the forehead, near the left and right ears, the rear head, and over the eyelids (MeasID#138, #277, #122, #91, #438, and #451 respectively, referring to the measurement schemes in Appendix D).

Some examples of the signal fluctuation are shown in Figure 6-3. The fast fluctuation is smaller than the slow fluctuation during the reference state. The summary of experimental results is shown in Table 6-1. The mean of the fast fluctuation was about 0.013%, and the mean of the slow fluctuation was between 0.051% and 0.064%, i.e. 4.25-4.94 times higher than that of the fast fluctuation. The REG amplitude was also investigated here on the same data of the above investigation by determining the change over a REG cycle compared to the mean voltage value, as shown in (6.1). The REG amplitude was between 0.142% and 0.146%.

$$REG\ Amplitude = \frac{|MaxVoltageValue - MinVoltageValue|}{MeanVoltageValue\ of\ the\ investigated\ cycle} \tag{6.1}$$

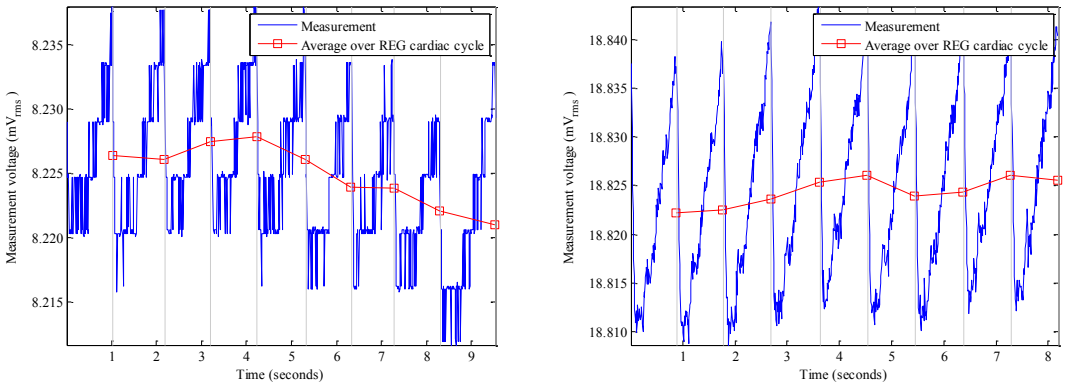

(a) (b)

Figure 6-3 REG signal during reference state (the blue lines) and its average over cardiac cycle (the red lines): (a) obtained from the 1 mA_{pk-pk} version and (b) obtained from the 2 mA_{pk-pk} version of fEITER.

Table 6-1 Baseline fluctuation and REG amplitude of two versions of fEITER system

Baseline fluctuation/ REG amplitude	Average change[(1)]	
	The 1 mA_{pk-pk} excitation system	The 2 mA_{pk-pk} excitation system
Fast fluctuation	0.012%±0.001%	0.013%±0.002%
Slow fluctuation	0.051%±0.004%	0.064%±0.014%
REG amplitude	0.146%±0.029%	0.142%±0.019%

(1) Mean ± Standard deviation

The change during the reference state was the sum of the baseline fluctuation and the REG amplitude that was 0.159-0.21%. This range was within the range reported by (Bodo et al., 2005), i.e. the pulsatile change of REG was caused by the 1-10% change of the total conductivity, or equivalent to 0.0003-0.67% change on the boundary voltages (based on the same assumption used in Section 2.3.4). To ensure that an observed response is the true targeted evoked response, the amplitude of the response to stimulation should be larger than this sum.

6.2.2 Auditory Startle Response

An auditory startle response (ASR) was investigated in this research in 12 trials (three subjects) with the 1 mA_{pk-pk} fEITER system, on three trials (one subject) with the 2 mA_{pk-pk} fEITER system, and on two trials (one subject) with the 1 mA_{rms} fEITER system. The subjects were asked to sit in a quiet room with/without a blindfold and then were startled with party poppers (Figure 6-4). The stimulation times were recorded by a microphone. Six EIT measurements: at the front, rear, left and right ears, and over left and right eyelids (the same as used in the previous section) were chosen for investigation. Note that the front and the right eyelid measurements have reversed polarity relative to the others, since the measurement is performed between the electrode near the outward current electrode for the positive polarity and that near the inward current electrode for the negative polarity. Therefore, the polarity must be inverted for the front and the right eyelid cases in the relevant figures. Note that, according to the simulation result explained in Section 6.1, the increase of voltage amplitude implies the decrease of conductivity. Two example sets of measurements are shown in Figure 6-5 (obtained from the 1 mA_{pk-pk} fEITER system) and from Figure 6-6 (obtained from the 1 mA_{rms} fEITER system).

(a) (b) (c)

Figure 6-4 Experiment configuration: (a) subjects sat in a quiet room with blindfold wearing, (b) party poppers were used as stimuli, and (c) a microphone with a pre-amplifier was used as a startling sound detector.

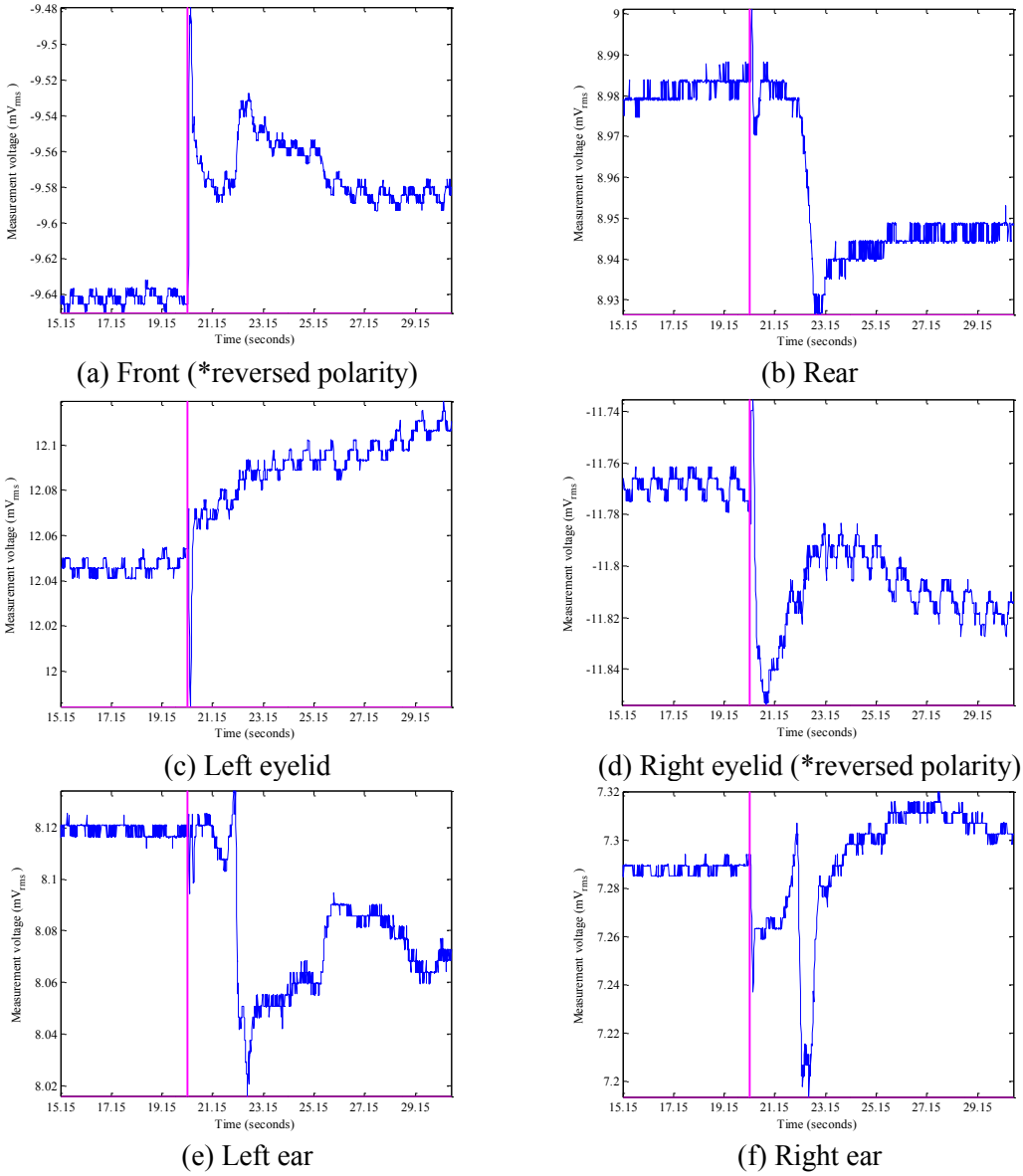

(a) Front (*reversed polarity) (b) Rear

(c) Left eyelid (d) Right eyelid (*reversed polarity)

(e) Left ear (f) Right ear

Figure 6-5 Example of ASRs obtained from the 1 mA$_{pk-pk}$ fEITER system: measured at (a) the front, (b) the rear, (c) the left eyelid, (d) the right eyelid, (e) the left ear, and (f) the right ear. The magenta trace is the stimulus marker.

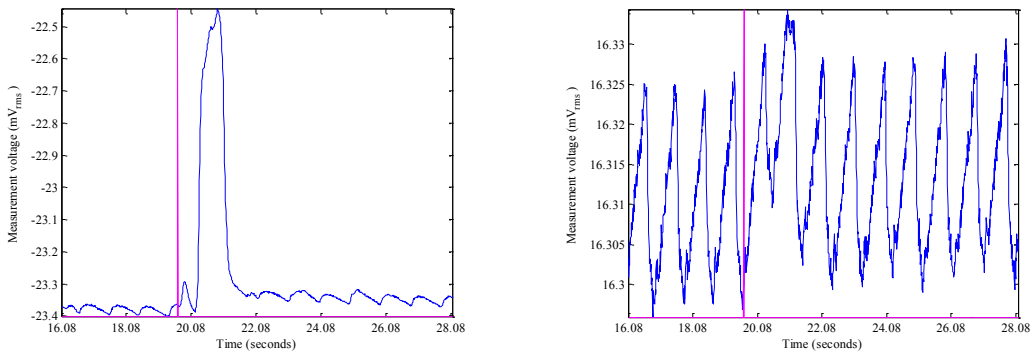

(a) Front (*reversed polarity)

(b) Rear

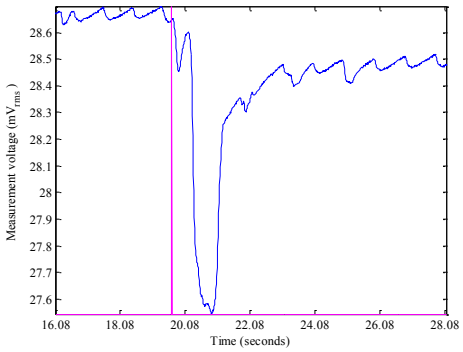

(c) Left eyelid

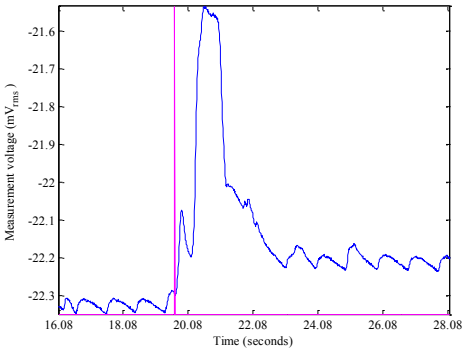

(d) Right eyelid (*reversed polarity)

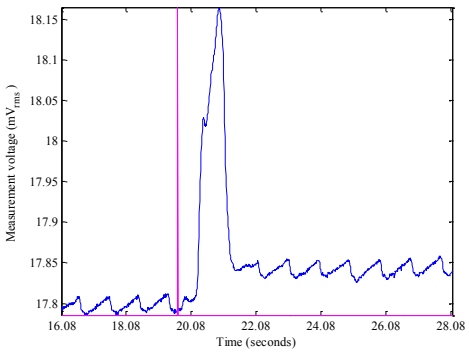

(e) Left ear

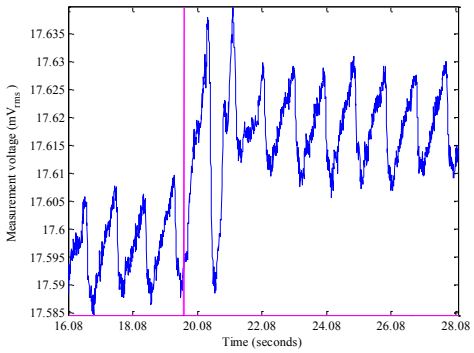

(f) Right ear

Figure 6-6 Example of ASRs obtained from the 1 mA_{rms} fEITER system: measured at (a) the front, (b) the rear, (c) the left eyelid, (d) the right eyelid, (e) the left ear, and (f) the right ear. The magenta trace is the stimulus marker.

The characteristic of ASR on the circumstance of EIT was found in this research as in Figure 6-7. There were three components contained in the response: N1, P2, and N2 ("N" and "P" denote to the increase and the decrease of conductivity respectively). The frequency of occurrence of these components was unequal as illustrated in Figure 6-8. The component N1 had the highest frequency of occurrence

at 57%. The frequency of occurrence of the next two components (P2 and N2) were respectively smaller, i.e. 47% and 38%. The absence of N1 did not cause the absence of remaining components, and this is consistent with the observation reported in (Viswanathan and Freeman, 2004), however, that study was based on visual evoked response. The frequencies of response occurrence were lower at the ear sites (the closest sites to the auditory cortex), i.e. 50%, 32%, and 24% for N1, P2, and N2 respectively. However, even though N2 had the lowest frequency, the changing amplitude on both ear sides was highest i.e. -0.61% on average (Figure 6-9). Meanwhile, the average changes in amplitude were only -0.30% for N1 and 0.27% for P2, although these were less than the half of the N2 amplitude change.

Except for the rear site, the changing behaviour of all sites, shown in Figure 6-9, was consistent with the proposed response characteristic (Figure 6-7). However, large drifting (more than 0.6%) can be obviously noticed in the front, probably due to undesired responses from the face muscles or the partial effect of electromyography (EMG). Additionally, due to the large change at the front site, the change at the rear site which was much smaller could be a false response (as explained in Section 6.1). The change of the rear was only 7-30% of the change of the front. Furthermore, the response at the rear had reversed polarity component to the proposed characteristic. From this, we can conclude that there was no significant change at the rear.

Response latency could be evidence to confirm the emerging of ASR (Figure 6-10). The latency of N1 of all sites was at 147 ms (the standard deviation was only 17 ms). This number was close to the latency of 100 ms of N100 component of EEG as explained in Section 2.4.1. This suggests that the N1 response of the EIT signals has a neuronal source (Mayhew et al., 2010a). However, the EIT components of P2 and N2 were not matched to the latency of P200 of EEG (occurring at 200 ms), i.e. the latencies of EIT components were much slower 4.4-9.7 times. The slower EIT response of P2 and N2 components suggests that they may arise from the BOLD response (haemodynamic response) rather than from neuronal response like N1 (Mayhew et al., 2010a). This may be the reason that the amplitude of N2 was 101% higher than that of N1. It was also possible to observe that the difference in latency of P2 and N2 between at the ear and the eyelid sites were very large. The latencies of

P2 were 1.94 s for the ear sites and 0.89 s for the eyelid sites; whilst the latency of N2 was 2.89 s for the ear sites and 4.54 s for the eyelid sites, i.e. much slower. Note that the amplitude of N2 of the eyelid sites was very uncertain (varied from -0.19% to +0.25%). These imply that the influence of haemodynamic response on the different sites could be different.

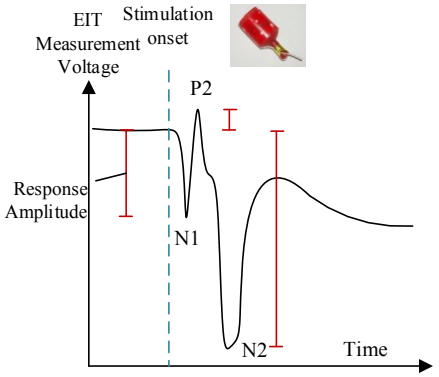

Figure 6-7 Characteristic of auditory startle response (ASR) on EIT signals

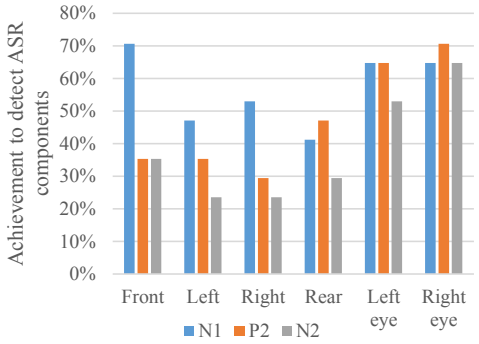

Figure 6-8 Achievement to detect ASR components on 4 subjects and 17 stimulations, obtained from all versions of fEITER systems

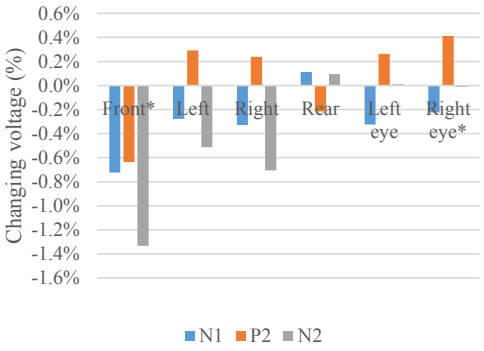

Figure 6-9 Changing of component voltages towards ASR on 3 subjects and 12 stimulations, obtained from the 1 mA_{pk-pk} fEITER system. *The front and the right eye data were inverted in polarity to make them comparable.

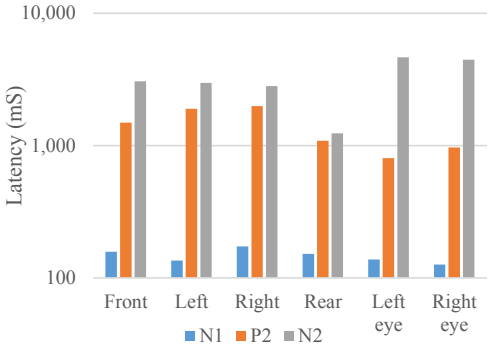

Figure 6-10 Latency of ASR components on 3 subjects and 12 stimulations, obtained from the 1 mA_{pk-pk} fEITER system.

6.2.3 CO_2 Reactivity Response

Eight trials on seven volunteers were performed by breathing 5%-concentration CO_2 in room air for two minutes. Five phases of trials were designed: 60 second-breathing room air (Phase 1), 10 second-breathing room air and 50

second-breathing of CO_2 (Phase 2), 60 second-breathing of CO_2 (Phase 3), 10 second-breathing of CO_2 and 50 second-breathing room air (Phase 4), and 60 second-breathing room air (Phase 5). A transcranial Doppler (TCD) was used to measure the change of blood flow velocity (FV) of both middle cerebral arteries (MCAs). In the meantime, the electrocardiographic signal (ECG) was recorded. EIT measurement was recorded by the 1 mA_{pk-pk} fEITER system. This procedure was approved by the National Health Service Research Ethics Committees (NHS RECs) and the Medicines and Healthcare products Regulatory Agency (MHRA). Additionally, averaging over a REG cardiac cycle was applied due to the slow response of this stimulation type. Only four sites were chosen for the investigation: the front, the left and right ear sides, and the rear.

Surprisingly, no consistent characteristic among the measurements of all trials can be found. Some example responses are shown in Figure 6-11. Figure 6-11(a) and (b) show the increase of conductivity in Phase 2 and the decrease in Phase 4. This characteristic corresponded with the expected response (explained in Section 2.4.2) (called "positive" example). However, the characteristic of the example responses shown in Figure 6-11(c) and (d) did not correspond with the expected response (called "negative" example). Instead, the conductivity decreased in Phase 2 and increased in Phase 4. The amplitude of measurement voltage change after the beginning of CO_2 breathing for approximately 53 REG cardiac pulses (42 seconds), i.e. Phase 2, was uncertain. It ranged between -1.24% and +2.25%. Similarly, the changing amplitude after the end of CO_2 breathing for approximately 52 REG cardiac pulses (43 seconds), i.e. Phase 4, was also uncertain. It ranged between -1.78% and 0.63%. Since the changing behaviour of each measurement sites and that of each trial data set were uncertain, it can be concluded that no correlation was found between the EIT measurements and the TCD measurements.

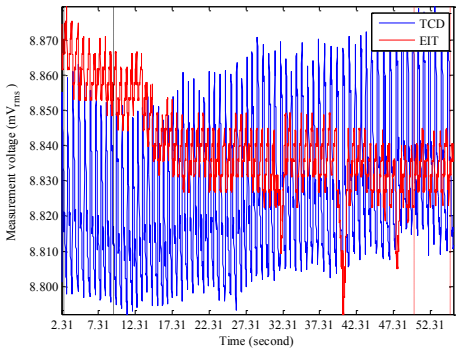

(a) Positive response example of Phase 2

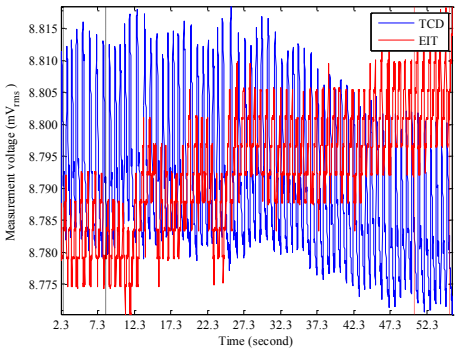

(b) Positive response example of Phase 4

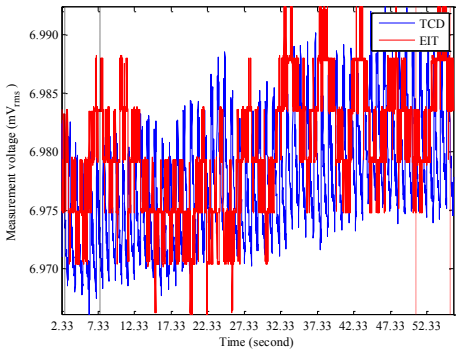

(c) Negative response example of Phase 2

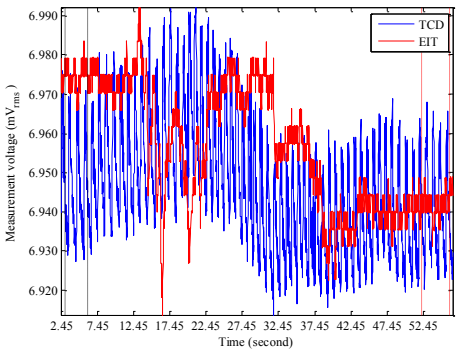

(d) Negative response example of Phase 4

Figure 6-11 Example of CO_2 reactivity responses measured at the right site: (a,c) are the responses at Phase 2, and (b,d) are the responses at Phase 4. (a,b) are positive response examples. (c,d) are negative response examples. The blue lines are the right TCD measurements, and the red lines are the EIT voltage measurements. The decrease in voltage indicates the increase of conductivity (as explained in Section 6.1). The duration between the black dash lines is the reference period. The duration between the red dash lines is the investigated period.

The correlation between the EIT and the TCD measurements was very difficult to investigate due to the large discrepancy in the number of EIT and TCD measurements. Since the nature of CO_2 reactivity response produces global change inside the cranium (rather than local change), the bulk conductivity data derived from all measurements could be applicable (see Chapter 3). Some plots of the bulk conductivity data and TCD measurements are shown in Figure 6-12. Bulk conductivity data was more effective to compare with TCD measurements in this case.

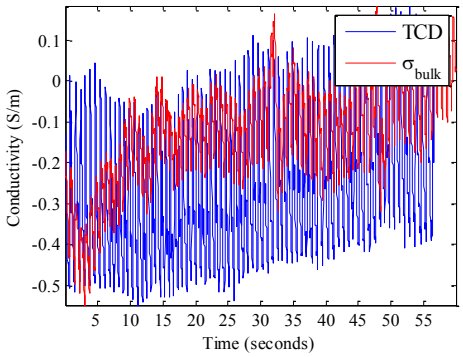

(a) Positive response example of Phase 2

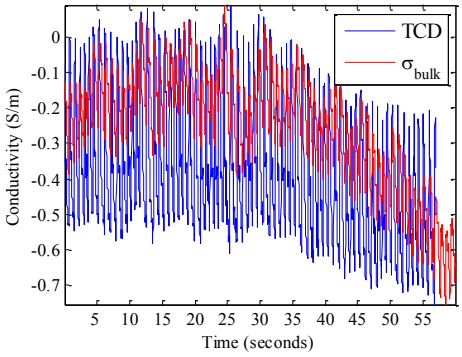

(b) Positive response example of Phase 4

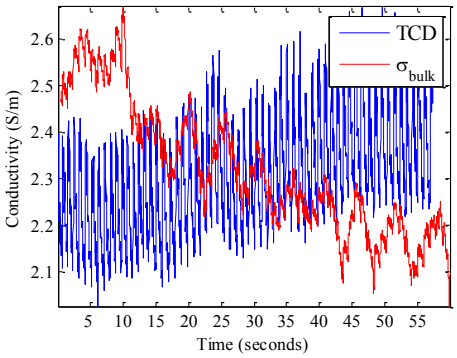

(c) Negative response example of Phase 2

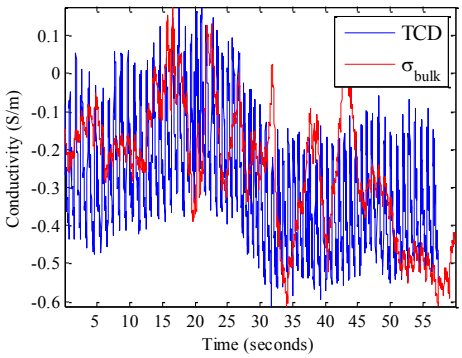

(d) Negative response example of Phase 4

Figure 6-12 Comparison between the bulk conductivity data (the red lines) and the TCD measurements (the blue lines) towards CO_2 reactivity response (the same data set to Figure 6-11): (a,c) are the responses at Phase 2, and (b,d) are the responses at Phase 4. (a,b) are positive response examples. (c,d) are negative response examples.

Ideally, the global conductivity was supposed to be increased during the breathing of CO_2 due to the increase in cerebral blood flow (CBF). 50% of Phase 2-trials were in agreement to this statement, but only 38% of Phase 4-trials were in agreement. The non-corresponding outcomes may be caused by the subject movement or the large conductivity change in the scalp. Additionally, another possible reason was due to the change of heart rate. The heart rate during the experiments tended to be decreased and oscillated during the breathing of CO_2 (Figure 6-13). The ripples of the heart rate can also be observed in the EIT measurements (Figure 6-11) and also the bulk conductivity data (Figure 6-12). Although there is no report in the literature indicating how the heart rate impacts the conductivity, it could be related to the haemodynamic change in the scalp.

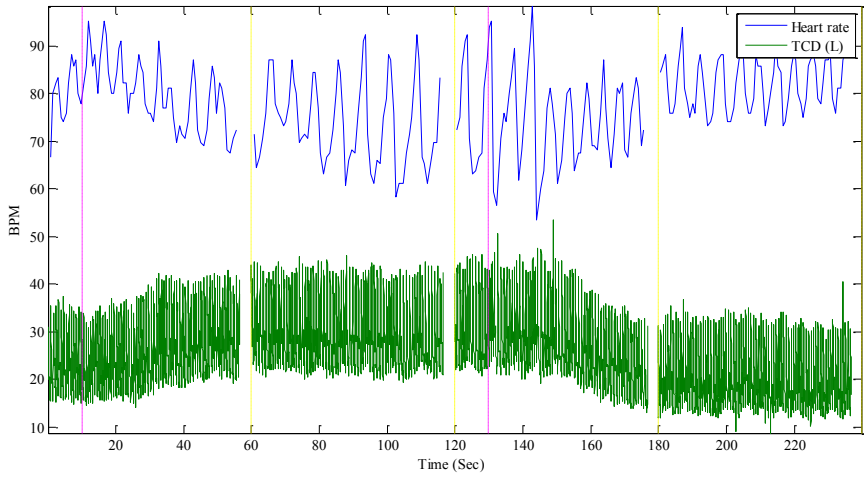

Figure 6-13 Example of the heart rate oscillation (the blue line) before and after the breathing of CO_2, compared to TCD measurement (the green line). The vertical yellow lines are the beginning of Phases – from Phase 2 to Phase 4. The duration between two vertical dashed magenta lines are the period of CO_2 breathing.

6.2.4 Transient Hyperaemic Response (THR)

Transient Hyperaemic Response (THR) can be obtained by the Transient Hyperaemic Response Test (THRT). The physiological change is expected to be local, and subject movement is unnecessary during the test. Therefore, THRT should be advisable for investigating the efficiency of head EIT in the early stage. Seventeen trials were performed on five subjects with a 5-second occlusion at the left or the right middle cerebral artery (MCA) (Figure 6-14). The trials were approved by NHS RECs and MHRA. ECG and TCD measurements were record during the tests. The 1 $mA_{pk\text{-}pk}$ fEITER system was used in all trials. Averaging the data over a REG cardiac cycle was applied. Six sites were chosen for the investigation: the left-front, the left and right ear sides, the right-rear, and over the left and right eyelids.

Some TCD and EIT measurements are shown in Figure 6-16 and Figure 6-17 for the left occlusion, and Figure 6-18 and Figure 6-19 for the right occlusion. The increase of voltage implies the decrease of conductivity as explained in Section 6.1 (please bear in mind that the front and the right eyelid measurement data are reverse in polarity). In general, all EIT measurements were consistent with the TCD measurement of the occlusion side. When the occlusion side was swapped, all the responses were inverted except for the eyelid sites where the response characteristic was still unchanged. During the occlusion, the conductivity was considerately

decreased on the occlusion side and was slightly increased on the non-occlusion side. However, although the change at the left-front was consistent with that of the left, the change at the rear-right was opposite to that of the right. This indicates the uncorrelated characteristic at the rear. On the eyelid sites, the conductivity was always decreased despite the fact that the occlusion had been swapped. This is probably due to the dominant source of the change at the eyelid sites being in the frontal face muscles, not inside the cranium. It is also noticeable that the EIT baseline was changed after releasing the occlusion in almost all cases. The new baseline was unsteady for at least five REG cardiac cycles (4-5 seconds). The behaviour of this baseline change was different to that of TCD. The consistency of the responses among the trials is shown in Figure 6-15. The average consistency is 89% for all sites, and 87% for only the ear sites (closest to the occlusion site).

Figure 6-14 Transient Hyperaemic Response Test (THRT)

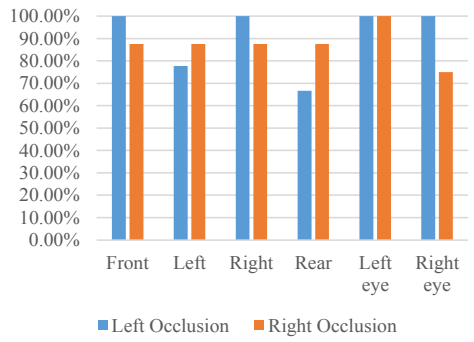

Figure 6-15 Consistency of THRT responses on the left and the right occlusion

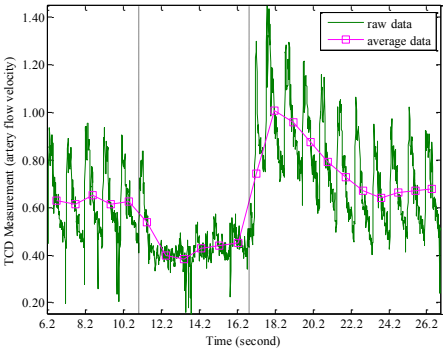

(a) Left ear (occlusion side)

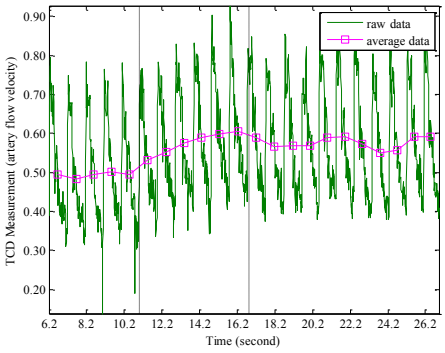

(b) Right ear

Figure 6-16 Example of TCD measurements of the left occlusion: measured on (a) the left ear, and (b) the right ear. The duration between two dash lines is the occlusion period. The magenta lines are the averages over REG cardiac cycle.

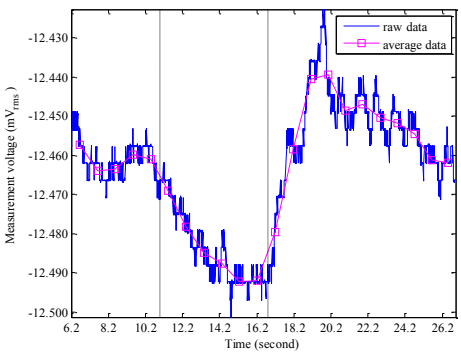

(a) Front (*reversed polarity)

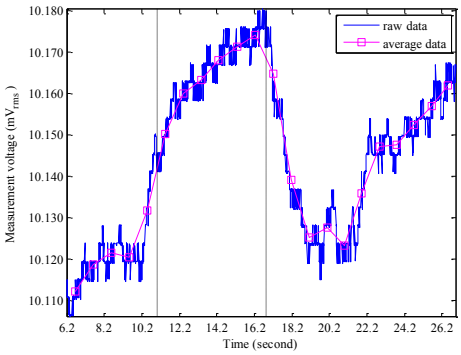

(b) Rear

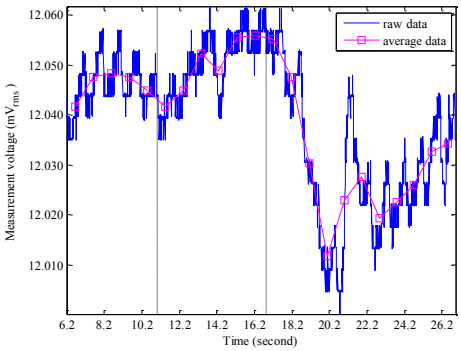

(c) Left eyelid

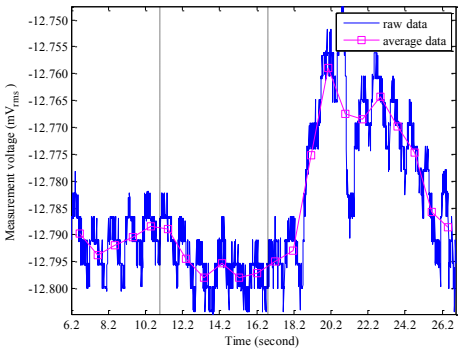

(d) Right eyelid (*reversed polarity)

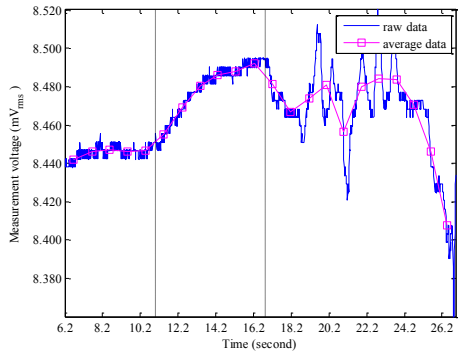

(e) Left ear (occlusion side)

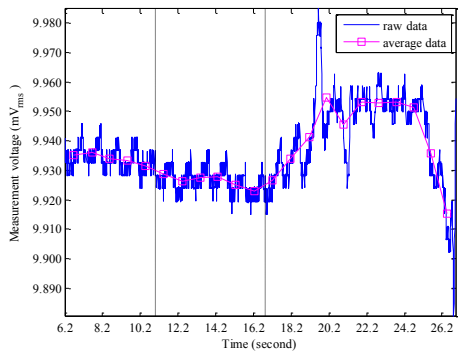

(f) Right ear

Figure 6-17 Example of THR of the left occlusion obtained from EIT instrument: measured at (a) the left-front, (b) the right-rear, (c) the left eyelid, (d) the right eyelid, (e) the left ear, and (f) the right ear. The duration between two dash lines is the occlusion period. The magenta lines are the averages over REG cardiac cycle.

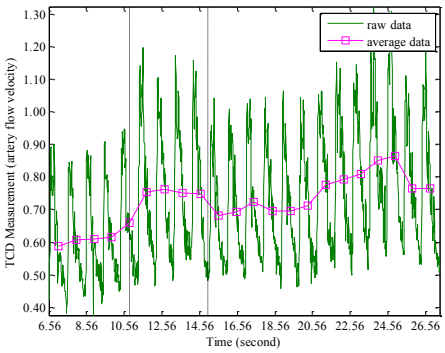

(a) Left ear

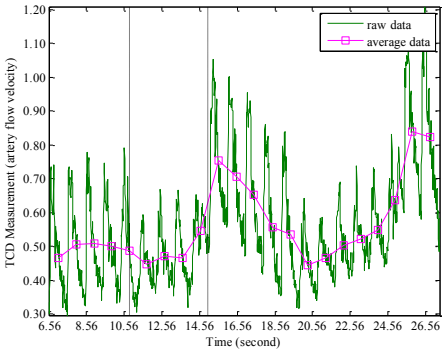

(b) Right ear (occlusion side)

Figure 6-18 Example of TCD measurements of the right occlusion: measured on (a) the left ear, and (b) the right ear. The duration between two dash lines is the occlusion period.

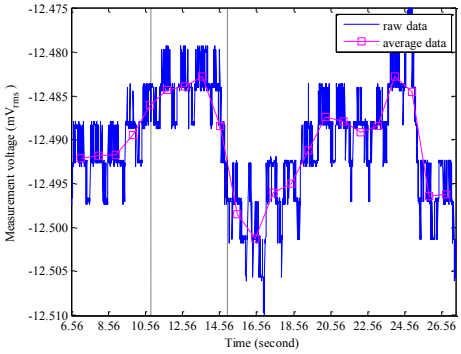

(a) Front (*reversed polarity)

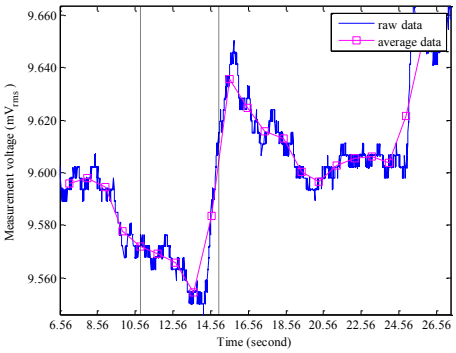

(b) Rear

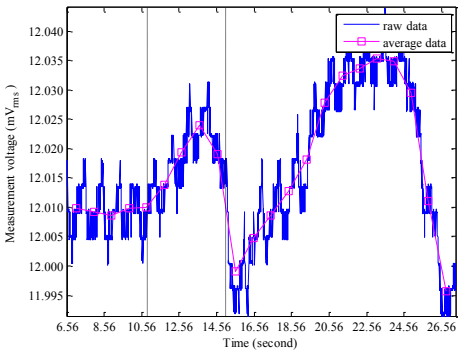

(c) Left eyelid

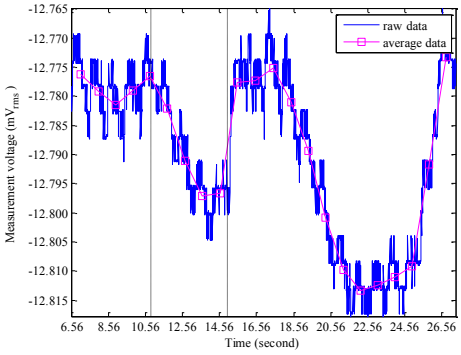

(d) Right eyelid (*reversed polarity)

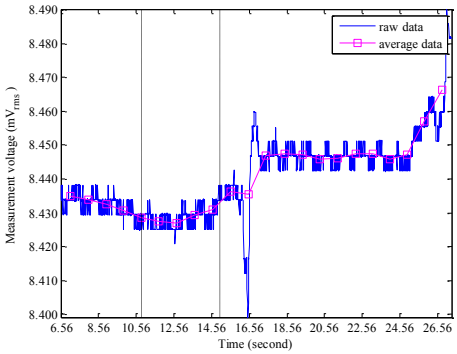

(e) Left ear

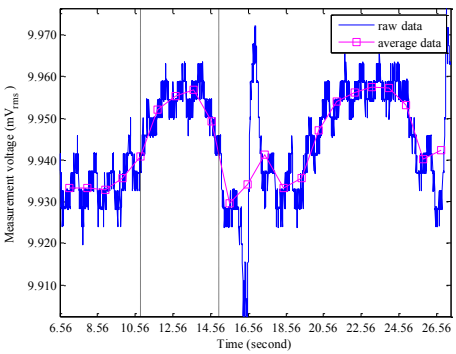

(f) Right ear (occlusion side)

Figure 6-19 Example of THR of the right occlusion obtained from EIT instrument: measured at (a) the left-front, (b) the right-rear, (c) the left eyelid, (d) the right eyelid, (e) the left ear, and (f) the right ear. The duration between two dash lines is the occlusion period.

The summary of EIT response amplitude changes is shown in Table 6-2. The average amplitude of the measurement change was between -0.15% and 0.24% during occlusion and was between -0.03% and 0.16% after the occlusion was released. During occlusion, the amplitude of voltage measurements was 0.24% increased (i.e. conductivity was decreased) on the occlusion side and was 0.15% decreased (i.e. conductivity was increased) on the non-occlusion side. After the occlusion, most responses were returned to about normal. However, the exception is the non-occlusion side, since the amplitude of voltage measurements was 0.16% (i.e. conductivity was decreased).

Table 6-2 The amplitude of voltages measurement change of THR

Occlusion side	During occlusion			After occlusion		
	Front site	Occlusion side	Non-occlusion side	Front site	Occlusion side	Non-occlusion side
Left	-0.22%	0.24%	-0.09%	0.11%	-0.04%	0.14%
Right	0.21%	0.24%	-0.22%	-0.09%	-0.01%	0.18%
Mean	0.22%(1)	0.24%	-0.15%	0.10%	-0.03%	0.16%

(1) Mean of absolute values

6.3 Discussion and Conclusion

Even though EIT has been reported to be usable in particular clinical applications, e.g. lung EIT, there is still doubt regarding its applicability to the head. Compared to other clinical EIT applications, the amplitude of voltage measurement change of head EIT is much smaller. Physiological noise is also regularly contaminated in measurement signal. To preliminarily evaluate the possibility of EIT to head applications, the amplitude of the voltage measurement change due to evoked responses and also the amplitude of physiological noise must be investigated first.

The physiological noise (or sometimes called “resting noise”) was determined in this research as the sum of the fluctuation of measurement baseline and the amplitude of the Rheoencephalographic signal (REG). The experimental result shows that the fast and the slow fluctuation of measurement baseline were approximately 0.013% and 0.064% respectively. While the REG amplitude was 0.146%. Therefore, the detectable amplitude of investigated response should be

larger than the sum of the baseline fluctuation and the REG amplitude, i.e. between 0.159% for the fast change, and 0.21% for the slow change.

Three types of stimulation were investigated: auditory startle response (ASR), CO_2 reactivity response, and Transient Hyperaemic Response (THR). However, to investigate these responses with EIT measurements, we must be aware that a change in conductivity of a certain region can induce change on all boundary measurements even though these measurements are far from the region having the change. According to the simulation in this research (Section 6.1), in order to localise a conductivity change by boundary measurements, all poor sensitivity measurements should be ignored. Among the remaining measurements based on the same current pattern, the measurements where the change of voltage amplitude is less than 35% of the maximum change also should be ignored, since they could be "false responses" (Section 6.1). In other words, even the small change on the measurements is noticeable, it may be no conductivity change near the measured region.

In the case of ASR, three components were found in the response: N1, P2, and N2. 50% of the trials displayed the component N1 (determined on the near-ear measurement sites) which is attributed to the N100 component of EEG response characteristic (Section 6.2.2). The latency of this N1 component was 147 ms, close to the EEG N100 latency (about 100 ms). This suggests that the N1 response is a neuronal response. The amplitude of N1 was -0.30%, i.e. the conductivity was increased. Two further components were found (P2 and N2) which could be the haemodynamic response. This is because their latencies were much slower (1.94 s and 2.89 s respectively) than the latency of the EEG P200 (about 200 ms) and also the amplitude of N2 was much larger (-0.61%) than that of N1. However, only 32% of the trials found P2 and only 24% found N2. This indicates that the frequency of occurrence of the haemodynamic response is lower than that of the neuronal response. Additionally, although these components were found at the forehead and near the eyelids, the response may be influenced by the face muscles. This is because substantial drift was found on the forehead site, and the latencies of P2 and N2 at the eyelid sites were significantly different to those at the ear sites. The amplitude of the change at the eyelid sites of N2 was inconsistent among the trials in voltage polarity

as well. In the case of the response at the rear head site, there is no reliable evidence to confirm that the change emerged.

In the situation of CO_2 reactivity response where CBF was increased during CO_2 breathing, the manner of conductivity change should be global, i.e. the change can be consistently observed at any position inside the cranium. The conductivity change should be sufficiently large to measure. However, according to the experimental results (Section 6.2.3), the four chosen EIT measurements showed inconsistent change. The amplitude of voltage measurement changes was very varied: between -1.24% and +2.25% during the breathing of CO_2, and between -1.78% and 0.63% after the breathing. When converting the measurement data to bulk conductivity data (Chapter 3), 50% of the trials during the breathing of CO_2 were successful to show the expected increase of bulk conductivity, although only 38% were successful to show the return of conductivity. This raises two questions: 1) Why was EIT measurements unable to detect the expected change with 100% success even when the change was large? and 2) Why were many local changes obtained from EIT measurements different to the global change obtained from TCD? The answers to these questions could be: this uncorrelated behaviour may be true due to the complicated mechanism of the reactivity, the subject movement, or the effect of the heart rate changing which may somehow influence the blood volume in the scalp. The change in the scalp could be more profound than the expected-to-detect change that occurred inside the cranium. However, these questions require further investigation.

In the case of THR, the change was generated locally. The characteristic of the EIT change found from two side-occlusion trials was similar to the TCD measurement with 87% consistency at the ear sites (Section 6.2.4). The correspondence of the left and the right occlusion was also very good. The conductivity decreased on the occlusion side and slightly increased on the non-occlusion side. However, the changing manner on the eye sites was exceptional. The conductivity was always found to be decreased, even when the occlusion side was changed. During the occlusion period, the changing amplitude of the measurements was 0.24% at the occlusion side and 0.15% at the non-occlusion. Whilst, after the

occlusion, all sites were almost completely returned (remaining -0.03% can be detected), except for the non-occlusion side i.e. the reverse change emerged with 0.16% change.

In summary, EIT is able to detect evoked responses if the amplitude of the desired responses is sufficiently large and the amplitude of undesired responses is sufficiently small. More specifically, the desired response should be more profound than the combination of REG and usual fluctuation of the measurement baseline. Since the sum of the amplitude of REG and the baseline fluctuation obtained from the experiments was 0.21%, this number should be the minimum amplitude of desired response to stimulation. Furthermore, the extracted signal also needs to be examined to ensure it is not "false response". The response where the amplitude of the voltage measurement changes seems sufficiently large is not necessarily the response from the brain. It could originate from the change in the scalp.

Regarding the results of the stimulation experiments where a small voltage change is expected, ASR (producing 0.30% voltage change) was able to be detected with 50% success rate. The success rate was superior on THR case, 87%, even though the amplitude of the voltage change was not significantly different to that of the ASR case. This is probably due to the nature of haemodynamic change being larger in volume. In the case of CO_2 reactivity response where the voltage change is larger than the previous two cases, the patterns of measurement voltages change were generally inconsistent with the expected behaviour. Only 50% and 38% of the trials during and after the breathing of CO_2 were consistent with the expected behaviour. This may be caused by the subject movement during experimenting.

Chapter 7 Reconstructed Images of Evoked Responses

In this chapter, the proposed nonlinear difference imaging approach was used to reconstruct experimental data of REG, ASR, THR, and CO_2 reactivity response. A generic model containing 208,311 elements was chosen. The region of non-interest was imposed to the skull region. The summary of reconstruction settings can be found in the Appendix I.6.

7.1 Reconstructed Images of Rheoencephalographic Signal

A sample set of reconstructed images of Rheoencephalography (REG) is shown in Figure 7-1. The changing behaviour in conductivity among two trials (on one subject) were 100% consistent. The conductivity was decreased at the frontal region at the peak of REG and returned to normal later on.

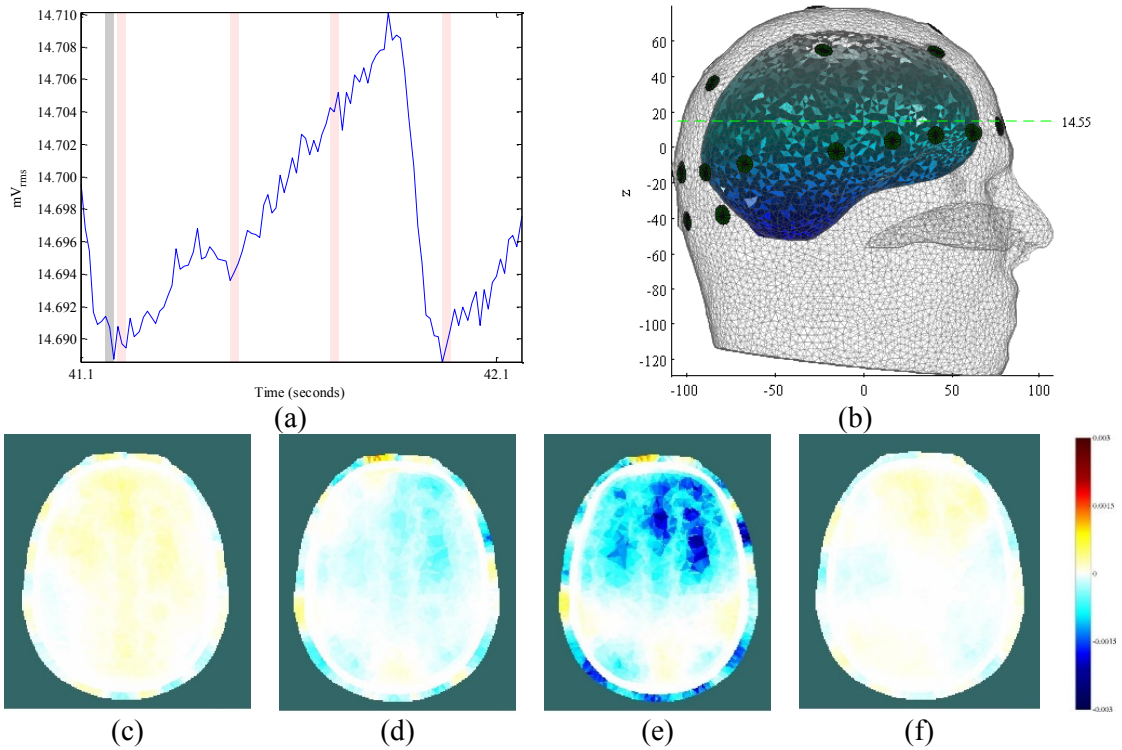

Figure 7-1 Difference EIT imaging of REG over a REG cardiac cycle measured with the 1 mA_{rms} version of fEITER. A measurement performed near the left ear site is shown in (a). The grey highlighted area is the reference period of the images. The red highlighted areas, from the left to the right, are the input data of the reconstructed image (c) – (f) respectively (the top of the images is the location of subject's forehead). The red and the blue colour of images denote the increase and the decrease of conductivity respectively. The image plane for (c) – (f) is shown in (b). All measured data were averaged over 30 ms i.e. the effective imaging speed was reduced to 33.33 fps.

7.2 Reconstructed Images of Evoked Responses

7.2.1 Auditory Startle Response (ASR)

The example images of auditory startle response (ASR) are shown in Figure 7-2 and Figure 7-3. The change in conductivity can be observed at the front, the left, and the right side after a few hundred milliseconds from the stimulation onset (N1 component). Surprisingly, although the N1 component can be observed in only 50% of the measurements (Section 6.2.2), the change at the left and/ or the right ear region can be observed in 82% of the images for the 17 trials (on four subjects). This discrepancy could be due to the very small change in the measurement voltage which was very difficult to notice by manual inspection. A good example is shown in Figure 7-3(b). The peak of N1 cannot be observed on the left measurement, like it does on the front measurement which can be clearly seen (see circles on Figure 7-3(a) and (b)). Meanwhile, a slight increase in conductivity in the brain region can be seen at the left side of the image (Figure 7-3(c)).

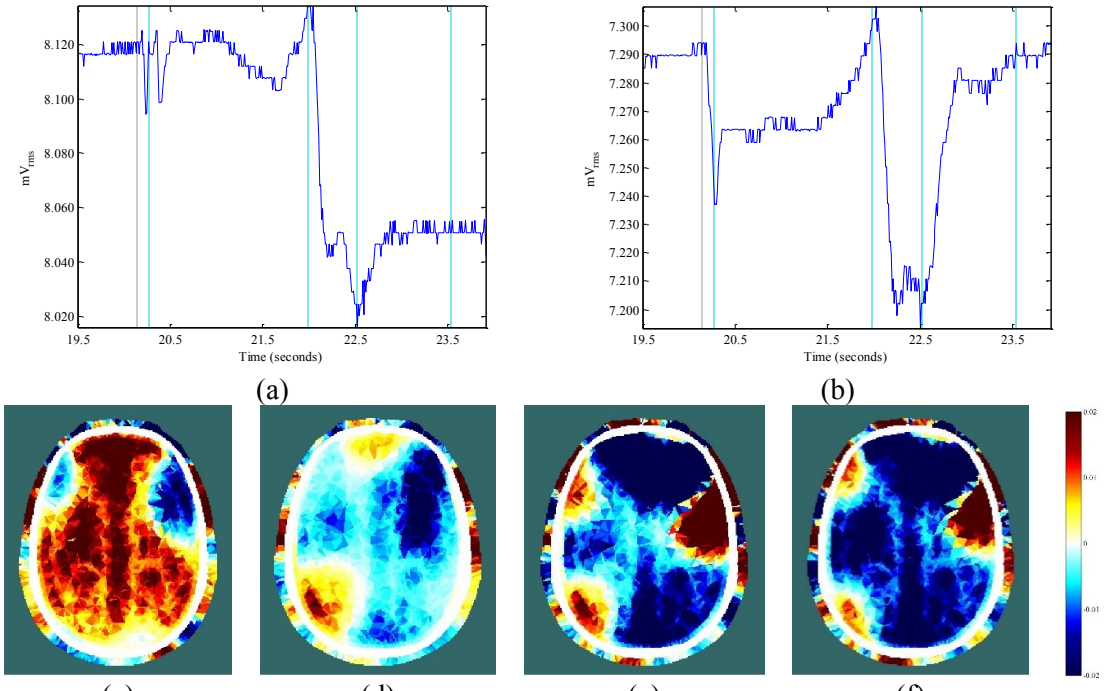

Figure 7-2 Difference EIT imaging of ASR (of the example data shown in Figure 6-5) measured with the 1 mA_{pk-pk} version of fEITER. Measurements performed near the left and the right ear sites are shown in (a) and (b) respectively. The grey highlighted areas indicate the stimulation time (at 20.13 s). The light blue highlighted areas, from the left to the right, indicate the presence time of N1 (at 20.26 s), P2 (at 21.97 s), and N2 (at 22.51 s), and the returning time (at 23.53 s). The images of these times are shown in (c) to (f) respectively. All measured data were averaged over 30 ms.

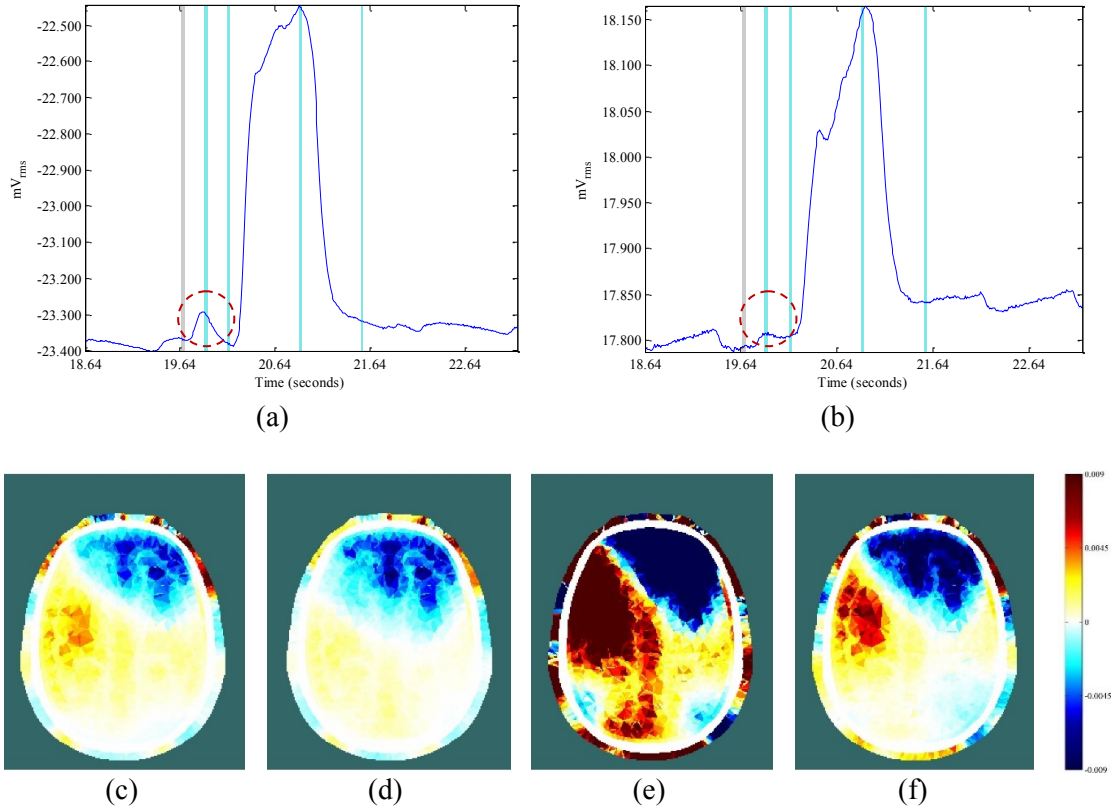

Figure 7-3 Difference EIT imaging of ASR (of the example data shown in Figure 6-6) measured with the 1 mA_{rms} version of fEITER. Measurements performed on the forehead (reversed polarity) and near the left ear site are shown in (a) and (b) respectively. The grey highlighted areas indicate the stimulation time (at 19.66 s). The light blue highlighted areas, from the left to the right, indicate the presence time of N1 (at 19.89 s), P2 (at 20.14 s), and N2 (at 20.89 s), and the returning time (at 21.55 s). The images of these times are shown in (c) to (f) respectively. All measured data were averaged over 30 ms.

Although the changing manner of conductivity during N1 was consistent with the expected activation regions as in Section 2.4.1, the cause for the change in the frontal region remains unclarified. They could be either due to the brain or the face muscle movement. Only 65% of the trials show the change in the frontal region while 12% of those do not show the left and the right ear change. The changing manner of conductivity during N2, where the response amplitude is usually larger, seemed to be similar to that of N1 with 82% consistency (determined only from the change at the left and the right ear sites). However, the large conductivity change has been clearly identified in only certain regions of the images.

7.2.2 CO_2 Reactivity Response

The images of CO_2 reactivity response on eight trials (on seven subjects) were reconstructed, and some images are shown in Figure 7-4 and Figure 7-5. In general, the locations of change were very inconsistent among the images of eight trial-data. During CO_2 breathing, the increase in conductivity can be observed in the frontal region in 37.5% of the trials, in the rear region in 50%, and in both ear side regions in 12.5%. Meanwhile, after the end of the CO_2 breathing period for approximately 40 seconds, no sign of the brain returning to the pre-stimulus state can be seen in any images of Phase 4. More specifically, the response locations observable in Phase 2 were still observable in the same locations in Phase 4. Based on these results, EIT looks unlikely to monitor the stimulus.

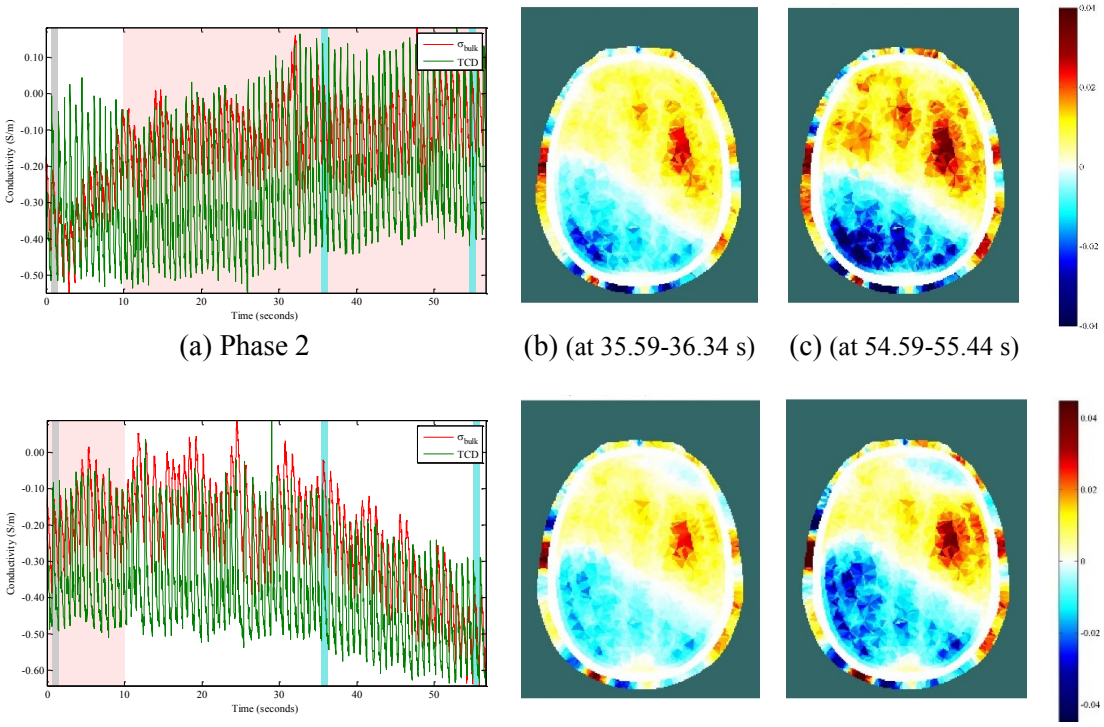

(a) Phase 2 (b) (at 35.59-36.34 s) (c) (at 54.59-55.44 s)

(d) Phase 4 (e) (at 35.44-36.36 s) (f) (at 54.97-55.85 s)

Figure 7-4 Difference EIT imaging of CO_2 reactivity response (of the positive example data shown in Figure 6-12(a)-(b)) measured with the 1 mA_{pk-pk} version of fEITER. The bulk conductivity and TCD measurement are shown in (a) and (d). The top row is the results of Phase 2, and the bottom row is the results of Phase 4. The light red highlighted areas indicate the period of breathing 5%-CO_2. The grey highlighted areas are the reference periods of reconstruction (at 0.7-1.5 s). The light blue highlighted areas are the interested periods which were used to reconstruct the images in (b)-(c) and (e)-(f): (b) and (e) are at about 35 s after the beginning of each phase, (c) and (f) are at about 55 s after the beginning of each phase. All measured data were averaged over 30 ms.

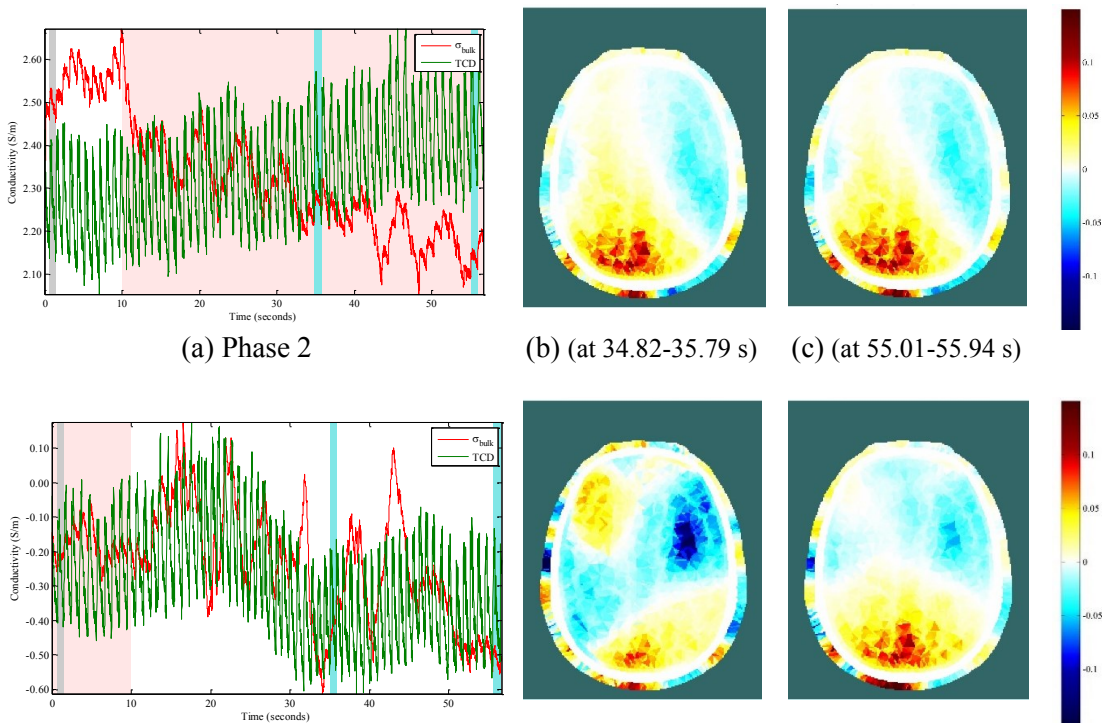

(a) Phase 2 (b) (at 34.82-35.79 s) (c) (at 55.01-55.94 s)

(d) Phase 4 (e) (at 35.01-35.81 s) (f) (at 55.54-56.48 s)

Figure 7-5 Difference EIT imaging of CO_2 reactivity response (of the negative example data shown in Figure 6-12(c)-(d)) measured with the 1 mA_{pk-pk} version of fEITER. The bulk conductivity and TCD measurement are shown in (a) and (d). The top row is the results of Phase 2, and the bottom row is the results of Phase 4. The light red highlighted areas indicate the period of breathing 5%-CO_2. The grey highlighted areas are the reference periods of reconstruction (at 0.7-1.5 s). The light blue highlighted areas are the interested periods which were used to reconstruct the images in (b)-(c) and (e)-(f): (b) and (e) are at about 35 s after the beginning of each phase, (c) and (f) are at about 56 s after the beginning of each phase. All measured data were averaged over 30 ms.

7.2.3 Transient Hyperaemic Response (THR)

The example images of transient hyperaemic response (THR) are shown in Figure 7-6 and Figure 7-7. During the occlusion period, the decrement of conductivity can be obviously seen on the occlusion side, with a corresponding increment of conductivity on the non-occlusion side. This response is consistent with what was reported in (Durduran and Yodh, 2014, Shang et al., 2011). Regarding the reconstructed images obtained from 17 trials (on five subjects), 76% of the trials conformed to the above observation. This percentage value was a little lower than the percentage of the measurement consistency of 87% found in Section 6.2.4.

After the occlusion was released, the image magnitude of the change on the occlusion and the non-occlusion side was decreased to very low level, in 59% of the

trials. 18% of the trials showed the increment of conductivity on the occlusion side, with a corresponding decrement of conductivity on the non-occlusion side (this behaviour was opposite to the behaviour during the occlusion). The remaining 24% of trials showed the increase of magnitude on both sides instead. The latter changing behaviour was not expected. It was probably caused by the poor electrode attachment or the large different geometry between the subject head and the generic model. This presumption is plausible because all trials resulting in this unexpected behaviour were carried out on the same date and were obtained from the same subject.

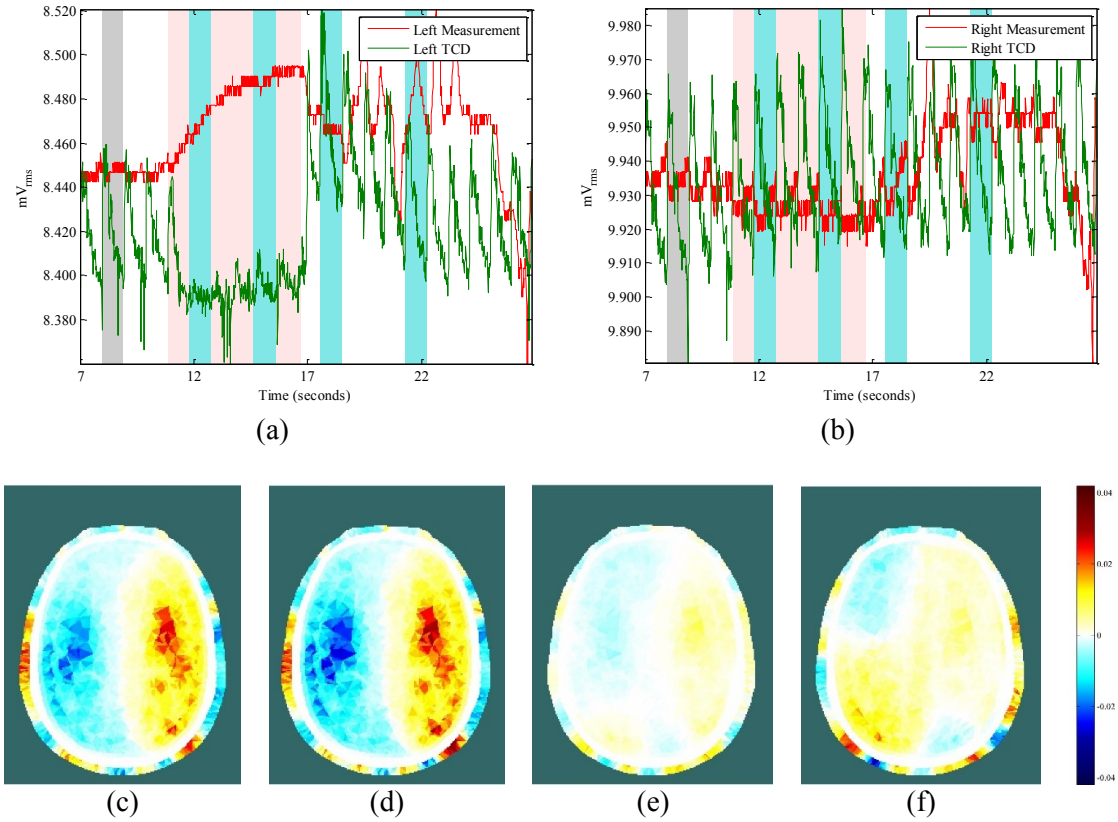

Figure 7-6 Difference EIT imaging of THR (of the example data shown in Figure 6-16 and Figure 6-17) – left occlusion, measured with the 1 mA_{pk-pk} version of fEITER. Measurements performed near the left and the right ear sites are shown in (a) and (b) respectively. The light red highlighted areas indicate the period of occlusion (at 11.01-16.82 s). The grey highlighted areas are the reference periods of reconstruction (at 8.12-9.04 s). The light blue highlighted areas, from the left to the right, are the interested periods which were used to reconstruct the images in (c) – (f) respectively. All measured data were averaged over a REG cardiac cycle i.e. the effective imaging speed was reduced to about 1 fps.

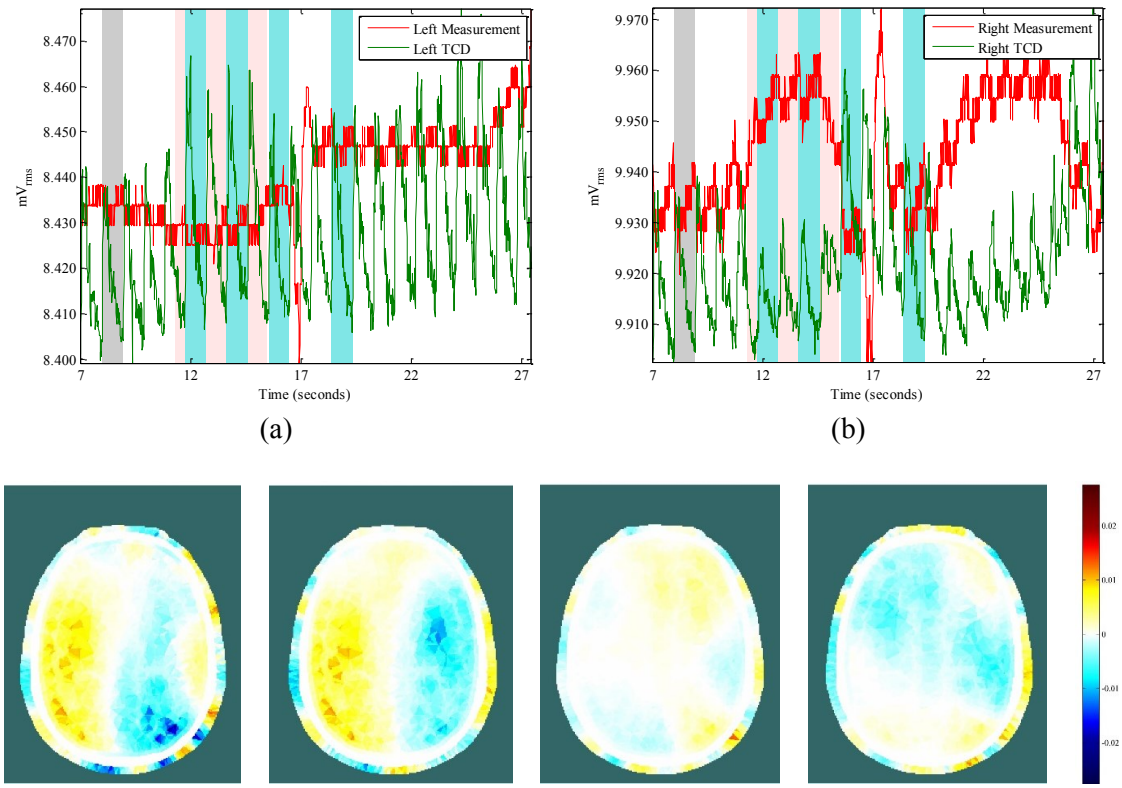

Figure 7-7 Difference EIT imaging of THR (of the example data shown in Figure 6-18 and Figure 6-19) – right occlusion, measured with the 1 mA_{pk-pk} version of fEITER. Measurements performed near the left and the right ear sites are shown in (a) and (b) respectively. The light red highlighted areas indicate the period of occlusion (at 10.86-15.02 s). The grey highlighted areas are the reference periods of reconstruction (at 7.56-8.49 s). The light blue highlighted areas, from the left to the right, are the interested periods which were used to reconstruct the images in (c) – (f) respectively. All measured data were averaged over a REG cardiac cycle.

7.3 Magnitude of Conductivity Change towards REG and Evoked Responses

Apart from the pattern of conductivity changes due to the REG and the evoked responses explained in the previous sections, the magnitude of the conductivity change is also very useful knowledge to determine the possibility of detecting the change, even though the changes may not be associated just with the brain. The magnitude of conductivity change in the reconstructed images can be imprecise due to the fact that image magnitude can be much smaller than the true conductivity by at least eight times (Section 5.3.1). Furthermore, the image

magnitude depends on the degree of regularisation as well. The individual values of the magnitude of the changes shown in Table 7-1 are only to integrate the relative change between tissues under the studies in this research. They should not be used as nominal tissue values.

The magnitude of the change in each tissue regions is evaluated independently in this research. The maximum conductivity change within the period of investigation was used as the response magnitude. In the case of the REG, the images of a REG cardiac cycle were investigated. In the case of the evoked responses, the origins of the change could be either due to neuronal response or haemodynamic response which is larger in magnitude, but slower latency. The investigation in this case then was focused on the period beginning from when the stimulus was delivered to when the response returned to be almost steady.

Table 7-1 Magnitude of conductivity change (in percentage) of REG and evoked responses occurring in different tissues

Tissues	The magnitude of conductivity change of the evaluated REG and evoked responses (mean±standard deviation in %)			
	REG (2 trials, 1 subject)	ASR (17 trials,4 subjects)	CO_2 inhalation (8 trials, 7 subjects)	THR (17 trials, 5 subjects)
Scalp	1.07%	11.85±12.23%	61.28±69.73%	22.54±17.22%
CSF	0.06%	0.74± 0.76%	3.73± 3.99%	1.38± 1.06%
Grey matter	1.17%	8.08± 7.79%	46.99±54.38%	22.91±21.59%
White matter	1.05%	7.35± 8.08%	41.11±46.58%	20.09±18.21%

The summary of magnitudes of conductivity change (in percentage) is shown in Table 7-1. The magnitude of REG in the brain region (containing grey matter and white matter) was about 1%. In the cases of ASR and CO_2 reactivity, the conductivity changes in the scalp were 30-60% larger than the changes occurring in the brain region. Meanwhile in THR case, the conductivity changes in the scalp region were approximately similar to the change occurring in the brain region. This indicated that the conductivity change in the scalp of the THR case was smaller (in ratio) than the other cases. The conductivity changes in the CSF region were only 6-10% of the changes in the brain region in all brain stimulation cases. The changes in the brain region in the ASR case were three and six times smaller than those in the

case of THR and CO_2 reactivity respectively. When comparing the measurement voltage change found in Chapter 6, the summary is shown in Table 7-2.

Table 7-2 Summary of observed changes on the measurements and the reconstructed images

Types of responses	Measurement traces		Reconstructed images		
	Amplitude	Consistency	Magnitude(1)	Consistency	Locations of the changes
REG	0.14%	100%	1.17%	100%	The change was at the front.
ASR	0.30% (at N1)	50%	8.08%	82.35%	The change was at the left, the right, and the front regions.
CO_2	2.25% (during the breathing of CO_2)	Phase 2: 50% Phase 4: 37.50%	46.99%	Phase 2: 50% Phase 4: 0%	The conductivity increase was mostly at the front and the rear region during CO_2 breathing. However, no sign of conductivity returning after the end of CO_2 breathing.
THR	0.24% (during occlusion)	86.81%	22.91%	76.47%	The conductivity was decreased on the occlusion side and increased on the non-occlusion side during occlusion.

(1) The magnitudes of the conductivity change in the grey matter region

7.4 Discussion and Conclusion

Reconstructed images of Rheoencephalographic signal (REG) and the three types of responses; Auditory Startle Response (ASR), CO_2 reactivity response, and Transient Hyperaemic Response (THR), are shown in this chapter. Even though the signal analyses of Chapter 6 on these responses on scalp measurement can help, to some extent, interpreters to perceive what is occurring inside the head, image reconstruction is still of interest as a diagnostic tool. The reliability of these images still needs to be investigated further.

In the reference period, when there is no stimulation, any changes occurring are mainly associated to REG. The images of REG were reconstructed here (Section 7.1). The decrease in conductivity of 1% in the frontal region of the brain can be observed with 100% consistency in all cases. In the case of ASR, the reconstructed images during the period of N1 component showed that the positive changes in

conductivity were at the frontal, the left and the right regions (Section 7.2.1) with 82% consistency. The identified locations of the changes and the trend were in agreement with the regions reported in many studies (Billings et al., 2009, Cosmo et al., 2004, Garrido et al., 2009, Klivington and Galambos, 1968, Walsh et al., 2005). However, 35% of the trials did not detect the change in the frontal region. This may indicate that the frontal region was not the primary region to respond to the simulation. Meanwhile, the locations of change during the period of the N2 component were generally similar to the N1, but the magnitude of the change was larger. 18% of the trials showed different behaviour during N2. Therefore, the larger and the slower responses during N2 probably indicate that they were the haemodynamic response, and the behaviour of this response was more complex than that of the response during N1. In other words, even though the consequence of the neuronal response, i.e. haemodynamic response, can be used to localise the change, the consistency was decreased by at least 18%.

When the magnitude of the change was as large as in the case of CO_2 reactivity, the localisation was expected to be significantly improved with very high consistency. The reconstructed images showed the magnitude of the change of this case was six times larger than those of ASR (Section 7.3). In fact, in the case of CO_2 reactivity, the consistency was very low at 37.50% at the frontal region, 50% at the rear, and 12.50% at the left and the right regions, during the breathing of CO_2 (Section 7.2.2). The change occurring during the breathing did not return to the pre-stimulus state after the end of CO_2 breathing in all cases. This may be due to the change in the scalp tissue rather than the change inside the cranium. Therefore, the expectation at the beginning was not realised in this case. The large conductivity change occurring in the brain may coexist with a large (or even larger) change in the scalp or other tissues. In this circumstance, the brain changes cannot be reconstructed because of the overwhelming effect of physiological noise. This leads us to conclude that EIT is not suitable for CO_2 reactivity response study.

The reconstructed images from the THR test seem the most suitable to EIT to observe cerebral blood intervention. The consistency of the measurement and that of the reconstructed images were both quite high: 87% for the measurement (Section

6.2.4) and 76% for the changing in the reconstructed images (Section 7.2.3). The magnitude of the change of the reconstructed images was also large, i.e. three times larger than that of the ASR case (Section 7.3). Furthermore, the nature of this type of stimulation is less affected by subject movement. During the occlusion, the decrease of conductivity is clearly observable at the occlusion side, and a considerable increase can be observed at the non-occlusion side. However, the conductivity pattern after releasing the occlusion was inconsistent. This might have been caused by experimental or modelling errors, as all of the dubious images were reconstructed from the data of the same subject and on the same date.

In addition, considering the changing behaviour of the images of REG, it could be presumed that the changing in the frontal region can occur more easily than others. Since it is unclear whether the source of the conductivity change in REG originated from inside the cranium or scalp (or face muscles), the emphasis of the investigation was shifted from the frontal region. This statement is supported by the inconsistency of the conductivity change in the frontal region in the THR case.

Additionally, according to all images shown in this chapter, the reconstruction algorithm and its settings used in this study performed with sufficient quality. To specifically identify the location of the change is still very difficult. This is probably due to the use of the smoothness prior which blurs the image. The changing volume reconstructed in the images was 20-30% of the head's total volume, which is probably a bit too large, in light of various images from other modalities, such as BOLD fMRI.

Chapter 8 Conclusion and Future Work

8.1 Conclusion

Implementing EIT on brain applications is widely acknowledged to be exceptionally difficult. An accurate subject model and accurate head tissue conductivities are required. The EIT instrument must be able to detect small physiological voltage change. The reconstruction algorithm used should be able to deal with large modelling error and noise, as well as the limit of computational memory. Most importantly, EIT verification on real head applications is required.

In this thesis, several head models with the inclusion of electrode geometry were carefully constructed. The use of non-subject models caused up to 18% increase of measurement prediction error. The inclusion of electrode geometry was able to reduce the prediction error by 4%. It was also found that the mesh resolution of the models did not significantly improve the prediction error, i.e. less than 1% improvement.

Two important tissue conductivities were estimated in vivo: 0.5842 S/m for scalp conductivity and 0.0084 S/m for skull conductivity. The use of other conductivity values reported in literature caused up to 77% increase of measurement prediction error. Careful selection of these conductivities is then very important. Note that in a circumstance when these conductivity values are not available, high value of skull conductivity reported in literature is advisable.

The functional EIT for Evoked Response (fEITER) system was verified for its capability for head applications. Some modifications of the fEITER system were carried out in this research. The data readout was changed from 16-bit length to 24-bit length, resulting in the improvement of the system precision of the current circuit and the measurement circuit by 25% and 36% respectively. The truncation error was also reduced by 183 times. Furthermore, the amplitude of excitation current was increased from 1 mA_{pk-pk} to 2 mA_{pk-pk} or 1 mA_{rms}. This resulted in the improvement of measurement sensitivity by at least two times.

Modelling error was found to be a very important cause of reconstruction failure when reconstructing with the absolute imaging approach. A nonlinear difference imaging approach was proposed to deal with the large modelling error. This novel approach in conjunction with the Regularised Newton-Krylov Generalized Minimal Residual reconstruction algorithm (Newton-Krylov GMRes) and the smoothness prior was found suitable for EIT applications on the head. The effect of the modelling error and the need for large computational memory were substantially reduced. The reconstruction accuracy of this approach depends on the change of conductivity and the accuracy of the model geometry and the conductivities used. The novel approach, along with the evaluated generic reconstruction parameters and a generic head model, has been confirmed to be successful for head EIT applications. However, even using the novel approach, the reconstruction artefacts in the scalp region are notably large. The conductivity change in an image in the scalp region then should be ignored. The magnitude of the conductivity change in the brain region was also found to be much smaller than the true magnitude by at least eight times.

Three types of brain stimulation were investigated in this thesis: auditory startle response (ASR), CO_2 reactivity response, and transient hyperaemic response (THR). In the case of ASR, 50% of the trials were found to show the neuronal response on the voltage measurements, i.e. N1 response component, where the average amplitude was 0.30%, and the average latency was 147 ms. Less than 32% of the trials were found to show the haemodynamic response, i.e. P2 and N2, where the latency was longer than 3 s and the amplitude was larger than 0.61%. When determining from the reconstructed images, 82% of the trials were consistent. The conductivity change was observable in the expected regions, i.e. the left, the right, and the front region. The N1 response observed here is the first neuronal response ever to be reported using EIT. The haemodynamic response is consistent with BOLD data, and is plausible also in the light of the THR data discussed below.

In the case of THR, the average amplitude of the measurement change was 0.24% during the occlusion. The magnitude of the conductivity change was three times larger than that of the ASR case. The consistency of the voltage measurements

and the images among the trials were high and not much different, i.e. 87% and 76% respectively. The behaviour of the conductivity change was in agreement with expectation. During the occlusion period, the decrement of conductivity occurred on the occlusion side with a corresponding increment of conductivity on the non-occlusion side. About 76% of the trials showed return to the pre-occlusion state. This is the first reported observation, by EIT, of the distribution of conductivity change inside the cranium in response to a known mechanical intervention of cerebral blood flow.

In the case of CO_2 reactivity response, the amplitude of the measurement change was 2.25%, and the magnitude of the conductivity change was six times larger than that of the ASR case. Even though the change was large, the consistencies of the voltage measurements and the reconstructed images of all trials were poor, i.e. 50%, during the breathing of CO_2 (Phase 2), and 0-37.5%, after the end of CO_2 breathing (Phase 4). The return of conductivity did not occur at Phase 4 in all trials. Therefore, EIT seems unable to monitor the CO_2 reactivity response, probably due to the subject movement. The change occurring in the scalp during the tests may overwhelm the change inside the cranium

8.2 The Future of EIT on Head Applications

On the basis of the above work, it is arguable that, EIT is only suitable for certain types of brain applications. ASR and THR are possible applications: ASR is suitable for neurophysiological study; THR is suitable for cerebral blood flow examination. However, the localisation information in reconstructed images is very coarse. The future of EIT for head applications seems not to be in the hand of reconstruction engineers or hardware designers anymore, but rather in the hand of medical practitioners to determine whether these coarse images are sufficiently informative, or not. On the other hand, EIT has high temporal resolution which could be further improved in the future. The real-time imaging of the brain in the order of a few hundred microseconds seems impractical as brain activity occurs at very high speed. However, to cope with many data frames, fast reconstruction algorithms are necessary. Therefore, in the future, EIT improvements can be developed through the

collaboration with medical practitioners on only specific brain applications. The consolidation of EIT images with reliable technologies, e.g. fMRI, is necessary. Novel reconstruction methodologies are still required for better spatial resolution and better reconstruction speed. EIT, unfortunately, appears not to be ready yet for routine clinical applications on the head.

8.3 Future Work

The further development of brain EIT requires close collaboration with neurologists. Additional types of brain responses such as visual evoked response (VER) should be investigated with the modified fEITER system. The periodic stimulation such as auditory evoked response (AER) should also be performed. The impact of the physiological change in scalp should be further investigated as well.

Reconstruction improvement is another imperative task which must be carried out in parallel. Measurement signal filtering and image post-filtering could be utilised to obtain more precise source localisation. Other kinds of prior information e.g. total variation prior (TV prior) could be a possible option to improve the spatial resolution of reconstructed images. The principle of dual models to improve the computational time is attractive. Furthermore, the anisotropic model, and/or the second-order finite element model are also worthwhile studying to reduce the impact of modelling error.

Even though the hardware improvement did not qualitatively improve the outcome of EIT in this research, this statement is based on a single frequency system. The lower excitation frequency theoretically leads to a larger response, which should increase the possibility of detecting the conductivity change of EIT. However, the change to use a new frequency leads to a new problem. This is because the tissue conductivities will be changed, the response amplitude will be altered, the sensitivity could be changed in the different scale on different kinds of tissues, and the noise amplitude and the behaviour of physiological noise could be different to the currently used frequency. Will multi-frequency EIT (MFEIT) be successful on head applications? Significant further investigations are required.

References

Abascal, J.-F. P. J., Arridge, S. R., Atkinson, D., Horesh, R., Fabrizi, L., Lucia, M. D., Horesh, L., Bayford, R. H. and Holder, D. S. (2008a) 'Use of anisotropic modelling in electrical impedance tomography; Description of method and preliminary assessment of utility in imaging brain function in the adult human head', *NeuroImage,* 43(2), pp. 258-268.

Abascal, J.-F. P. J., Arridge, S. R., Bayford, R. H. and Holder, D. S. (2008b) 'Comparison of methods for optimal choice of the regularization parameter for linear electrical impedance tomography of brain function', *Physiol. Meas.,* 29, pp. 1319–1334.

Abascal, J.-F. P. J., Arridge, S. R., Lionheart, W. R. B., Bayford, R. H. and Holder, D. S. (2007) 'Validation of a finite-element solution for electrical impedance tomography in an anisotropic medium', *Physiol. Meas. ,* 28, pp. S129–S140.

Adler, A. 'Variability in EIT Images of Lungs: Effect of Image Reconstruction Reference '. *The 12th International Conference on Electrical Bio-impedance and the EIT- ICEBI04*, Poznan, Poland, 20–24 June 2004.

Adler, A., Gaggero, P. O. and Maimaitijiang, Y. (2011) 'Adjacent stimulation and measurement patterns considered harmful', *Physiol. Meas. ,* 32, pp. 731-744.

Adler, A. and Guardo, R. (1996) 'Electrical Impedance Tomography: Regularized Imaging and Contrast Detection', *IEEE Transactions on Medical Imaging,* 15(2), pp. 170-179.

Adler, A. and Lionheart, W. R. B. (2006) 'Uses and abuses of EIDORS: an extensible software base for EIT', *Physiol. Meas. ,* 27, pp. S25–S42

Ahsan, S. T. (2010) *Low noise electrical impedance tomography for sub-second brain function imaging wiht real time current monitoring.* PhD thesis, The University of Manchester.

Ahsan, S. T. and McCann, H. 'Ensuring safe EIT operation on human subjects', *Proc. IXth International Conference on Electrical Impedance Tomography*, Hanover, NH, USA. 2008, 83-86.

Akhtari, M., Bryant, H. C., Mamelak, A. N., Flynn, E. R., Heller, L., Shih, J. J., Mandelkern, M., Matlachov, A., Ranken, D. M., Best, E. D., DiMauro, M. A., Lee, R. R. and W.W.Sutherling (2002) 'Conductivities of Three-Layer Live Human Skull', *Brain Topography,* 14(3), pp. 151-167.

Akhtari, M., Bryant, H. C., Mamelak, A. N., Heller, L., Shih, J. J., Mandelkern, M., Matlachov, A., Ranken, D. M., Best, E. D. and Sutherling, W. W. (2000) 'Conductivities of Three-Layer Human Skull', *Brain Topography,* 13(1), pp. 29-42.

Anas, M. N., Norali, A. N. and Rehman, M. 'Development of a low cost precision blood resistivity measurement device based on Thompson Lampard Theorem', *2012 International Conference on Biomedical Engineering (ICoBE)*, Penang, 27-28 February 2012.

Aristovich, K. Y., Santos, G. S. d., Packham, B. C. and Holder, D. S. (2014) 'A method for reconstructing tomographic images of evoked neural activity with electrical impedance tomography using intracranial planar arrays', *Physiol. Meas.,* 35, pp. 1095–1109.

Arridge, S. R., Kaipio, J. P., Kolehmainen, V., Schweiger, M., Somersalo, E., Tarvainen, T. and Vauhkonen, M. (2006) 'Approximation errors and model reduction with an application in optical diffusion tomography', *Inverse Problems* 22, pp. 175-195.

Bagshaw, A. P., Liston, A. D., Bayford, R. H., Tizzard, A., Gibson, A. P., Tidswell, A. T., Sparkes, M. K., Dehghani, H., Binnie, C. D. and Holder, D. S. (2003) 'Electrical impedance tomography of human brain function using reconstruction algorithms based on the finite element method', *Neuroimage,* 20(2), pp. 752-764.

Barber, D. C. and Brown, B. H. (1984) 'Applied potential tomography', *J. Phys. E: Sci. Instrum,* 17, pp. 723-733.

Bashar, R., Li, Y. and Wen, P. 'A Study of white matter and skull inhomogeneous anisotropic tissue conductivities on EEG forward head modeling', *11th International Conference on Computer and Information Technology - ICCIT 2008*, Khulna, Bangladesh, 24-27 Dec. 2008.

Baumann, S. B., Wozny, D. R., Kelly, S. K. and Meno, F. M. (1997) 'The Electrical Conductivity of Human Cerebrospinal Fluid at Body Temperature', *IEEE transactions on biomedical engineering,* 44(3), pp. 220-223.

Bayford, R. H., Boone, K. G., Hanquan, Y. and Holder, D. S. (1996) 'Improvement of the positional accuracy of EIT images of the head using a Lagrange multiplier reconstruction algorithm with diametric excitation', *Physiol. Meas. ,* 17, pp. A49–A57.

Baysal, U. and Haueisen, J. (2004) 'Use of a priori information in estimating tissue resistivities—application to human data in vivo', *Physiol. Meas. ,* 25 pp. 737-748.

Billings, C. J., Tremblay, K. L., Stecker, G. C. and Tolin, W. M. (2009) 'Human evoked cortical activity to signal-to-noise ratio and absolute signal level', *Hearing Research* 254, pp. 15-24.

Blad, B. and Baldetorp, B. (1996) 'Impedance spectra of tumour tissue in comparison with normal tissue; a possible clinical application for electrical impedance tomography', *Physiol. Meas. ,* 17, pp. A105–A115.

Bodo, M. and Pearce, F. J. 'Rheoencephalography (REG) as a Non-Invasive Monitoring Alternative for the Assessment of Brain Blood Flow', *Paper presented at the RTO HFM Symposium on "Combat Casualty Care in Ground Based Tactical Situations: Trauma Technology and Emergency Medical Procedures"*, St. Pete Beach, USA, 16-18 August 2004: Published in RTO-MP-HFM-109.

Bodo, M., Pearce, F. J., Baranyi, L. and Armonda, R. A. (2005) 'Changes in the intracranial rheoencephalogram at lower limit of cerebral blood flow autoregulation', *Physiol. Meas. ,* 26, pp. S1–S17.

Bodo, M., Pearce, F. J., Montgomery, L. D., Rosenthal, M., Kubinyi, G., Thuroczy, G., Braisted, J., Forcino, D., Morrissette, C. and Nagy, I. (2003) 'Measurement of Brain Electrical Impedance: Animal Studies in Rheoencephalography', *Aviation, Space, and Environmental Medicine,* 74(5), pp. 506-511.

Boone, K. G. (1995) *The possible use of applied potential tomography for imaging action potentials in the brain.* PhD, University College London.

Boone, K. G. and Holder, D. S. (1995) 'Design considerations and performance of a prototype system for imaging neuronal depolarization in the brain using 'direct current' electrical resistance tomography', *Physiol. Meas. ,* 16, pp. A87-A98.

Boone, K. G. and Holder, D. S. (1996) 'Current approaches to analogue instrumentation design in electrical impedance tomography', *Physiol. Meas.,* 17, pp. 229-247.

Bouhamidi, A., Jbilou, K., Reichel, L. and Sadok, H. (2012) 'A generalized global Arnoldi method for ill-posed matrix equations', *Journal of Computational and Applied Mathematics,* 236(8), pp. 2078-2089.

Boyle, A., Borsic, A. and Adler, A. (2012) 'Addressing the computational cost of large EIT solutions', *Physiol. Meas. ,* 33, pp. 787-800.

Brown, B. H. (2001) 'Medical impedance tomography and process impedance tomography: a brief review', *Meas. Sci. Technol.,* 12, pp. 991-996.

Brown, B. H. and Barber, D. C. (1988) 'Possibilities and problems of real-time imaging of tissue resistivity', *Clin. Phys. Physiol. Meas.,* 9, pp. 121-125.

Burger, H. C. and Milaan, J. B. v. (1943) 'Measurements of the specific Resistance of the human Body to direct Current.', *Acta Medica Scandinavica,* CXIV(VI).

Calvetti, D. and Somersalo, E. (2007) *Introduction to Bayesian Scientific Computing Ten Lectures on Subjective Computing.* Springer Science+Business Media, LLC.

Cheney, M., Isaacson, D. and Newell, J. C. (1999) 'Electrical Impedance Tomography', *Society for Industrial and Applied Mathematics,* 41(1), pp. 85–101.

Clerc, M., Adde, G., Kybic, J., Papadopoulo, T. e. and Badier, J.-M. (2005) 'In vivo Conductivity Estimation with Symmetric Boundary Elements', *International Journal of Bioelectromagnetism (IJBEM),* 7(1).

Cosmo, G. D., Aceto, P., A.Clemente and Congedo, E. (2004) 'Auditory Evoked Potentials', *Minerva Anestesiol,* 70, pp. 293-297.

Dannhauer, M., Lanfer, B., Wolters, C. H. and Knosche, T. R. (2011) 'Modeling of the human skull in EEG source analysis', *Human Brain Mapping,* 32, pp. 1383-1399.

Davidson, J. L., Little, R. A., Wright, P., Crabb, M., Naish, J., Morgan, A., Parker, G. J. M., Lionheart, W. R. B., Kikinis, R. and McCann, H. 'MRI-informed functional EIT lung imaging', *13th International Conference on Biomedical Applications of Electrical Impedance Tomography*, Tianjin, China, 2012-05-23.

Davidson, J. L., Pomfrett, C. J. D. and McCann, H. 'Predicted EIT current densities in the brain using a 3D anatomically realistic model of the head', *13th International Conference on Electrical Bioimpedance and the 8th Conference on Electrical Impedance Tomography - ICEBI 2007 and IFMBE Proceedings*, 376-379.

Davidson, J. L., Wright, P., Ahsan, S. T., Robinson, R. L., Pomfrett, C. J. D. and McCann, H. (2010) 'fEITER – a new EIT instrument for functional brain imaging', *Journal of Physics: Conference Series 224 (2010) 012025*.

Dehghani, H. and Soleimani, M. (2007) 'Numerical modelling errors in electrical impedance tomography', *Physiol. Meas. ,* 28, pp. S45–S55.

Dehghani, H., Soni, N., Halter, R., Hartov, A. and Paulsen, K. D. (2005) 'Excitation patterns in three-dimensional electrical impedance tomography', *Physiol. Meas. ,* 26, pp. S185–S197.

Dowrick, T., Santos, G. S. D., Vongerichten, A. and Holder, D. (2015) 'Parallel, multi frequency EIT measurement, suitable for recording impedance changes during epilepsy', *Journal of Electrical Bioimpedance,* 6, pp. 37-43.

Durduran, T. and Yodh, A. G. (2014) 'Diffuse correlation spectroscopy for non-invasive, micro-vascular cerebral blood flow measurement', *NeuroImage,* 85, pp. 51-63.

Elazar, Z., Kado, R. T. and Adey, W. R. (1966) 'Impedance changes during epileptic seizures', *Epilepsia,* 7(4), pp. 291-307.

Fabrizi, L., McEwan, A., Oh, T., Woo, E. J. and Holder, D. S. (2009) 'An electrode addressing protocol for imaging brain function with electrical impedance tomography using a 16-channel semi-parallel system', *Physiol. Meas. ,* 30, pp. S85–S101.

Fabrizi, L., McEwan, A., Woo, E. and Holder, D. S. (2007) 'Analysis of resting noise characteristics of three EIT systems in order to compare suitability for time difference imaging with scalp electrodes during epileptic seizures', *Physiol. Meas. ,* 28, pp. S217–S236.

Fabrizi, L., Sparkes, M., Horesh, L., Abascal, J. F. P.-J., McEwan, A., Bayford, R. H., Elwes, R., Binnie, C. D. and Holder, D. S. (2006) 'Factors limiting the application of electrical impedance tomography for identification of regional conductivity changes using scalp electrodes during epileptic seizures in humans', *Physiol. Meas. ,* 27, pp. S163–S174.

Faes, T. J. C., Meij, H. A. v. d., Munck, J. C. d. and Heethaar, R. M. (1999) 'The electric resistivity of human tissues (100 Hz-10 MHz): a meta-analysis of review studies', *Physiol. Meas. ,* 20, pp. 87-102.

Farquharson, C. G. and Oldenburg, D. W. (2004) 'A comparison of automatic techniques for estimating the regularization parameter in non-linear inverse problems', *Geophys. J. Int. ,* 156, pp. 411-425.

Ferree, T. C., Eriksen, K. J. and Tucker, D. M. (2000) 'Regional head tissue conductivity estimation for improved EEG analysis', *IEEE Transactions on Biomedical Engineering,* 47 (12), pp. 1584-1592.

Foster, K. R. and Lukaski, H. C. (1996) 'Whole-body impedance what does it measure?', *The American Journal of Clinical Nutrition* 64, pp. 388S-396S.

Frerichs, I., Pulletz, S., Elke, G., Gawelczyk, B., Frerichs, A. and Weiler, N. (2011) 'Patient examinations using electrical impedance tomography—sources of interference in the intensive care unit', *Physiol. Meas. ,* 32, pp. L1-L10.

Frerichs, I., Scholz, J. and Weiler, N. (2006) *Electrical Impedance Tomography and its Perspectives in Intensive Care Medicine. Yearbook of Intensive Care and Emergency Medicine Volume 2006*, p. 437-447.

Freygang, J. W. H. and Landau, W. M. (1955) 'Some relations between resistivity and electrical activity in the cerebral cortex of the cat', *Journal of Cellular and Comparative Physiology* 45(3), pp. 377-392.

Fu, F., Li, B., Dai, M., Hu, S.-J., Li, X., Xu, C.-H., Wang, B., Yang, B., Tang, M.-X., Dong, X.-Z., Fei, Z. and Shi, X.-T. (2014) 'Use of Electrical Impedance Tomography to Monitor Regional Cerebral Edema during Clinical Dehydration Treatment', *PLOS ONE* 9(12).

Galambos, R. and Velluti, R. (1968) 'Evoked resistance shifts in unanesthetized cats', *Experimental Neurology,* 22(2), pp. 243-252.

Gamache, F. W., Dold, G. M. and Myers, R. E. (1975) 'Changes in cortical impedance and EEG activity induced by profound hypotension', *Am J Physiol. ,* 228(6), pp. 1914-1920.

Gao, N., Zhu, S. A. and He, B. (2005) 'Estimation of electrical conductivity distribution within the human head from magnetic flux density measurement', *Physics in Medicine and Biology,* 50, pp. 2675-2687.

Garrido, M. I., Kilner, J. M., Stephan, K. E. and Friston, K. J. (2009) 'The mismatch negativity: A review of underlying mechanisms', *Clin Neurophysiol,* 120(3), pp. 453-463.

Gazzola, S., Novati, P. and Russo, M. R. (2014) 'On Krylov projection methods and Tikhonov regularization', *Electronic Transactions on Numerical Analysis* 44, pp. 83-123.

Gersch, W. 'Transfer Functions Estimation: A Smoothness Priors Method', *Proceedings of 23rd Conference on Decision and Control* Las Vegas, NV, USA, December 1984.

Gibson, A., Bayford, R. H. and Holder, D. S. (2000) 'Two-dimensional finite element modelling of the neonatal head', *Physiol. Meas. ,* 21, pp. 45-52.

Gilad, O., Ghosh, A., Oh, D. and Holder, D. S. (2009a) 'A method for recording resistance changes non-invasively during neuronal depolarization with a view

to imaging brain activity with electrical impedance tomography', *Journal of Neuroscience Methods* 180, pp. 87-96.

Gilad, O. and Holder, D. S. (2009) 'Impedance changes recorded with scalp electrodes during visual evoked responses: Implications for Electrical Impedance Tomography of fast neural activity', *NeuroImage* 47, pp. 514-522.

Gilad, O., Horesh, L. and Holder, D. S. (2005a) 'Non-Invasive Imaging of Synchronized Neuronal Activity using Low Frequency Electrical Impedance Tomography', *Proceedings of the 3rd European Medical & Biological Engineering Conference (EMBEC 05),* 11(1), pp. 179-182.

Gilad, O., Horesh, L. and Holder, D. S. 'Non-invasive imaging of synchronized neuronal activity using low frequency electrical impedance tomography', *Proceedings of the 3rd European Medical & Biological Engineering Conference (EMBEC 05), IFMBE*, Prague, 179-182.

Gilad, O., Horesh, L. and Holder, D. S. (2007) 'Design of electrodes and current limits for low frequency electrical impedance tomography of the brain', *Med. Bio. Eng. Comput. ,* 45, pp. 621-633.

Gilad, O., Horesh, L. and Holder, D. S. (2009b) 'A modelling study to inform specification and optimal electrode placement for imaging of neuronal depolarization during visual evoked responses by electrical and magnetic detection impedance tomography', *Physiol. Meas. ,* 30, pp. S201–S224.

Giller, C. A. (1991) 'A Bedside Test for Cerebral Autoregulation Using Transcranial Doppler Ultrasound', *Acta Neurochir (Wien)* 108, pp. 7-14.

Gonçalves, S., Munck, J. C. d. and Verbunt, J. P. A. 'In Vivo Measurement of Skull and Brain Resistivities with EIT Based Method and Analysis of SEF/SEP Data', *The 23rd Annual International Conference of the IEEE Engineering in Medicine and Biology Society*, 2001, 1006-1008.

Gonçalves, S., Munck, J. C. d., Verbunt, J. P. A., Heethaar, R. M. and Silva, F. H. L. d. 'In Vivo Measurement of the Brain and Skull Resistivities Using an EIT-Based Method and the Combined Analysis of SEF/SEP Data', *IEEE transactions on biomedical engineering*, SEPTEMBER 2003

1124-1128.

Gonçalves, S. I., Munck, J. C. d., Verbunt, J. P. A., Bijma, F., Heethaar, R. M. and Silva, F. L. d. 'In Vivo Measurement of the Brain and Skull Resistivities Using an EIT-Based Method and Realistic Models for the Head', *IEEE transactions on biomedical engineering*, June 2003

Gooskens, I., Schmidt, E. A., Czosnyka, M., Piechnik, S. K., Smielewski, P., Kirkpatrick, P. J. and Pickard, J. D. (2003) 'Pressure-autoregulation, CO2 reactivity and asymmetry of haemodynamic parameters in patients with carotid artery stenotic disease. A clinical appraisal', *Acta Neurochir* 145, pp. 527-532.

Graham, B. M. and Adler, A. (2006) 'Objective selection of hyperparameter for EIT', *Physiol. Meas. ,* 27, pp. S65–S79.

Griffiths, H. (1988) 'A phantom for electrical impedance tomography', *Clin. Phys. Physiol. Meas. ,* 9, pp. 15-20.

Hadamard, J. 1902. Sur les problèmes aux dérivées partielles et leur signification physique.

Halter, R. J., Hartov, A. and Paulsen, K. D. (2008) 'A Broadband High-Frequency Electrical Impedance Tomography System for Breast Imaging', *IEEE Transactions on Biomedical Engineering* 55(2), pp. 650-659.

Hansen, P. C. (1998) *Rank-Deficient and Discrete Ill-Posed Problems Numerical Aspects of Linear Inversion.* SIAM Society for Industrial and Applied Mathematics.

Harreveld, A. V. and Schadé, J. P. (1962) 'Changes in the electrical conductivity of cerebral cortex during seizure activity', *Experimental Neurology,* 5(5), pp. 383-400.

Hartov, A., Demidenko, E., Soni, N., Markova, M. and Paulsen, K. (2002) 'Using voltage sources as current drivers for electrical impedance tomography', *Meas. Sci. Technol. ,* 13, pp. 1425-1430.

Hirsch, F. G., Texter, E. C., Wood, L. A., Ballard, W. C., Horan, F. E., Wright, I. S., Frey, C. and Starr, D. (1950) 'The Electrical Conductivity of Blood: I. Relationship to Erythrocyte Concentration', *The American Society of Hematology*.

Hoekema, R., Wieneke, G. H., Leijten, F. S. S., Veelen, C. W. M. v., Rijen, P. C. v., G.J.M.Huiskamp, Ansems, J. and Huffelen, A. C. v. (2003) 'Measurement of the Conductivity of Skull, Temporarily Removed During Epilepsy Surgery', *Brain Topography,* 16(1), pp. 29-38.

Holder, D. (1989) 'Impedance changes during evoked nervous activity in human subjects: implications for the application of applied potential tomography (APT) to imaging neuronal discharge', *Clin Phys Physiol Meas.,* 10(3), pp. 267-274.

Holder, D. (1993) *Clinical and Physiological Applications of Electrical Impedance Tomography.* CRC Press

Holder, D. (2005) *Electrical impedance tomography: methods, history and applications.* Bristol: Institute of Physics.

Holder, D. S. (1992a) 'Detection of cerebral ischaemia in the anaesthetised rat by impedance measurement with scalp electrodes: implications for non-invasive imaging of stroke by electrical impedance tomography', *Clin. Phys. Physial. Meas.,* 13(1), pp. 63-75.

Holder, D. S. (1992b) 'Detection of cortical spreading depression in the anaesthetised rat by impedance measurement with scalp electrodes: implications for non-invasive imaging of the brain with electrical impedance tomography', *Clin. Phys. Physiol. Meas. ,* 13(1), pp. 77-86.

Holder, D. S. (1992c) 'Electrical Impedance Tomography (EIT) of Brain function', *Brain Topography,* 5(2), pp. 87-93.

Holder, D. S. (1992d) 'Electrical impedance tomography with cortical or scalp electrodes during global cerebral ischaemia in the anaesthetised rat', *Clin. Phys. Physiol. Meas.,* 13(1), pp. 87-98.

Holder, D. S. and Gardner-Medwin, A. R. (1988) 'Some possible neurological applications of applied potential tomography', *Clin. Phys. Physiol. Meas.,* 9, pp. 111-119.

Holder, D. S., Rao, A. and Hanquan, Y. (1996) 'Imaging of physiologically evoked responses by electrical impedance tomography with cortical electrodes in the anaesthetized rabbit', *Physiol. Meas. ,* 17, pp. A179–A186.

Horesh, L. (2006) *Some Novel Approaches in Modelling and Image Reconstruction for Multi-Frequency Electrical Impedance Tomography of the Human Brain.* PhD thesis, University College London.

Horesh, L., Schweiger, M., Arridge, S. R. and Holder, D. S. (2007) 'Large-Scale Non-Linear 3D Reconstruction Algorithms for Electrical Impedance Tomography of the Human Head', *World Congress on Medical Physics and Biomedical Engineering 2006 IFMBE Proceedings,* 14/6 JC26, pp. 3862-3865.

Horesh, L., Schweiger, M., Bollhöfer, M., Douiri, A., Holder, D. S. and Arridge, S. R. (2005) 'Multilevel Preconditioning for 3D Large-Scale Soft-Field Medical Applications Modelling', *International Journal of Information and Systems Sciences* 2(4), pp. 532-556.

Hossman, K. (1971) 'Cortical steady potential, impedance and excitability changes during and after total ischaemia of cat brain', *Exp. Neurol.,* 32, pp. 163-175.

Hu, L., Wang, H., Zhao, B. and Yang, W. (2007) 'A hybrid reconstruction algorithm for electrical impedance tomography', *Meas. Sci. Technol.,* 18, pp. 813-818.

Kaipio, J. and Somersalo, E. (2007) 'Statistical inverse problems: Discretization, model reduction and inverse crimes', *Journal of Computational and Applied Mathematics* 198, pp. 493-504.

Kaipio, J. P., Kolehmainen, V., Somersalo, E. and Vauhkonen, M. (2000) 'Statistical inversion and Monte Carlo sampling methods in electrical impedance tomography', *Inverse Problems* 16, pp. 1487-1522.

Khambete, N. D., Brown, B. H. and Smallwood, R. H. (2000) 'Movement artefact rejection in impedance pneumography using six strategically placed electrodes', *Physiol. Meas.,* 21, pp. 79-88.

Kim, B. S., Isaacson, D., Xia, H., Kao, T.-J., Newell1, J. C. and Saulnier, G. J. (2007) 'A method for analyzing electrical impedance spectroscopy data from breast cancer patients', *Physiol Meas. ,* 28(7), pp. S237–S246.

Klivington, K. A. and Galambos, R. (1968) 'Rapid Resistance Shifts in Cat Cortex During Click-Evoked Responses', *J Neurophysiol,* 31(4), pp. 565-573.

Koksal, A. and Eyuboglu, B. M. (1995) 'Determination of optimum injected current patterns in electrical impedance tomography', *Physiol. Meas. ,* 16, pp. A99-AI09.

Kolehmainen, V., Schweiger, M., Nissilä, I., Tarvainen, T., Arridge, S. R. and Kaipio, J. P. (2009) 'Approximation errors and model reduction in three-dimensional diffuse optical tomography', *Journal of the Optical Society of America. A, Optics, Image Science, and Vision,* 26(10), pp. 2257-2268.

Kolehmainen, V., Vauhkonen, M., Karjalainen, P. A. and Kaipio, J. P. (1997) 'Assessment of errors in static electrical impedance tomography with adjacent and trigonometric current patterns', *Physiol. Meas.,* 18, pp. 289–303.

Kosterich, J. D., Foster, K. R. and Pollack, S. R. (1983) 'Dielectric permittivity and electrical conductivity of fluid saturated bone', *IEEE Trans. Biomed. Eng,* 30(2), pp. 81-86.

Lai, Y., Drongelen, W. v., Ding, L., Hecox, K. E., Towle, V. L., Frim, D. M. and He, B. (2005) 'Estimation of in vivo human brain-to-skull conductivity ratio from simultaneous extra- and intra-cranial electrical potential recordings', *Clinical Neurophysiology* 116, pp. 456-465.

Latikka, J., Kuurne, T. and Eskola, H. (2001) 'Conductivity of living intracranial tissues', *Phys. Med. Biol. ,* 46, pp. 1611–1616.

Latikkal, J. A., Hyttinen, J. A., Kuume, T. A., Eskola, H. J. and Malmivuo, J. A. 'The conductivity of brain tissues: comparison of results in vivo and in vitro measurements', *Proceedings of the 23rd Annual International Conference of the IEEE Engineering in Medicine and Biology Society*, 910-912.

Law, S. K. (1993) 'Thickness and resistivity variations over the upper surface of the human skull', *Brain topography,* 6(2), pp. 99-109.

Levin, J. M., Frederick, B. d., Ross, M. H., Fox, J. F., Rosenberg, H. L. v., Kaufman, M. J., Lange, N., Mendelson, J. H., Cohen, B. M. and Renshaw, P. F. (2001) 'Influence of baseline hematocrit and hemodilution on BOLD fMRI activation', *Magnetic Resonance Imaging,* 19(8), pp. 1055–1062.

Lionheart, W. R. B. (2004) 'EIT reconstruction algorithms: pitfalls, challenges and recent developments', *Physiol. Meas. ,* 25, pp. 125-142.

Lionheart, W. R. B., Lidgey, F. J., McLeod, C. N., Paulson, K. S., Pidcock, M. K. and Shi, Y. (1997) 'Electrical Impedance Tomography for High Speed Chest Imaging', *Physica Medica,* 13, pp. 247-249.

Liston, A., Bayford, R. and Holder, D. (2012) 'A cable theory based biophysical model of resistance change in crab peripheral nerve and human cerebral cortex during neuronal depolarisation: implications for electrical impedance tomography of fast neural activity in the brain', *Med Biol Eng Comput,* 50, pp. 425-437.

Liston, A. D., Bayford, R. H. and Holder, D. S. (2004) 'The effect of layers in imaging brain function using electrical impedance tomograghy', *Physiol. Meas. ,* 25, pp. 143-158.

Liston, A. D., Bayford, R. H., Tidswell, A. T. and Holder, D. S. (2002) 'A multi-shell algorithm to reconstruct EIT images of brain function', *Physiol. Meas. ,* 23, pp. 105-119.

Liu, D., Kolehmainen, V., Siltanen, S., Laukkanen, A. m. and Seppanen, A. (2015a) 'Estimation of conductivity changes in a region of interest with electrical impedance tomography', *Inverse problems and imaging,* 9(1), pp. 211-229.

Liu, D., Kolehmainen, V., Siltanen, S. and Seppänen, A. (2015b) 'A nonlinear approach to difference imaging in EIT; assessment of the robustness in the presence of modelling errors', *Inverse Problems,* 31.

Liu, N. (2007) *ACT4: A High-Precision, Multi-frequency Electrical Impedance Tomograph.* Ph.D., Rensselaer Polytechnic Institute, United States.

Logothetis, N. K. and Wandell, B. A. (2004) 'Interpreting the BOLD signal', *Annu Rev Physiol.,* 66, pp. 735-769.

Lüders, E., Steinmetz, H. and Jäncke, L. (2002) 'Brain size and grey matter volume in the healthy human brain', *Neuroreport,* 13(17), pp. 2371-2374.

Manwaring, P. K., Moodie, K. L., Hartov, A., Manwaring, K. H. and Halter, R. J. (2013) 'Intracranial Electrical Impedance Tomography: A Method of Continuous Monitoring in an Animal Model of Head Trauma', *Anesth Analg.,* 117(4), pp. 866–875.

Marieb, E. N. and Hoehn, K. (2007) *Human Anatomy & Physiology (Seventh Edition).* Pearson Education Inc.

Marin, G., Guerin, C., Baillet, S., Garnero, L. and Meunier, G. r. (1998) 'Influence of Skull Anisotropy for the Forward and Inverse Problem in EEG: Simulation Studies Using FEM on Realistic Head Models', *Human Brain Mapping,* 6(4), pp. 250-269.

Martinsen, O. G. and Grimnes, S. (2001) 'Facts and myths about electrical measurement of stratum corneum hydration state', *Dermatology,* 202(2), pp. 87-89.

Mayhew, S. D., Dirckx, S. G., Niazy, R. K., Iannetti, G. D. and Wise, R. G. (2010a) 'EEG signatures of auditory activity correlate with simultaneously recorded fMRI responses in humans', *NeuroImage* 49, pp. 849-864.

Mayhew, S. D., Macintosh, B. J., Dirckx, S. G., Iannetti, G. D. and Wise, R. G. (2010b) 'Coupling of simultaneously acquired electrophysiological and haemodynamic responses during visual stimulation', *Magnetic Resonance Imaging,* 28, pp. 1066-1077.

McCann, H., Ahsan, S. T., Davidson, J. L., Robinson, R. L., Wright, P., Bryan, A., Pollard, B. J., Quraishi, T. and Pomfrett, C. J. D. 'Preliminary observations with fEITER data under auditory stimulation', *Proc. XIIth International Conference on Electrical Impedance Tomography*, Univ. of Bath, 2011-05-04, 135-138.

McCann, H., Ahsan, S. T., Davidson, J. L., Robinson, R. L., Wright, P. and Pomfrett, C. J. D. (2011) 'A portable instrument for high-speed brain function imaging:

fEITER'. *33rd Annual International Conference of the IEEE EMBS*, August 30 - September 3, 2011. Boston, Massachusetts USA.

McCann, H., Polydorides, N., Murrieta-Lee, J. C., Ge, K., Beatty, P. and Pomfrett, C. J. D. 'Sub-second functional imaging by Electrical Impedance Tomography', *Proceedings of the 28th IEEE EMBS Annual International Conference*, New York City, USA, Aug 30-Sept 3, 2006.

McEwan, A., Cusick, G. and Holder, D. S. (2007a) 'A review of errors in multi-frequency EIT instrumentation', *Physiol. Meas. 28 (2007) S197–S215*.

McEwan, A. L., Romsauerova, A., Horesh, L. and Holder, D. S. 'Performance improvements in a MF-EIT system for acute stroke: The UCL Mk2.5'. *World Congress on Medical Physics and Biomedical Engineering, IFMBE Proceedings* Seoul, South Korea, 3886-3889.

Mozumder, M., Tarvainen, T., Kaipio, J. P., Arridge, S. R. and Kolehmainen, V. (2014) 'Compensation of modeling errors due to unknown domain boundary in diffuse optical tomography', *Journal of the Optical Society of America. A, Optics, Image Science, and Vision,* 31(8), pp. 1847-1855.

Muller, J., Rinnerthaler, M., Poewe, W. and Kofler, M. (2007) 'Auditory Startle Reaction in Primary Blepharospasm', *Movement Disorders,* 22(2), pp. 268-272.

Murphy, E. K., Mahara, A. and Halter, R. J. (2016) 'A Novel Regularization Technique for Microendoscopic Electrical Impedance Tomography ', *IEEE Transactions on Medical Imaging,* (TBA).

Murrieta-Lee, J. C., Pomfrett, C. J. D., Beatty, P. C. W., Mussel, C. B., Waterfall, R. C., Polydorides, N. and McCann, H. 'EIT voltage changes on the human scalp due to brain stimulus', *Proceedings. 15th International Conference on Electronics, Communications and Computers, 2005.* , 28-02 Feb. 2005, 229-234.

Murrieta-Lee, J. C., Pomfrett, C. J. D., Beatty, P. C. W., Polydorides, N., Mussel, C. B., Waterfall, R. C. and McCann, H. 'Sub-second observations of EIT voltage changes on the human scalp due to brain stimulus', *26th Annual International Conference of the IEEE Engineering in Medicine and Biology Society (IEMBS '04)* 1-5 Sept. 2004, 1317-1320

Näätänen, R., Pakarinen, S., Rinne, T. and Takegataa, R. (2004) 'The mismatch negativity (MMN): towards the optimal paradigm', *Clinical Neurophysiology,* 115(1), pp. 140-144.

Nash, S. G. and Sofer, A. (1996) *Linear and Nonlinear Programming.* The McGraw-Hill Companies, Inc.

Nicholson, P. W. (1965) 'Specific Impedance of Cerebral White Matter', *Experimental Neurology,* 13(4), pp. 386-401.

Nissinen, A., Heikkinen, L. M. and Kaipio, J. P. (2008) 'The Bayesian approximation error approach for electrical impedance tomography—experimental results', *Meas. Sci. Technol.,* 19(015501).

Nissinen, A., Heikkinen, L. M., Kolehmainen, V. and Kaipio, J. P. (2009) 'Compensation of errors due to discretization, domain truncation and unknown contact impedances in electrical impedance tomography', *Meas. Sci. Technol. ,* 20(105504).

Nissinen, A., Kolehmainen, V. and Kaipio, J. P. (2010) 'Compensation of errors due to incorrect model geometry in electrical impedance tomography', *Journal of Physics: Conference Series,* 224(012050).

NissinenVille, A., Kolehmainen, P. and Kaipio, J. P. (2011) 'Compensation of Modelling Errors Due to Unknown Domain Boundary in Electrical Impedance Tomography', *IEEE Transaction on Medical Imaging,* 30(2), pp. 231-242.

Novati, P. and Russo, M. R. (2014) 'A GCV based Arnoldi-Tikhonov regularization method', *BIT Numer Math* 54, pp. 501-521.

Oh, T., Gilad, O., Ghosh, A., Schuettler, M. and Holder, D. S. (2011a) 'A novel method for recording neuronal depolarization with recording at 125–825 Hz: implications for imaging fast neural activity in the brain with electrical impedance tomography', *Med Biol Eng Comput* 49, pp. 593-604.

Oh, T. I., Wi, H., Kim, D. Y., Yoo, P. J. and Woo, E. J. (2011b) 'A fully parallel multi-frequency EIT system with flexible electrode configuration: KHU Mark2', *Physiol. Meas. ,* 32, pp. 835-849.

Oh, T. I., Woo, E. J. and Holder, D. (2007) 'Multi-frequency EIT system with radially symmetric architecture: KHU Mark1', *Physiol. Meas.,* 28, pp. S183–S196

Oostendorp, T. F. and Delbeke, J. 'The conductivity of the human skull in vivo and in vitro', *Engineering in Medicine and Biology, 1999. 21st Annual Conf. and the 1999 Annual Fall Meeting of the Biomedical Engineering Soc. - BMES/EMBS Conference*.

Oostendorp, T. F., Delbeke, J. and Stegeman, D. F. (2000) 'The Conductivity of the Human Skull: Results of In Vivo and In Vitro Measurements', *IEEE transactions on biomedical engineering,* 47(11).

Ouypornkochagorn, T., McCann, H. and Polydorides, N. 'Tackling Modelling Error in the Application of Electrical Impedance Tomography to the Head', *37th Annual International Conference of the IEEE Engineering in Medicine and Biology Society (EMBC)*, Milan, Italy, 25-29 August, 2015.

Ouypornkochagorn, T., McCann, H., Terzija, N., Parry-Jones, A. and Polydorides, N. 'Electrical Impedance Measurement of Cerebral Haemodynamics', *16th International Conference on Biomedical Applications of Electrical Impedance Tomography*, Neuchatel, Switzerland, 2-5 June, 2015.

Ouypornkochagorn, T., Polydorides, N. and McCann, H. 'In Vivo Estimation of the Scalp and Skull Conductivity', *15th International Conference on Biomedical Applications of Electrical Impedance Tomography*, Gananoque, Ontario, Canada, 24-26 April, 2014.

Parkes, L. M., Lange, F. P. d., Fries, P., Toni, I. and Norris, D. G. (2007) 'Inability to Directly Detect Magnetic Field Changes Associated With Neuronal Activity', *Magnetic Resonance in Medicine,* 57, pp. 411-416.

Pascalis, V. D., Cozzuto, G. and Russo, E. (2013) 'Effects of personality trait emotionality on acoustic startle response and prepulse inhibition including N100 and P200 event-related potential', *Clinical Neurophysiology,* 124(2), pp. 292-305.

Patterson, R. P., Zhang, J., Mason, L. I. and Jerosch-Herold, M. (2001) 'Variability in the cardiac EIT image as a function of electrode position, lung volume and body position', *Physiol. Meas.,* 22, pp. 159-166.

Perez, J. J., Guijarro, E. and Barcia, J. A. (2004) 'Influence of the scalp thickness on the intracranial contribution to rheoencephalography', *Phys. Med. Biol,* 49, pp. 4383-4394.

Peters, F. C. and Barra, L. P. S. (2010) 'Some numerical results on the influence of measurement strategies and load patterns in the EIT inverse problem', *Journal of Physics: Conference Series 224 (2010) 012145*.

Pfützner, H. (1984) 'Dielectric analysis of blood by means of a raster-electrode technique', *Medical and biological engineering and computing* 22(2).

Pollard, B. J., Pomfrett, C. J., Bryan, A., Quraishi, T., Davidson, J. L. and McCann, H. (2011) 'Functional electrical impedance tomography by evoked response (fEITER): Sub-second changes in brain function during induction of anaesthesia with propofol: 7AP1-6', *European Journal of Anaesthesiology* 28, pp. 97-98.

Polydorides, N. (2002) *Image Reconstruction Algorithms for Soft-field Tomography.* PhD thesis, The University of Manchester Institute of Science and Technology.

Polydorides, N. and Lionheart, W. R. B. (2002) 'A Matlab toolkit for three-dimensional electrical impedance tomography: a contribution to the Electrical Impedance and Diffuse Optical Reconstruction Software project', *Meas. Sci. Technol.,* 13, pp. 1871–1883.

Popovic, D., Bodo, M., Pearce, F., Albert, S. v., Garcia, A., Settle, T. and Armonda, R. (2013) 'Assessment of cerebral blood flow autoregulation (CBF AR) with rheoencephalography (REG): studies in animals', *Journal of Physics: Conference Series* 434(012042).

Rafiei-Naeini, M. and McCann, H. (2008) 'Low-noise current excitation sub-system for medical EIT', *Physiol. Meas. ,* 29, pp. 173-184.

Raicu, V., Kitagawa, N. and Irimajiri, A. (2000) 'A quantitative approach to the dielectric properties of the skin', *Phys. Med. Biol.,* 45(2), pp. L1-L4.

Ramon, C., Schimpf, P., Haueisen, J., Holmes, M. and Ishimaru, A. (2004) 'Role of Soft Bone, CSF and Gray Matter in EEG Simulations', *Brain Topography,* 16(4), pp. 245-248.

Ramon, C., Schimpf, P. H. and Haueisen, J. (2006) 'Influence of head models on EEG simulations and inverse source localizations', *BioMedical Engineering OnLine,* 5(10).

Ranck, J. J. B. (1964) 'Specific impedance of cerebral cortex during spreading depression, analysis of neuronal neuroglial, interstitial contributions', *Experimental Neurology,* 9(1), pp. 1-16.

Rao, A. (2000) *Electrical impedance tomography of brain activity : studies into its accuracy and physiological mechanisms.* PhD, University of London.

Reinius, H., Borges, J. B., Fredén, F., Jideus, L., Camargo, E. D. L. B., Amato, M. B. P., Hedenstierna, G., Larsson, A. and Lennmyr, F. (2015) 'Real-time ventilation and perfusion distributions by electrical impedance tomography during one-lung ventilation with capnothorax', *Acta Medica Scandinavica,* 59, pp. 354-368

Robinson, R. (2011) *Experimental study of electrophysiology using the fEITER system.* PhD thesis, The University of Manchester.

Robinson, R. L., Davidson, J. L., Wright, P., Pomfrett, C. J. D. and McCann, H. 'A Study of Composite Electrode-Tissue Impedance', *30th Annual International IEEE EMBS Conference*, Vancouver, British Columbia, Canada, August 20-24, 2008.

Rosell, J., Colominas, J., Riu, P., Pallas-Areny, R. and Webster, J. G. (1988) 'Skin impedance from 1 Hz to 1 MHz', *IEEE Trans. Biomed. Eng,* 35(8), pp. 649-651.

Roy, C. S. (1890) 'On the regulation of the blood-supply of the brain ', *J. Physiol. ,* 11, pp. 85-108.

Rush, S. and Driscoll, D. A. (1968) 'Current distribution in the brain from surface electrodes', *Anesth. Analg.,* 47(6), pp. 717-723.

Saad, Y. (2011) *Numerical Methods for Large Eigenvalue Problems.* The Society for Industrial and AppliedMathematics.

Sadleir, R. J., Tang, T., Tucker, A. S., Borum, P. and Weiss, M. 'Detection of Intraventricular Blood using EIT in a neonatal piglet model', *31st Annual International Conference of the IEEE EMBS*, Minneapolis, Minnesota, USA, September 2-6, 2009.

Saha, S. and Williams, P. A. (1989) 'Electric and dielectric properties of wet human cortical bone as a function of frequency', *IEEE Trans. Biomed. Eng,* 39(12), pp. 1298-1304.

Sakamoto, K. and Kanai, H. (1979) 'Electrical Characteristics of Flowing Blood', *IEEE Trans. Biomed. Eng.,* BME-26(12), pp. 685-695.

Salman, A., Malony, A., Turovets, S. and Tucker, D. 'Use of Parallel Simulated Annealing for Computational Modeling of Human Head Conductivity', *Lecture Notes in Computer Science, Computational Science – ICCS 2007*, 86-93.

Salman, A., Turovets, S., Malony, A., Eriksen, J. and Tucker, D. (2005) 'Computational Modeling of Human Head Conductivity', *Springer Lecture Notes in Computer Science LNCS 3514 - ICCS 2005*, pp. 631–638.

Sansen, W., Geeraerts, B., Petegem, W. V. and Steyaert, M. (1992) 'Electrical impedance tomography systems based on voltage drive', *Clin. Phys. Physiol. Meas.,* 13(39).

Sapkota, A., Fuse, T., Seki, M., Maruyama, O., MichikoSugawara and MasahiroTakei (2015) 'Application of electrical resistance tomography for thrombus visualization in blood', *Flow Measurement and Instrumentation*.

Saulnier, G. J., Liu, N., Tamma, C., Xia, H., Kao, T.-J., Newell, J. C. and Isaacson, D. 'An Electrical Impedance Spectroscopy System for Breast Cancer Detection '. *Proceedings of the 29th Annual International Conference of the IEEE EMBS*, Cité Internationale, Lyon, France, August 23-26, 2007.

Schwan, H. P. (1983) 'Electrical Properties of Blood and its Constituents: Alternating Current Spectroscopy', *Blut,* 46, pp. 185-197.

Schwarzkopf, S. B., Lamberti, J. S. and Smith, D. A. (1993) 'Concurrent assessment of acoustic startle and auditory P50 evoked potential measures of sensory inhibition', *Biol Psychiatry* 33, pp. 815-828.

Schweiger, M., Arridge, S. R. and Nissila, I. (2005) 'Gauss–Newton method for image reconstruction in diffuse optical tomography', *Phys. Med. Biol. ,* 50, pp. 2365–2386.

Shang, Y., Cheng, R., Dong, L., Ryan, S. J., Saha, S. P. and Yu, G. (2011) 'Cerebral monitoring during carotid endarterectomy using near-infrared diffuse optical spectroscopies and electroencephalogram', *Phys. Med. Biol. ,* 56, pp. 3015-3032.

Shi, X., Dong, X., Shuai, W., You, F., Fu, F. and Liu, R. (2006) 'Pseudo-polar drive patterns for brain electrical impedance tomography', *Physiol. Meas. 27 (2006) 1071–1080*.

Smielewski, P., Czosnyka, M., Kirkpatrick, P., McEroy, H., Rutkowska, H. and Pickard, J. D. (1996) 'Assessment of Cerebral Autoregulation Using Carotid Artery Compression', *Stroke* 27(12), pp. 2197-2203.

Suh, H. S., Lee, W. H. and Kim, T.-S. (2012) 'Influence of anisotropic conductivity in the skull and white matter on transcranial direct current stimulation via an anatomically realistic finite element head model', *Physics in Medicine and Biology,* 57(21), pp. 6961-6980.

Syed, H., Borsic, A., Hartov, A. and Halter, R. J. (2012) 'Anatomically accurate hard priors for transrectal electrical impedance tomography (TREIT) of the prostate', *Physiol. Meas.,* 33, pp. 719-738.

Tang, C., You, F., Cheng, G., Gao, D. and Fu, F. (2008) 'Correlation Between Structure and Resistivity Variations of the Live Human Skull', *Biomedical Engineering, IEEE Transactions on,* 55(9), pp. 2286-2292.

Tarits, P., Jouanne, V., Menvielle, M. and Roussigno, M. (1994) 'Bayesian statistics of non-linear inverse problems: example of the magnetotelluric 1-D inverse problem', *Geophys. J. Int. ,* 119, pp. 353-368.

Tehrani, J. N., Anderson, C., Jin, C., Schaik, A. v., Holder, D. and McEwan, A. (2010) 'Feasibility of electrical impedance tomography in haemorrhagic stroke treatment using adaptive mesh', *Journal of Physics: Conference Series 224 (2010) 012065*.

Tidswell, A. T., Gibson, A., Bayford, R. H. and Holder, D. S. (2001a) 'Electrical impedance tomography of human brain activity with a two-dimensional ring of scalp electrodes', *Physiol. Meas.,* 22, pp. 167-175.

Tidswell, A. T., Gibson, A., Bayford, R. H. and Holder, D. S. (2001b) 'Validation of a 3D reconstruction algorithm for EIT of human brain function in a realistic head-shaped tank', *Physiol. Meas.,* 22, pp. 177-185.

Tidswell, T., Gibson, A., Bayford, R. H. and Holder, D. S. (2001c) 'Three-Dimensional Electrical Impedance Tomography of Human Brain Activity', *NeuroImage,* 13, pp. 283-294.

Towers, C. M., McCann, H., Wang, M., Beatty, P. C., Pomfrett, C. J. D. and Beck, M. S. (2000) '3D simulation of EIT for monitoring impedance variations within the human head', *Physiol. Meas. ,* 21, pp. 119-124.

Turovets, S., Salman, A., Malony, A., Poolman, P., Davey, C. and Tucker, D. 'Anatomically Constrained Conductivity Estimation of the Human Head Tissues in Vivo: Computational Procedure and Preliminary Experiments', *World Congress on Medical Physics and Biomedical Engineering 2006 - IFMBE Proceedings*, 3854-3857.

Ultchin, Y., Nachaliel, U. and Ori, A. (2002) 'Indirect calculation of breast tissue impedance values', *Physiol. Meas. ,* 23, pp. 177-182.

Vaisman, N., Weintrop, N., Blumental, A., Yosefberg, Z. and Vardi, P. (1999) 'Gastric emptying in patients with type I diabetes mellitus', *Ann. NY Acad. Sci.,* 873, pp. 506-511.

Viklands, T. and Gulliksson, M. (2000) *Fast solution of discretized optimization problems: Optimization tools for solving nonlinear ill-posed problems. ISNM International Series of Numerical Mathematics* Berlin, p. 255–264.

Visser, K. R. 'Electric conductivity of stationary and flowing human blood at low frequencies', *Proceedings of the Annual International Conference of the IEEE Engineering in Engineering in Medicine and Biology Society*.

Visser, K. R., Lamberts, R., Korsten, H. H. M. and Zijstra, W. G. (1976) 'Observations on blood flow related electrical impedance changes in rigid tubes', *Pflugers Arch.,* 336, pp. 289-291.

Viswanathan, A. and Freeman, R. D. (2004) 'Neurometabolic coupling in cerebral cortex reflects synaptic more than spiking activity', *Nature Neuroscience,* 10(10).

Walsh, P., Kane, N. and Butler, S. (2005) 'The clinical role of evoked potentials', *Neurol Neurosurg Psychiatry* 76, pp. ii16–ii22.

Wang, G., Yang, L., Worrell, G. and He, B. 'The relationship between conductivity uncertainties and EEG source localization accuracy', *Annual International Conference of the IEEE Engineering in Medicine and Biology Society - EMBC 2009*, 3-6 Sept. 2009, 4799-4802.

Watson, S. J., Smallwood, R. H., Brown, B. H., Cherian, P. and Bardhan, K. D. (1996) 'Determination of the relationship between the pH and conductivity of gastric juice', *Physiol. Meas. ,* 17, pp. 21-27.

Webster, V. L. and Mahajan, R. P. (2002) 'Transient Hyperaemic Response to Assess Vascular Reactivity of Skin; Effect of Locally Iontophoresed Sodium Nitroprusside', *British Journal of Anaesthesia* 89(2), pp. 265-70.

Wendel, K. and Malmivuo, J. 'Correlation between Live and Post Mortem Skull Conductivity Measurements', *28th Annual International Conference of the IEEE Engineering in Medicine and Biology Society, 2006 - EMBS '06*, Aug. 30 2006-Sept. 3 2006, 4285-4288.

Wilkinson, A. J., Randall, E. W., Cilliers, J. J., Durrett, D. R., Naidoo, T. and Long, T. (2005) 'A 1000-Measurement Frames/Second ERT Data Capture System With Real-Time Visualization', *IEEE Sensors Journal,* 5(2), pp. 300-307.

Wilson, A. J., Milnes, P., Waterworth, A. R., Smallwood, R. H. and Brown, B. H. (2001) 'Mk3.5: a modular, multi-frequency successor to the Mk3a EIS/EIT system', *Physiol. Meas. ,* 22, pp. 49-54.

Wolters, C. H., Anwander, A., Tricoche, X., Weinstein, D., Koch, M. A. and MacLeod, R. S. (2006) 'Influence of tissue conductivity anisotropy on EEG/MEG field and return current computation in a realistic head model: A simulation and visualization study using high-resolution finite element modeling', *NeuroImage* 30(3), pp. 813-826.

Wtorek, J. and Polinski, A. (2005) 'The contribution of blood-flow-induced conductivity changes to measured impedance', *IEEE Transactions on Biomedical Engineering,* 52(1).

Xu, C.-H., Wang, L., Shi, X.-T., You, F.-S., Fu, F., Liu, R.-G., Dai, M., Zhao, Z.-W., Gao, G.-D. and Dong, X.-Z. (2010) 'Real-time Imaging and Detection of Intracranial Haemorrhage by Electrical Impedance Tomography in a Piglet Model', *The Journal of International Medical Research,* 38(5), pp. 1596-1604.

Yamamoto, T. and Yamamoto, Y. (1976) 'Electrical properties of the epidermal stratum corneum', *Med. Biol. Eng.,* 14(5), pp. 494-500.

Yerworth, R. J., Bayford, R. H., Brown, B., Milnes, P., Conway, M. and Holder, D. S. (2003) 'Electrical impedance tomography spectroscopy (EITS) for human head imaging', *Physiol. Meas. ,* 24, pp. 477–489.

Yerworth, R. J., Bayford, R. H., Cusick, G., Conway, M. and Holder, D. S. (2002) 'Design and performance of the UCLH Mark 1b 64 channel electrical

impedance tomography (EIT) system, optimized for imaging brain function', *Physiol. Meas.,* 23, pp. 149-158.

Yue, X. and McLeod, C. (2008) 'FPGA design and implementation for EIT data acquisition', *Physiol. Meas. ,* 29, pp. 1233–1246.

Zhang, Y., Drongelen, W. v. and He, B. (2006) 'Estimation of in vivo brain-to-skull conductivity ratio in humans', *Applied Physics Letters,* 89.

Appendices

Appendix A Head Tissue Conductivities

Table A-1 Conductivity of the human scalp/ skin obtained from literature

No	Studies	Conductivity (S/m)	Measurement method/ Remark
1	Scalp (Gonçalves et al., 2003b)	0.3322 SD13%	The data were obtained from EIT measurement with (realistic) BEM subject head models containing 3 tissues: brain, skull, and scalp. EIT was operated on $10\mu A_{rms}$ 60 Hz current with 1,250 Hz acquisition rate. The number of electrodes was 64. The number of subjects was 6. The conductivity of the scalp was assumed to be that of the brain.
2 2.1 2.2 2.3 2.4	Scalp (Gonçalves et al., 2001, Gonçalves et al., 2003a) EIT method with individual radii models EIT method with a generic radii model MEG/EEG method with individual radii models MEG/EEG method with a generic radii mode	 0.3859 0.3270 0.4277 0.4292	EIT method was used the similar configuration to (Gonçalves et al., 2003b), but it was carried on spherical models. MEG/EEG method was based on SEF/SEP experiments with 151 MEG channels and 64 EEG channels. The number of subjects was 5.
3	Scalp (Baysal and Haueisen, 2004)	0.315 SD6.65%	Use statistical technique (MiMSEE). The SEF/SEP data were obtained from EEG and MEG with 32 electrodes on 9 subjects. Realistic BME models were used containing 3 tissues: brain, skull, and scalp.
4	Scalp (Burger and Milaan, 1943)	0.4348	Measured with a DC current system on a human head.
5 5.1 5.2	Skin (Raicu et al., 2000) Moisten skin (with saline) Dry skin	 0.010 0.001	Measured by an impedance analyser with 2 electrodes on the neck skin. The experimental frequency was ranged from 100 Hz – 100 MHz. The displayed values are the approximate values at 10 kHz.
6	Skin (Faes et al., 1999)	0.3040 (0.2358-0.3922)	Measured with a 100 Hz – 10 MHz supply voltage system on skin (with 68% water content). The displayed values are the approximate values at 10 kHz.
7 7.1 7.2	Skin (Yamamoto and Yamamoto, 1976) Stratum corneum on the skin Deeper skin	 0.0001 0.22	Measured with a 10 kHz supply voltage system on forearm skin. The displayed values are the approximate values at 10 kHz.

Table A-2 Conductivity of the human skull obtained from literature

No	Studies	Conductivity (S/m)	Measurement method/ Remark
1	(Dannhauer et al., 2011)	0.01	The measurement was based on EEG with 118 electrodes (used EEG forward problem with FEM model).
1.1	Radial conductivity	0.0093	
1.2	Tangential conductivity	0.015	
2	(Tang et al., 2008)		The measurement was performed by 4 electrode technique with 0.5 mA at 1 Hz – 4 MHz.
2.1	Standard trilayer skull	0.0126±0.0029	
2.2	Quasi-trilayer skull	0.0069±0.0015	
2.3	Standard compact skull	0.0038±0.0008	
2.4	Quasi-compact skull	0.0050±0.0008	
2.5	Dentate suture skull	0.0173±0.0059	
2.6	Squamous suture skull	0.0078±0.0028	
3	(Baysal and Haueisen, 2004)	0.016 SD7.84% (or SD1.3m)	(similar to item 3 of Table A-1)
4	(Hoekema et al., 2003)		The measurement was performed by 4 electrode technique with 25 mA at 10 Hz. The samples were excised skull pieces, immersed in the subject's blood at the body temperature.
4.1	11 year-old	0.0801 SD0.0055	
4.2	25 year-old	0.0712 SD0.0083	
4.3	36 year-old	0.0537 SD0.0043	
4.4	46 year-old	0.0344 SD0.0023	
4.5	50 year-old	0.0320 SD0.0045	
4.6	68 year-old	0.0214 SD0.0013	
5	(Gonçalves et al., 2003b)	0.0082 SD18% (or SD0.001476)	(similar to item 1 of Table A-1)
6	(Gonçalves et al., 2001, Gonçalves et al., 2003a)		(similar to item 2 of Table A-1)
6.1	EIT method with individual radii models	0.0113	
6.2	EIT method with a generic radii model	0.0049	
6.3	MEG/EEG method with individual radii models	0.0086	
6.4	MEG/EEG method with a generic radii mode	0.0062	
7	(Akhtari et al., 2002)		The measurement was performed by 4 electrode technique with 0.2-0.4 mA at 10-90 Hz.
7.1	Tri-layer skull, cadaver	0.0033	
7.2	Tri-layer skull, live	0.00953 (0.00850-0.0114)	
7.3	Top-layer skull, live	0.00617	
7.4	Spongiform-layer skull	0.0214	
7.5	Lower-layer skull, live	0.00487	
8	(Oostendorp and Delbeke, 1999, Oostendorp et al., 2000)		EIT was used with 33 electrodes and 1μA(Pulse) 10-1 kHz. A BEM model was used in the estimation. For the vitro case, the sample was preserved for a few days.
8.1	In vivo	0.015±0.003	
8.2	In vitro	0.0131SD0.0007	
9	(Law, 1993)		The measurement was performed by 4 electrode technique with 100Hz.
9.1	Without suture	0.0132±0.0103	
9.2	With suture	0.0324	

Table A-3 Ratios of human scalp conductivity, skull conductivity, and brain conductivity obtained from literature

No	Studies	Ratios of the conductivities of scalp: skull : brain	Measurement method/ Remark
1	(Dannhauer et al., 2011)	40: 1: 40	(similar to item 1 of Table A-1)
2	(Wang et al., 2009)	- : 1: 20	The estimation was based on EEG with 31 electrodes, and 3 layer-BEM realistic models. The number of subjects was 2.
3	(Zhang et al., 2006)	- : 1: 18.7±2.1	The EIT measurement was carried on 2 pediatric epilepsy patients with 32 scalp electrodes. The excitation was performed on the cortex with 2 implanted subdural grids. The current was 1-10 mA 50Hz. An FEM realistic model was used for all patient estimations. Only 3 tissues were determined.
4 4.1 4.2	(Lai et al., 2005) 3 layer spherical model 4 layer spherical model	 - : 1: 25±7 - : 1: 21.3	EIT method was used with the similar configuration to (Zhang et al., 2006), but a 3-layer and a 4-layer spherical model (CSF was added) were used. The number of patients was 5 and 3 for the first and the second model respectively.
5	(Clerc et al., 2005)	25 : 1: -	EIT method was used with 32 electrodes, operated with 0.1 mA 110 Hz current. A subject BEM head model was used containing 2,242 surfaces.
6	(Baysal and Haueisen, 2004)	20.330: 1: 23.073 (Scalp)SD1.2966% (Brain)SD0.1709%	(similar to item 3 of Table A-2)
7	(Gonçalves et al., 2003b)	- : 1: 23 to 56 - : 1: 41.67 (average)	(similar to item 1 of Table A-2)
8 8.1 8.2 8.3 8.4	(Gonçalves et al., 2001, Gonçalves et al., 2003a) EIT method with individual radii models EIT method with a generic radii model MEG/EEG method with individual radii models MEG/EEG method with a generic radii mode	 - : 1: 14 to 67 - : 1: 38 (average) - : 1: 30 to 127 - : 1: 72.2 (average) - : 1: 27 to 66 - : 1: 47.8 (average) - : 1: 43 to 86 - : 1: 66.8 (average)	(similar to item 2 of Table A-2)
9	(Oostendorp et al., 2000)	15 : 1: 15	(similar to item 8 of Table A-2
10	(Rush and Driscoll, 1968)	80 : 1: 80	Tested on a tank containing a half human skull.

Table A-4 Conductivity of the human cerebrospinal fluid (CSF) obtained from literature

No	Studies	Conductivity (S/m)	Measurement method/ Remark
1	(Latikka et al., 2001)	1.25	Measured with 2 needle electrodes, 2μA 50kHz current. The measurement was performed in vivo on 9 patients.
2	(Baumann et al., 1997)	1.802@37°C 10kHz 1.794@37°C 1kHz 1.456@25°C 10kHz	Measured with 2 electrodes, 10μA 10-10kHz current on a cell unit.
3	(Kosterich et al., 1983)	1±0.1	Measured with a 10-100MHz supply voltage system on a cell unit.

Table A-5 Conductivity of the human grey and the white matter obtained from literature

No	Studies	Conductivity of the grey matter (S/m)	Conductivity of the white matter (S/m)	Remark
1	(Latikka et al., 2001)	0.2849 (0.1848-0.5155)	0.2556 (0.2096-0.3067)	(similar to item 1 of Table A-4)
2	(Kosterich et al., 1983)	0.33@5Hz 0.43@5kHz	0.76@5Hz	(similar to item 3 of Table A-4)

Table A-6 Conductivity of the human blood obtained from literature

No	Studies	Conductivity (S/m)	Measurement method/ Remark
1	(Anas et al., 2012)	0.6452 (0.625-1.053) @10kHz 25°C	Measured in a test cell with 1k-20kHz supply voltage system.
2	(Faes et al., 1999)	0.66 (0.5236-0.8333)	(similar to item 6 of Table A-1)
3	(Visser, 1989)	Overall: 0.7 @37°C Longitudinal conductivity: 0.86 Transverse conductivity: 0.475	Measured with a 100kHz supply voltage system.
4	(Pfützner, 1984)	0.45 @40% Haematocrit, 21°C	Measured with a 10-100kHz supply voltage system
5	(Schwan, 1983)	0.8	Measured with the voltage frequency of Alpha-dispersion (<3MHz).
6	(Hirsch et al., 1950)	0.515@47.87% Haematocrit 30°C 0.646@39.33% Haematocrit 30°C	Measured with a 1.075-19kHz supply voltage system.

Appendix B Recent Medical-designed EIT Systems

Table B-1 Some recent EIT systems

System	Number of Channels	Excitation Current Frequency	Current Amplitude	Recording Speed (fps)	Signal-to-Noise Ratio (SNR) (dB)
fEITER (Davidson et al., 2010, McCann et al., 2011b)	32	10 kHz	1 mA_{pk-pk}	100 fps	80 dB
Sheffield Mk3a (McEwan et al., 2007a, Wilson et al., 2001)	16	9.6 kHz–1.2 MHz	Totally 300 μA_{rms}	33 fps	55 dB for single frequency drive 25 dB for multi-frequency drive
Sheffield Mk3.5 (Wilson et al., 2001, Yerworth et al., 2003)	8	2 kHz – 1.6 MHz	Totally 300 μA_{rms}	25 fps	40 dB
UCL Mk2.5 (McEwan et al., 2007b)	64	20 Hz – 1 MHz	293 μA_{rms}	0.12 fps – 1 fps	40 dB
UCL Mk1b (Yerworth et al., 2002)	64	225 Hz – 77 kHz	the maximum permissible current (IEC60601-1)	3 fps	50 dB
Renselaer ACT4 (Liu, 2007, Kim et al., 2007)	72	300 Hz – 1 MHz	Totally <3.5 mA_{peak} at 5 kHz and <55 mA_{peak} at 1 MHz	NA	90 dB
OXBACT-5 (Yue and McLeod, 2008)	32	Programmable	400 μA_{rms} each channel	25 fps	NA
OXBACT-3 (Lionheart et al., 1997)	32	10 kHz - 160 kHz	1 mA_{rms} each channel	25 fps	NA
Dartmouth (Halter et al., 2008)	64	10 kHz - 10 MHz	n/a	30 fps	94 dB
KHU Mark2 (Oh et al., 2011b)	64	10 Hz – 1 MHz	n/a	100 fps	84 dB
KHU Mark1 (Oh et al., 2007)	64	10 Hz – 500 kHz	0.2 mA_{pk-pk} - 2 mA_{pk-pk}	3 fps	99 dB

Appendix C Specification of fEITER System

Table C-1 Specification of the original version of fEITER (continue overleaf)

No	Specification	Value	Remark
1	Number of electrodes supported	32	Excluded ground electrode
2	Excitation current	1 mA_{pk-pk} 10 kHz (original version)/ 2 mA_{pk-pk} 10 kHz or 1 mA_{rms} 10 kHz (modified version)	Single frequency
3	Recording rate	100 frames per second	Frame period is 10 ms.
4	Reported signal-to-noise (SNR) ratio	80 dB	Reported in (Rafiei-Naeini and McCann, 2008)
5	Sampling rate of Analog-to-Digital Converter (ADC)	500,000 sampling per second	Sampling period is 2 μs.
6	Number of samples to determine a frame measurement data	Regarding 250 samples (over 500 μs) of a frame - The first 50 samples are ignored. - The rest of 200 samples are used to compute a measurement value.	
7	ADC resolution	16-bit resolution	
8	DAC resolution	16-bit resolution	
9	Measurement circuit gain	9.8214 (original version)/ 7.0244 (modified version)	
10	Current monitoring circuit gain	9.8214	
11	Common-Mode Rejection Ratio (CMRR) of the electronic components	Approximately 92 dB at 10 kHz operating frequency	
12	V_{dd} (the drain voltage, the positive supply) and V_{ss} (the source voltage, the negative supply) of the electronic components	3 V_{DC} and 0 V_{DC} respectively	
13	Output impedance	10 MΩ	
14	Input impedance for capturing external signals	47 kΩ (ADC port)	Capture by CED Micro 1401mkII
15	Maximum internal clock	100 MHz	
16	Head box enclosure standard	NEMA IP65	Complete protection against contact (dust tight), water projected by a nozzle (6.3 mm)
17	Bit length of PSD accumulator resisters	16 bits (16-bit data readout) (original version)/ 24 bits (24-bit data readout) (modified version)	22-bit truncation (original version)/ 14-bit truncation (modified version)

No	Specification	Value	Remark
18	Number of current patterns	20 opposite driving direction patterns	
19	Total number of measurements per frame	546 adjacent measurements	27 or 28 parallel measurements per current pattern
20	Marker signal sampling rate	100 Hz	Generate by CED Micro 1401 mkII
21	External signal sampling rate	500,000 Hz	Capture by CED Micro 1401 mkII
22	USB port transfer rate	500,000 samples of 8-bit length data per second, with PFI0 port reading trigger	Refer to National Instrument M Series Mulifunction DAQ specification

Appendix D Current Drive Patterns and Measurement Schemes of fEITER

Current driving and measurement of fEITER system are based on the electrode layout of the international standard 10-20 (EEG) system. However, four extra-locations on the occipital region are added (location 27, 28, 30, and 31). The electrode layout of fEITER system is shown in Figure D-1 (a), which is comparable to the 10-20 system as the layout shown in Figure D-1 (b). Mapping locations between the two layouts are shown in Table D-1.

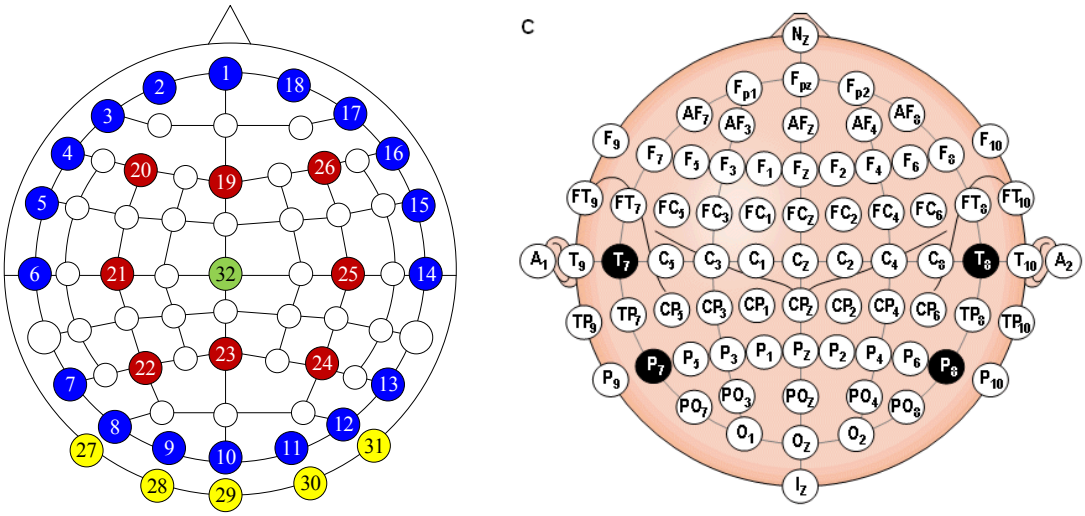

(a) (b)

Figure D-1 (a) Electrode locations of fEITER system (b) Electrode locations of the standard 10-20 system

Table D-1 The mapping of electrode locations between the layout used in fEITER system and the layout of the 10-20 system

fEITER System	10-20 System
1	Fpz
2	Fp1
3	AF7
4	F7
5	FT7
6	T7
7	P7
8	PO7

fEITER System	10-20 System
9	O1
10	Oz
11	O2
12	PO8
13	P8
14	T8
15	FT8
16	F8

fEITER System	10-20 System
17	AF8
18	Fp2
19	Fz
20	F3
21	C3
22	P3
23	Pz
24	P4

fEITER System	10-20 System
25	C4
26	F4
27	-
28	-
29	Iz
30	-
31	-
32	Cz

Twenty current drive patterns in near-diametric driving directions are designed in fEITER system. The list of driving pairs is shown in Table D-2 (the current is flowed from Electrode #CP+ to Electrode #CP-). These patterns can be categorised into four different driving schemes: lower ring scheme, main ring diametric scheme, main ring horizontal scheme, and upper ring scheme (Figure D-2) (note that CPID#15 is in both the main ring diametric scheme and the main ring horizontal scheme).

Table D-2 Current drive patterns of fEITER: the current is flowed from Electrode #CP+ to #CP-

CPID	CP+	CP-
1	1	30
2	1	27
3	22	26
4	9	18
5	7	16
6	3	12
7	1	28
8	8	12
9	5	15
10	1	29

CPID	CP+	CP-
11	4	13
12	8	17
13	7	13
14	20	24
15	6	14
16	1	31
17	1	10
18	2	11
19	21	25
20	19	23

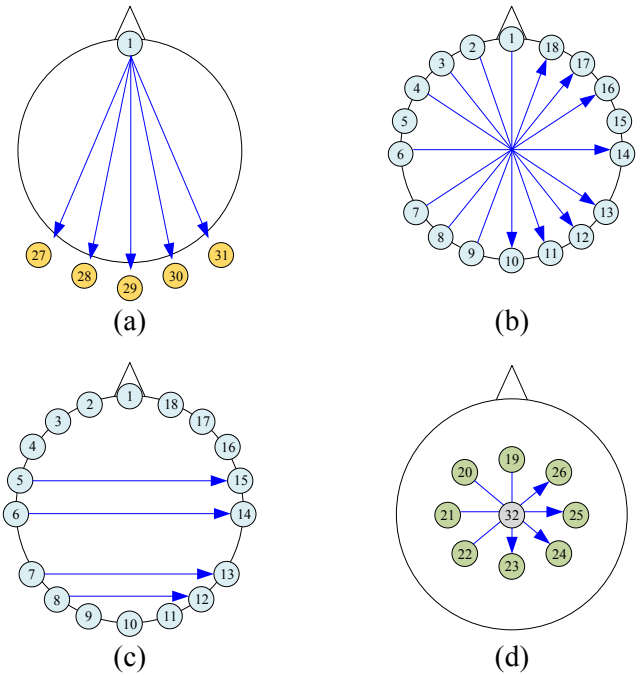

Figure D-2 Four categories of current drive patterns: (a) lower ring patterns (b) main ring diametric patterns (c) main ring horizontal patterns, and (d) upper ring patterns

Totally 546 measurements are measured in every period of 10 ms as the detail in Table D-3. The current is driven from electrode #CP+ to electrode #CP-, and the measurement performed on the electrode pair #Meas+ and #Meas-. The number of measurements performed on each current drive pattern is between 27 and 28. Since, 37 measurements are not adjacent measurements (highlighted with the grey colour in Table D-3), 509 adjacent measurements then were only chosen for the reconstruction with all human data used in this research.

Table D-3 Measurement schemes of fEITER: measure between electrode #Meas+ to #Meas-

MeasID	CP+	CP-	Meas+	Meas-
1	1	30	2	3
2	1	30	3	4
3	1	30	4	5
4	1	30	5	6
5	1	30	6	7
6	1	30	7	8
7	1	30	8	9
8	1	30	9	10
9	1	30	10	11
10	1	30	11	12
11	1	30	12	13
12	1	30	13	14
13	1	30	14	15
14	1	30	15	16
15	1	30	16	17
16	1	30	17	18
17	1	30	18	19
18	1	30	19	20
19	1	30	20	21
20	1	30	21	22
21	1	30	22	23
22	1	30	23	24
23	1	30	24	25
24	1	30	25	26
25	1	30	26	27
26	1	30	27	28
27	1	30	28	29
28	1	30	31	32
29	1	27	2	3
30	1	27	3	4
31	1	27	4	5
32	1	27	5	6
33	1	27	6	7
34	1	27	7	8
35	1	27	8	9

MeasID	CP+	CP-	Meas+	Meas-
36	1	27	9	10
37	1	27	10	11
38	1	27	11	12
39	1	27	12	13
40	1	27	13	14
41	1	27	14	15
42	1	27	15	16
43	1	27	16	17
44	1	27	17	18
45	1	27	18	19
46	1	27	19	20
47	1	27	20	21
48	1	27	21	22
49	1	27	22	23
50	1	27	23	24
51	1	27	24	25
52	1	27	25	26
53	1	27	28	29
54	1	27	29	30
55	1	27	30	31
56	1	27	31	32
57	22	26	1	2
58	22	26	2	3
59	22	26	3	4
60	22	26	4	5
61	22	26	5	6
62	22	26	6	7
63	22	26	7	8
64	22	26	8	9
65	22	26	9	10
66	22	26	10	11
67	22	26	11	12
68	22	26	12	13
69	22	26	13	14
70	22	26	14	15

MeasID	CP+	CP-	Meas+	Meas-
71	22	26	15	16
72	22	26	16	17
73	22	26	17	18
74	22	26	18	19
75	22	26	19	20
76	22	26	20	21
77	22	26	23	24
78	22	26	24	25
79	22	26	27	28
80	22	26	28	29
81	22	26	29	30
82	22	26	30	31
83	22	26	31	32
84	9	18	1	2
85	9	18	2	3
86	9	18	3	4
87	9	18	4	5
88	9	18	5	6
89	9	18	6	7
90	9	18	7	8
91	9	18	10	11
92	9	18	11	12
93	9	18	12	13
94	9	18	13	14
95	9	18	14	15
96	9	18	15	16
97	9	18	16	17
98	9	18	19	20
99	9	18	20	21
100	9	18	21	22
101	9	18	22	23
102	9	18	23	24
103	9	18	24	25
104	9	18	25	26
105	9	18	26	27
106	9	18	27	28
107	9	18	28	29
108	9	18	29	30
109	9	18	30	31
110	9	18	31	32
111	7	16	1	2
112	7	16	2	3
113	7	16	3	4
114	7	16	4	5
115	7	16	5	6
116	7	16	8	9
117	7	16	9	10
118	7	16	10	11
119	7	16	11	12
120	7	16	12	13
121	7	16	13	14
122	7	16	14	15
123	7	16	17	18
124	7	16	18	19

MeasID	CP+	CP-	Meas+	Meas-
125	7	16	19	20
126	7	16	20	21
127	7	16	21	22
128	7	16	22	23
129	7	16	23	24
130	7	16	24	25
131	7	16	25	26
132	7	16	26	27
133	7	16	27	28
134	7	16	28	29
135	7	16	29	30
136	7	16	30	31
137	7	16	31	32
138	3	12	1	2
139	3	12	4	5
140	3	12	5	6
141	3	12	6	7
142	3	12	7	8
143	3	12	8	9
144	3	12	9	10
145	3	12	10	11
146	3	12	13	14
147	3	12	14	15
148	3	12	15	16
149	3	12	16	17
150	3	12	17	18
151	3	12	18	19
152	3	12	19	20
153	3	12	20	21
154	3	12	21	22
155	3	12	22	23
156	3	12	23	24
157	3	12	24	25
158	3	12	25	26
159	3	12	26	27
160	3	12	27	28
161	3	12	28	29
162	3	12	29	30
163	3	12	30	31
164	3	12	31	32
165	1	28	2	3
166	1	28	3	4
167	1	28	4	5
168	1	28	5	6
169	1	28	6	7
170	1	28	7	8
171	1	28	8	9
172	1	28	9	10
173	1	28	10	11
174	1	28	11	12
175	1	28	12	13
176	1	28	13	14
177	1	28	14	15
178	1	28	15	16

MeasID	CP+	CP-	Meas+	Meas-
179	1	28	16	17
180	1	28	17	18
181	1	28	18	19
182	1	28	19	20
183	1	28	20	21
184	1	28	21	22
185	1	28	22	23
186	1	28	23	24
187	1	28	24	25
188	1	28	25	26
189	1	28	26	27
190	1	28	29	30
191	1	28	30	31
192	1	28	31	32
193	8	12	1	2
194	8	12	2	3
195	8	12	3	4
196	8	12	4	5
197	8	12	5	6
198	8	12	6	7
199	8	12	9	10
200	8	12	10	11
201	8	12	13	14
202	8	12	14	15
203	8	12	15	16
204	8	12	16	17
205	8	12	17	18
206	8	12	18	19
207	8	12	19	20
208	8	12	20	21
209	8	12	21	22
210	8	12	22	23
211	8	12	23	24
212	8	12	24	25
213	8	12	25	26
214	8	12	26	27
215	8	12	27	28
216	8	12	28	29
217	8	12	29	30
218	8	12	30	31
219	8	12	31	32
220	5	15	1	2
221	5	15	2	3
222	5	15	3	4
223	5	15	6	7
224	5	15	7	8
225	5	15	8	9
226	5	15	9	10
227	5	15	10	11
228	5	15	11	12
229	5	15	12	13
230	5	15	13	14
231	5	15	16	17
232	5	15	17	18

MeasID	CP+	CP-	Meas+	Meas-
233	5	15	18	19
234	5	15	19	20
235	5	15	20	21
236	5	15	21	22
237	5	15	22	23
238	5	15	23	24
239	5	15	24	25
240	5	15	25	26
241	5	15	26	27
242	5	15	27	28
243	5	15	28	29
244	5	15	29	30
245	5	15	30	31
246	5	15	31	32
247	1	29	2	3
248	1	29	3	4
249	1	29	4	5
250	1	29	5	6
251	1	29	6	7
252	1	29	7	8
253	1	29	8	9
254	1	29	9	10
255	1	29	10	11
256	1	29	11	12
257	1	29	12	13
258	1	29	13	14
259	1	29	14	15
260	1	29	15	16
261	1	29	16	17
262	1	29	17	18
263	1	29	18	19
264	1	29	19	20
265	1	29	20	21
266	1	29	21	22
267	1	29	22	23
268	1	29	23	24
269	1	29	24	25
270	1	29	25	26
271	1	29	26	27
272	1	29	27	28
273	1	29	30	31
274	1	29	31	32
275	4	13	1	2
276	4	13	2	3
277	4	13	5	6
278	4	13	6	7
279	4	13	7	8
280	4	13	8	9
281	4	13	9	10
282	4	13	10	11
283	4	13	11	12
284	4	13	14	15
285	4	13	15	16
286	4	13	16	17

MeasID	CP+	CP-	Meas+	Meas-
287	4	13	17	18
288	4	13	18	19
289	4	13	19	20
290	4	13	20	21
291	4	13	21	22
292	4	13	22	23
293	4	13	23	24
294	4	13	24	25
295	4	13	25	26
296	4	13	26	27
297	4	13	27	28
298	4	13	28	29
299	4	13	29	30
300	4	13	30	31
301	4	13	31	32
302	8	17	1	2
303	8	17	2	3
304	8	17	3	4
305	8	17	4	5
306	8	17	5	6
307	8	17	6	7
308	8	17	9	10
309	8	17	10	11
310	8	17	11	12
311	8	17	12	13
312	8	17	13	14
313	8	17	14	15
314	8	17	15	16
315	8	17	18	19
316	8	17	19	20
317	8	17	20	21
318	8	17	21	22
319	8	17	22	23
320	8	17	23	24
321	8	17	24	25
322	8	17	25	26
323	8	17	26	27
324	8	17	27	28
325	8	17	28	29
326	8	17	29	30
327	8	17	30	31
328	8	17	31	32
329	7	13	1	2
330	7	13	2	3
331	7	13	3	4
332	7	13	4	5
333	7	13	5	6
334	7	13	8	9
335	7	13	9	10
336	7	13	10	11
337	7	13	11	12
338	7	13	14	15
339	7	13	15	16
340	7	13	16	17

MeasID	CP+	CP-	Meas+	Meas-
341	7	13	17	18
342	7	13	18	19
343	7	13	19	20
344	7	13	20	21
345	7	13	21	22
346	7	13	22	23
347	7	13	23	24
348	7	13	24	25
349	7	13	25	26
350	7	13	26	27
351	7	13	27	28
352	7	13	28	29
353	7	13	29	30
354	7	13	30	31
355	7	13	31	32
356	20	24	1	2
357	20	24	2	3
358	20	24	3	4
359	20	24	4	5
360	20	24	5	6
361	20	24	6	7
362	20	24	7	8
363	20	24	8	9
364	20	24	9	10
365	20	24	10	11
366	20	24	11	12
367	20	24	12	13
368	20	24	13	14
369	20	24	14	15
370	20	24	15	16
371	20	24	16	17
372	20	24	17	18
373	20	24	18	19
374	20	24	21	22
375	20	24	22	23
376	20	24	25	26
377	20	24	26	27
378	20	24	27	28
379	20	24	28	29
380	20	24	29	30
381	20	24	30	31
382	20	24	31	32
383	6	14	1	2
384	6	14	2	3
385	6	14	3	4
386	6	14	4	5
387	6	14	7	8
388	6	14	8	9
389	6	14	9	10
390	6	14	10	11
391	6	14	11	12
392	6	14	12	13
393	6	14	15	16
394	6	14	16	17

MeasID	CP+	CP-	Meas+	Meas-
395	6	14	17	18
396	6	14	18	19
397	6	14	19	20
398	6	14	20	21
399	6	14	21	22
400	6	14	22	23
401	6	14	23	24
402	6	14	24	25
403	6	14	25	26
404	6	14	26	27
405	6	14	27	28
406	6	14	28	29
407	6	14	29	30
408	6	14	30	31
409	6	14	31	32
410	1	31	2	3
411	1	31	3	4
412	1	31	4	5
413	1	31	5	6
414	1	31	6	7
415	1	31	7	8
416	1	31	8	9
417	1	31	9	10
418	1	31	10	11
419	1	31	11	12
420	1	31	12	13
421	1	31	13	14
422	1	31	14	15
423	1	31	15	16
424	1	31	16	17
425	1	31	17	18
426	1	31	18	19
427	1	31	19	20
428	1	31	20	21
429	1	31	21	22
430	1	31	22	23
431	1	31	23	24
432	1	31	24	25
433	1	31	25	26
434	1	31	26	27
435	1	31	27	28
436	1	31	28	29
437	1	31	29	30
438	1	10	2	3
439	1	10	3	4
440	1	10	4	5
441	1	10	5	6
442	1	10	6	7
443	1	10	7	8
444	1	10	8	9
445	1	10	11	12
446	1	10	12	13
447	1	10	13	14
448	1	10	14	15

MeasID	CP+	CP-	Meas+	Meas-
449	1	10	15	16
450	1	10	16	17
451	1	10	17	18
452	1	10	18	19
453	1	10	19	20
454	1	10	20	21
455	1	10	21	22
456	1	10	22	23
457	1	10	23	24
458	1	10	24	25
459	1	10	25	26
460	1	10	26	27
461	1	10	27	28
462	1	10	28	29
463	1	10	29	30
464	1	10	30	31
465	1	10	31	32
466	2	11	3	4
467	2	11	4	5
468	2	11	5	6
469	2	11	6	7
470	2	11	7	8
471	2	11	8	9
472	2	11	9	10
473	2	11	12	13
474	2	11	13	14
475	2	11	14	15
476	2	11	15	16
477	2	11	16	17
478	2	11	17	18
479	2	11	18	19
480	2	11	19	20
481	2	11	20	21
482	2	11	21	22
483	2	11	22	23
484	2	11	23	24
485	2	11	24	25
486	2	11	25	26
487	2	11	26	27
488	2	11	27	28
489	2	11	28	29
490	2	11	29	30
491	2	11	30	31
492	2	11	31	32
493	21	25	1	2
494	21	25	2	3
495	21	25	3	4
496	21	25	4	5
497	21	25	5	6
498	21	25	6	7
499	21	25	7	8
500	21	25	8	9
501	21	25	9	10
502	21	25	10	11

MeasID	CP+	CP-	Meas+	Meas-
503	21	25	11	12
504	21	25	12	13
505	21	25	13	14
506	21	25	14	15
507	21	25	15	16
508	21	25	16	17
509	21	25	17	18
510	21	25	18	19
511	21	25	19	20
512	21	25	22	23
513	21	25	23	24
514	21	25	26	27
515	21	25	27	28
516	21	25	28	29
517	21	25	29	30
518	21	25	30	31
519	21	25	31	32
520	19	23	1	2
521	19	23	2	3
522	19	23	3	4
523	19	23	4	5
524	19	23	5	6
525	19	23	6	7
526	19	23	7	8
527	19	23	8	9
528	19	23	9	10
529	19	23	10	11
530	19	23	11	12
531	19	23	12	13
532	19	23	13	14
533	19	23	14	15
534	19	23	15	16
535	19	23	16	17
536	19	23	17	18
537	19	23	20	21
538	19	23	21	22
539	19	23	24	25
540	19	23	25	26
541	19	23	26	27
542	19	23	27	28
543	19	23	28	29
544	19	23	29	30
545	19	23	30	31
546	19	23	31	32

Appendix E Improved Firmware of the 24-bit Read-out fEITER

The original 16-bit read-out firmware (module: smPSD.vhd)

```
entity sm_PSD is
Port ( 
    (Omitted)
    si_bit_1,sq_bit_1 : out std_logic_vector(WORD_LENGTH downto 0);
    ...
    si_bit_35,sq_bit_35 : out std_logic_vector(WORD_LENGTH downto 0);
    (Omitted)

architecture Behavioral of sm_PSD is
    (Omitted)
    variable si_bit_temp1,sq_bit_temp1:std_logic_vector(WORD_LENGTH downto
    0);
    ...
    variable si_bit_temp35,sq_bit_temp35:std_logic_vector(WORD_LENGTH downto
    0);
    (Omitted)
    si_bit_temp1:= X"0000"; sq_bit_temp1:= X"0000";
    ...
    si_bit_temp35:= X"0000"; sq_bit_temp35:= X"0000";
    (Omitted)
    when strnsfr =>
    si_bit_temp1(15 downto 0):=std_logic_vector(si_temp1(37 downto 22));
    ...
    sq_bit_temp35(15 downto 0):=std_logic_vector(sq_temp35(37 downto 22));
    (Omitted)
```

The 24-bit read-out firmware (module: smPSD.vhd)

```
constant DATA_LENGTH:positive :=16-1+8;
entity sm_PSD is
Port ( 
    (Omitted)
    si_bit_1,sq_bit_1 : out std_logic_vector(DATA_LENGTH downto 0);
    ...
    si_bit_35,sq_bit_35 : out std_logic_vector(DATA_LENGTH downto 0);
    (Omitted)
architecture Behavioral of sm_PSD is
    (Omitted)
    variable si_bit_temp1,sq_bit_temp1:std_logic_vector(DATA_LENGTH downto
    0);
    ...
    variable si_bit_temp35,sq_bit_temp35:std_logic_vector(DATA_LENGTH downto
    0);
    (Omitted)
    si_bit_temp1:= X"000000"; sq_bit_temp1:= X"000000";
    ...
    si_bit_temp35:= X"000000"; sq_bit_temp35:= X"000000";
    (Omitted)
    when strnsfr =>
    si_bit_temp1(DATA_LENGTH downto 0) := std_logic_vector(si_temp1(37
    downto 14));
    ...
    sq_bit_temp35(DATA_LENGTH downto 0) := std_logic_vector(sq_temp35(37
    downto 14));
    (Omitted)
```

Appendix F Data Stream Format of the 24-bit Read-out fEITER

The data stream structure of the modified versions of fEITER is shown in Figure F-1. The structure is generally similar to the structure of the original version of fEITER, described in (Ahsan, 2010), but the data width of phase-sensitive detection (PSD) data is increased from 16 bits to 24 bits. The sampling rate of the analog-to-digital converter is 2 μs. In a PSD data, 250 samplings of a measurement are used to compute. Therefore, to complete all 20 current patterns listed in the previous appendix, frame duration is then 10 ms (2 μs × 250 samplings × 20 current patterns). The stream begins with the impedance checking word ("Z-Check"), following with 1-minute duration data of PSD data (more precisely, 59.98 s or 5,998 frames). Each frame comprises the data of 20 current patterns (CP Blocks), where a CP block comprises four sections: block header, 33 measurement data blocks, 2 current data blocks, and a block tail.

The block header and the tail consist of the data synchronization word ("Sync Word"), the current pattern identification data ("CP Identification check" and "CPCounter"), the measurement and current drive checking ("ADCSat", "Current Drive Check", and "BadSine"), and the data read from the digital output ports of CED Micro1401 ("Stimulus Marker"). Meanwhile, the measurement and the current data blocks have the same data structure comprising the composition of the In-phase component ("I") and the Quadrature component ("Q"). Each component has 24 bits, and the least significant bit (LSB), i.e. "IL" or "QL", is sent out to the connected PC first. The total storage required for each recording is 26,638,002 Bytes.

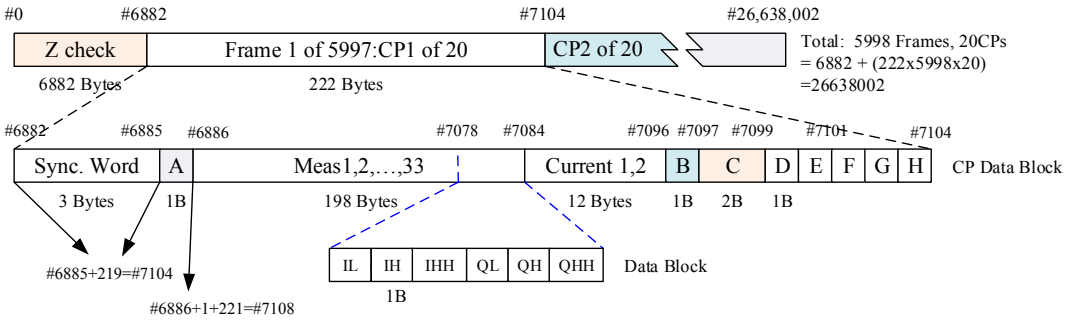

A	ADCSat 1-8
B	CP Identification check
C	CPCounter bit 1-16
D	ADCSat 9-12 , CPCounter bit 20-17
E	ADCSat 13-19, BadSine
F	Current Drive Check, BadSine
G	ADCSat 20-26, Stimulus Marker1
H	ADCSat 27-33, Stimulas Marker2

Figure F-1 The data stream structure of the modified fEITER firmware (24-bit data read-out version)

Appendix G New Phantom Circuit

Resistor phantom (or resistor network/ wheel phantom) is usually designed for preliminary test an EIT instrument. Basically, it is a symmetrical network of resistors, designed for producing a certain set of known measurement values. These values must be in the measurable range of the instrument. The circuit could be simple as shown in (Fabrizi et al., 2007), or more complicated, e.g. some resistors are changeable or capacitors are able to be added (Griffiths, 1988). The new resistor phantom of fEITER system (Figure G-1) is newly build, which is sturdier and less tolerance than the old resistor phantom (not explained here). The schematic of the new resistor phantom is shown in Figure G-2. The load resistors are 160 Ω-resistors and 560 Ω-resistors. The resistors of 21.5 Ω are used as trans-resistors. The pin connectors of the phantom are located in the same locations of the electrode receptacles of the fEITER head box. Therefore, direct plugging the phantom to the head box is allowed, i.e. no additional leads are required.

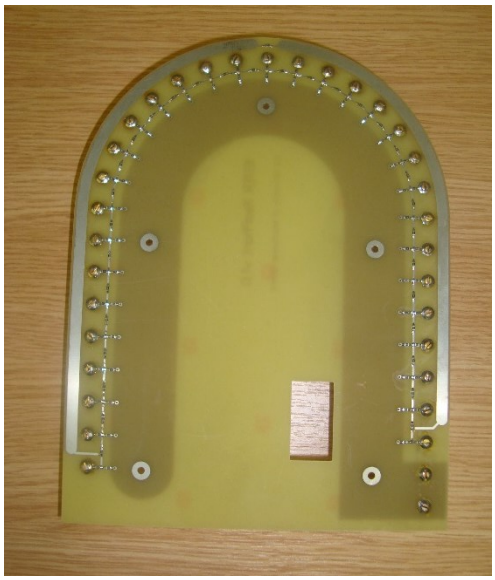

Figure G-1 The new resistor wheel phantom of fEITER system

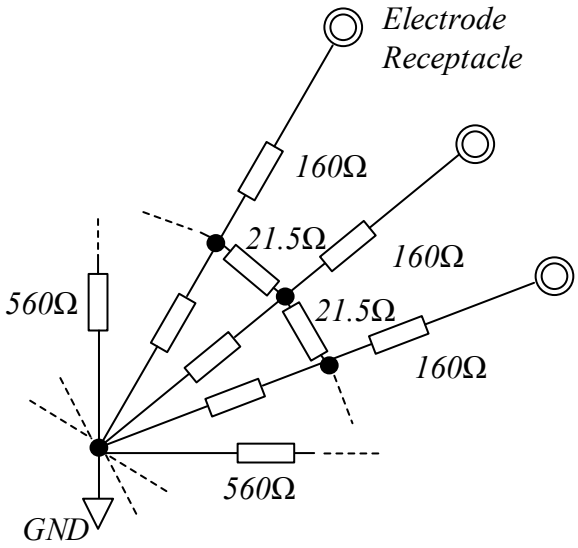

Figure G-2 The circuit of the new resistor wheel phantom

Appendix H Magnitude of Conductivity Changes due to Brain Stimulations

Table H-1 The reported magnitude of conductivity changes due to brain stimulations (continue overleaf)

Conditions/ Stimulations	Subjects	EEG/ EIT settings	Changing conductivity (Δσ)/ impedance (ΔZ) (mean±standard deviation)
Total ischaemia (Hossman, 1971)	Cats	0.1 Hz pulse, 6-10 μA, measure at the cortex	(+) 148% (ΔZ)
Global cerebral ischaemia, by diathermy of the vertebral arteries (Holder, 1992d)	Rats	50 kHz, 22-56 $\mu A_{pk\text{-}pk}$, 1/60 fps, record over 200 minutes, measure at the cortex	(+) 50%-200% (ΔZ)
Cerebral ischaemia (lasted for 5-30 minutes), by occluding the carotid arteries (Holder, 1992a)	Rats	50 kHz, 22-56 $\mu A_{pk\text{-}pk}$, 1/60 fps, record over 200 minutes, measure at the cortex	(+) 15%-60% (ΔZ) The changing amplitude of the scalp measurement voltages was 10%-20% of those measured on the cortex
Monitoring head trauma (Manwaring et al., 2013)	Piglets	50 kHz, 5 mA, 100 fps, measure at the scalp with an additional intracranial electrode; Trauma were produced by ballooning.	(-)8.98±8.58%(balloon inflation) (Δσ) (+)7.40±6.93%(balloon deflation) (Δσ) (-)15.35±9.06%(blood injection) (Δσ)
Spreading depression (Freygang and Landau, 1955)	Cat	Square wave (NA Hz) NA current, measured on the cortex and underlying tissues	(+) 23±2% at the upper 0.8 mm from the cortex (ΔZ) (+) 5.5±0.7% in the depths of 0.5 to 1.5 mm of the cortex (ΔZ) (-) 52±0.5% in the white matter (ΔZ)
Cortical spreading depression (CSD) (Holder, 1992b)	Rats	50 kHz, 22-56 $\mu A_{pk\text{-}pk}$, 1/60 fps, record over 200 minutes, measure at the cortex	(+) 39±4.8% (ΔZ) Unexpected (-) 0.8±0.2% (ΔZ) was found when measured on the skin due to the increase in the temperature of the cortex
Spreading depression (Holder and Gardner-Medwin, 1988)	Rats	50kHz, NA current, measure at the cortex	(+) 30% on the cortex (ΔZ) (+) 15% on the dura (ΔZ) (+) 2-3% on the skull (ΔZ) (-) 1% on the scalp (ΔZ)
Spreading depression (Holder, 1992b, Ranck, 1964)	Rabbits	50 kHz, 22-56 $\mu A_{pk\text{-}pk}$, measure at the cortex	(+) 73% (ΔZ) @ 5 Hz (+) 77% (ΔZ) @ 500 Hz (+) 43% (ΔZ) @ 50 kHz
Spreading depression (Boone, 1995)	Rabbits	DC, 5 μA	(+) 5-20% (ΔZ)

Conditions/ Stimulations	Subjects	EEG/ EIT settings	Changing conductivity (Δσ)/ impedance (ΔZ) (mean±standard deviation)
Edema (Fu et al., 2014)	Human patients	50 kHz, 1 mA, 1 fps (10 frames were averaged for one data), measure at the scalp	(+) 531% during the dehydration treatment (ΔZ)
Hypotension (Gamache et al., 1975)	Monkeys	NA	(+) 27% (ΔZ)
Epilepsy (Fabrizi et al., 2006)	Humans	38.4 kHz, 2.2 mA, 2-2.5 fps, 258 measurements, measure at the scalp	60-450% (Δσ) - not concordant with the outcomes from EEG and fMRI
Epilepsy (Dowrick et al., 2015)	Rat	2.2 kHz – 2.6 kHz, 50 μA, 1,000 fps, measure at the cortex	(+) 6.28% (ΔZ) @ 2.2 kHz (+) 3.91% (ΔZ) @ 2.6 kHz
Epilepsy (Elazar et al., 1966, Harreveld and Schadé, 1962)	Rabbits and cats	AC Current (NA Hz) 1,000 fps recording speed	(+) 3-12% (ΔZ)
Focal and generalized epileptic activity (Rao, 2000)	Rabbits	51 kHz, 5 mA, measured on the cortex	(+) 5.5-7.1% (ΔZ) With direct measurement, the changing amplitude was (+) 9.5-14.3% (ΔZ).
Evoked physiological activity (Liston et al., 2012)	Human cortex model	DC, used the cable theory, based on a biophysical model	(-) 0.6% (0.06-1.7%) (ΔZ)
Direct cortical stimulation (Freygang and Landau, 1955)	Cat	Square wave (NA Hz) NA current, measured on the cortex.	(-) 3.1±0.8% (ΔZ)
Direct cortical stimulation (Holder and Gardner-Medwin, 1988)	Rats	50kHz, NA current, measure at the cortex	Max change was 0.01% (ΔZ)
Sensory evoked potential (SEP) (Boone, 1995)	Rabbits	DC, 5 μA; The stimulus was a 70 V pulse of duration 0.5 ms, applied to the median nerve, measured on the auditory cortex.	(-) 0.01-0.03% (ΔZ)
Sensory evoked potential (SEP) (Holder et al., 1996)	Rabbits	50 kHz, 1 mA, 1/15 fps, record over 10-20 minutes, measure at the cortex; SEP was produced at the forepaw with a 0.1 ms square wave, delivered at 5 Hz for 3 minutes	(-) 2.7±2.4% (ΔZ) The change over the neighbouring area was (+) 2.9±2%. The latency of P1 was 13.8±1.5 ms, and that of N1 was 32.8±3.0 ms. SEP amplitude was about 30μV.

Conditions/ Stimulations	Subjects	EEG/ EIT settings	Changing conductivity (Δσ)/ impedance (ΔZ) (mean±standard deviation)
Somatosensory stimulation (Sensory evoked potential -SEP) (Oh et al., 2011a)	Rats	125-1,225 Hz, 5 μA, measured on the cortex; SEP was produced at the contralateral forepaw with a 0.1 ms square wave, delivered at 2 Hz.	(-) 0.074±0.01% @ 125 Hz (-) 0.070±0.006% @ 225 Hz (-) 0.027±0.005% @ 325 Hz (-) 0.022±0.003% @ 625 Hz (-) 0.01±0.01% @ 1225 Hz (All were ΔZ)
Sensory evoked potential (SEP) (Tidswell et al., 2001a, Tidswell et al., 2001c)	Humans	50 kHz, 1-2.5 mA, 1/25 fps, 258 measurements, measure over the scalp; SEP were produced at the wrist with a 3Hz, 0.1 ms square wave, delivered at 3 Hz for 75 seconds.	The change was 0.19±0.02% (ΔZ). The latency of the response was 5.8±0.9 S.
Motor response (Tidswell et al., 2001c)	Humans	50 kHz, 1-2.5 mA, 1/25 fps, 258 measurements, measure over the scalp; Motor stimulation was produced by sequential apposition of the thumb with self-pace.	The change was 0.34±0.05% (ΔZ)
Visual evoked response (VER) (Holder et al., 1996)	Rabbits	50 kHz, 1 mA, 1/15 fps, record over 10-20 minutes, measure at the cortex; VER was evoked by photic stimulation to both eyes, delivered at 10 Hz for 2.5 minutes	(-) 4.5±2.7% (ΔZ) The change over the neighbouring area was (+) 1.7±1.1%. The latency of the initial response was 25±1.3 ms. VER amplitude was about 90μV.
Visual evoked response (VER) (Tidswell et al., 2001a, Tidswell et al., 2001c)	Humans	50 kHz, 1-2.5 mA, 1/25 fps, 258 measurements, measure at the scalp; VER was evoked by 0.6º checkerboard oscillating at 8 Hz.	The change was 0.43±0.05% (ΔZ)
Visual evoked response (VER) (Holder and Gardner-Medwin, 1988, Holder, 1989)	Humans	50kHz, NA current, measure at the scalp; VER was evoked by flash stimulation	Max change was 0.005% (ΔZ)
Visual evoked response (VER) (Gilad et al., 2005b)	Humans	Used bipolar square wave (NA Hz) 100-200 μA, measure at the scalp; VER was evoked by 41.7/60º checkerboard oscillating at 2 Hz.	Max change was 0.01% (ΔZ) Expected P100 was observable.

Conditions/ Stimulations	Subjects	EEG/ EIT settings	Changing conductivity (Δσ)/ impedance (ΔZ) (mean±standard deviation)
Visual evoked response (VER) (Gilad and Holder, 2009, Gilad et al., 2009b)	Humans	Used bipolar square wave (1 Hz) 100-1,000 μA (295 μA mean), 1,024 fps, measure at the scalp; VER was evoked by 41.7/60º checkerboard oscillating at 2 Hz.	(-) 0.0010±0.0005% (ΔZ) (0.30±0.15 μV) In the case of prediction, the estimated change was 0.0039±0.0034% (1.03±0.75 μV).
Auditory evoked response (AER) (Gilad et al., 2009b, Gilad et al., 2009a, Klivington and Galambos, 1968)	Cats	10 kHz, NA current; AER was evoked by click stimuli with 0.1 ms pulse, 74 dB, measured on the auditory cortex.	(-) 0.003% (ΔZ) in the cortex (-) 0.03% (ΔZ) in subcortical nuclei
Nerve stimulation (Holder and Gardner-Medwin, 1988)	Frog sciatic nerves	50kHz, NA current	Max change was 0.02% (ΔZ)
Nerve stimulation (Boone, 1995)	Crab nerves	DC, 5 μA, measured on the nerve with 1-4 mm spacing between drive electrodes	(-) 0.01% (ΔZ) for transverse measurement (-) 1.0±0.6% (ΔZ) for longitudinal measurement
Nerve stimulation (Gilad et al., 2009a)	Crab nerves	Square wave of 1 Hz, 1-10 μA, measured on the nerve with 2-8 mm spacing between drive electrodes	(-) 0.85±0.4% (ΔZ)
Nerve stimulation (Oh et al., 2011a)	Crab nerve	125-825 Hz, 5-10 μA, measured on the nerve with 2-8 mm spacing between drive electrodes	(-) 0.33±0.05%@125 Hz (-) 0.19±0.03%@175 Hz (-) 0.08±0.01%@475 Hz (-) 0.05±0.01%@825 Hz (All were measured @ 2mm. And all were ΔZ)
Nerve stimulation (Liston et al., 2012)	Crab nerve model	DC, used the cable theory, based on a biophysical model	(-) 2.8% (ΔZ)

Remark:

The conductivities or impedances displayed in the table are kept to be the same of the literature. The change in impedance $\Delta Z(\%)$ can be converted to the change in conductivity $\Delta\sigma(\%)$ by this formula: $\Delta\sigma(\%)=\left(\frac{1}{1+\Delta Z(\%)/100}-1\right)\times 100.$

Appendix I Simulation and Experiment Test Cases

I.1 Case 1: Two-Dimension Circular Phantom

The simulation was performed on two 175mm-diameter concentric layers models: one was the forward finite element model containing 10,816 elements (Figure I-1(a)) and another one was the inverse model containing 9,216 elements (Figure I-1(b)). Four layers regarding as the scalp (the outermost), skull, CSF, and brain (the innermost) were generated with the configuration shown in Table I-1. For the inverse model, the scalp layer was thicker and less conductive, whilst the skull layer was thinner and more conductive. Three inclusions were simulated with two schemes as the configuration in Table I-2 and Figure I-1(c): small change scheme and large change scheme. The number of measurements was 208, performed on 16-electrode configuration and 1 mA_{rms} excitation current with diametric driving patterns. The SNR was simulated with 50 dB. Non-linear regularised Gauss-Newton algorithm was used with 10 iterations. The regularisation parameter was 0.1 for the absolute imaging approach, and 0.001 for the novel difference imaging approach.

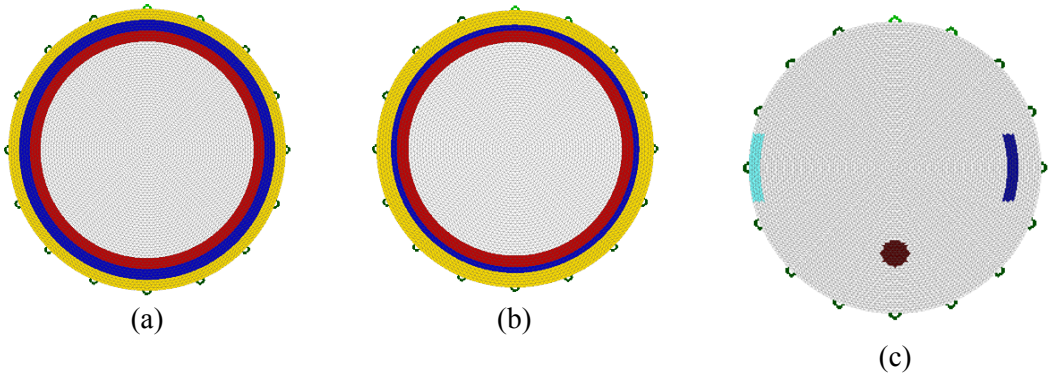

(a) (b) (c)

Figure I-1 Head-like models and inclusion locations of Case 1: (a) the forward model, (b) the inverse model, (c) three inclusion simulated in the forward model in the layer of the scalp (light blue colour), the CSF (the dark blue colour), and the brain (brown colour).

Table I-1 Thicknesses and conductivities of models used in Case 1

Layer	Forward Model		Inverse Model	
	Thickness (mm)	Conductivity (S/m)	Thickness (mm)	Conductivity (S/m)
Scalp	7	0.58	8.87	0.4348
Skull	6	0.008	3.54	0.0154
CSF	7	1.802	7.08	1.802
Brain	radius = 65	0.2849	radius=65.5	0.2849

Table I-2 Conductivity of the inclusions of the simulation schemes used in Case 1

Testing Object	Location	Scheme1: Small change Conductivity S/m (%, S/m)	Scheme2: Large change Conductivity S/m (%, S/m)
Inclusion 1	Scalp	0.551 (-5%, -0.03)	0.493 (-15%, -0.09)
Inclusion 2	CSF	1.748 (-3%, -0.05)	1.623 (-10%, -0.18)
Inclusion 3	Brain	0.646 (+127%,+0.36)	0.646 (+127%,+0.36)

I.2 Case 2: Simple Tank Situation

The experiment was performed on a 250-mm diameter cylindrical tank filled with 2.7 S/m-conductivity saline (Figure I-2(a)). Thirty-two electrodes installed on two planes, and 420 measurements were recorded by fEITER system with $1mA_{pk-pk}$ current. The electrode plane heights were 32 mm and 76 mm. These heights were intentionally shifted in the inverse model, i.e. the heights were 42 mm (10 mm shifted distance) and 78 mm (2 mm shifted distance) (Figure I-2(b)). The testing inclusion was a 50-mm-diameter aluminium rod. The number of elements of the inverse model was 34,560, and the geometry of an electrode in the model was set to a point with 1,200 $\Omega \cdot m^2$-contact impedance. Due to the high computation memory required, Newton-Krylov General Minimal Residual (Newton-Krylov GMRes) method was used to reconstruct, in addition with the smoothness prior with 0.001-regularisation parameter. The number of Krylov subspaces was 200 and the number of iteration was 10. The absolute imaging approach and the novel difference imaging approach were investigated.

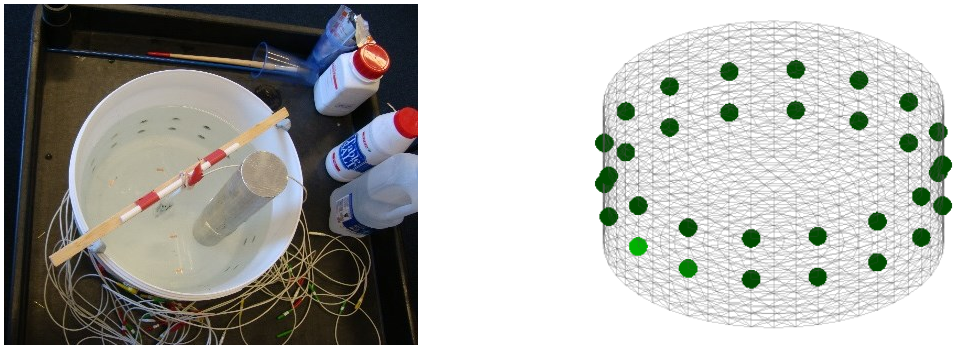

(a) (b)

Figure I-2 Experiment configuration of Case 2: (a) the cylindrical tank filled with saline - the aluminium rod was used as the inclusion, (b) the inverse model. The electrode plane's heights were intentionally shifted from the exact heights.

I.3 Case 3: Head-Like Tank Situation

The experiment was performed on a head-shape tank filled with 2.7 S/m conductivity saline (Figure I-3(a)). Thirty-two electrodes were placed all around the head tank as the layout shown in Appendix D. The inverse model used in reconstruction was not constructed from the head-shape tank model, but it was constructed from a MR image of a human head. The head model was included with the geometry of 10-mm-diameter electrodes (Figure I-3(c)), containing 93,687 elements. The distance between the nasion and the inion, and between the left-right preauriculars of the head tank were both 360 mm, but these distances of the inverse model were both approximately 380 mm. Testing inclusion was a carrot which was 28 mm in length and 13.5 mm in radius (Figure I-3(b)). The carrot was dipped with its full length into the centre of the tank and then moved to the left and the right. fEITER system was used to measure with $1mA_{pk\text{-}pk}$ excitation current (in diametric direction) and 546 measurements per recording frame. The recording speed was actually 100 frame per second, however, the measurements were averaged over 50 records, i.e. the effective imaging speed was reduced to 2 fps, for reducing measurement noise. Regularised Newton-Krylov GMRes method used in the previous case were used again in this case, but the regularisation parameter was changed to $1x10^{-3}$ for the absolute imaging approach, or $1x10^{-7}$ for the novel difference imaging approach.

(a) (b) (c)

Figure I-3 Experiment configuration of Case 3: (a) the head-like tank filled with saline, (b) the arbitrary geometry of the tank and the carrot used as the inclusion, (c) the inverse model constructed from the MR image of a human

I.4 Case 4: Head-Like Tank Situation with a Skull-Like Material

The head-like tank as well as the configuration used in Case 3 were used again in this case. However, a honeydew melon peel was put inside the tank, regarding as the skull (Figure I-4(b)). The peel was in ellipsoid-like shape having approximately 89.13 mm in major radius and 71.62 mm in minor radius, where the thickness was approximately 10 mm (Figure I-4(a)). The peel was naturally dried for a week for minimising the moisture content, and this resulted in small deformation of the geometry. The peel geometry was generated into the inverse model with 10 mm-thickness ellipse having 85 mm in major radius and 70 mm in minor radius (Figure I-4(c)). The procedure of carrot dipping was slightly changed from the previous case. Since the peel freely floated in the saline fluid, the carrot was gently dipped into the centre of the melon peel and slowly removed out to avoid the movement of the peel. The absolute imaging approach and the novel difference imaging approach were investigated.

Since the conductivity of the peel was unknown, the conductivity estimation explained in Chapter 3 was repeated here with the regularisation parameter of $1x10^{-3}$ and the initial guess conductivity of 0.1 S/m. Furthermore, the peel conductivity was kept to be unchanged in the reconstruction process as the region of non-interest.

(a) (b) (c)

Figure I-4 Experiment configuration of Case 4: (a) the honeydew melon (before removing the content and before drying and the carrot used as the inclusion (b) the peel after drying and installing inside the head-like tank (c) the inverse model – the middle layer is imposed as the peel layer

I.5 Case 5: Cylindrical Tank Situation

The simulation was performed on an 828 element-cylindrical tank model. The tank was homogeneous with 32 electrodes installed (Figure I-5). The simulated

current was 1 mA_{rms} driving in near-diametric directions, and 896 measurements were performed. The background conductivity was 20 S/m. Two inclusions were simulated with the conductivity of 29 S/m (+45%) and 15 S/m (-25%). The contact impedance was set at 0.1 $\Omega \cdot m^2$. No noise was simulated in this simulation.

Two Krylov subspace methods were investigated: Newton-Krylov Generalized Minimal Residual method (GMRes) based on Arnoldi projection, and Quasi-Minimal Residual (QMR) based on Lanczos projection. The number of subspaces was 500. The smoothness prior information was used (Horesh, 2006, Horesh et al., 2007) with the regularisation parameter of $1x10^{-8}$. Regularised Gauss-Newton method was used to solve the projected problem (obtained by the Arnoldi projection or the Lanczos projection) with two options of very low regularisation parameter, i.e. $1x10^{-14}$ and $1x10^{-12}$.

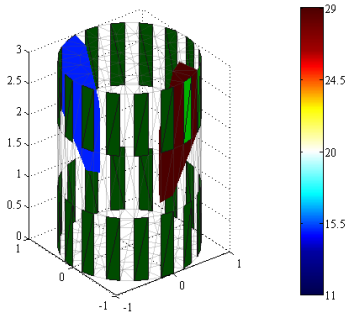

Figure I-5 Simulation configuration of Case 5: the cylindrical tank filled with saline with two inclusions

I.6 Case 6: Realistic Head Situation

The experiment was performed on a healthy male subject during the left carotid artery compressing for Transient Hyperaemic Response Test (THRT). fEITER system used in Case 3 was used again here. An electrode array was attached on the scalp as the layout shown in Appendix D. ZipPrep electrodes were used and the contact impedance was set to 1,200 $\Omega \cdot m^2$ (Robinson et al., 2008, Robinson, 2011). The current drive patterns and the measurement schemes were followed the configuration explained in Appendix D with 100 fps recording speed.

Regularised Newton-Krylov GMRes method was used to reconstruct with 200 Krylov subspace configuration. Non-regularised Gauss-Newton method was

used to solve the projected problem. The smoothness prior was selected with the regularisation parameter of $1x10^{-7}$ (this value was evaluated by the L-Curve method). The number of iteration was 15, and the past step length strategy (proposed in Section 5.2) for avoiding the divergence was engaged. The initial guess conductivities were the values proposed in Chapter 3. The region of non-interest was set to the skull for all used models. The reconstruction was carried on Intel i7-3770 3.40GHz with 16 GByte memories. The computer operation system was Windows 7. EIDORS' forward solver was used (Adler and Lionheart, 2006, Polydorides and Lionheart, 2002), ran on Matlab R2014a.

Six head models from three origins were constructed in this research. All models were investigated for the possibility to use as generic models and for determining the suitable mesh resolution (Figure I-6 and Figure I-7). Three of them were remeshed from the model received from University College London, named "synthesized models", containing 158,168 elements (coarse mesh resolution), 208,311 elements (medium mesh resolution), and 274,128 elements (fine mesh resolution). For these models, the geometry of the grey matter and the white matter were different to the reality, and the naval cavity was included. The next model, named "non-subject model", was constructed from an MR image of a non-subject, containing 212,658 elements. Due to the superb quality of this MR image, the geometry of this non-subject model was very good. However, the symmetricity of the left and the right side was not good, because, may be, the MR image was needed to realign before to be used for construction. The two last models, named "subject models", were constructed from a subject MR image, containing 178,480 elements and 298,312 elements. However, the quality of the MR image was not good. The tissue geometries then were not accurate, in particular, that of the skull. Note than the electrode geometry was manually included in all models.

Due to the presence of pulsation Rheoencephalographic (REG) signal in the measurements, the frame data over cardiac cycles were averaged before reconstruction. The reference data of the experiment was the average of the measurements from the 1053^{rd} to the 1144^{nd} frame (850 ms period, i.e. a cardiac cycle), in the period before performing the occlusion. The investigated data was the

average of the measurements from the 1319th frame to the 1407th frame (880 ms period), in the period of carotid artery compression on the left side, that was the 3rd cardiac cycle after the occlusion started.

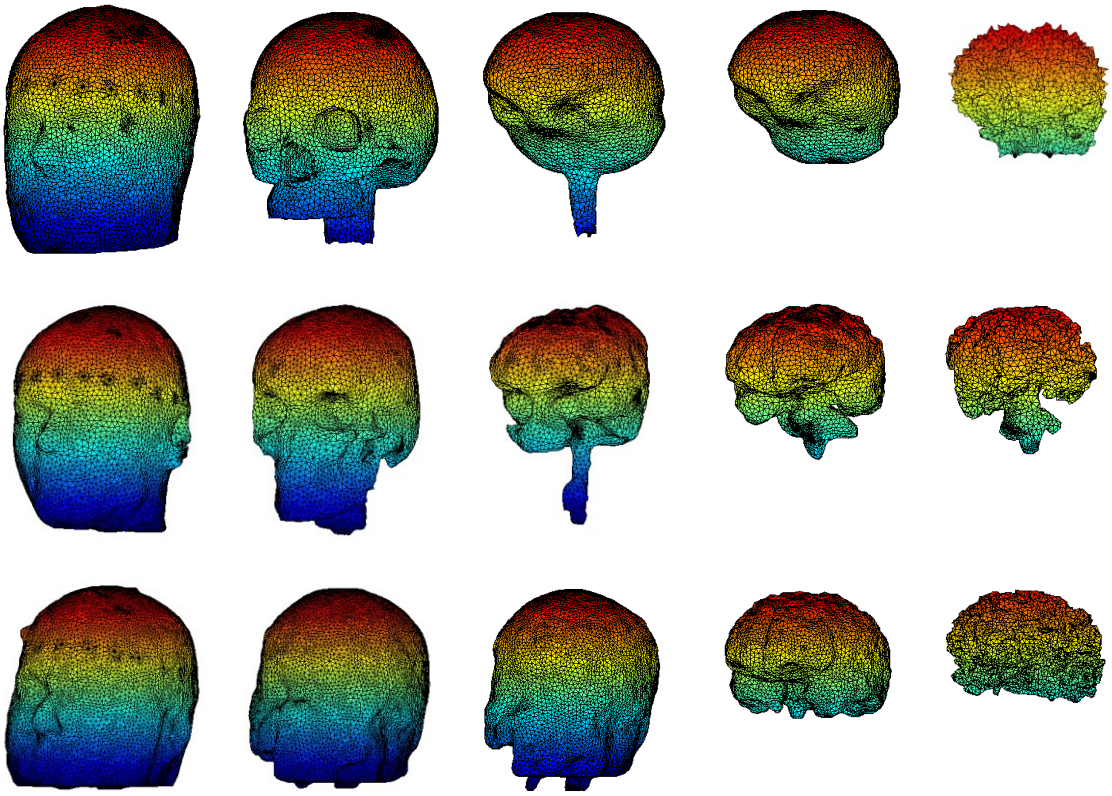

Figure I-6 Tissue geometries of the head models used in Case 6: (upper row) the synthesized head model, (middle row) the non-subject head model, and (bottom row) the subject head model. Each model comprises five important tissues: (from the left to the right) the scalp with electrode geometry integration, the skull, the cerebrospinal fluid (CSF), the grey matter, and the white matter

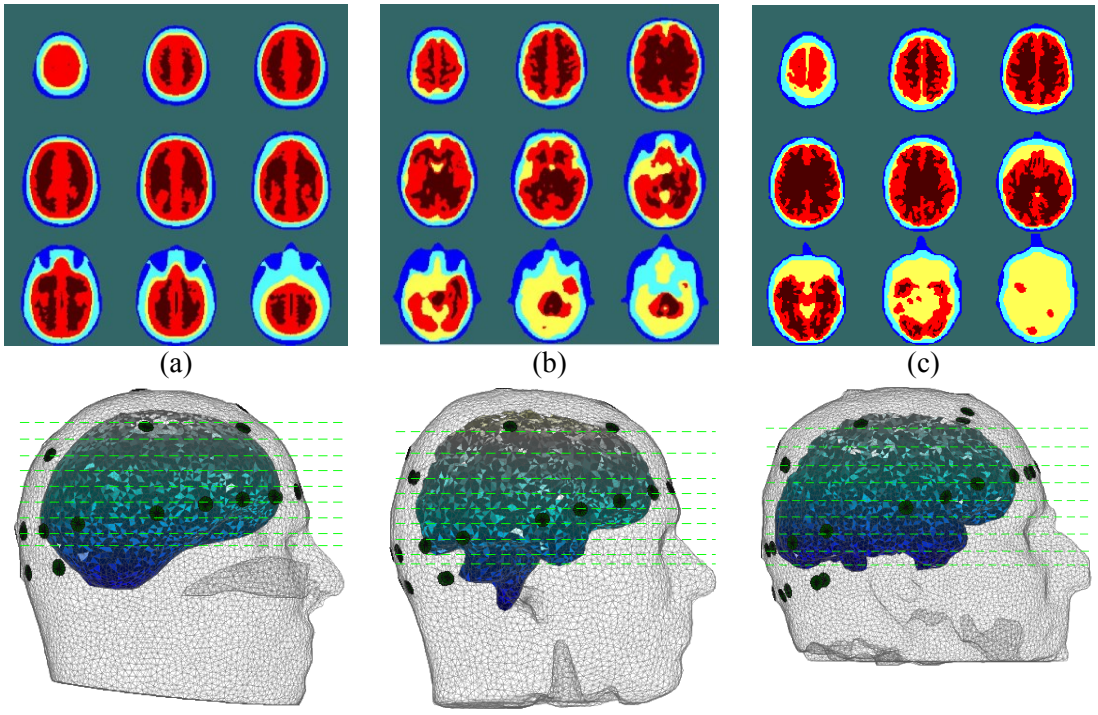

Figure I-7 Transversal sections of the models shown in Figure I-6: (a) the synthesized head model, (b) the non-subject head model, and (c) the subject head model. The section plane locations of (a-c) are shown in (d-f).

Appendix J Published Papers

1. Ouypornkochagorn, T., McCann, H. and Polydorides, N. 'Tackling Modelling Error in the Application of Electrical Impedance Tomography to the Head', 37th Annual International Conference of the IEEE Engineering in Medicine and Biology Society (EMBC), Milan, Italy, 25-29 August, 2015.
2. Ouypornkochagorn, T., McCann, H., Terzija, N., Parry-Jones, A. and Polydorides, N. 'Electrical Impedance Measurement of Cerebral Haemodynamics', 16th International Conference on Biomedical Applications of Electrical Impedance Tomography, Neuchatel, Switzerland, 2-5 June, 2015.
3. Ouypornkochagorn, T., Polydorides, N. and McCann, H. 'In Vivo Estimation of the Scalp and Skull Conductivity', 15th International Conference on Biomedical Applications of Electrical Impedance Tomography, Gananoque, Ontario, Canada, 24-26 April, 2014.
4. Polydorides, N., Ouypornkochagorn, T. and McCann, H. 'An approximate gradient for fast nonlinear inversion of the EIT model', 16th International Conference on Biomedical Applications of Electrical Impedance Tomography, Neuchatel, Switzerland, 2-5 June, 2015.
5. Polydorides, N., Ouypornkochagorn, T. and McCann, H. 'Inequality Constrained EIT Modelling and Inversion', 15th International Conference on Biomedical Applications of Electrical Impedance Tomography, Gananoque, Ontario, Canada, 24-26 April, 2014.